NASA
Reference
Publication
1292, Vol. II

March 1993

The Atmospheric Effects of Stratospheric Aircraft: Report of the 1992 Models and Measurements Workshop

Volume II—Comparisons With Global Atmospheric Measurements

NASA

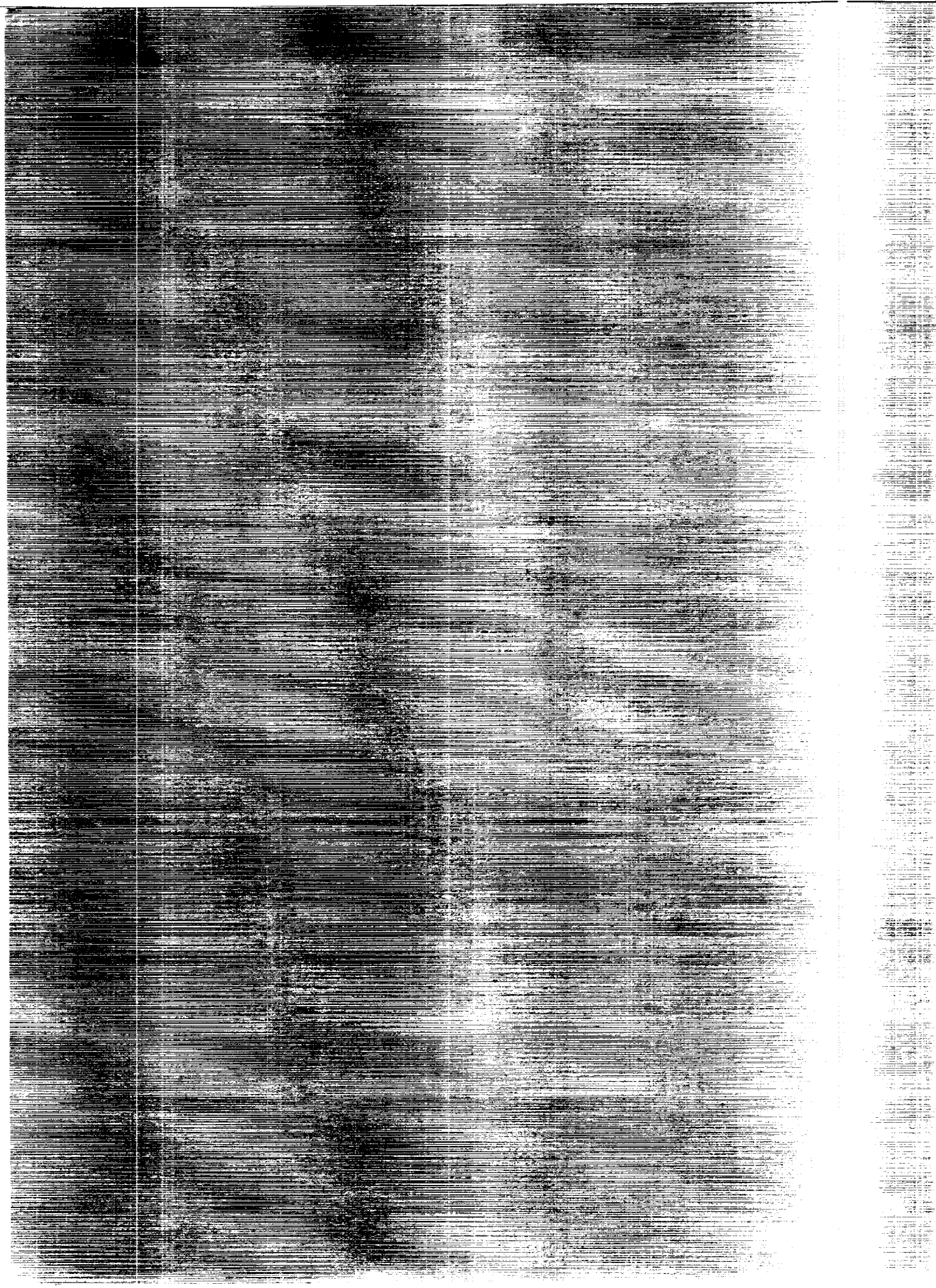

NASA Reference Publication 1292, Vol. II

1993

The Atmospheric Effects of Stratospheric Aircraft: Report of the 1992 Models and Measurements Workshop

Volume II—Comparisons With Global Atmospheric Measurements

Edited by
Michael J. Prather
NASA Office of Space Science and Applications
Washington, D.C.

Ellis E. Remsberg
Langley Research Center
Hampton, Virginia

NASA
National Aeronautics and Space Administration
Office of Management
Scientific and Technical Information Program

Contributing Authors:

G. Anderson
C. Bruhl
B. Connor
A. Douglass
R. Eckman
D. Fahey
D. Fisher
I. Folkins
R. Garcia
C. Granier
W. Grose
M. Hitchman
C. Jackman
R. Kawa
J. Kaye
J. Kinnersley
D. Kinnison
M. Ko
M. Kurylo
R. McPeters
C. Miller
R. Nagatani
P. Newman
G. Pitari
C. Rinsland
R. Rood
J. Rosenfield
T. Sasaki
U. Schmidt
R. Seals
M. A. Smith
R. Stolarski
K.-K. Tung
D. Weisenstein
H. Wesoky
D. Wuebbles
G. Yue
Y. Yung
J. Zawodny

TABLE OF CONTENTS

VOLUME I

VOLUME II

VOLUME III

Key to Model Data in Plots

- ○ AER
- ● CALJPL
- □ CAMED-Theta
- ■ DUPONT
- ⊛ GISS
- △ GSFC
- ▲ ITALY
- ◇ LLNL
- ⊠ LLNL-ND
- ◬ MPI
- ◈ MRI
- ◆ NCAR
- ▽ NOCAR
- ▼ WASH

A: Temperature, Net Heating and Circulation

A: Temperature, Net Heating, and Circulation

Ronald M. Nagatani
National Meteorological Center

Joan E. Rosenfield
NASA-Goddard Space Flight Center

1: Temperature Comparisons

INTRODUCTION

There are two main temperature climatologies used by the models. One is that of temperatures from the National Meteorological Center (NMC) and the other is the Barnett and Corney (BC) (1985) climatology. The CAMED-theta model and the NCAR models calculate their temperatures interactively, while the ITALY model uses output from a three-dimensional general circulation model. Table A-1 summarizes the different models and their temperatures. The DUPONT, GSFC, CALJPL, and the WASH models use the NMC climatology developed by GSFC, while the MPI and old LLNL models use the BC climatologies. For this experiment, the new LLNL model also uses the prescribed BC climatology. The AER model also uses a climatological data set, but the upper stratosphere is quite different from the other two, as will be evident in its comparison. While the NCAR model calculates its temperatures above 15 km, it uses NMC climatological data below 10 km and linearly interpolates between 15 km. In comparing the model temperatures, we will be using the 8-year climatological temperatures for the period 1979-1986 from the National Meteorological Center as a basis for comparison, not necessarily implying that the temperatures are correct.

Table A-1. Temperature

	FIXED	CALCULATED
LLNL	BARNETT AND CORNEY	
LLNL(New)		INTERACTIVE
ITALY	3-D QG MODEL OUTPUT (OFFLINE)	
DUPONT	NMC	
GSFC	NMC	
CAMED		INTERACTIVE
AER	CLIMATOLOGY	
CALJPL	NMC	
MPI	BARNETT AND CORNEY	
WASH	NMC	
NCAR	NMC BELOW 10 km	INTERACTIVE ABOVE 15 km

The NMC temperatures are from daily operational analyses at 1200 GMT. Radiosondes and other ancillary data are included in the analyses from 1000 to 10 hPa in the northern hemisphere and 1000 to 100 hPa in the southern hemisphere. Only satellite data from NOAA operational

satellites are included in the analyses from 10 to 0.4 hPa in the northern hemisphere and 100 to 0.4 hPa in the southern hemisphere. Because there are discontinuities in the data when the satellites are changed, data have been adjusted to eliminate those discontinuities in a scheme described by Gelman et al. (1986). The BC climatologies use a combined climatology compiled by Oort (1983) for levels from 1000 to 50 hPa, the 30 hPa average from the Berlin Free University for January 1968 to December 1972, and satellite data from the Selective Chopper Radiometer (SCR) on Nimbus 5 (January 1973 - December 1974) and the Pressure Modulator Radiometer (PMR) on Nimbus 6 (June 1975 - July 1978) for levels above 30 mb.

TEMPERATURE DATA

Figures A-1a-1f show the model temperatures that were either prescribed for the models or calculated interactively. Figure A-1a shows the NMC climatology used by GSFC for March, June, September, and December. Figure A-1b shows the BC data used by the LLNL model, while the AER climatological data are shown in Figure A-1c. Figure A-1d shows the temperatures from the ITALY three-dimensional quasi-geostrophic model while Figures A-1e and 1-f show temperatures calculated from the NCAR and CAMED-theta models, respectively.

Some of the salient features in the figures are mentioned here, but the difference plots discussed in the next section show the differences more graphically and give an idea of the numerical differences. In general, the lower stratosphere is similar for most of the models except for the CAMED-theta model, which generates a tropical tropopause that is lower in altitude than shown by the other data. For the most part, the largest differences begin to appear near the polar regions at midstratospheric levels and above. The climatologies are similar at lower stratospheric levels because radiosondes are mainly used for levels up to the middle stratosphere but the upper stratospheric climatologies use different satellites, hence their larger differences. The models appear to have a tendency to generate polar stratospheric temperatures colder than the NMC temperatures.

DIFFERENCE PLOTS

Figures A-2a-2e are difference plots between the NMC temperature data and the various model temperatures. To put them in perspective with regard to interannual differences of the monthly zonal mean temperatures or the typical variance over the zone and month, see Nagatani et al. (1988) or Randel (1992). Figure A-2a is the difference between the NMC climatology and the BC climatology. The NMC data only go up to 0.4 hPa (54.37 km for z^*), so the strong differences shown above those levels are extrapolated data and are artifacts introduced into the levels where there are no data for NMC. The largest differences between the two climatologies in the lower stratosphere (below 30 km for z^*) are in December in the south polar regions near 20 km where BC is warmer by 10° C or greater than NMC and the north polar regions where BC is colder than NMC near 30 km. In June and September in the south polar regions, the cold polar region for NMC is lower in altitude than the BC cold polar region, causing a colder region for BC near 30 km overlaid by a warmer region. In the summer hemisphere at middle to upper stratosphere, the BC temperatures are warmer than the NMC temperatures, and in the winter hemisphere BC temperatures are colder than NMC temperatures. Overall, however, the temperatures in the lower stratosphere between the two climatologies are very similar.

The largest differences between NMC and the AER climatology are shown in Figure A-2b at upper stratospheric levels, where most of the differences are in the polar regions where AER shows a very cold polar region. The lower stratosphere looks similar except in September near 20 km over the south polar region, where AER is warmer than NMC.

ITALY, NCAR, and CAMED-theta in Figures A-2c-2e are model-generated temperatures that have similar high-latitude differences when compared with NMC temperatures. They all have a warmer northern hemisphere, upper stratospheric, summer polar region; in general a colder winter polar region, a colder northern hemisphere polar region in March, and a colder southern hemisphere polar region in September. The other prominent difference is the placement of the tropical tropopause at a lower altitude for the CAMED-theta model than most of the other data. This gives a pattern of colder temperatures overlaid by warmer temperatures, as shown in the tropical region in Figure A-2e.

SUMMARY

Except for the southern hemisphere regions where data are sparse, temperatures in the lower stratospheric region for the NMC, BC, and AER climatologies are quite similar. The upper stratosphere, however, is very different, leading to differences in gradients and absolute magnitudes, which will lead to heating rates that are quite different (*see* section 2: Heating Rate and Circulation Intercomparisons). The models generate polar regions that are cold compared to NMC standards, and CAMED-theta generates a tropical tropopause that appears to be lower than either the NMC or BC climatologies.

2: Heating Rate and Circulation Intercomparison

SOLAR HEATING AND INFRARED COOLING PROFILE

This section begins with a discussion of the results of the intercomparison of the solar heating and infrared cooling profile that were requested as part of experiments A and K. The standard atmosphere consisted of ATMOS 31N temperature, O_3, H_2O, and CH_4 profiles, together with a solar zenith angle of zero. No clouds or aerosols were included. The models that participated in this experiment were CALJPL, CAMED-theta, DUPONT, GSFC, LLNL, and WASH. This should be strictly a comparison of the radiative transfer used by the various models, since all the data are the same, except for possible differences in CO_2 amounts and any other trace gases included in the radiation models. All the models include O_3 in the UV and visible, and CO_2, O_3, and H_2O in the thermal infrared. Table A-2 shows the additional gases included in the various models.

Table A-2. Additional Gases Included in Radiation

Model*	$Q_{UV, VIS}$	$Q_{NEAR-IR}$	Q_{IR}
CALJPL	Same as NEAR-IR	O_2, H_2O, CO_2, CH_4	CH_4, N_2O
CAMED	O_2, NO_2	H_2O, CO_2, O_2, CH_4, N_2O	
DUPONT	O_2		
GSFC	O_2	H_2O, CO_2	
ITALY		H_2O, CO_2	
LLNL	O_2, NO_2	H_2O, CO_2, O_2	
NCAR		H_2O, CO_2, O_2	
WASH	O_2, NO_2	H_2O, CO_2	CH_4, N_2O

* The above models all include O_3 in the UV and VIS, and CO_2, O_3, and H_2O in the IR.

The solar heating rate profiles are shown in Figure A-3, both the full profile and the lower stratospheric part. For those groups which submitted both a scattering and no-scattering run, it is the scattering run that is plotted here. In the upper stratosphere there is an 11% difference between the largest heating rate (CALJPL) and the smallest (DUPONT). Much larger relative differences are seen in the lower stratosphere, where at 25 km there is a 33% difference between the largest and smallest heating rates. The models appear to be bunched into two groups, with CALJPL and WASH having larger values and CAMED-theta, DUPONT, GSFC, and LLNL having smaller values. Some of these differences can be understood by examining Figure A-4, which shows the solar heating with and without Rayleigh scattering for the LLNL and WASH models. The scattering appears to add 1 degree/day to the heating rate at 25 km. The CAMED-theta and DUPONT models do not include scattering, while the GSFC model uses a very simplified treatment to include the effects of scattering. Thus, it is likely that a large part of the differences in solar heating rates at 25 km can be ascribed to the varying treatments, or lack of treatment of molecular scattering. Other differences at this altitude can be ascribed to the additional gaseous species included and to the diverse algorithms used for the species transmission functions.

There are large differences in the upper tropospheric solar heating rates. These are most likely due to differing assumptions about tropospheric water vapor, since H_2O is defined in the model atmosphere only at 14 km and above.

The infrared cooling rate profiles are shown in Figure A-5, both the full profile and the lower stratospheric part. The upper stratosphere shows differences of 20%, with CALJPL having the largest cooling rates and LLNL the smallest. In the lower stratosphere the relative differences are much greater, with a 40% difference at 25 km. These differences do not appear to be entirely explained by the differing numbers of gases included (Table A-2) and must also be due to the varying radiative transfer algorithms used. Again, the large differences in the upper troposphere are most likely due to the assumptions made about the H_2O profile below 14 km.

In summary, there remain large relative differences between model heating rate profiles, especially in the lower stratosphere. In the thermal infrared these differences must be ascribed to the different gases included and the variations in the radiative transfer algorithms employed. In the solar spectrum some of the differences appear to arise from the inclusion or omission of molecular scattering. It appears that molecular scattering makes an important contribution to the net solar heating in the lower stratosphere and should be included in radiative heating computations.

TWO-DIMENSIONAL MODEL HEATING RATES

The global net heating rates used or diagnosed in the two-dimensional models are shown in Figure A-6 for the months of June, December, March, and September. These heating rates are from the individual model's atmosphere. In the figure the plots labeled NMC refer to runs that were designed to be used for comparison purposes, not as the "correct" results. These calculations use the radiative transfer model described in Rosenfield et al. (1987), updated with the new wide-band parameterization (Rosenfield, 1991) of ozone infrared absorption. The solar heating in the Huggins band of ozone has been updated to take into account newer absorption cross sections (WMO, 1986). For the absorption due to water vapor in the infrared, the pressure scaling of the water vapor amount has been modified in such a way that upper stratospheric cooling rates agree with line-by-line computations. This updated model is the one that has been used in the profile comparisons discussed above. The observational data sets used in the NMC runs are the same as those discussed in Rosenfield et al. (1987) except for the following changes. Eight years of both NMC temperature data and SBUV ozone data were used (1979-1986), as

discussed in Jackman et al. (1991). Monthly, zonally averaged LIMS H_2O profiles were used in the stratosphere, with a tropospheric climatology H_2O from the AFCRL Handbook of Geophysics and Space Environments (1965). The global heating rates shown for the GSFC model used the radiative transfer model and data sets as discussed in Rosenfield et al. (1987). These data sets included a 4-year average (1979-1982) of NMC temperatures and 1979 SBUV ozone.

Looking at Figure A-6, we see that for March and September all the models have heating in the low latitudes and cooling in the midlatitudes and high latitudes. For June and December there is generally widespread cooling in the mid- to high latitudes of the winter hemisphere, and heating in the tropics and summer hemisphere, although some models have regions of cooling in the summer hemisphere. The AER model heating rates are quite different from the rest in their relative symmetry about the equator and their much smaller cooling in the upper stratosphere of the winter hemisphere. It is not possible, however, to relate the magnitudes of heating or cooling to the results obtained in the profile intercomparison since the various two-dimensional models have such differing characteristics. As is shown in Table A-3, the CAMED-theta and NCAR models are interactive in temperature and O_3, the CALJPL, DUPONT, and GSFC models use observed temperatures and O_3, while other models are somewhere in between. To illustrate the effect that differing temperature data sets have on computed net heating rates, the net heating for December was calculated with the GSFC radiation model (updated) using two different temperature data sets, while keeping the ozone at the 1979 SBUV values. Figure A-7 shows this comparison. On the left is the average of 8 years of heating rates computed with the NMC temperature data set, while on the right are the heating rates computed with the Fleming et al. (1988) temperature data set. In the latter case there is a band of net cooling at 40 km which extends across all latitudes. Another intercomparison of the effect of differing temperatures on calculated global heating rates can be found in Olaguer et al. (1992).

Table A-3. Characteristics of Two-Dimensional Models

Model	Computation of Net Heating
AER	Prescribed
CALJPL	Observed T (NMC), O_3 (SBUV)
CAMED	Model T, O_3
DUPONT	Observed T (NMC), O_3 (SBUV)
GSFC	Observed T (NMC), O_3 (SBUV)
ITALY	3D Model T, O_3
LLNL	Observed T (Barnett and Corney), Model O_3
NCAR	Model T, O_3
WASH	Observed T (NMC), Model O_3

TWO-DIMENSIONAL MODEL VERTICAL VELOCITIES

The transport used in the AER, DUPONT, and ITALY models was the diabatic circulation, while that used in the CALJPL, GSFC, LLNL, and NCAR models was the residual circulation. The CAMED-theta and WASH models solved the equations in isentropic coordinates. Table A-4 summarizes the information available on the diffusion coefficients used in the models. Chapter 4, Model Descriptions should be consulted for further details.

The two-dimensional model vertical velocities for the months of June, December, March, and September are shown in Figure A-8. Regions of upwelling (downwelling) do not always correspond to regions of net heating (cooling) for two main reasons. First, in models using a residual rather than a diabatic circulation, terms in the thermodynamic equation such as the temperature tendency can be important, especially during the equinoctal months. Second, in some models a globally averaged net heating or vertical velocity is subtracted at each altitude to achieve mass balance. For example, in the GSFC model a globally averaged vertical velocity is computed at each pressure level, and this average is subtracted from the vertical velocity at each latitude in an area-weighted manner. The effect of doing this appears to be most evident in the LLNL and CALJPL models, where there is a globally averaged cooling around 40 km apparent in the heating rates. The vertical velocity fields for these models do not show this feature. They have a larger area of upwelling in the low latitudes than there is net heating. Another example is for the GSFC model, where in all months the calculated cooling over the polar regions from 10-15 km is forced into upward transport at the pole because of tropical cooling in the troposphere.

Table A-4. Stratospheric Diffusion Coefficients in Two-Dimensional Models

Model	$K_{yy}(10^5 m^2/s)$	$K_{zz}(m^2/s)$
AER	Variable, 3-10	0.1 below 40 km, 1.0 above
CALJPL	Variable, ~1	0.01
CAMED	Variable	0.3
DUPONT	Fixed, 3	Fixed, 0.1
GSFC	Variable, 0.1-20	0.2
ITALY	Variable, 0.1-20	Variable, < 0.05 - 0.3
LLNL	Variable, > 1	Variable, 0.1 - 0.25
WASH	Variable	0 except near top

For March and September the models generally have upwelling at low latitudes and downwelling at mid- to high latitudes. The LLNL model shows an unusual feature in the fall hemispheres of both months, which is downwelling in the lower stratosphere turning to upwelling above about 30 km. The CAMED, GSFC, and WASH models show a region of small upwelling in the polar regions in the southern hemisphere in September.

For the solsticial months the traditional simple picture of rising motion in the summer hemisphere and sinking motion in the winter hemisphere has changed to a more varied and complicated pattern. For June the model vertical velocities in the low latitudes show upwelling centered more on the low northern latitudes. There is a tilt with increasing altitude towards the northern hemisphere, except for the AER model. In the summer hemisphere, there are regions of both upwelling and downwelling, except for ITALY, which has upwelling throughout. The other models show upwelling at the higher altitudes, turning to downwelling below 40-50 km for LLNL and NCAR, below 30-40 km for AER, CALJPL, DUPONT, GSFC, and NOCAR, below 20 km for WASH, and below 15 km for CAMED. In the winter hemisphere all the models show a downwelling. There are, however, large, potentially significant differences in the magnitude of the velocities in the lower stratosphere. For example, at 20 km the downward velocities are about 0.25 mm/s for the GSFC and NOCAR models, while they are 0.5 mm/s or greater for the CALJPL, DUPONT, ITALY, LLNL, and WASH models. AER, CAMED, and NCAR vertical velocities in this region are somewhere in between. For the month of December, the patterns of positive and negative velocities are generally the mirror image of the June case.

REFERENCES

Air Force Cambridge Research Laboratories, *Handbook of Geophysics and Space Environments* (S. L. Valley, ed.) McGraw-Hill, New York, 1965.

Barnett, J. J., and M. Corney, Middle atmosphere reference model derived from satellite data, *Handbook for MAP, 16* (K. Labitzke, J. J. Barnett, B. Edwards, eds.) pp. 47-85, 1985.

Fleming, E. L., S. Chandra, M. R. Schoeberl, and J. J. Barnett, *Monthly Mean Global Climatology of Temperature, Wind, Geopotential Height, and Pressure for 0-120 km,* NASA Technical Memorandum No. 100697, NASA, Washington, D.C., 1988.

Gelman, M. E., A. J. Miller, K. W. Johnson, and R. M. Nagatani, 1986, Detection of long-term trends in global stratospheric temperature from NMC analyses derived from NOAA satellite data, *Adv. Space Res., 6*, 17-26, 1986.

Jackman, C. H., A. R. Douglass, S. Chandra, R. S. Stolarski, J. E. Rosenfield, and J. A. Kaye, Impact of interannual variability (1979-1986) of transport and temperature on ozone as computed using a two-dimensional photochemical model, *J. Geophys. Res., 96*, 5073-5079, 1991.

Nagatani, R. M., A. J. Miller, K. W. Johnson, and M. E. Gelman, 1988, *An Eight-Year Climatology of Meteorological and SBUV Ozone Data,* NOAA Technical Report NWS 40, U.S. Department of Commerce, 125 pp.

Olaguer, E. P., H. Yang, and K. K. Tung, A reexamination of the radiative balance of the stratosphere, *J. Atmos. Sci., 49*, 1242-1263, 1992.

Oort, A. H., 1983, "Global Atmospheric Statistics, 1958-1973," NOAA Professional Paper 14.

Randel, W. J., 1992, "Global Atmospheric Circulation Statistics, 1000-1 mb," NCAR Technical Note NCAR/TN-366+STR, 256 pp.

Rosenfield, J. E., M. R. Schoeberl, and M. A. Geller, A computation of the stratospheric diabatic circulation using an accurate radiative transfer model, *J. Atmos. Sci., 44*, 859-876, 1987.

Rosenfield, J. E., A simple parameterization of ozone infrared absorption for atmospheric heating rate calculations, *J. Geophys. Res., 96*, 9065-9074, 1991.

World Meteorological Organization (WMO), *Atmospheric Ozone 1985, Assessment of Our Understanding of Processes Controlling its Present Distribution and Change,* Global Ozone Research and Monitoring Project Report No. 16, WMO, Geneva, 1986.

FIGURE CAPTIONS

Figure A-1a. NMC climatology used by the GSFC model for 1979-86. Contour interval is 10K.

Figure A-1b. Barnett and Corney climatology used by LLNL model.

Figure A-1c. AER climatology.

Figure A-1d. Offline 3-D quasi-geostrophic model output temperatures used by the Italian 2-D model.

Figure A-1e. NCAR calculated temperatures.

Figure A-1f. CAMED-theta calculated temperatures.

Figure A-2a. Differences between Barnett and Corney and NMC. Contour interval is 2K.

Figure A-2b. Differences between AER and NMC.

Figure A-2c. Differences between ITALY and NMC.

Figure A-2d. Differences between NCAR and NMC.

Figure A-2e. Differences between CAMED-theta and NMC.

Figure A-3. Solar heating rate profiles for the ATMOS 31N atmosphere, overhead sun, from 0 to 60 km (left) and from 10 to 30 km (right).

Figure A-4. Solar heating rate profiles for the ATMOS 31N atmosphere, overhead sun, from two groups, with and without Rayleigh scattering. On the left the plot runs from 0 to 60 km, on the right, from 0 to 30 km. Note that the linestyles are different from those of Fig. A-3.

Figure A-5. Infrared cooling rate profiles for the ATMOS 31N atmosphere, from 0 to 60 km (left) and from 10 to 30 km (right).

Figure A-6. Net heating rates from the two-dimensional models for the four months of June, December, March, and September. Units are degree/day, with solid (dashed) contours denoting net heating (cooling).

Figure A-7. Net heating rates for December using the GSFC radiation with (left) NMC temperatures, and (right) Fleming et al. temperatures. For the NMC case, the heating rates are an 8-year average.

Figure A-8. Vertical velocities from the two-dimensional models for the four months of June, December, March, and September. Units are mm/s, with solid (dashed) contours denoting rising (falling) motion.

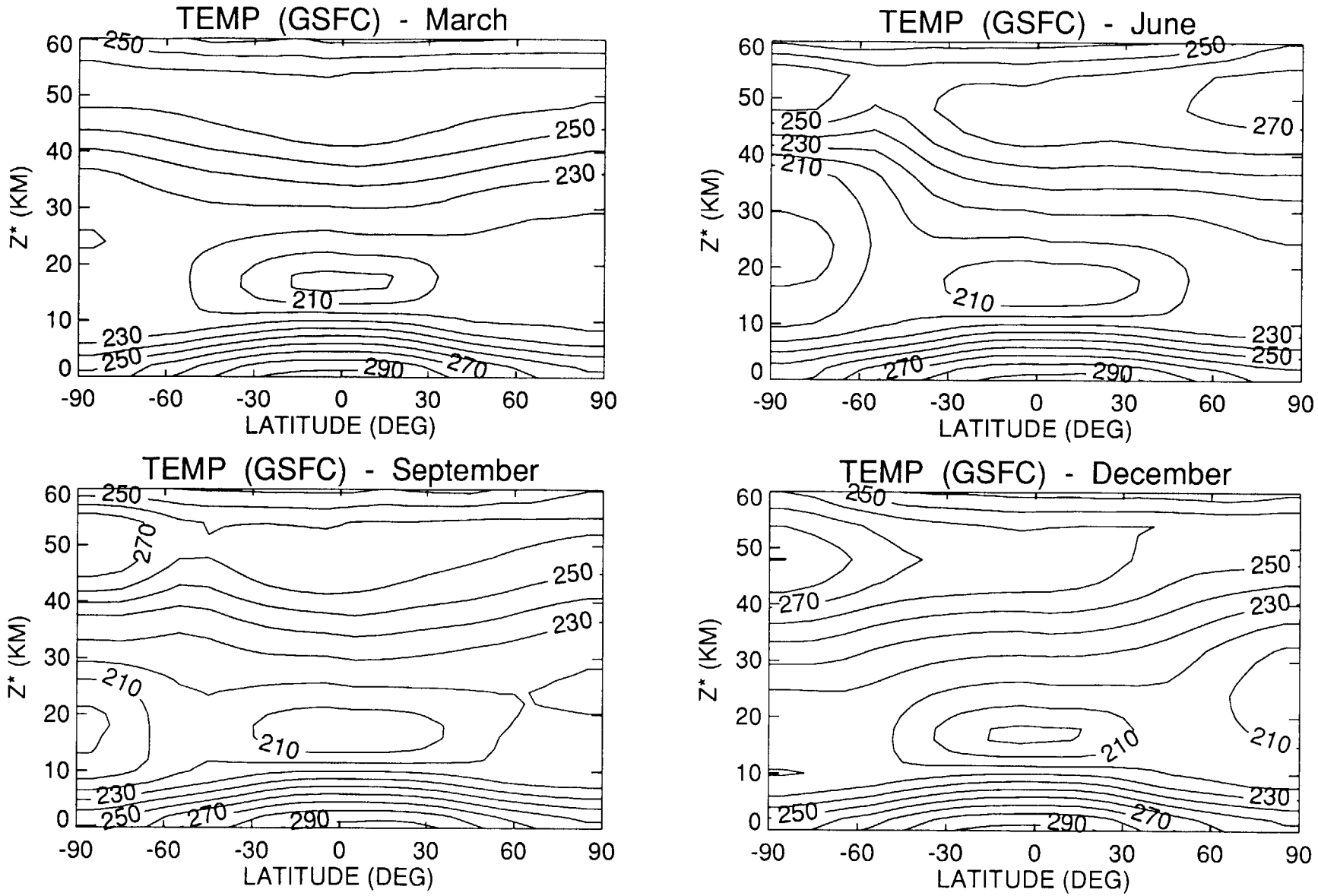
TEMP (GSFC) - March
TEMP (GSFC) - June
TEMP (GSFC) - September
TEMP (GSFC) - December
Z* (KM)
LATITUDE (DEG)
250
230
210
270
290

Figure A-1 a

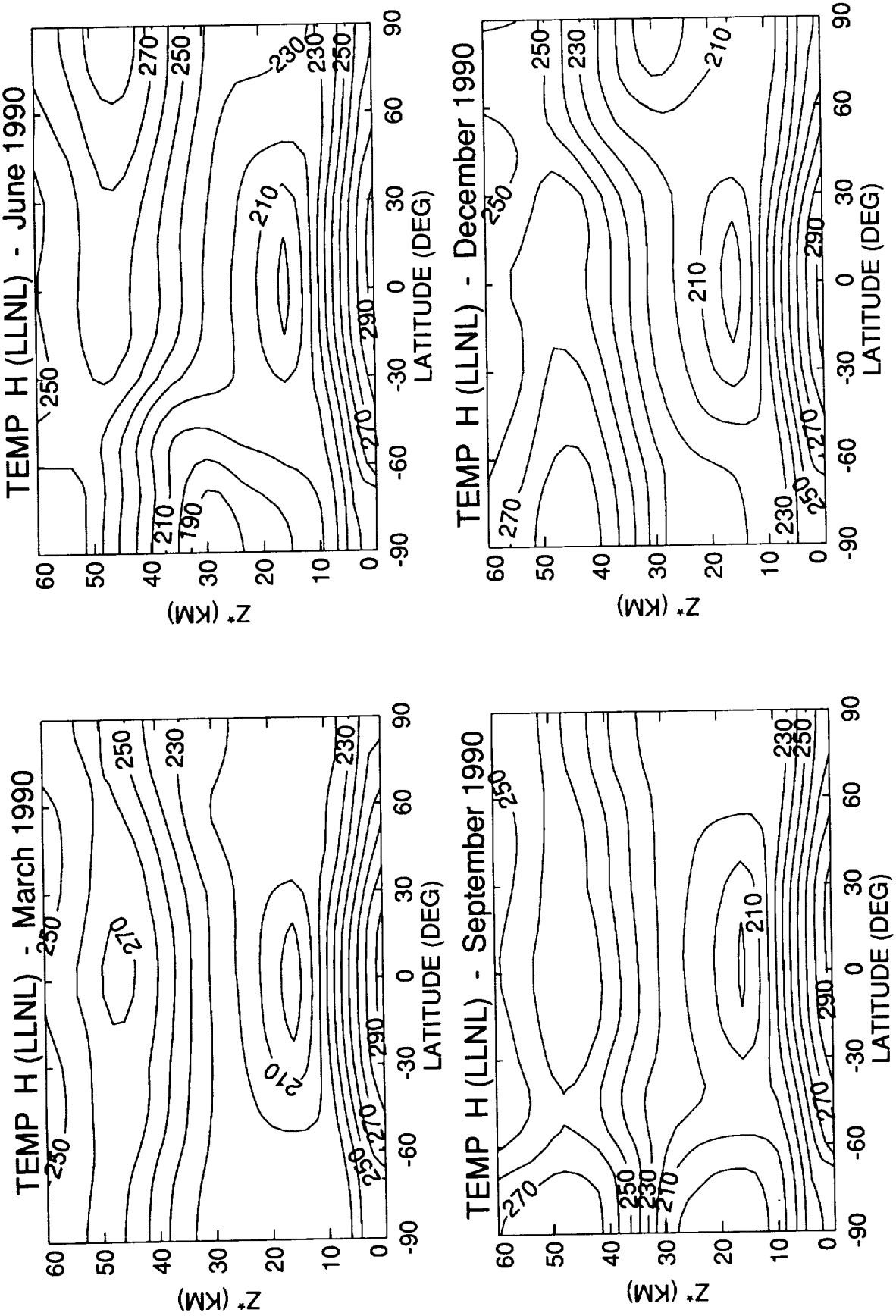
TEMP H (LLNL) - June 1990
TEMP H (LLNL) - December 1990
TEMP H (LLNL) - March 1990
TEMP H (LLNL) - September 1990
Z* (KM)
LATITUDE (DEG)

Figure A-1 b

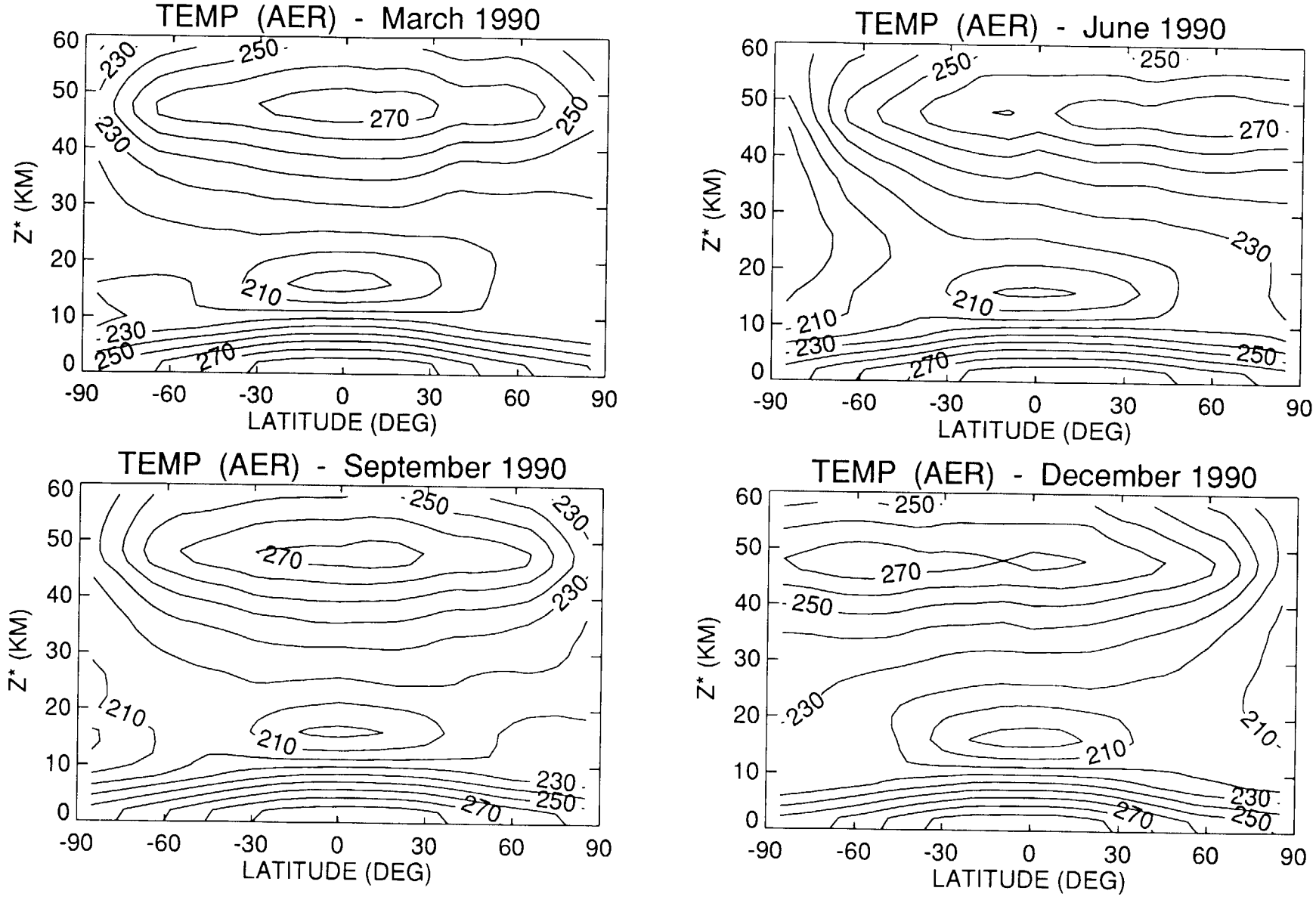
TEMP (AER) - March 1990
TEMP (AER) - June 1990
TEMP (AER) - September 1990
TEMP (AER) - December 1990
Z* (KM)
LATITUDE (DEG)
60
50
40
30
20
10
0
-90
-60
-30
0
30
60
90
210
230
250
270

Figure A-1 c

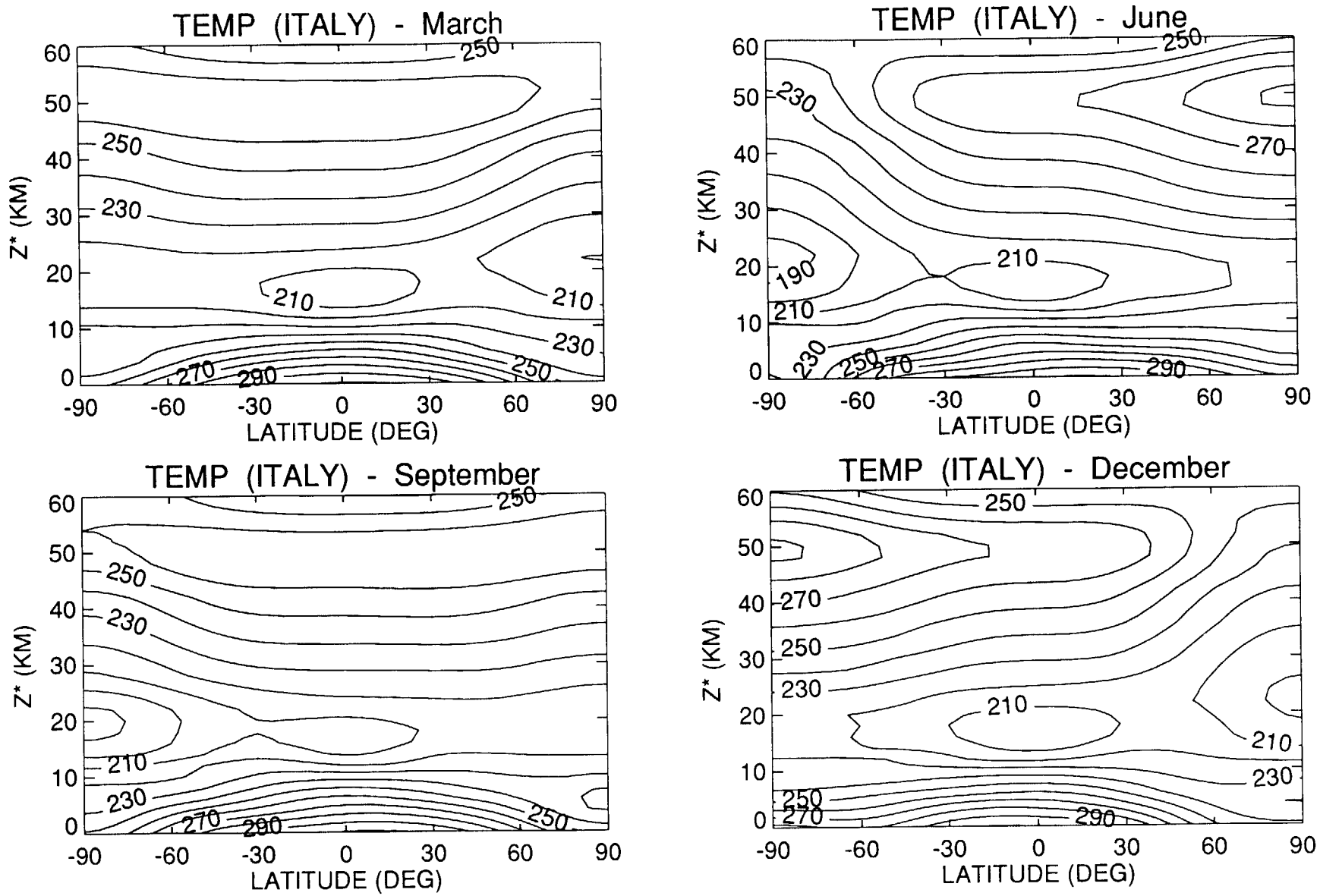
TEMP (ITALY) - March
TEMP (ITALY) - June
TEMP (ITALY) - September
TEMP (ITALY) - December
Z* (KM)
LATITUDE (DEG)
60
50
40
30
20
10
0
-90
-60
-30
0
30
60
90
250
230
210
270
290
190

Figure A-1 d

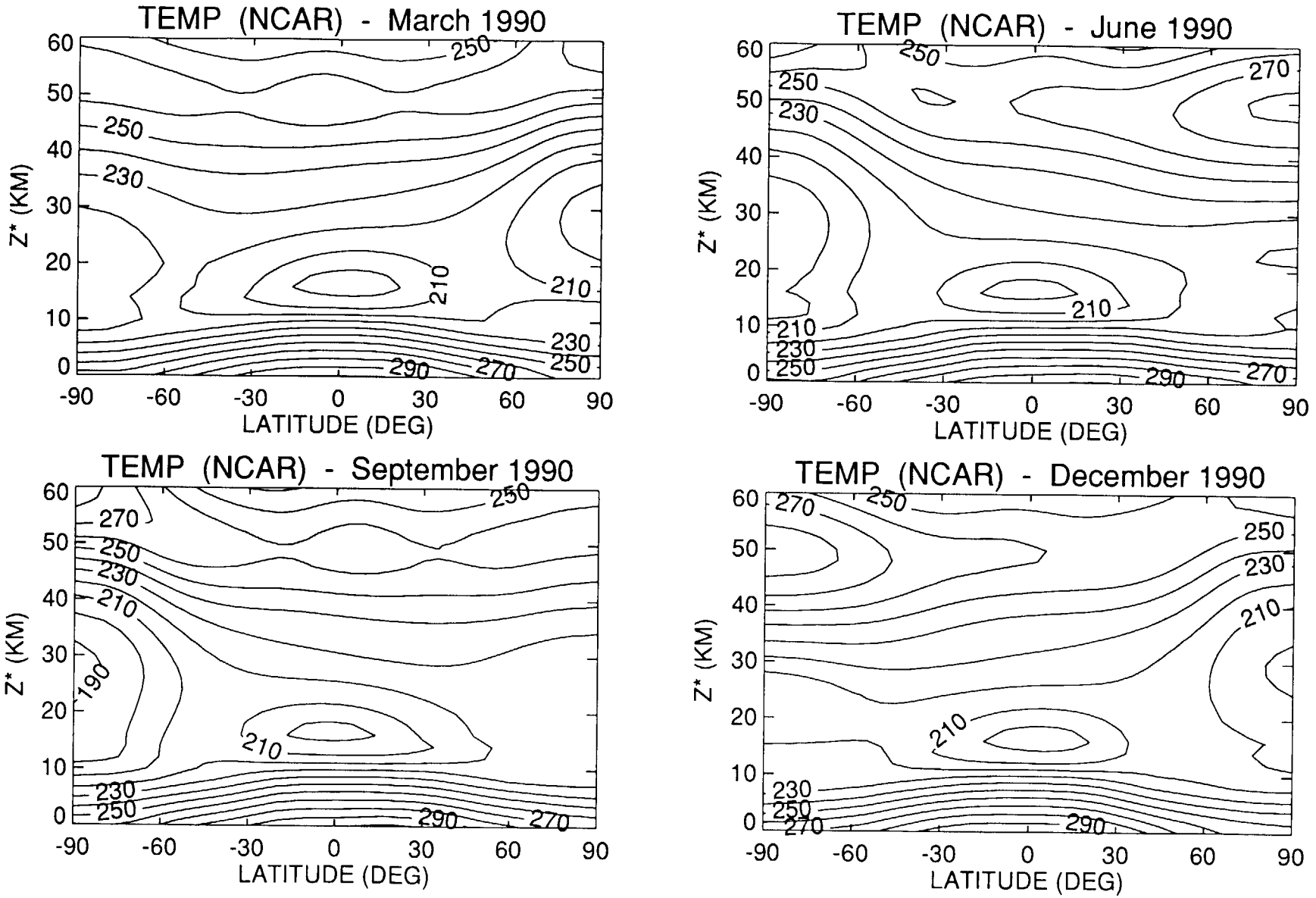
TEMP (NCAR) - March 1990
TEMP (NCAR) - June 1990
TEMP (NCAR) - September 1990
TEMP (NCAR) - December 1990
Z* (KM)
LATITUDE (DEG)
60
50
40
30
20
10
0
-90
-60
-30
0
30
60
90
250
230
210
190
270
290

Figure A-1 e

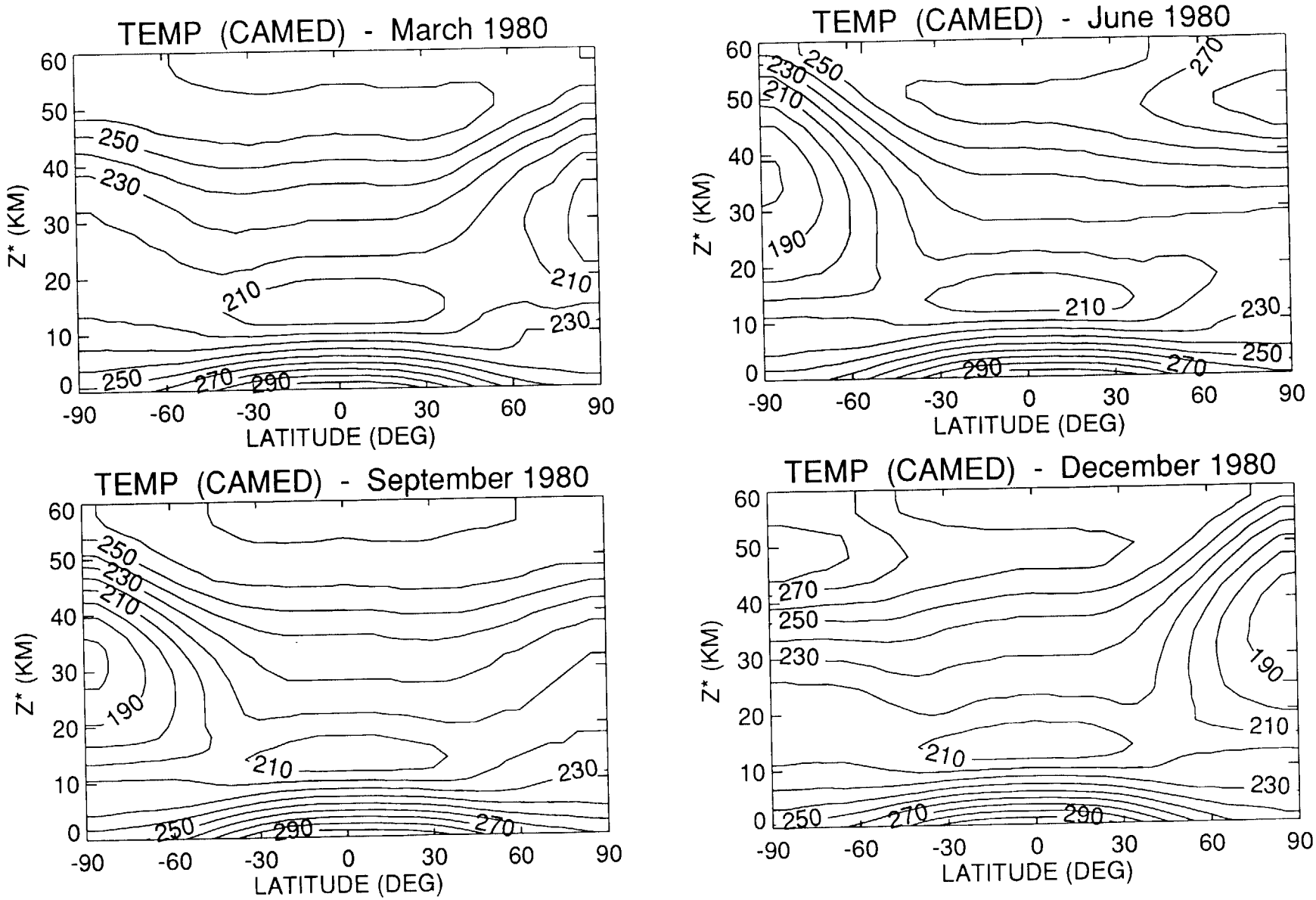
TEMP (CAMED) - March 1980
TEMP (CAMED) - June 1980
TEMP (CAMED) - September 1980
TEMP (CAMED) - December 1980
Z* (KM)
LATITUDE (DEG)
60
50
40
30
20
10
0
-90
-60
-30
0
30
60
90
190
210
230
250
270
290

Figure A-1 f

TEMPERATURE

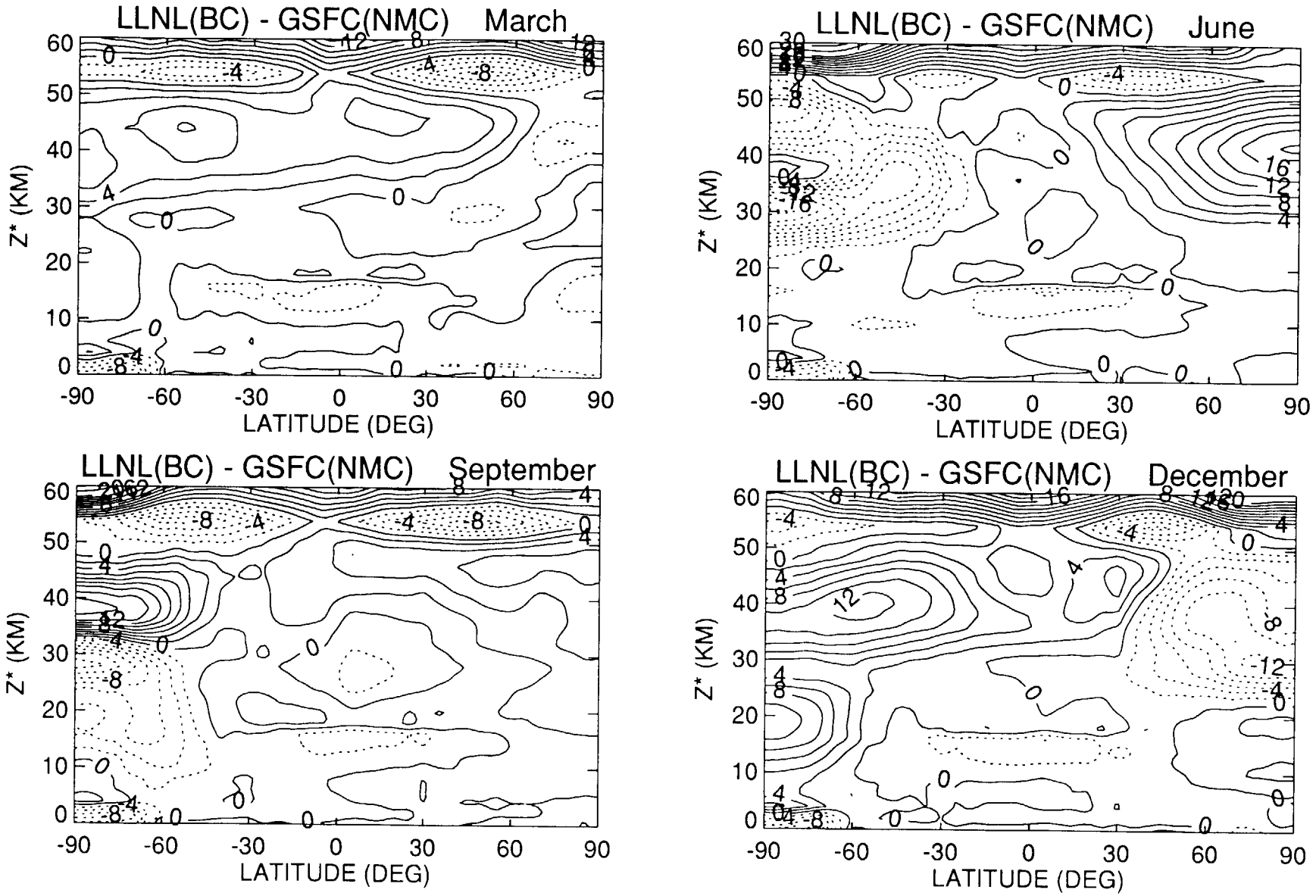

Figure A-2 a

TEMPERATURE

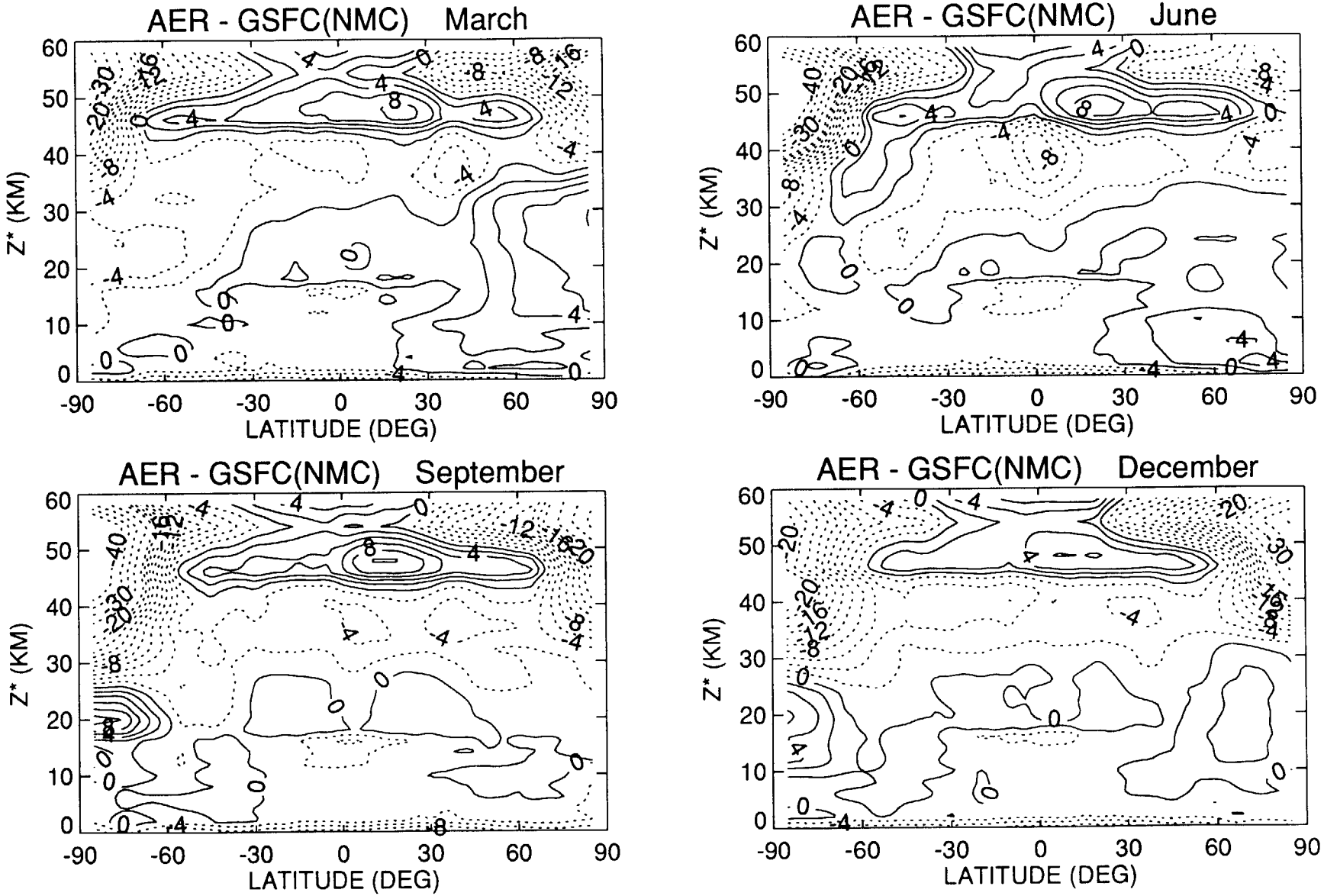

Figure A-2 b

TEMPERATURE

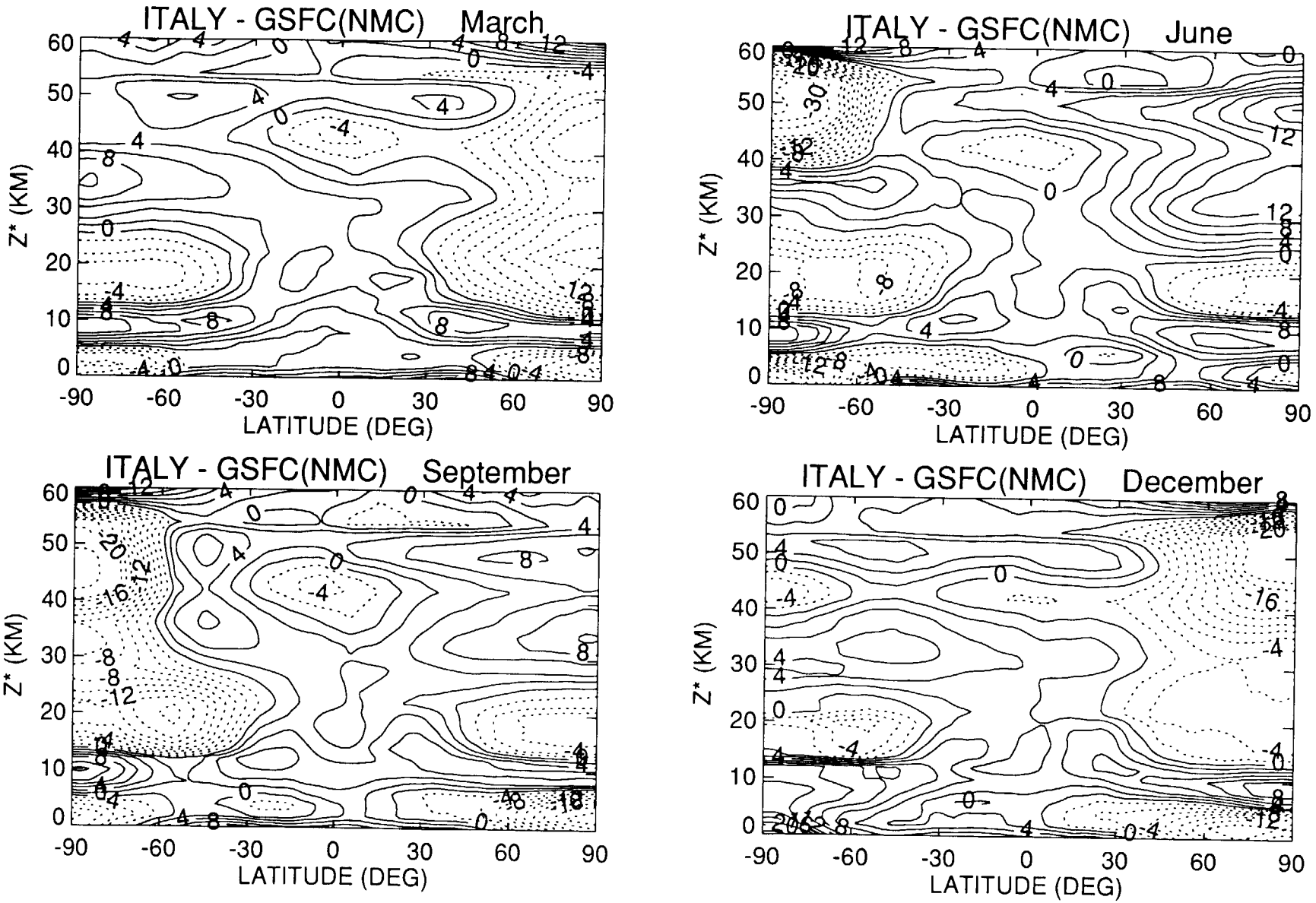

Figure A-2 c

TEMPERATURE

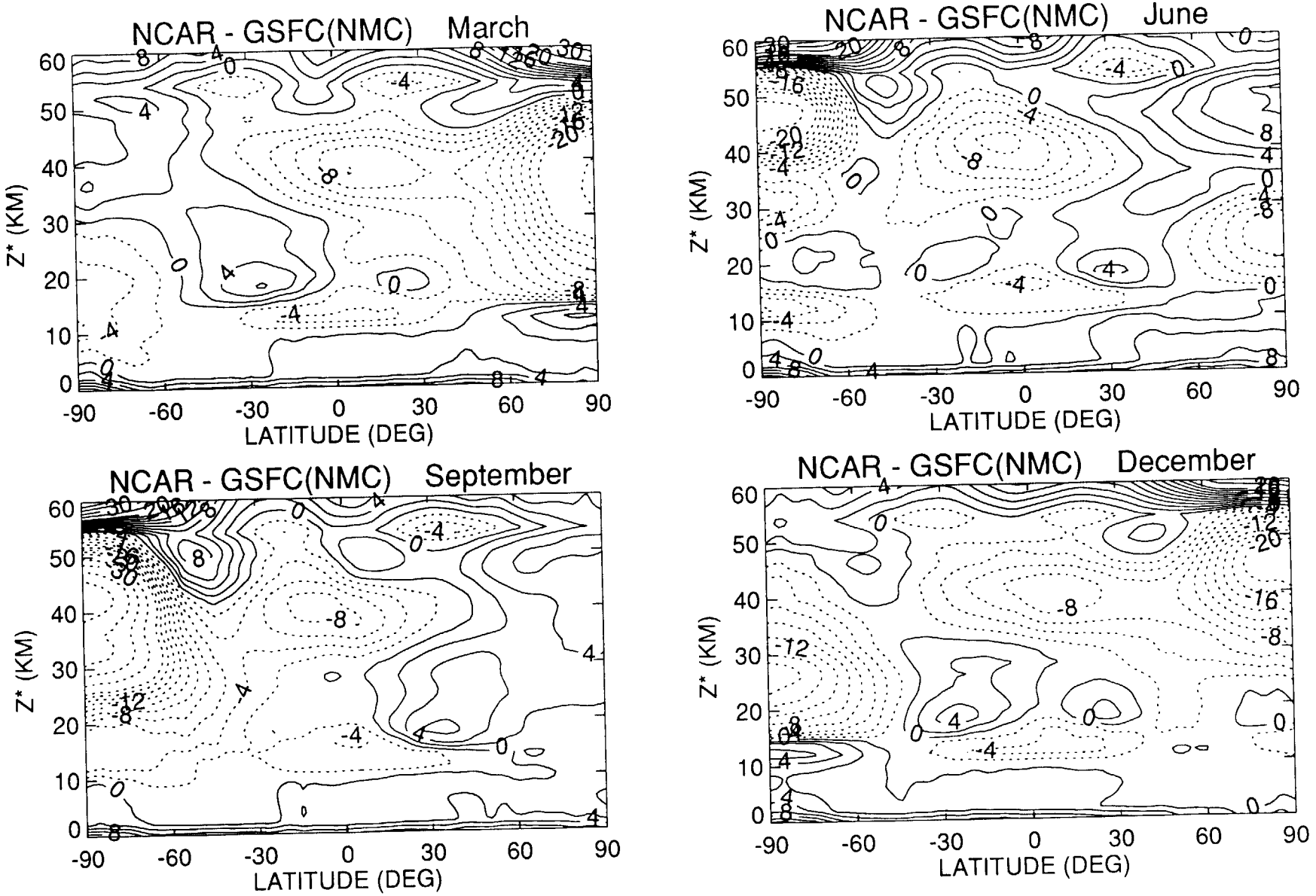

Figure A-2 d

TEMPERATURE

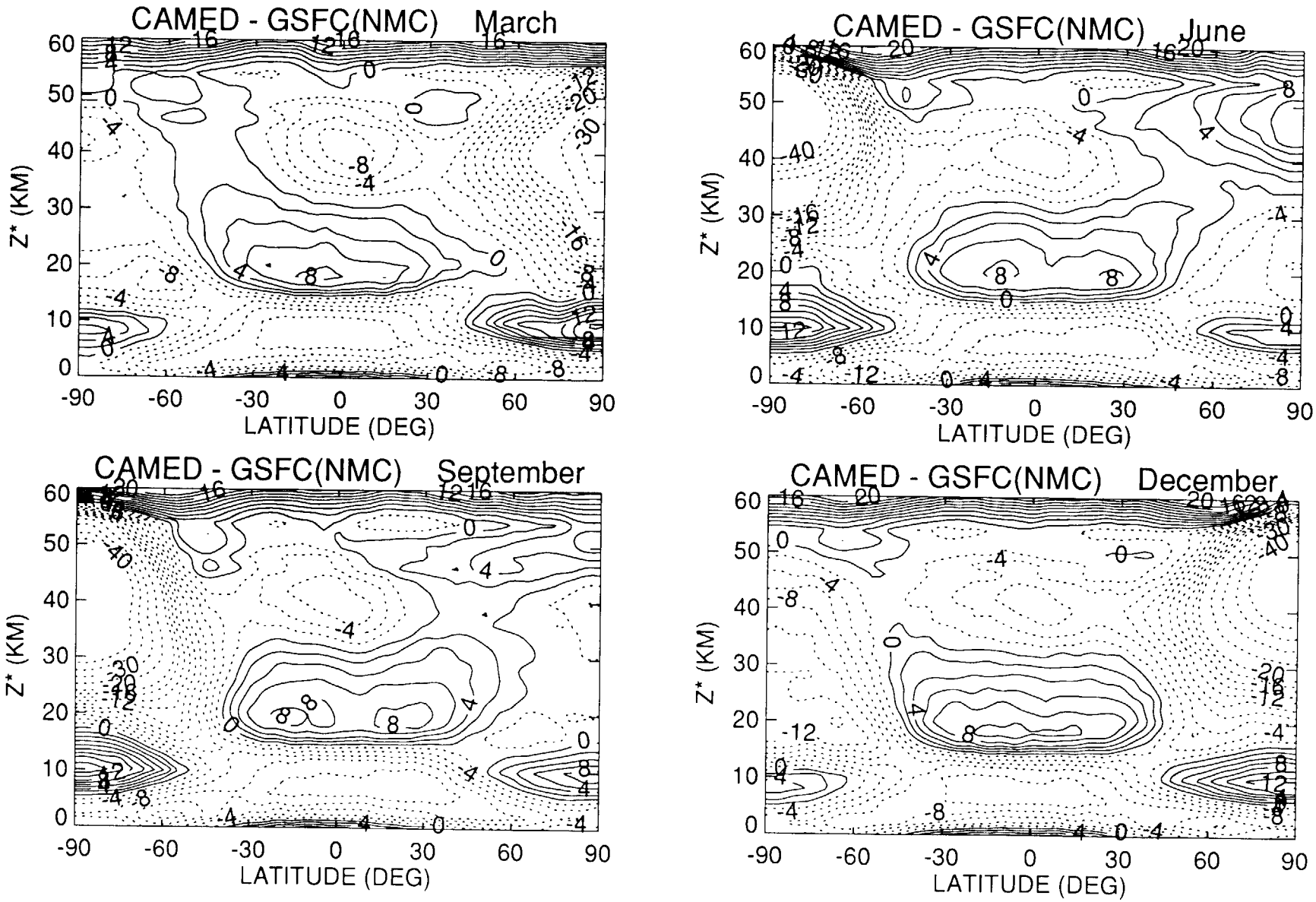

Figure A-2 e

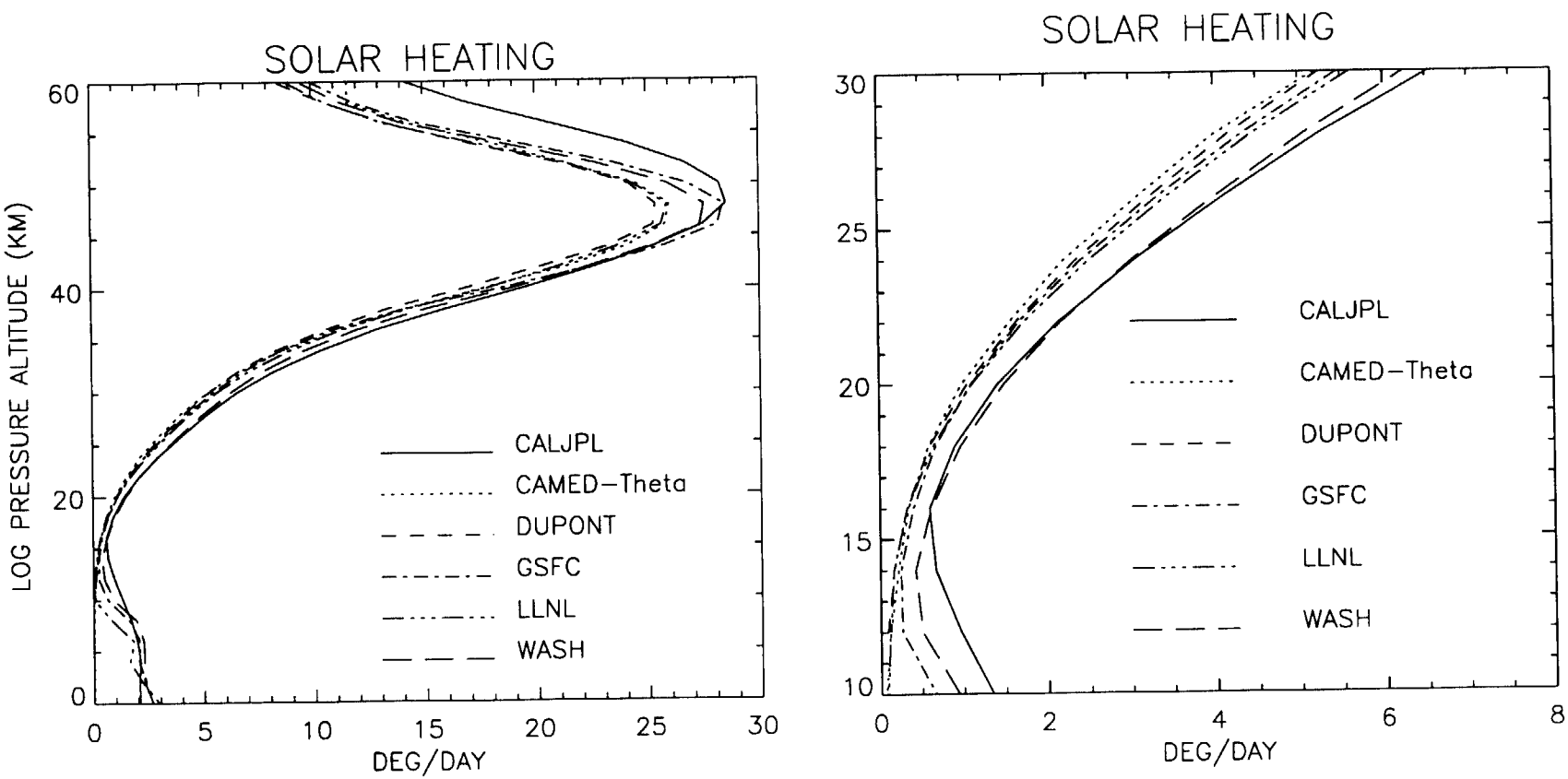
SOLAR HEATING
LOG PRESSURE ALTITUDE (KM)
60
40
20
0
0
5
10
15
20
25
30
DEG/DAY
CALJPL
CAMED–Theta
DUPONT
GSFC
LLNL
WASH
SOLAR HEATING
30
25
20
15
10
0
2
4
6
8
DEG/DAY
CALJPL
CAMED–Theta
DUPONT
GSFC
LLNL
WASH

Figure A-3

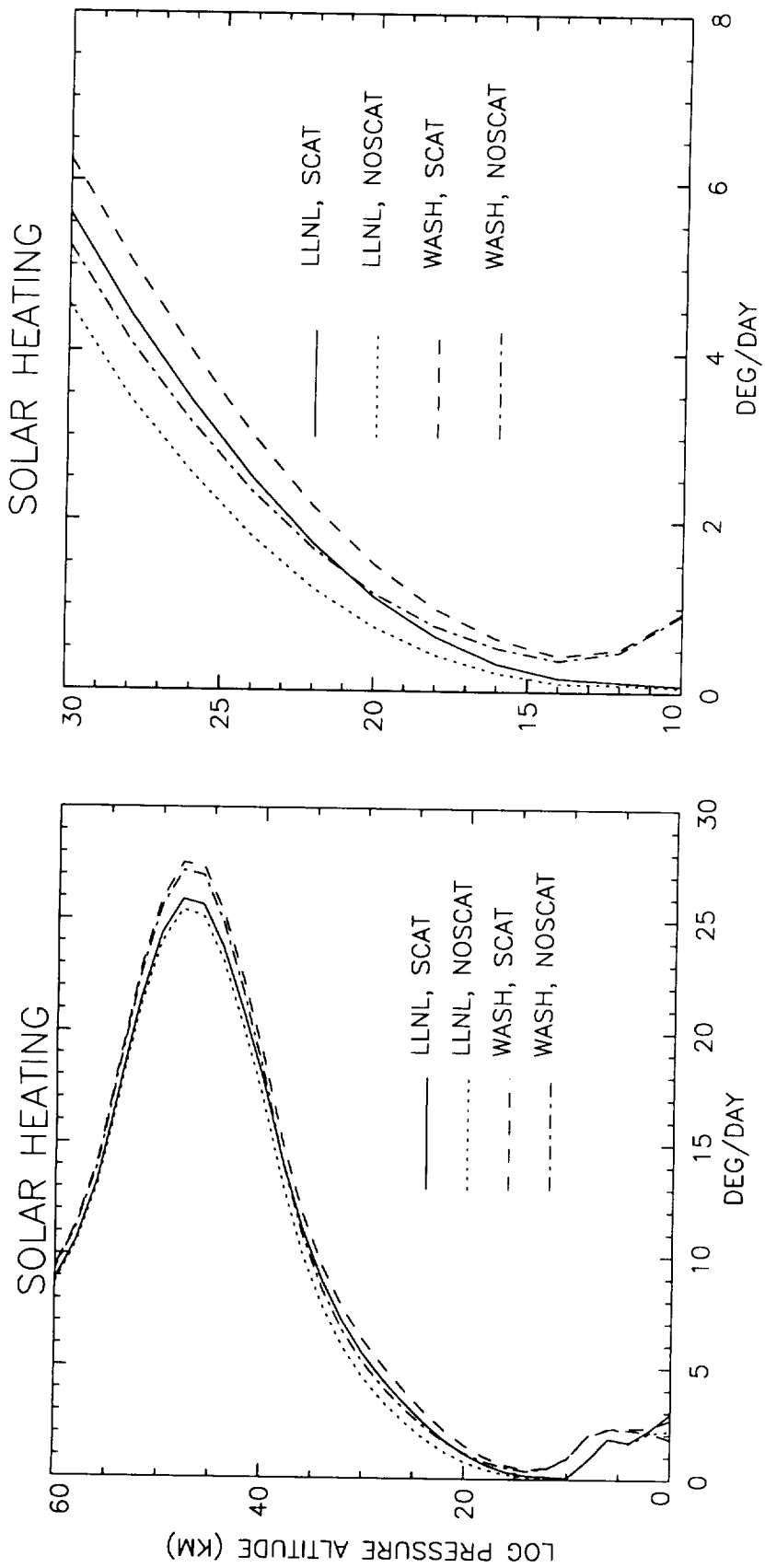
SOLAR HEATING
LLNL, SCAT
LLNL, NOSCAT
WASH, SCAT
WASH, NOSCAT
DEG/DAY
LOG PRESSURE ALTITUDE (KM)
SOLAR HEATING
LLNL, SCAT
LLNL, NOSCAT
WASH, SCAT
WASH, NOSCAT
DEG/DAY

Figure A-4

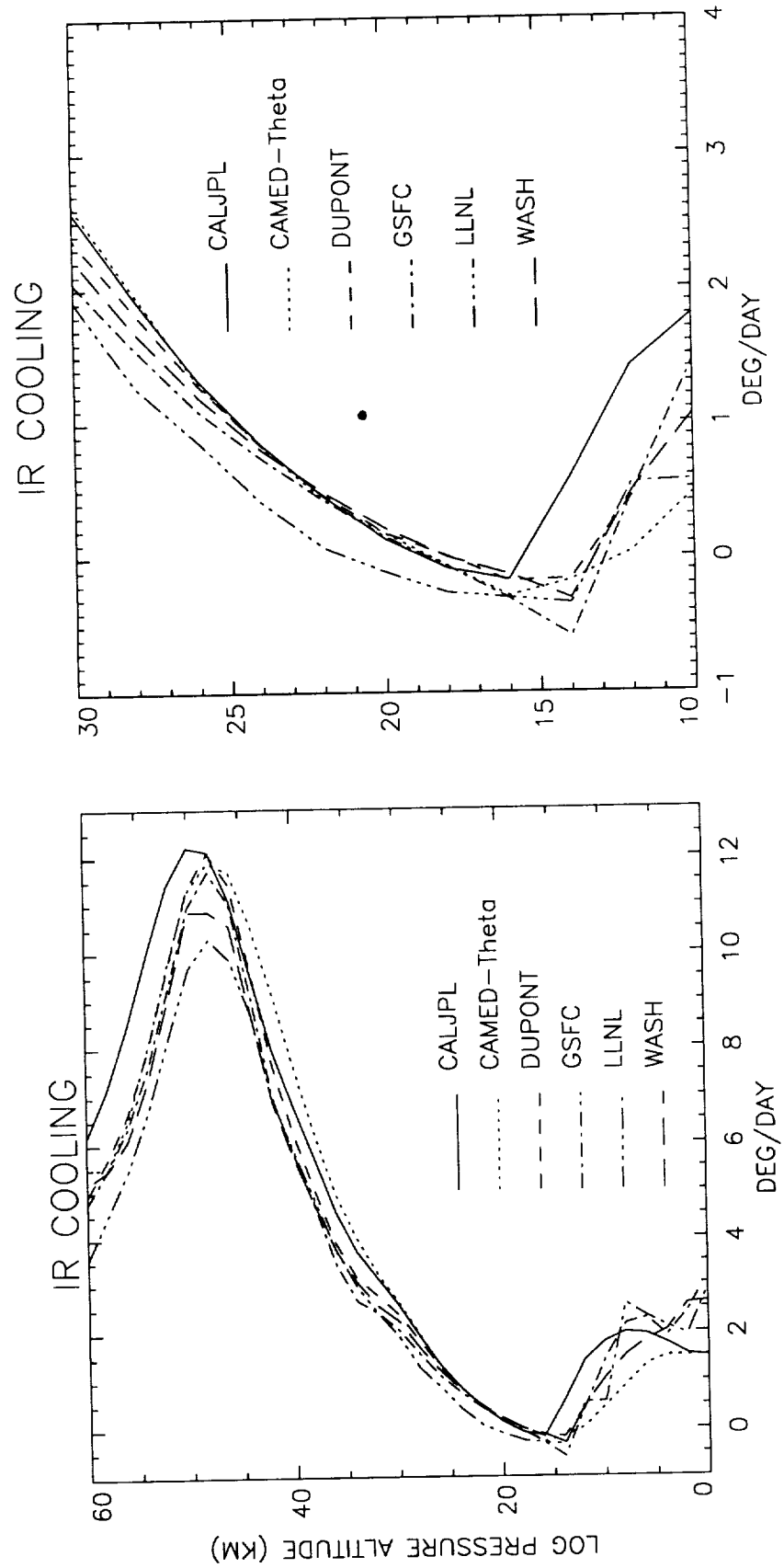
IR COOLING
CALJPL
CAMED-Theta
DUPONT
GSFC
LLNL
WASH
DEG/DAY
LOG PRESSURE ALTITUDE (KM)
IR COOLING
CALJPL
CAMED-Theta
DUPONT
GSFC
LLNL
WASH
DEG/DAY

Figure A-5

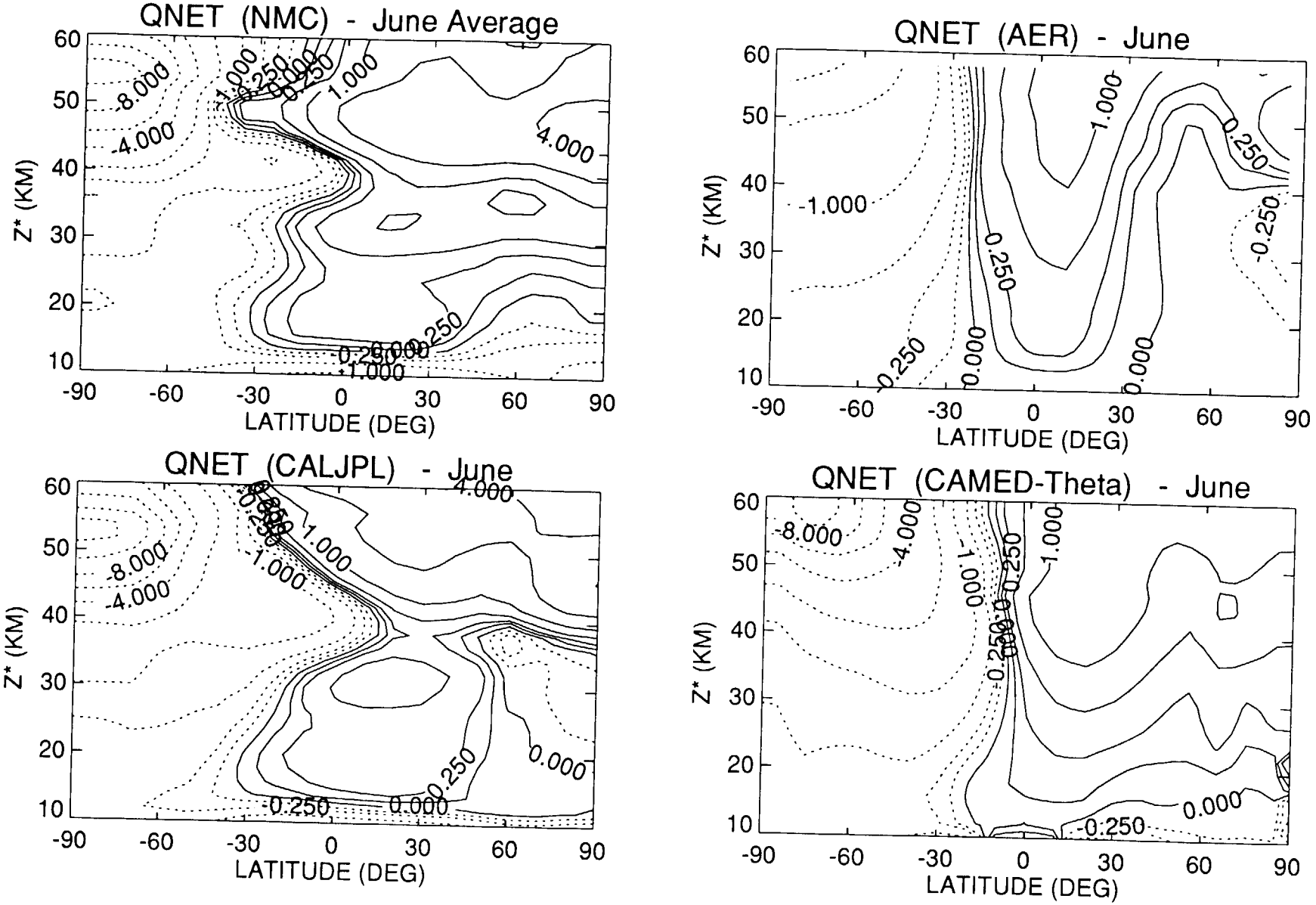
QNET (NMC) - June Average
QNET (AER) - June
QNET (CALJPL) - June
QNET (CAMED-Theta) - June
Z* (KM)
LATITUDE (DEG)
60
50
40
30
20
10
-90
-60
-30
0
30
60
90
-8.000
-4.000
-1.000
-0.250
0.000
0.250
1.000
4.000

Figure A-6

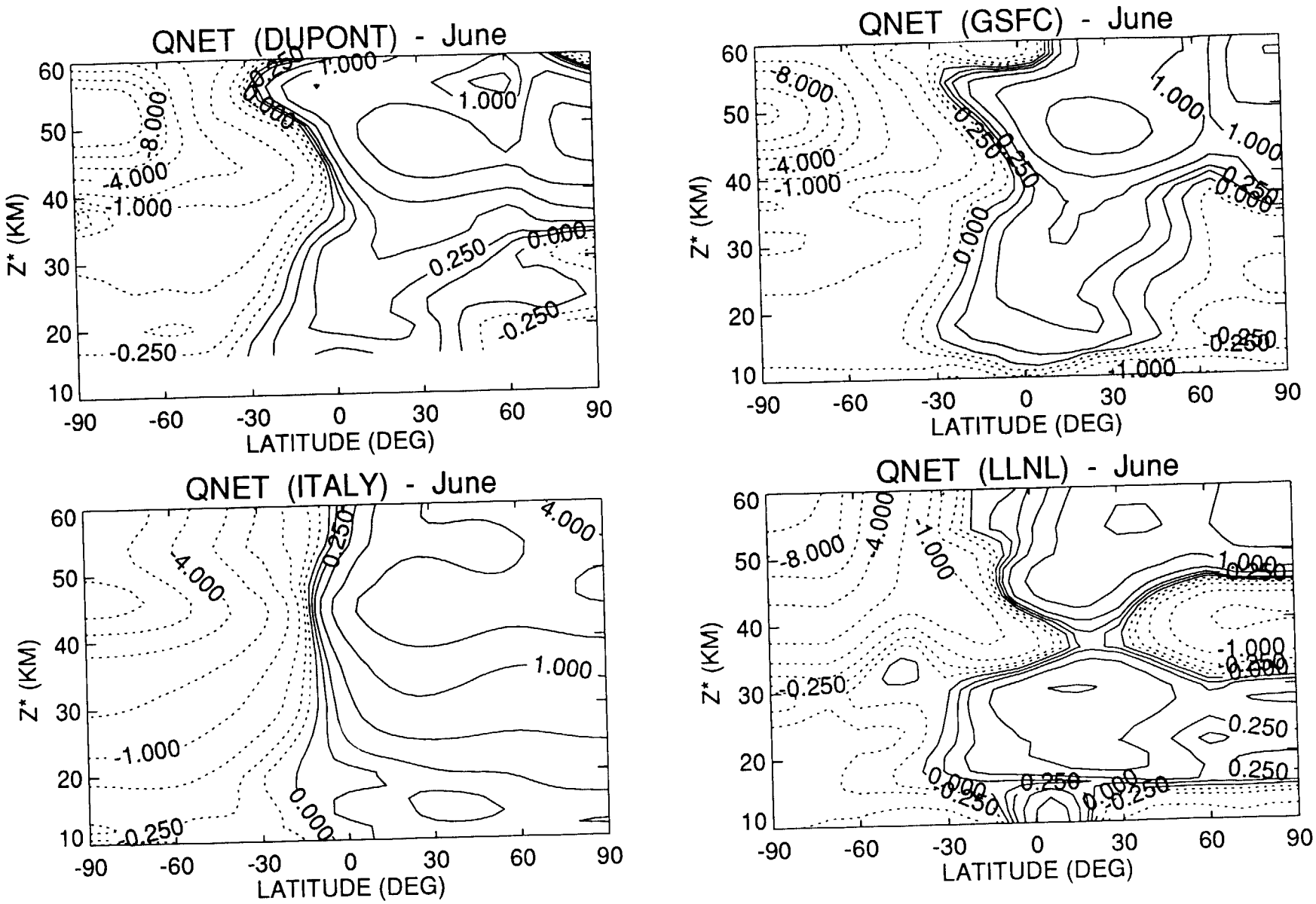

Figure A-6 (cont.)

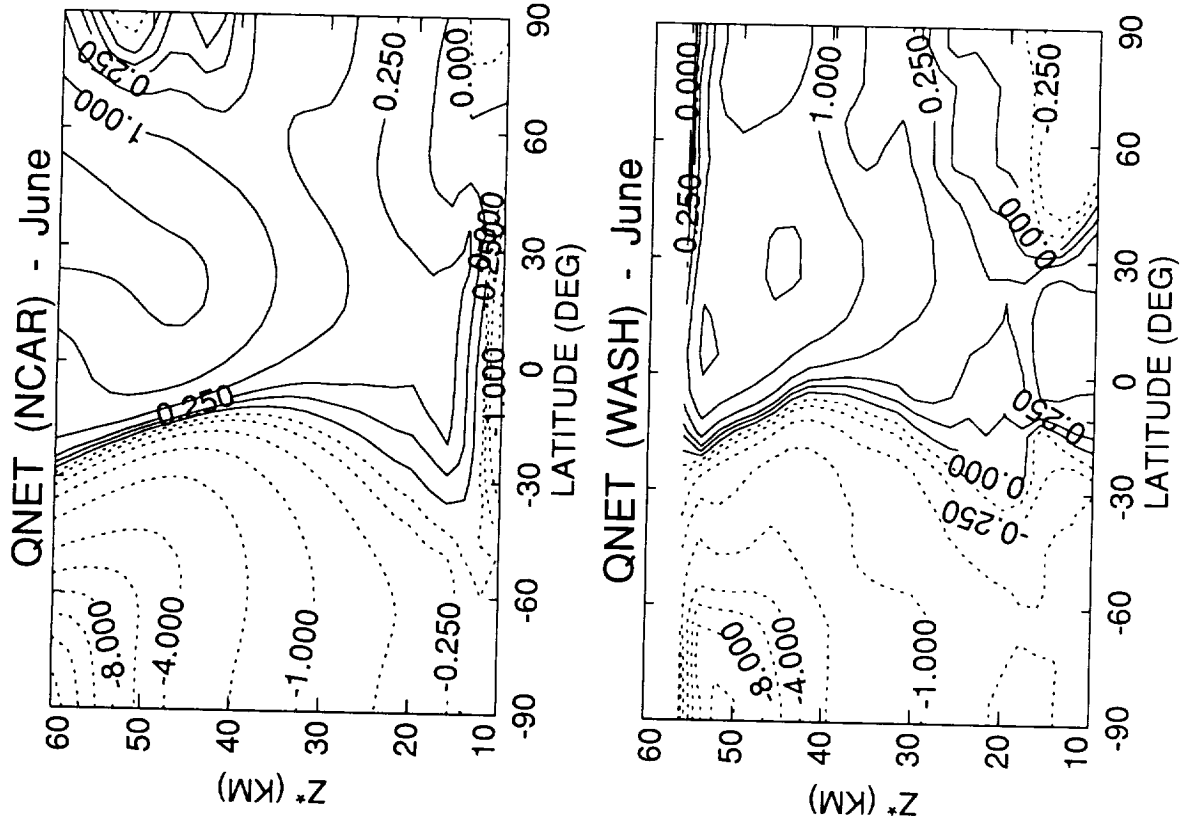

Figure A-6 (cont.)

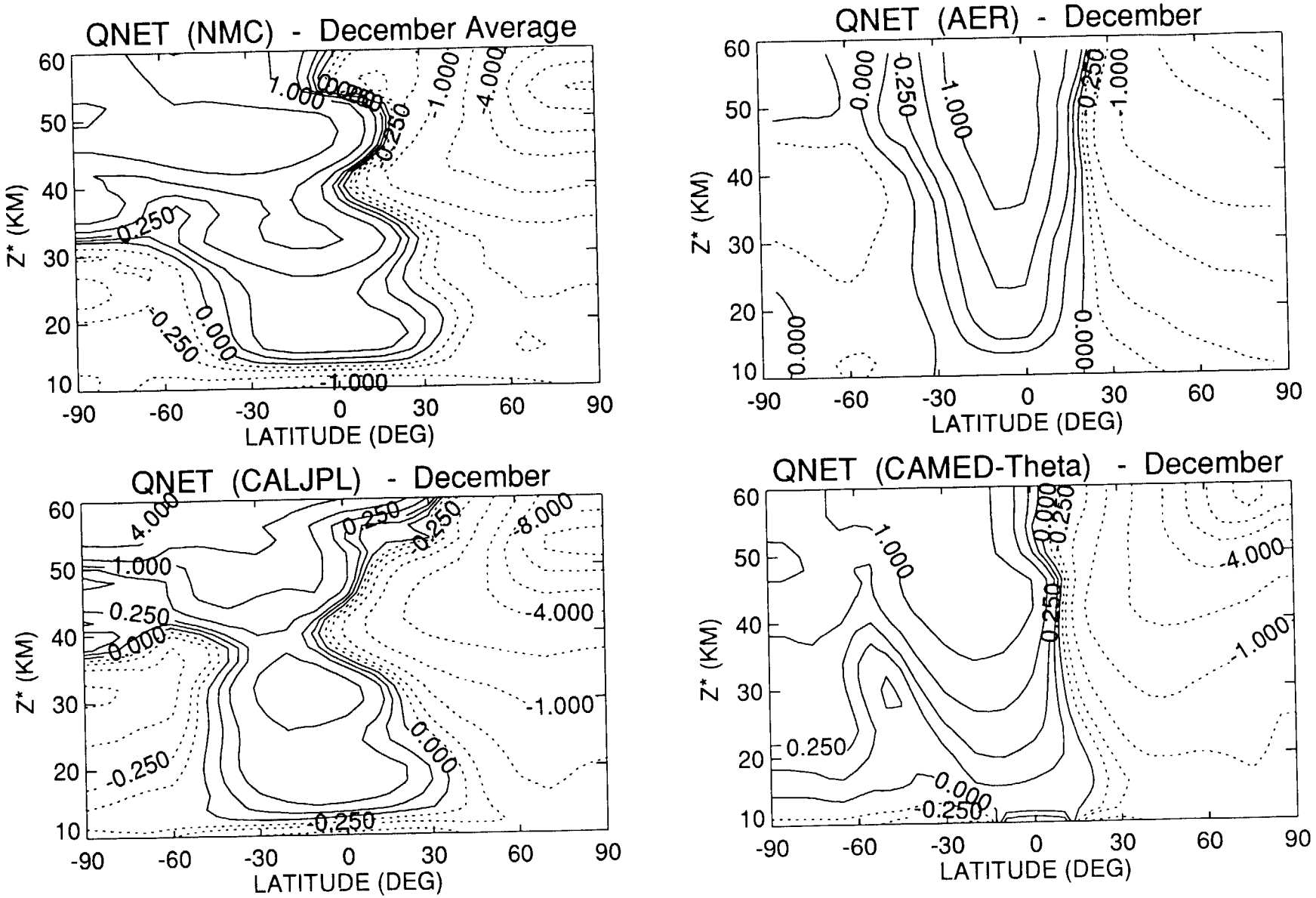

Figure A-6 (cont.)

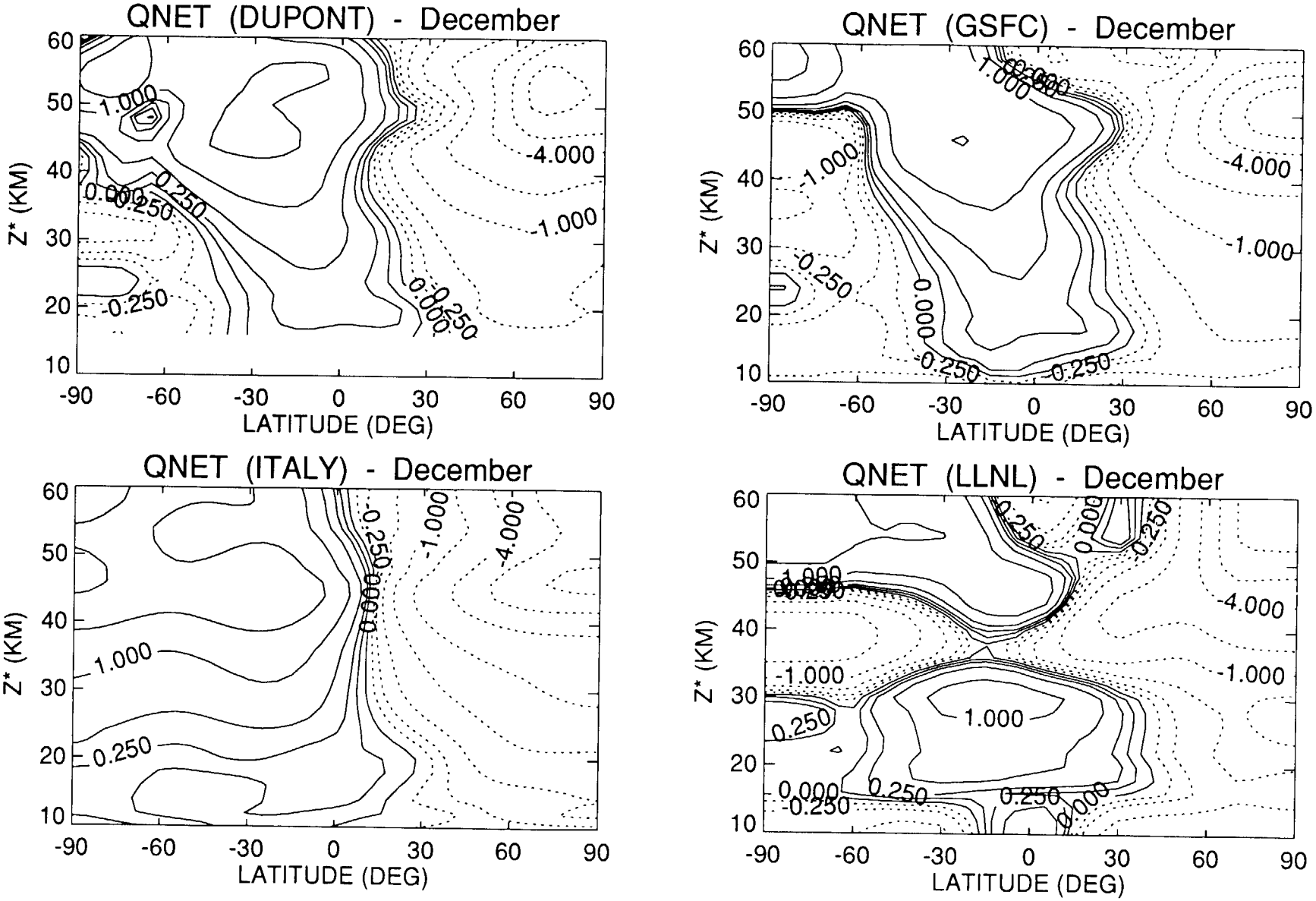

Figure A-6 (cont.)

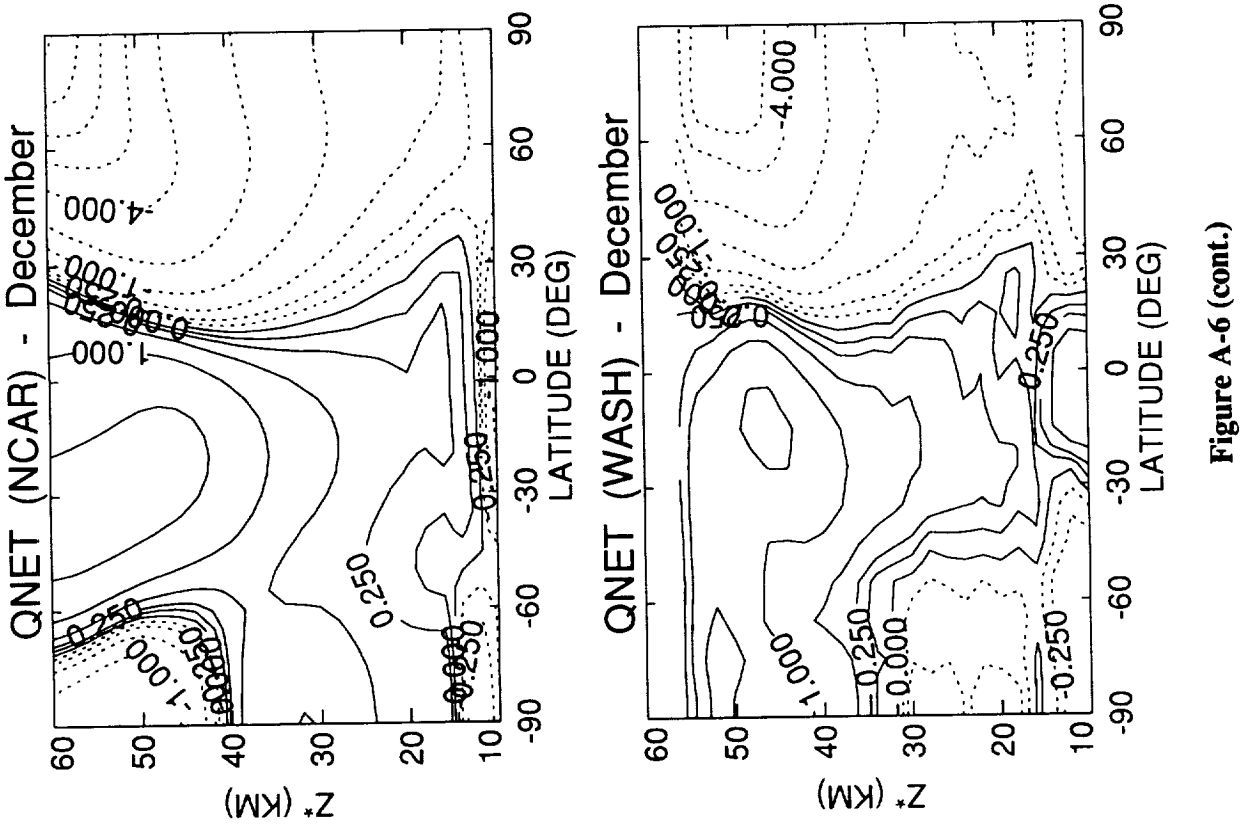

Figure A-6 (cont.)

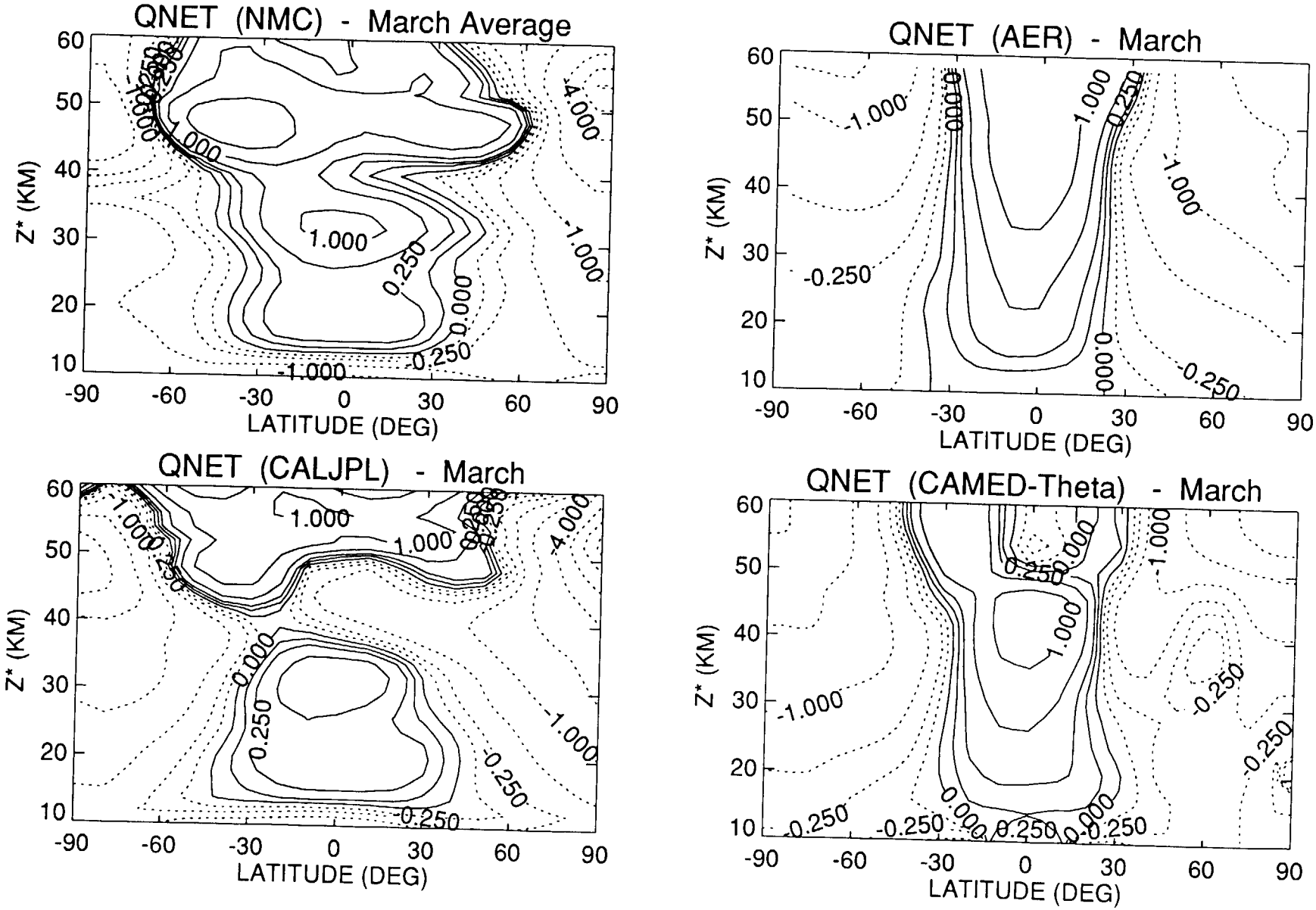

Figure A-6 (cont.)

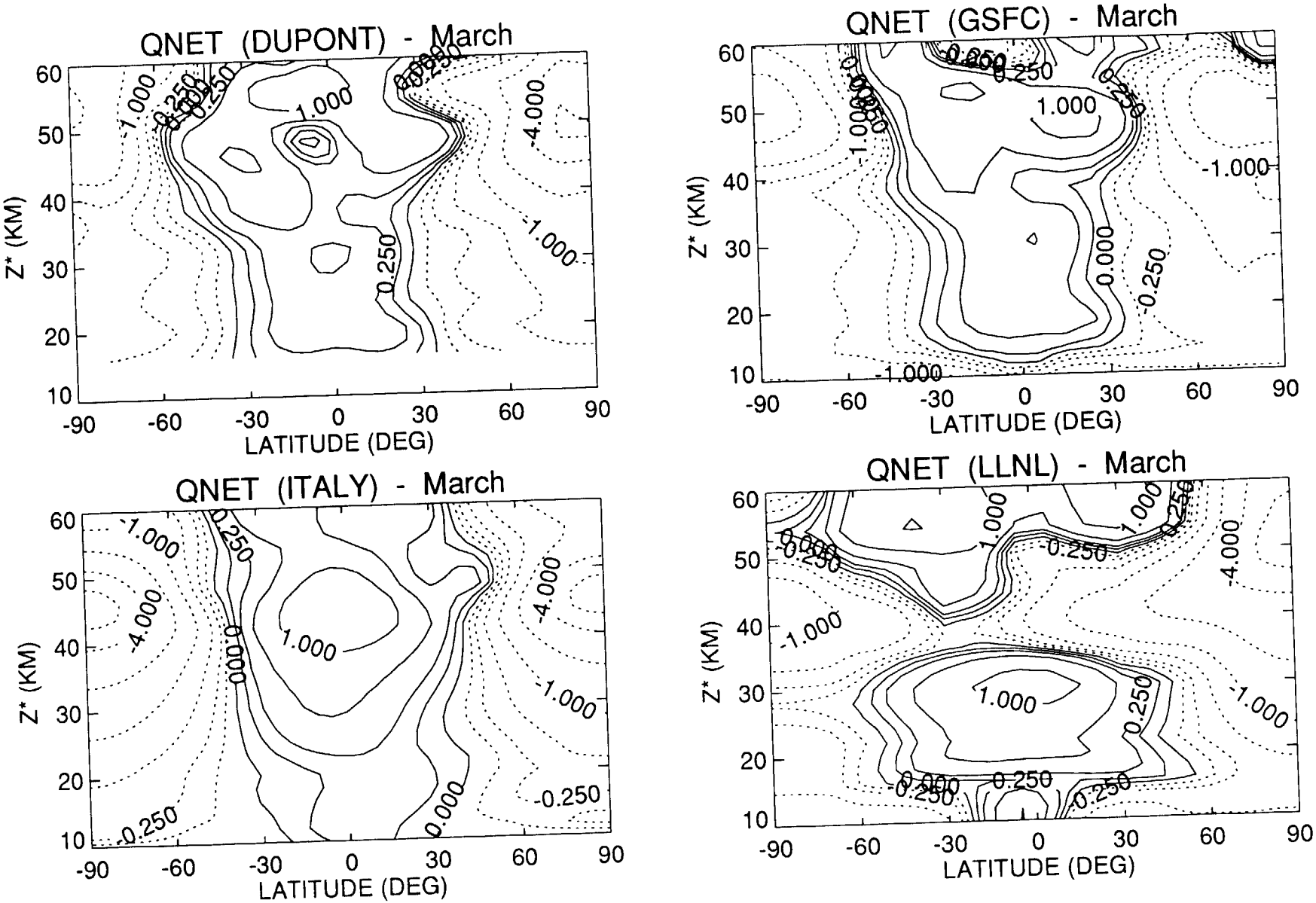

Figure A-6 (cont.)

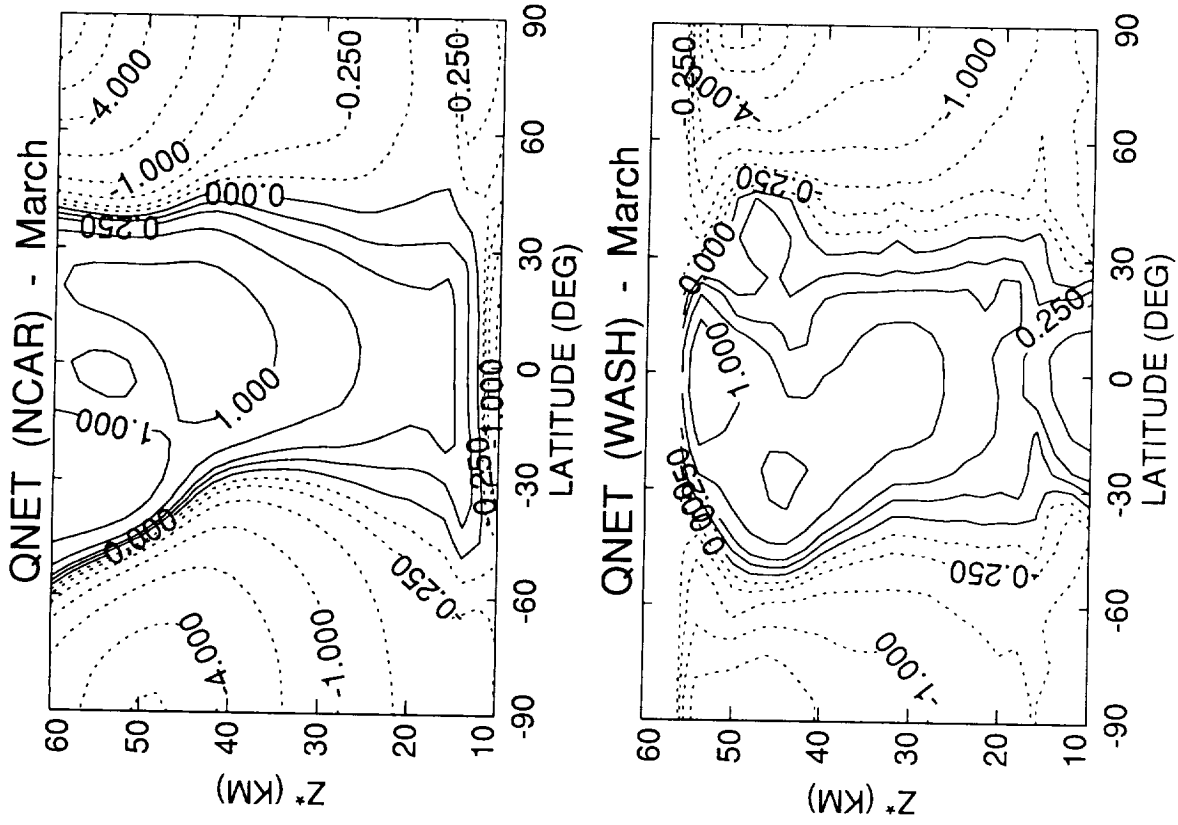

Figure A-6 (cont.)

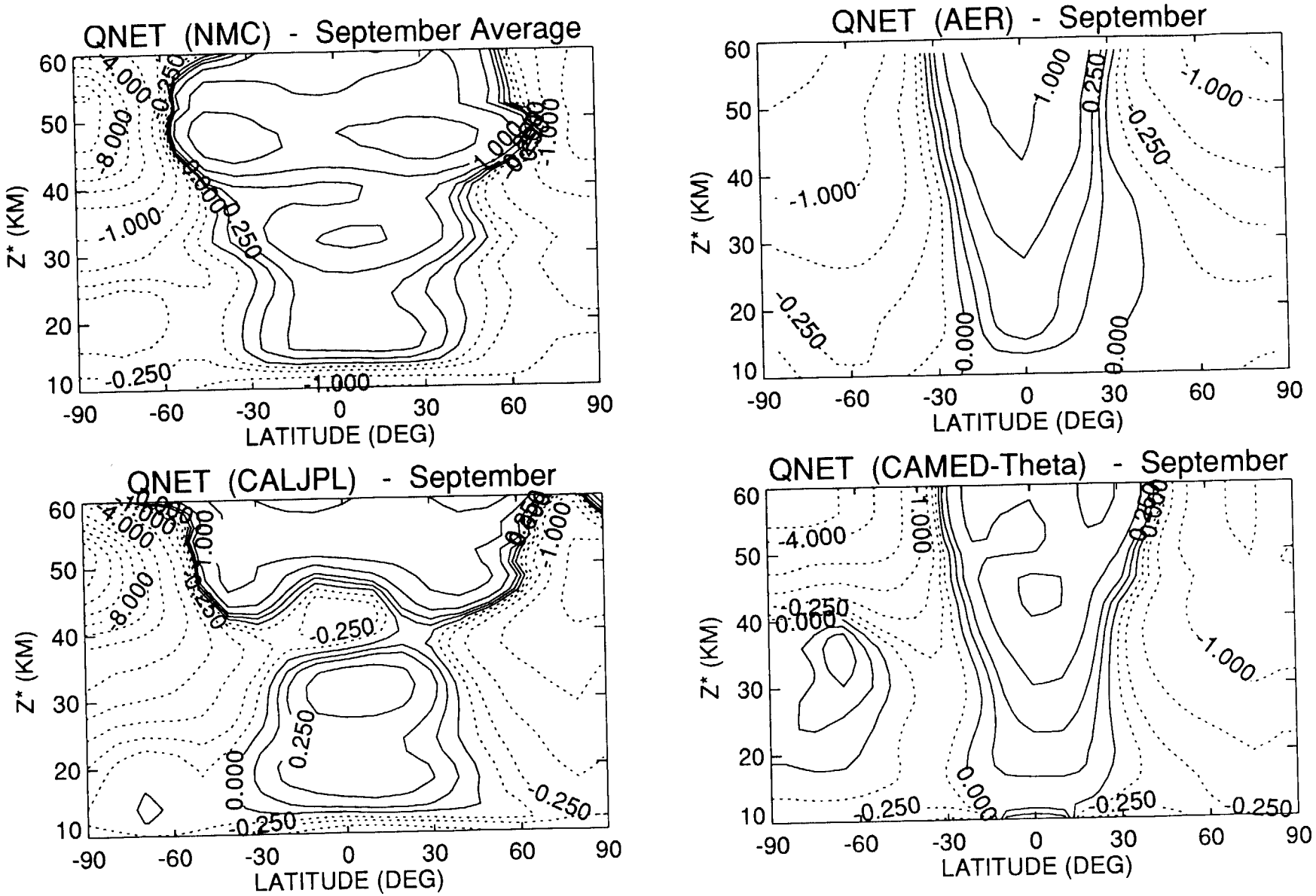

Figure A-6 (cont.)

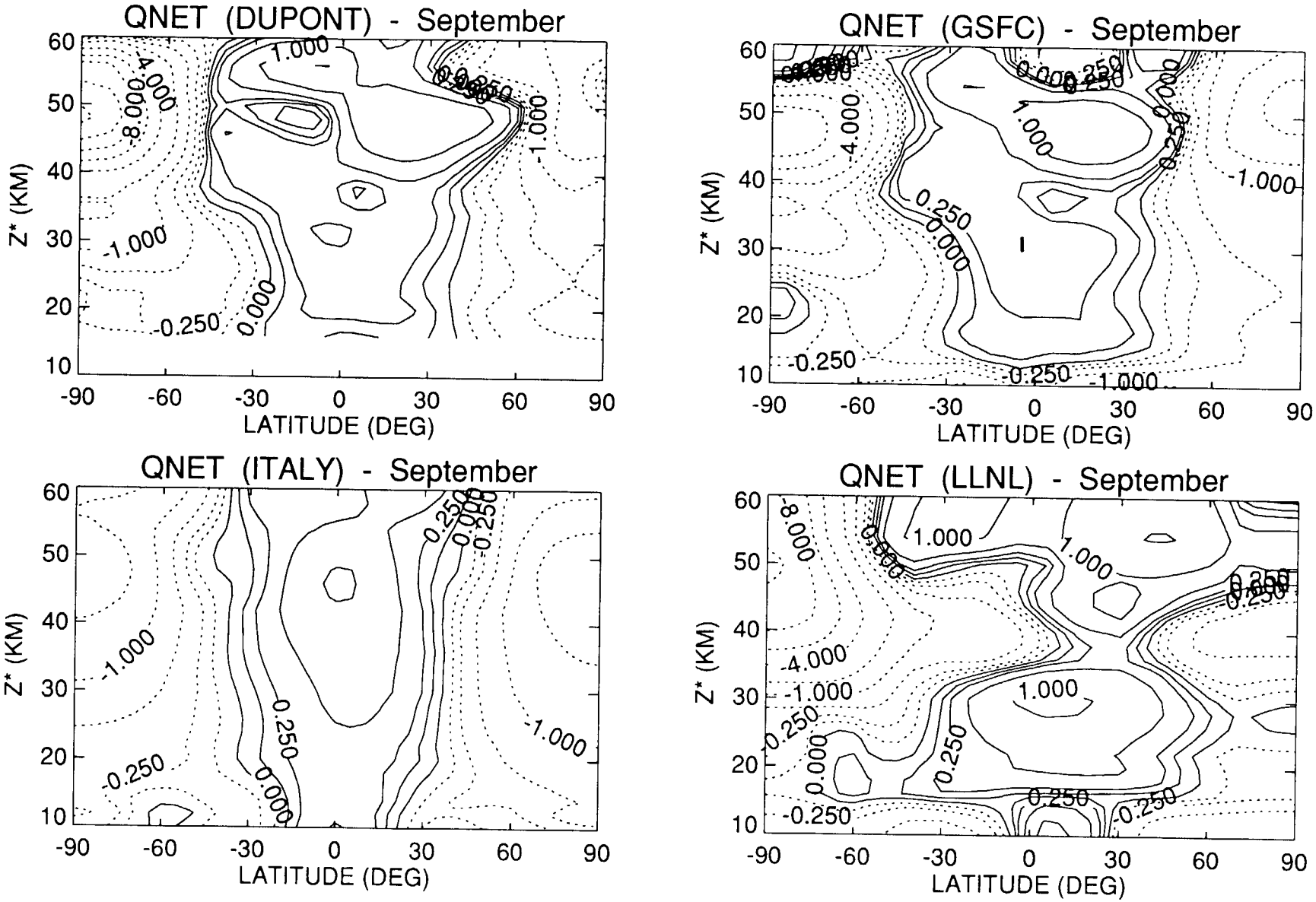

Figure A-6 (cont.)

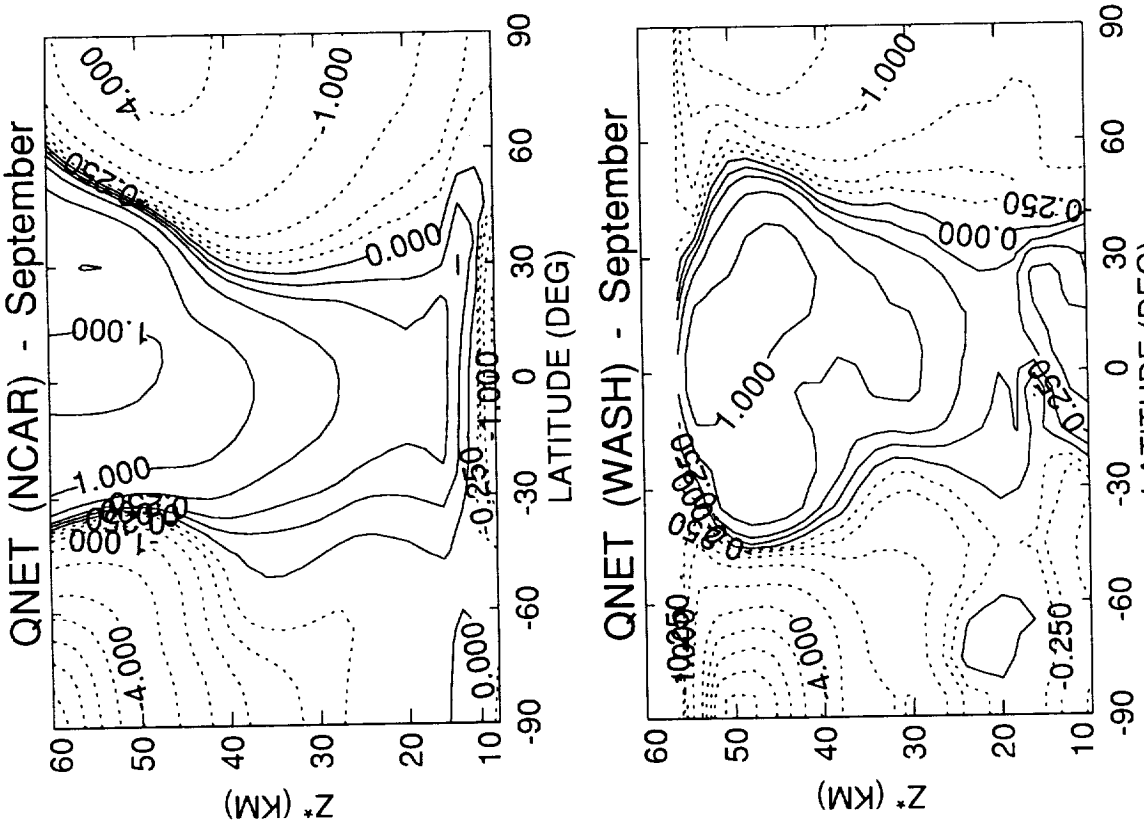

Figure A-6 (cont.)

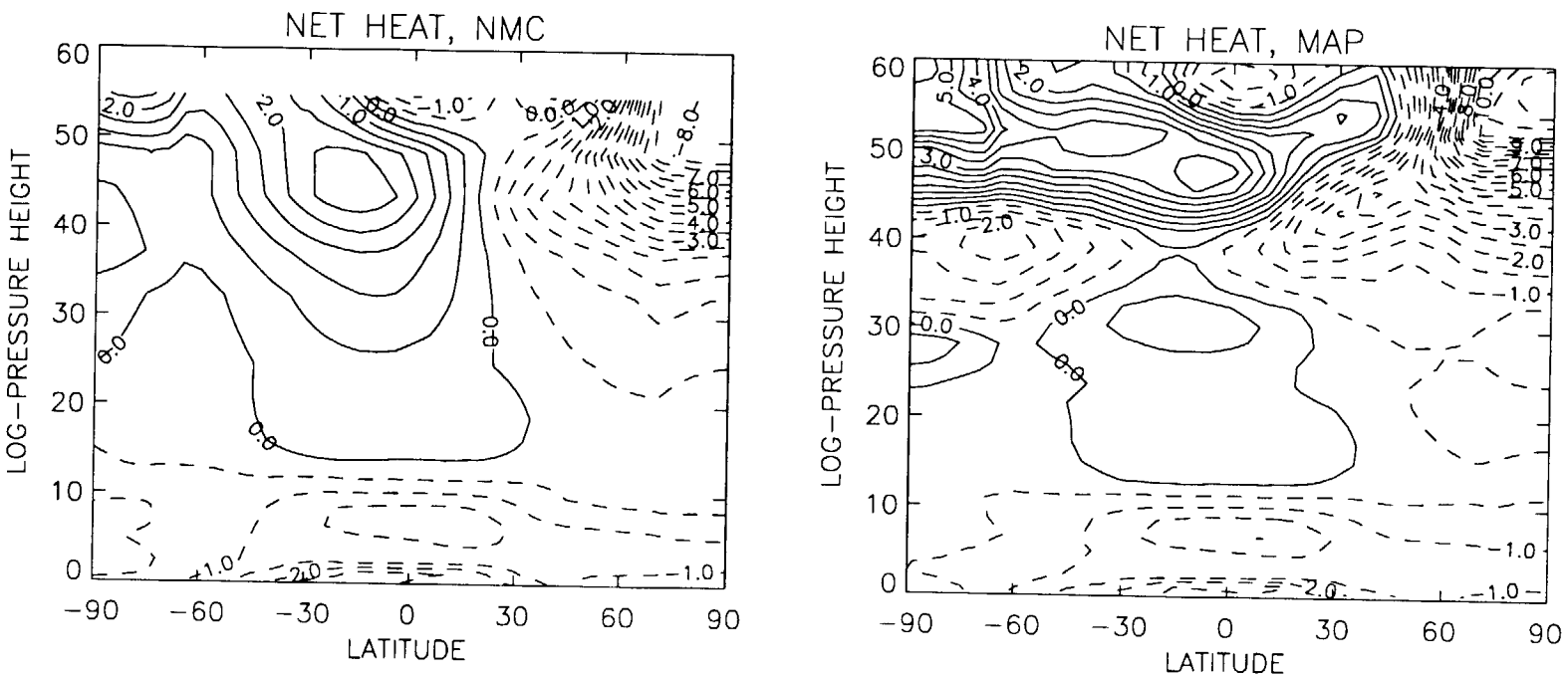
NET HEAT, NMC
LOG-PRESSURE HEIGHT
LATITUDE
60
50
40
30
20
10
0
-90
-60
-30
0
30
60
90
NET HEAT, MAP
LOG-PRESSURE HEIGHT
LATITUDE

Figure A-7

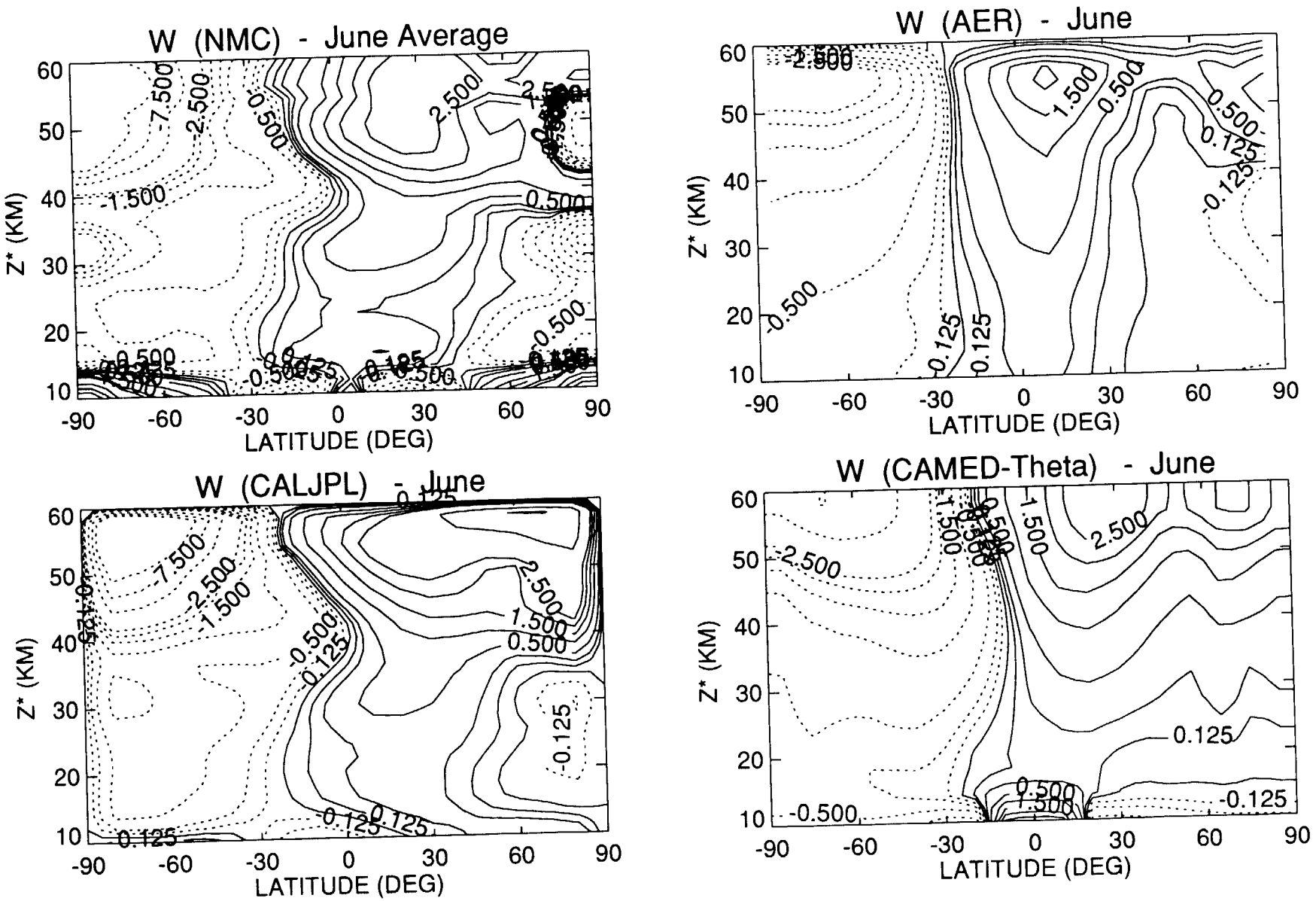
W (NMC) - June Average
W (AER) - June
W (CALJPL) - June
W (CAMED-Theta) - June
Z* (KM)
LATITUDE (DEG)

Figure A-8

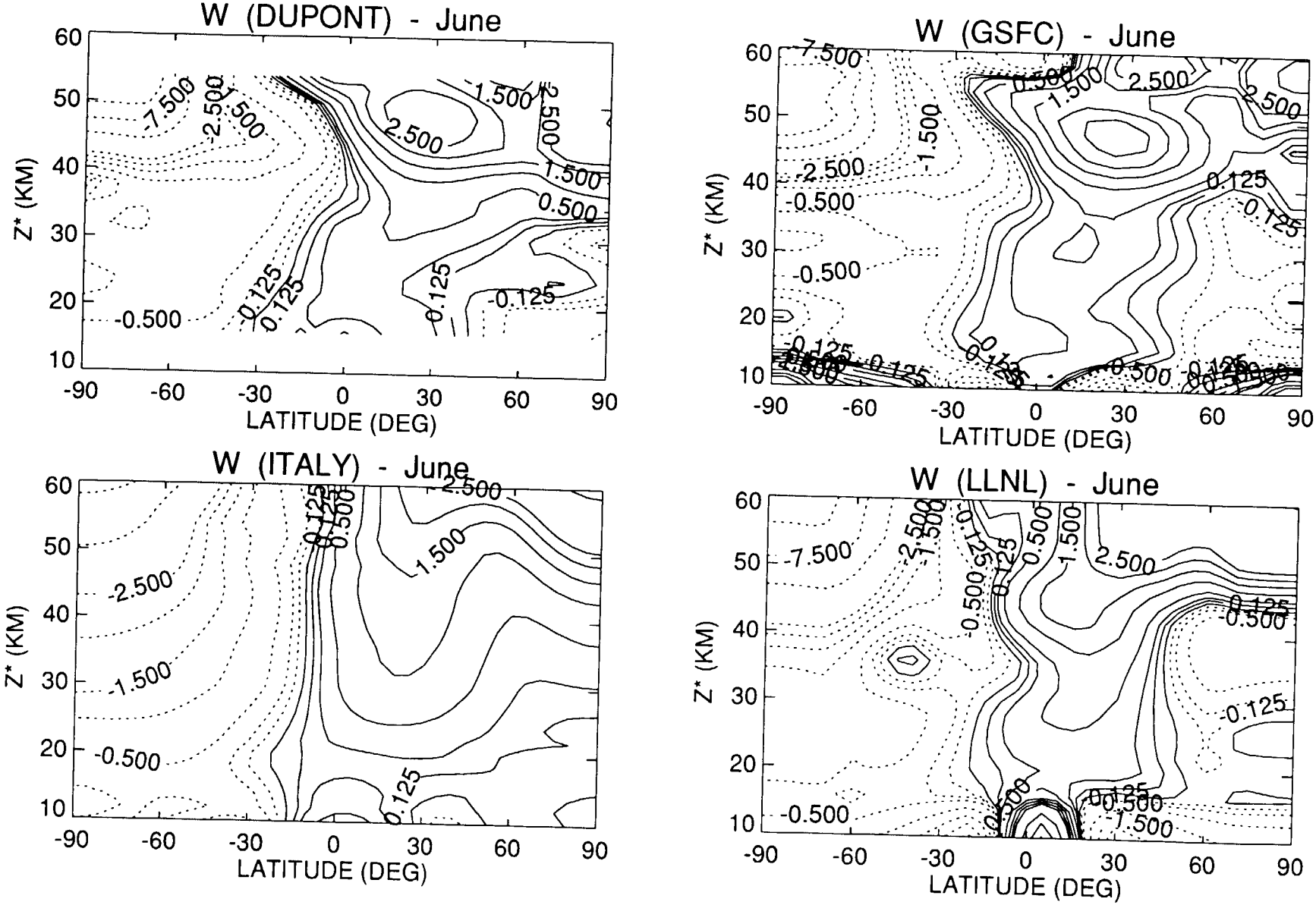

Figure A-8 (cont.)

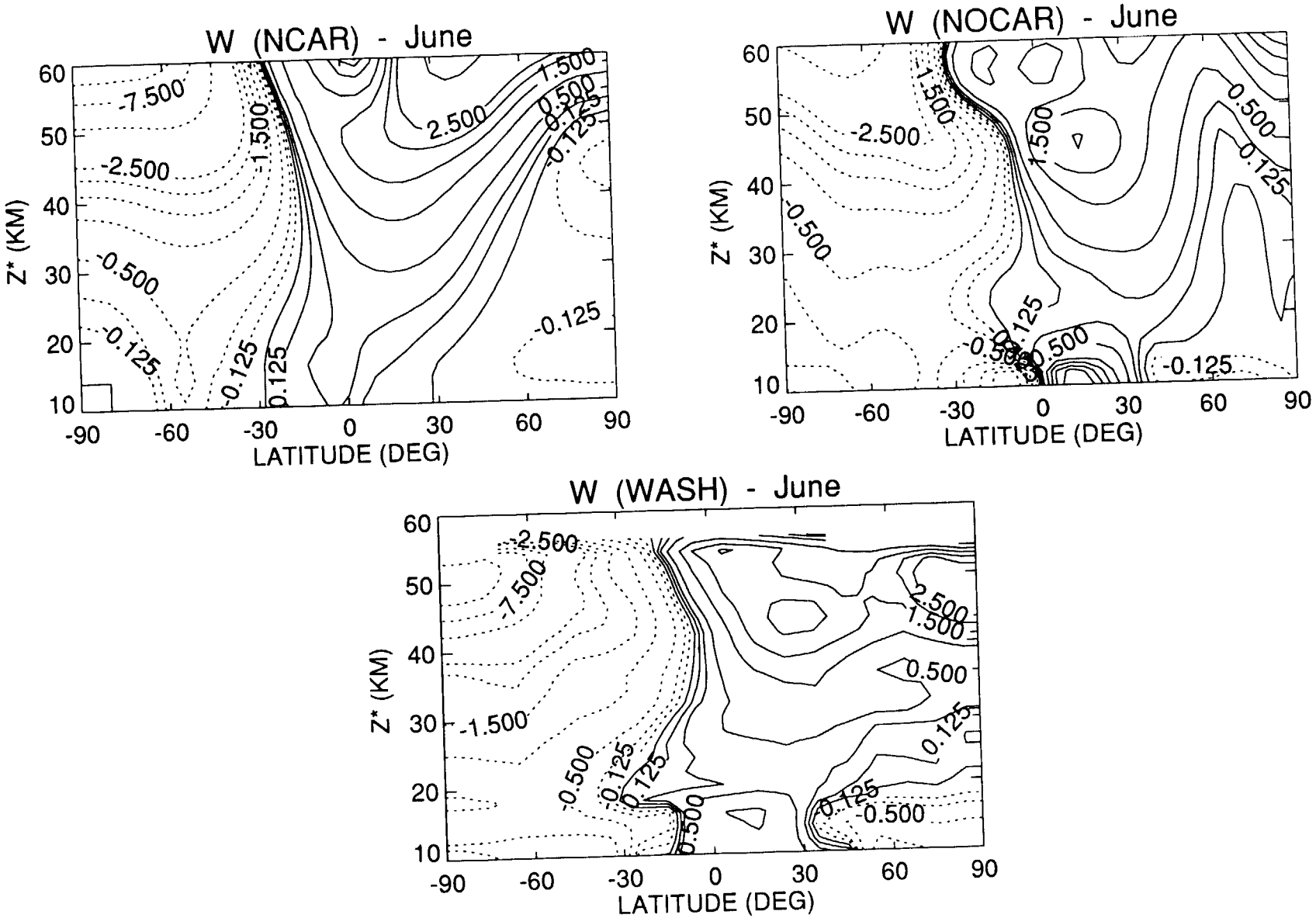

Figure A-8 (cont.)

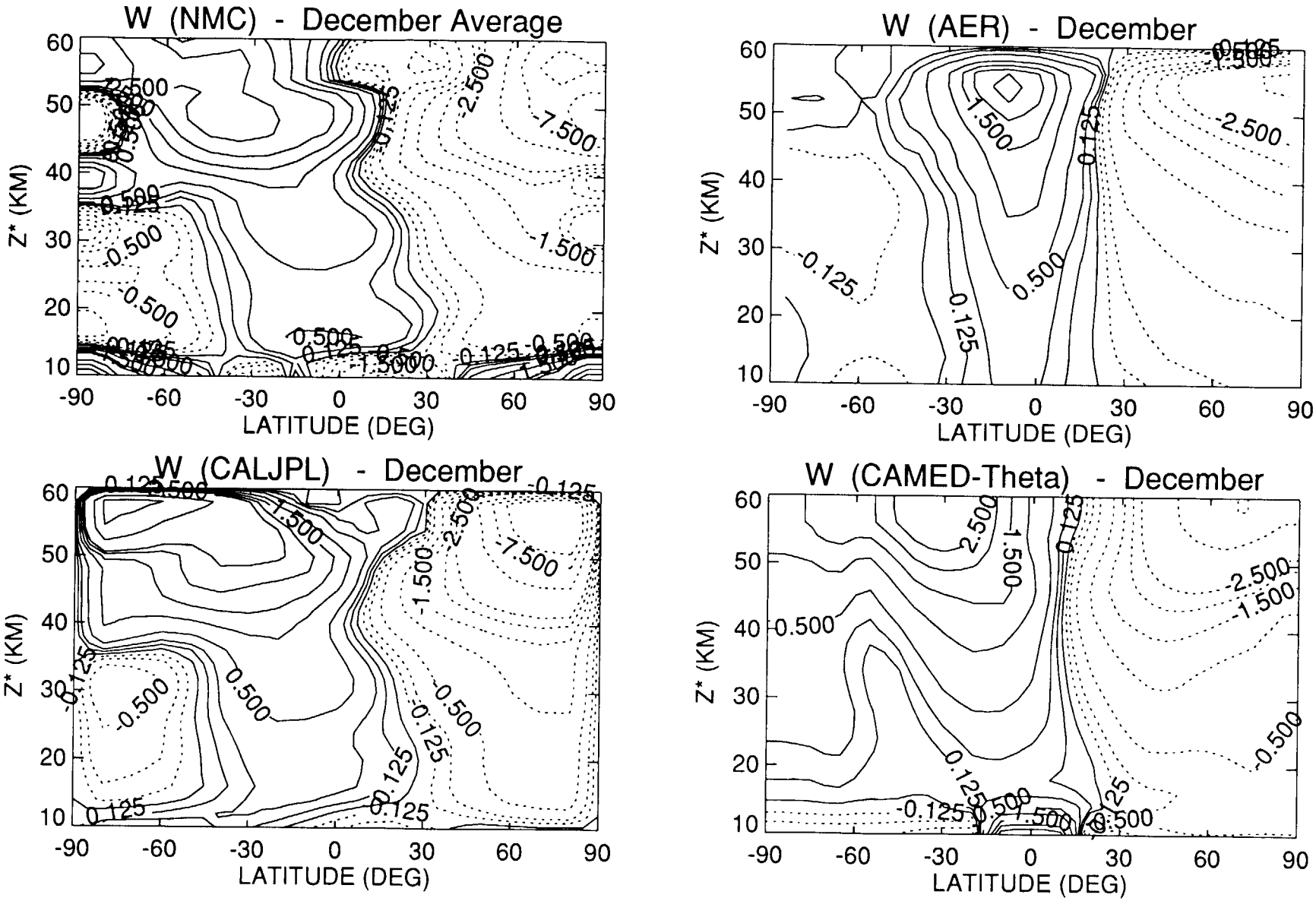

Figure A-8 (cont.)

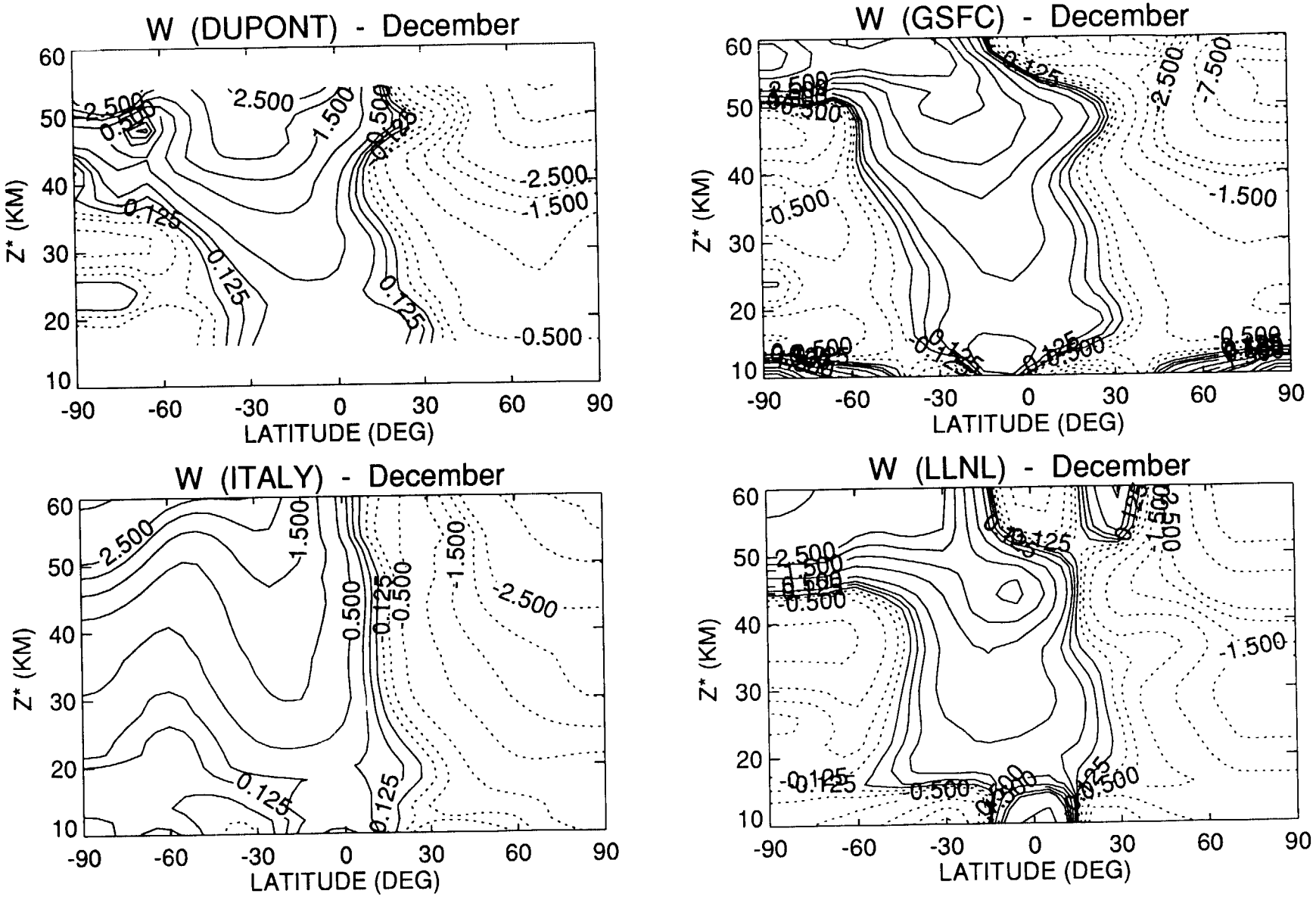

Figure A-8 (cont.)

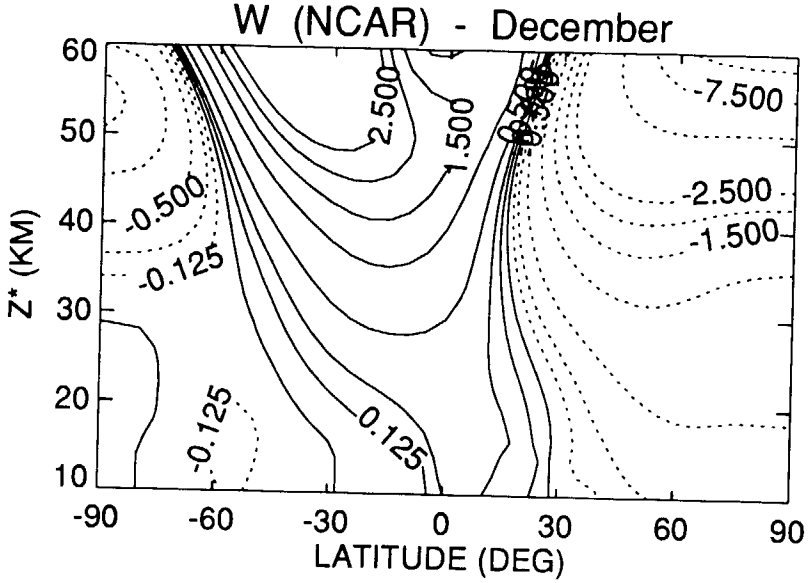

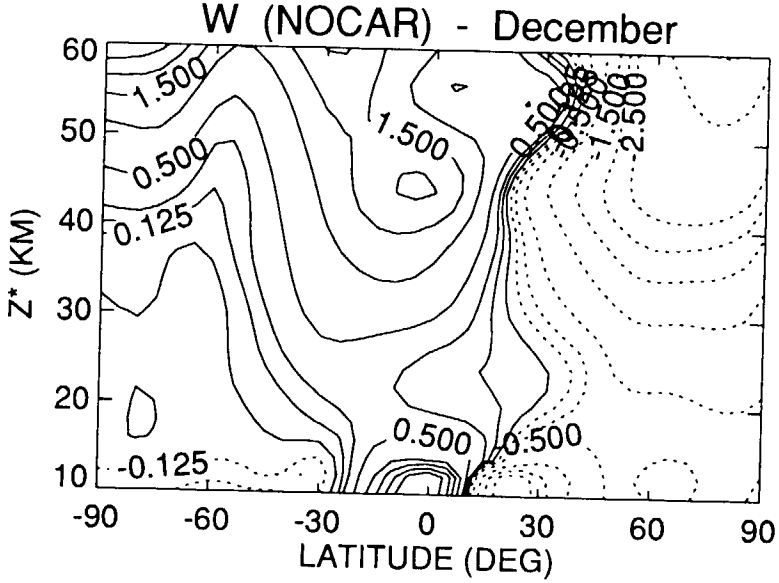

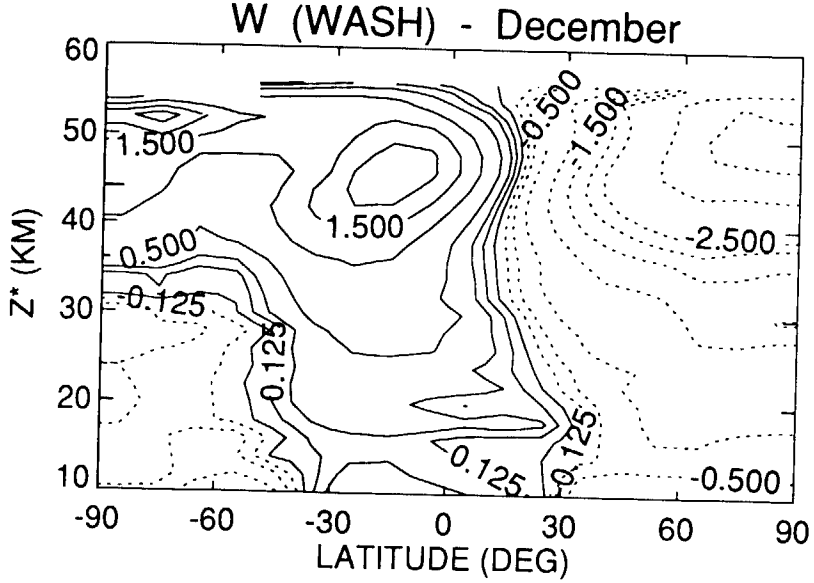

Figure A-8 (cont.)

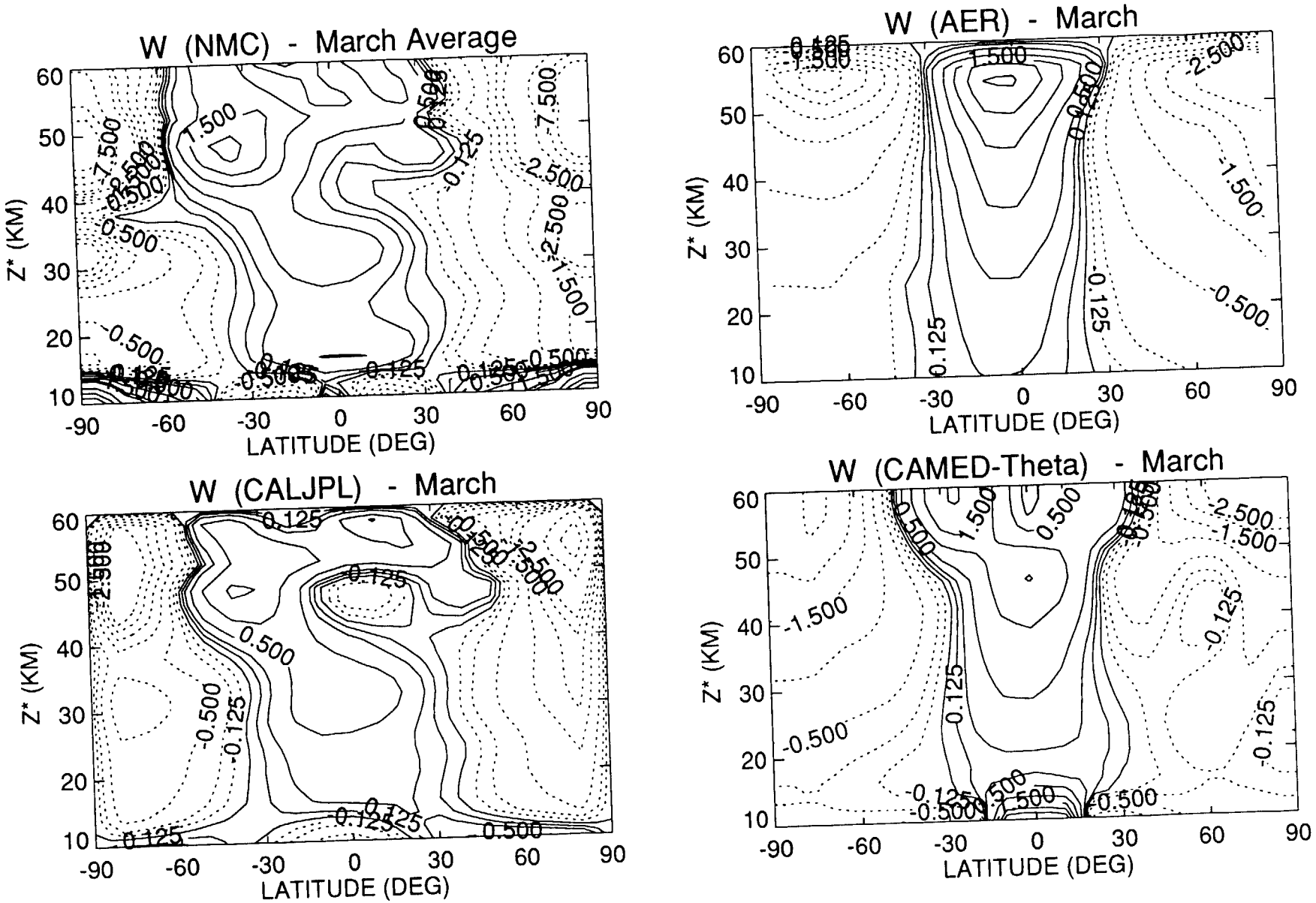

Figure A-8 (cont.)

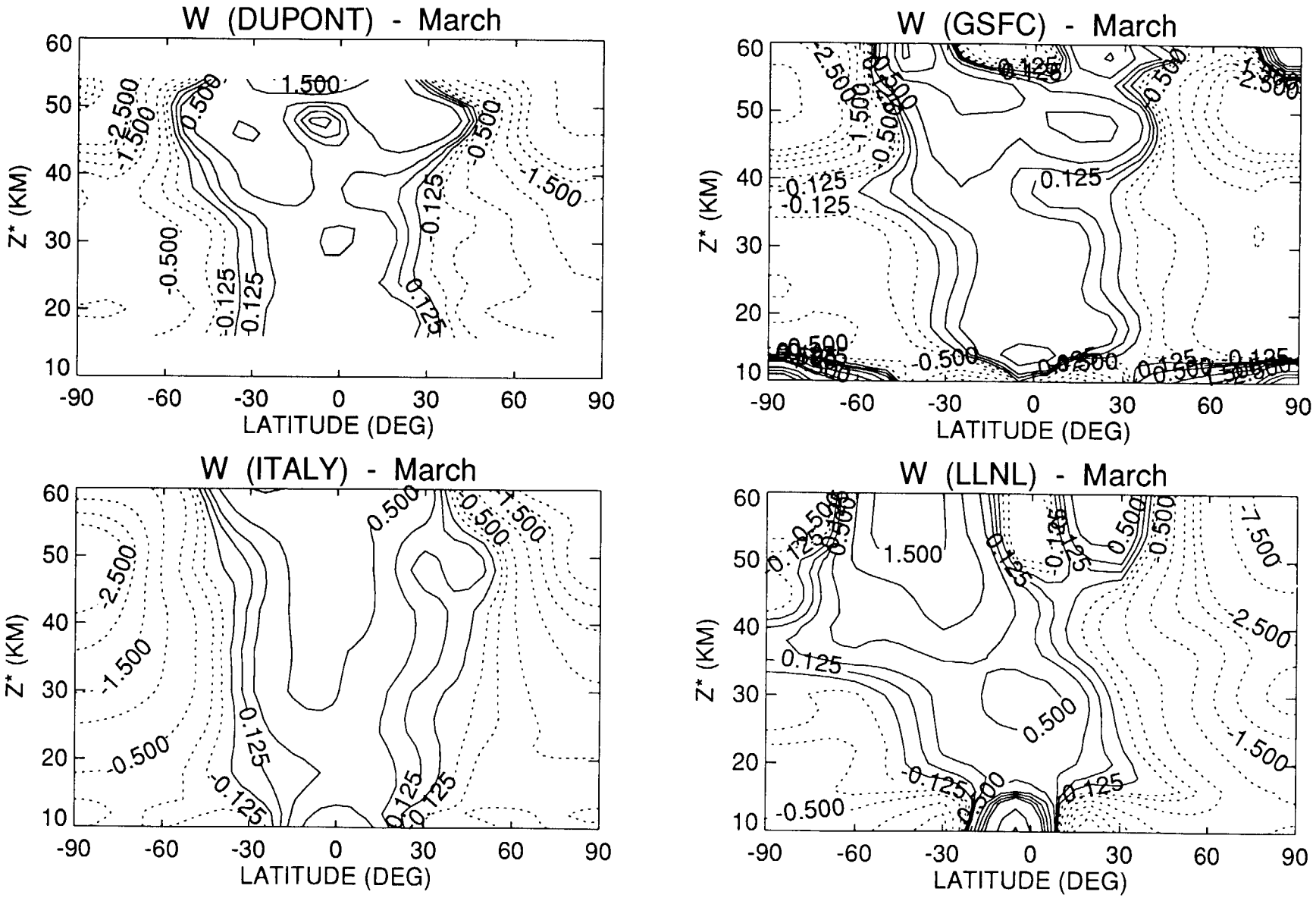

Figure A-8 (cont.)

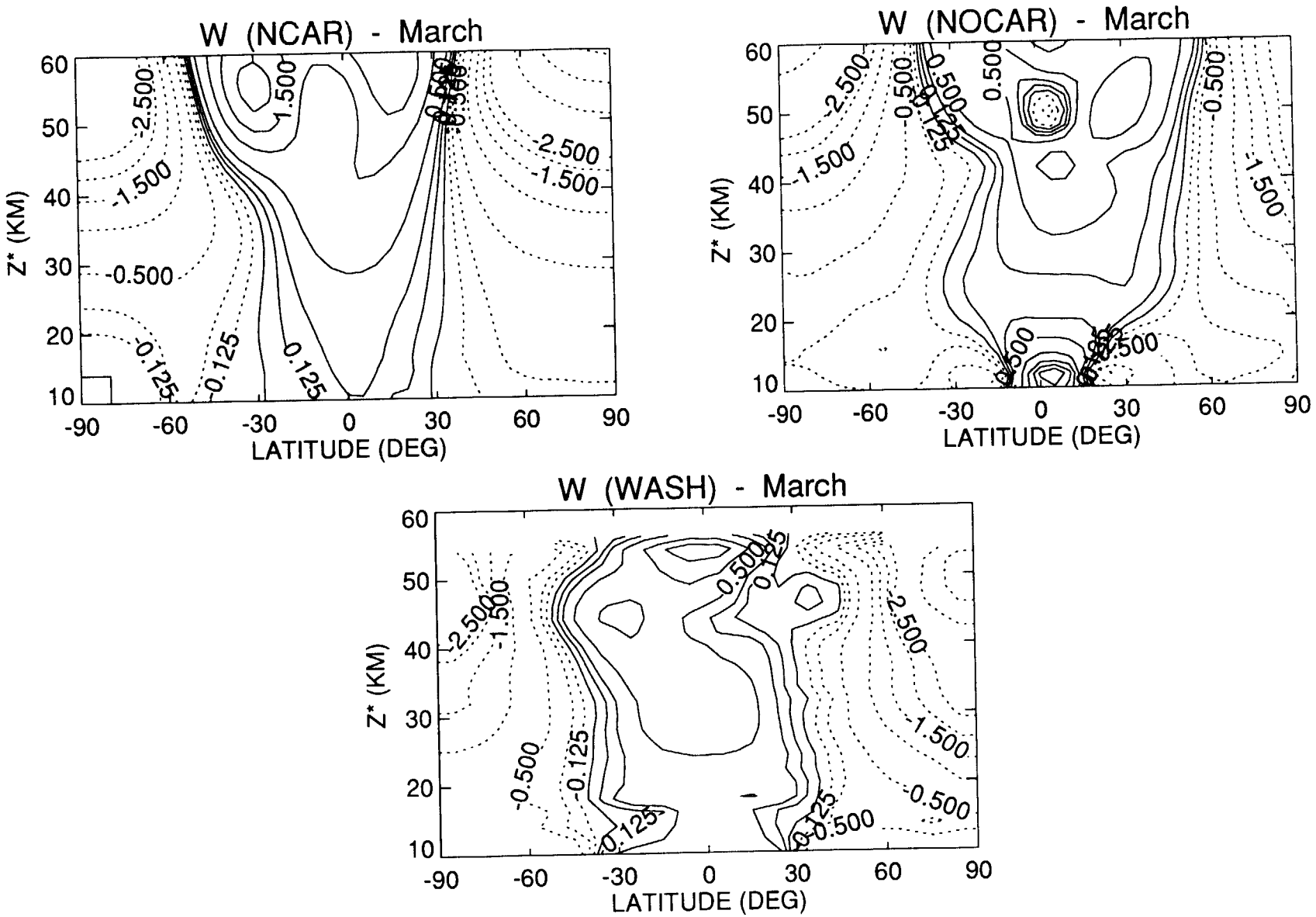

Figure A-8 (cont.)

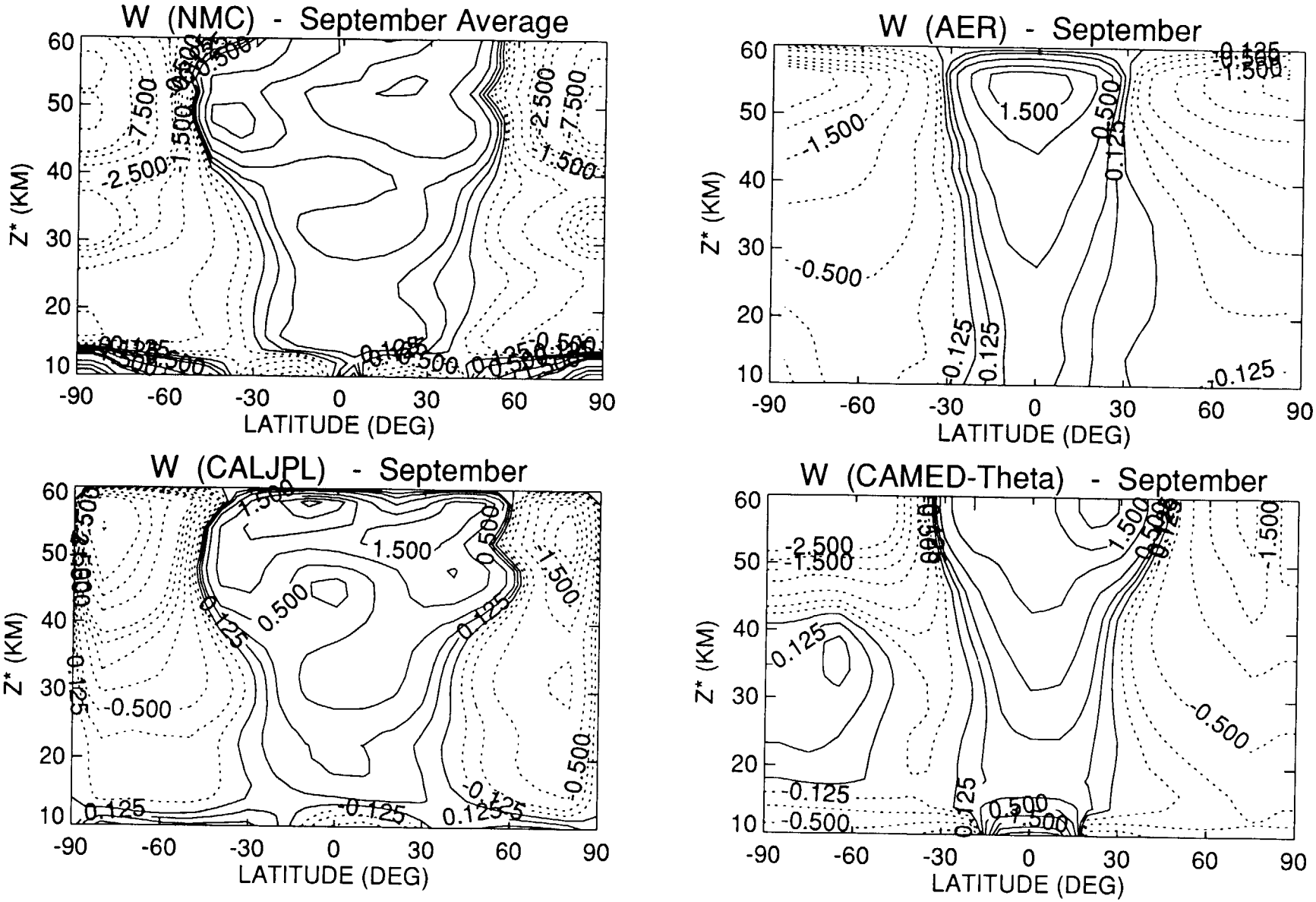

Figure A-8 (cont.)

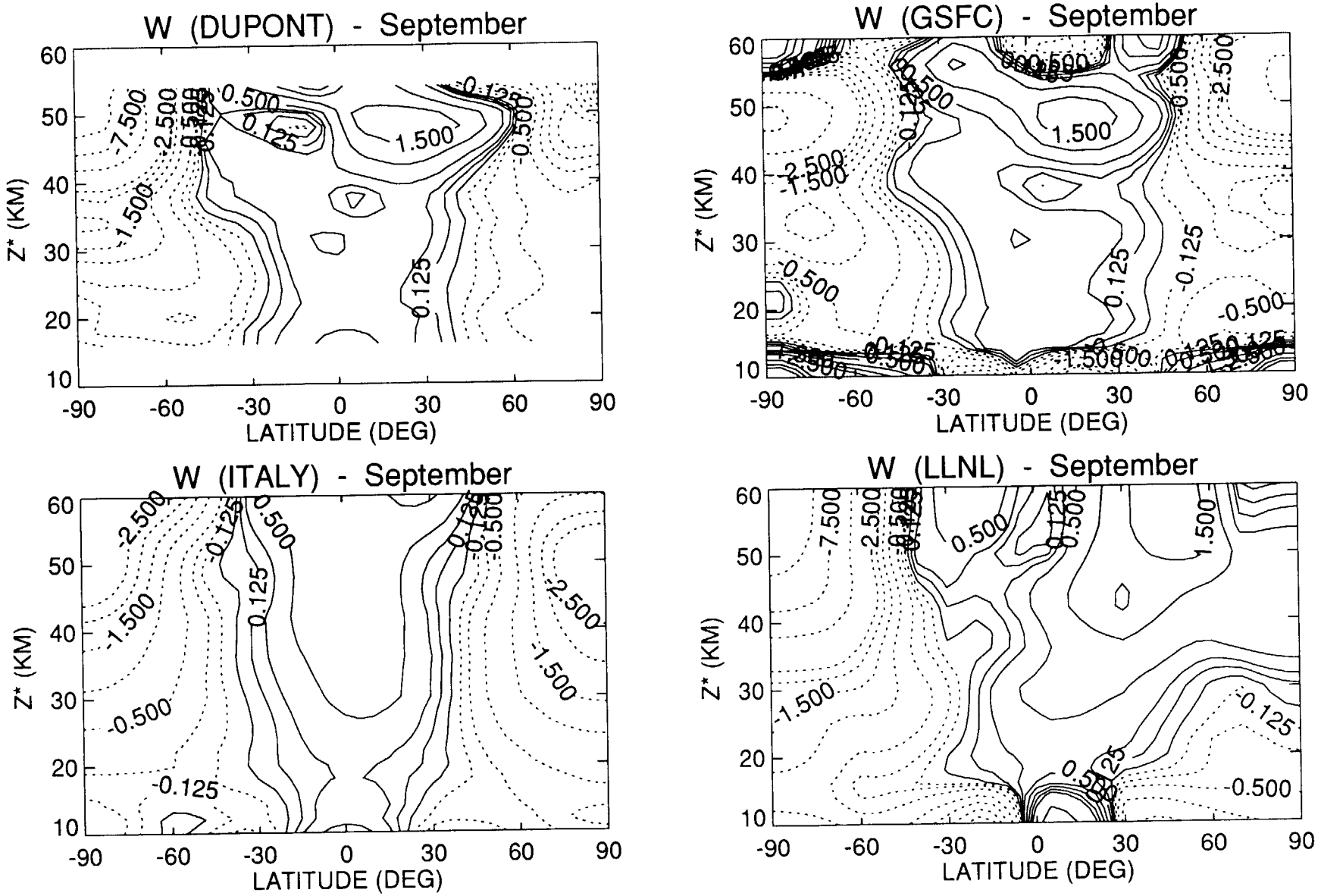

Figure A-8 (cont.)

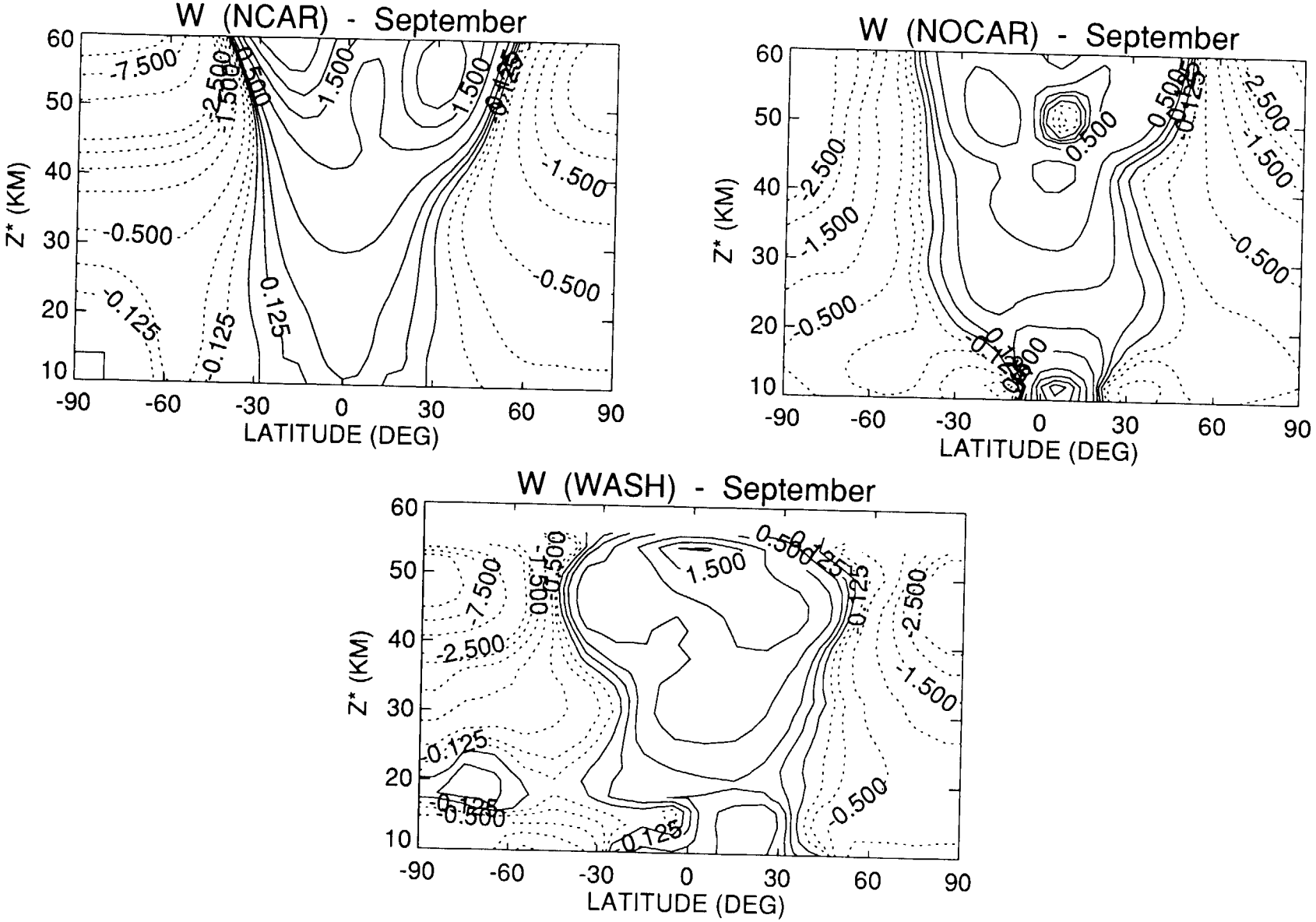

Figure A-8 (cont.)

B: Water Vapor

B: Water Vapor

Ellis E. Remsberg
NASA-Langley Research Center

INTRODUCTION

Water vapor is important for radiative and chemical processes in the stratosphere. It is also a useful tracer of stratospheric motions. But any model analysis of the water vapor budget in the lower stratosphere is complicated by the strong vertical gradients near the tropopause plus a condensation mechanism that "dries out" air as it enters the tropical stratosphere. The vertical and meridional H_2O gradients show general agreement in the midstratosphere from three quite different satellite data sources–Limb Infrared Monitor of the Stratosphere (LIMS), Stratospheric Aerosol and Gas Experiment (SAGE) II, and Atmospheric Trace Molecule Spectroscopy (ATMOS) (Remsberg et al., 1990; Chiou et al., 1992; Gunson et al., 1990). The greatest percentage of uncertainty for both in situ and satellite measurements of H_2O occurs for the 50 to 300 mb region or just where a fleet of high-speed civil transports (HSCT) would fly (Starr and Melfi, 1991).

Currently, researchers wonder whether the troposphere on the global scale is a net source region for H_2O to the stratosphere or vice versa. The net diabatic circulation brings methane and relatively dry air into the tropical stratosphere from below. There is a conversion of methane to water vapor in the upper stratosphere plus a net poleward and downward transport of air at higher latitudes. In this scenario the stratosphere represents a small net source of H_2O to the troposphere.

Kelly et al. (1991) find an asymmetry in upper tropospheric water vapor between the northern and southern hemispheres during winter, with the southern winter being drier. They ascribe this seasonal asymmetry to the colder temperatures in the Antarctic upper troposphere, leading to formation of ice crystals followed by their fallout to lower altitudes. They note that this asymmetry in H_2O is a striking extension downwards of the interhemispheric asymmetry observed in the stratosphere by the ER-2 (Kelly et al., 1990; Murphy et al., 1990). On the other hand, there is also an exchange of air between troposphere and stratosphere, primarily along the axes of the subtropical and the polar jet streams. Given the large gradient of H_2O across the jet axis, it is easy to imagine that there would be a net excess of H_2O remaining in the extratropical lower stratosphere as a result of this exchange (Foot, 1984; Tuck, 1989; Yung, unpublished data, 1992). However, other tracers show no obvious evidence of a large-scale injection of tropospheric air.

DATA SETS

Stratospheric water vapor has been reported from balloons and aircraft using either the frost point hygrometer or the Lyman-alpha fluorescence hygrometer techniques. A cryogenic collection technique has also been used on occasion. Up-looking, microwave remote sensors have also been used from airborne platforms. Limb-viewing remote measurements of H_2O have been obtained from balloon platforms using both mid- and far-infrared instrument techniques. Satellite data sets that are available include those from the LIMS and SAMS midinfrared experiments on the Nimbus-7 satellite and from the SAGE II near-infrared measurement of H_2O on an Atmospheric Explorer satellite. The Shuttle flight of ATMOS in 1985 provided several H_2O profiles for the middle atmosphere at high vertical resolution. Results from the Upper Atmosphere Research

Satellite (UARS) instruments (MLS, HALOE, ISAMS, and CLAES) are preliminary and, therefore, not available for the present comparisons.

The SAGE II data have been selected for model comparison in this report because (1) they extend into the upper troposphere during cloud-free viewing conditions (Rind et al., 1991, and (2) the data are near global and cover a 3-year period: 1986-1988. Monthly averages of the 3-year data set are used here. The SAGE II data are characterized by: (1) random error for single profiles of 18%; presumably it is much smaller when profiles are averaged (i.e., for the zonal mean). Systematic errors are estimated to be of the order 1 ppmv (about 35% to 20%) from 10 to 45 km, at least when aerosol and ozone interference is low (Chu et al., 1992); and (2) the data have been compared with the frost point and Lyman-alpha measurements in the lower stratosphere and with the Oort (1983) climatology in the upper troposphere. The LIMS data have much better overall sampling and are just as accurate, but they are limited to 7 months and have a lower boundary of 100 mb.

The SAGE II zonal mean H_2O cross section for March is shown in Figure B-1, and one can see minimum H_2O amounts of 2.5 to 3.5 ppmv just above the tropopause level and a very steep vertical gradient below. H_2O approaches the 6 ppmv level near 50 km, presumably the result of the gradual conversion of methane to H_2O at that altitude. The H_2O mixing ratio increases from equator-to-pole in the stratosphere at all z* levels, except perhaps at the highest latitudes in winter (not shown) when dehydration occurs in the Antarctic lower stratosphere and when there is strong diabatic descent into the upper stratosphere from the relatively dry, polar, lower mesosphere. The level of minimum H_2O coincides closely with the meridional slope of the tropopause and occurs 1 to 2 km higher. The mid- to high-latitude values of 3 to 3.5 ppmv have been observed by balloons and aircraft in southern hemisphere winter, but not in the northern hemisphere, so there is some uncertainty about the minimum H_2O values from SAGE II (Kelly et al., 1989, 1990; Hofmann et al., 1991; Schoeberl et al., 1992).

Figure B-2 is the LIMS minus SAGE II (divided by SAGE II) plot for March. Although the two data sets are from different years, the differences are deemed representative of any year because there is little interannual variability in the 3-year SAGE II data set. However, Mastenbrook and Oltmans (1983) have shown that there are clear annual and, especially, quasi-biennial oscillation (QBO) cycles in lower stratospheric water vapor at northern hemisphere midlatitudes. The agreement in Figure B-2 is within 30% throughout most of the stratosphere. Greatest differences occur in the lower tropical stratosphere, where both the LIMS and SAGE II error bars are also largest. An analysis of a subset of the LIMS data using improved spectral parameters for H_2O and a more accurate forward radiance algorithm indicates about a 10% increase in LIMS H_2O above about 22 km; there is almost no change at lower altitudes (Remsberg et al., 1992). Such a change for LIMS improves the comparison in Figure B-2 in the midstratosphere. A significant difference remains near 20 km at low latitudes and between 16 and 20 km at higher latitudes. Again, based on independent comparisons with balloon and aircraft data sets, it appears that the SAGE II H_2O is about right at low latitudes, a bit dry at mid to high northern latitudes, and about right poleward of 50S for winter/spring. SAGE II comparisons with the May 1985 ATMOS profiles at both 31N and 48S are within their respective error bars (Chiou et al., 1992).

MODEL H_2O

Model H_2O distributions are either specified or calculated, but these distributions determine the stratospheric abundance of H_2O. While many of the assumptions are

reasonable, they do not adequately represent the physical processes that change H_2O near the tropopause. Tropospheric H_2O is specified from a fixed relative humidity (NCAR, DUPONT, GSFC, MPI) as a function of latitude, altitude, and season; or based on fixed mixing ratio vs. z* (MRI); or scaled from a surface value (ITALY). Some models contain climatological H_2O (LLNL) or have H_2O set to a small value (CAMED-theta).

Many models contain fixed H_2O near the tropopause, because the model temperatures are not accurate enough to specify H_2O from saturation considerations. Some modelers prescribe tropopause H_2O based on LIMS data (ITALY, LLNL); some use other fixed values (DUPONT, CAMED-theta, MPI). Stratospheric H_2O is calculated in many models (CAMED, MRI, LLNL, MPI, DUPONT, NCAR, ITALY), whereas several use fixed monthly distributions based on the LIMS data (GSFC, AER). The various approaches for modeling H_2O must be borne in mind when evaluating the model/data differences in the next section. With respect to the modeling of PSC chemistry, most models prescribe the occurrence of a PSC based on a threshold temperature rather than a true calculation of saturation conditions. Therefore, an accurate determination of the local H_2O mixing ratio is not so essential. An exception to this is the PSC calculation of Rosenfield (1992).

RESULTS

Figure B-3 (a) through (l) shows plots of model minus SAGE II (divided by SAGE II) H_2O for March. Comparisons extend from z* = 10 to 50 km. Models (Figure B-3a, e, k, l) that rely on LIMS data in the stratosphere display a pattern similar to that in Figure B-2. However, it should be noted that Figure B-2 contains only LIMS nighttime data, whereas the models may have used an average of day and night LIMS data. Models (b, c, d, f, g, h, i, j) that calculate stratospheric water vapor are somewhat drier than the SAGE II values but by no more than 40%. Some models (b, f, g, i) are clearly influenced by the oxidation of CH_4 in the upper stratosphere. All of these models yield a "reasonable" representation of the observed H_2O. The DUPONT (d) and NCAR (j) models have the driest H_2O values overall.

Water vapor at the tropopause is quite variable from model to model. Those that have a parameterization for H_2O (a, d, e, f, h, j) give upper troposphere results that are "reasonable." The LLNL (g) and WASH (l) H_2O distributions are based on the climatology of Oort (1983), so the large differences below 16 km must be due to a substantial (order of 100%) difference between the SAGE II and RAOB hygristor results for H_2O. But H_2O estimates from hygristor data are biased too wet (Starr and Melfi, 1991). Tropospheric H_2O from the CAMED-theta model (c) is set very small. The NOCAR model (k) has no troposphere; its lower boundary is near 16 km. A new version of that model calculates H_2O and contains a troposphere, but results for H_2O are not yet available.

Figure B-4 contains time series plots of H_2O at z* = 20 km from SAGE II and from each of the models. All models are 1980 SS, except ITALY (1990 SS). MPI and NOCAR did not submit results for all 12 months. Of the models that calculate H_2O, the CALJPL, ITALY, and LLNL models agree best with SAGE II data. Tropical values are of the order 2.5 to 3.5 ppmv, and the meridional gradients are about right. There is a seasonal variation in the model H_2O. The ITALY model has a minimum at high latitudes for southern hemisphere winter/spring. Values shown in Figure B-4 are compared with the Airborne Antarctic Ozone Expedition (AAOE) and the Airborne Arctic Stratospheric Expedition (AASE) ER-2 H_2O measurements for August and September (about 2.0 to 3.0 ppmv) and for January and February (about 4.5 to 5.0 ppmv) in Schoeberl et al. (1992).

Comparisons at other z* levels can be made, and they are appropriate for gauging the quality of model H_2O distributions in the lower stratosphere and upper troposphere. Figure B-5 shows SAGE II results at z* = 16 km. A seasonal dependence is noted at low latitudes, which corresponds qualitatively to the seasonal variations in tropopause temperatures in the tropics.

CONCLUSIONS

Most models are somewhat drier than SAGE II H_2O from 50 to 20 km, but generally by no more than the SAGE II uncertainties (20% to 35%). Models that calculate H_2O agree more closely with the LIMS values (even after LIMS is corrected by 10%), but the LIMS uncertainties are also no smaller than 20%.

It is difficult for models to simulate the sharp vertical gradients of H_2O at the tropopause because of their limited resolution. To determine the amount of H_2O exchanged from the tropical troposphere to the stratosphere is even more difficult, because the calculated exchange relies on an accurate determination (to about 1 K) of tropopause temperature.

There is a critical need for higher quality H_2O data between 10 to 20 km. Seasonal data are needed and on a global scale. In particular, high quality H_2O measurements are needed in UADP at midlatitudes and low latitudes (e.g., from the STEP mission of 1987 and the upcoming SPADE missions in 1992/1993).

Accurate estimates of percentage changes in ambient H_2O resulting from a fleet of HSCTs must await these better baseline data sets and the higher resolution models. Estimates of relative change should be possible now, particularly with respect to stratospheric injections of H_2O along a flight corridor at high latitudes. To do this, the perturbation of the model water vapor should be relative to a fixed value. Relative humidity would increase up to the saturation value until the perturbation becomes dispersed. Still, these relative changes will be in error if the mechanism for removal of H_2O in the middle latitude stratosphere is not understood. If the concentration at the tropopause is fixed or if the flux is fixed by the drying-out mechanism, then the answers will be different.

REFERENCES

Chu, W. P., E. W. Chiou, J. C. Larsen, L. W. Thomason, D. Rind, J. J. Buglia, S. Oltmans, M. P. McCormick, L. R. McMaster, Algorithms and sensitivity analyses for SAGE II water vapor retrieval, *J. Geophys. Res.*, in press, 1992.

Chiou, E. W., M. P. McCormick, L. R. McMaster, W. P. Chu, J. C. Larsen, D. Rind, and S. Oltmans, Intercomparisons of stratospheric water vapor observed by satellite experiments: SAGE II versus LIMS and ATMOS, *J. Geophys. Res.*, in press, 1992.

Foot, J. S., Aircraft measurements of the humidity in the lower stratosphere from 1977 to 1980 between 45 N and 65 N, *Quart. J. R. Met. Soc., 110*, 303-319, 1984.

Gunson, M. R., C. B. Farmer, R. H. Norton, R. Zander, C. P. Rinsland, J. H. Shaw, and B.-C. Gao, Measurements of CH_4, N_2O, CO, H_2O, and O_3 in the middle atmosphere by the Atmospheric Trace Molecule Spectroscopy experiment on Spacelab 3, *J. Geophys. Res., 95*, 13867-13882, 1990.

Hofmann, D. J., S. J. Oltmans, and T. Deshler, Simultaneous balloonborne measurements of stratospheric water vapor and ozone in the polar regions, *Geophys. Res. Letts., 18*, 1011-1014, 1991.

Kelly, K. K., A. F. Tuck, and T. Davies, Wintertime asymmetry of upper tropospheric water between the northern and southern hemispheres, *Nature, 353*, 244-247, 1991.

Kelly, K. K., A. F. Tuck, L. E. Heidt, M. Loewenstein, J. R. Podolske, S. E. Strahan, and J. F. Vedder, A comparison of ER-2 measurements of stratospheric water vapor between the 1987 Antarctic and 1989 Arctic airborne missions, *Geophys. Res. Letts., 17*, 465-468, 1990.

Kelly, K. K., et al., Dehydration in the lower Antarctic stratosphere during late winter and early spring, 1987, *J. Geophys. Res., 94*, 11317-11358, 1989.

Mastenbrook, H. J., and S. J. Oltmans, Stratospheric water vapor variability for Washington, DC/Boulder, CO: 1964-82, *J. Atmos. Sci., 40*, 2157-2165, 1983.

Murphy, D. M., K. K. Kelly, A. F. Tuck, and M. H. Proffitt, Ice saturation at the tropopause observed from the ER-2 aircraft, *Geophys. Res. Letts., 17*, 353-356, 1990.

Oort, A. H., "Global Atmosphere Statistics, 1958-1973," NOAA Professional Paper 14, 1983.

Remsberg, E. E., J. M. Russell III, P. P. Bhatt, L. L. Gordley, and B. T. Marshall, A reassessment of the Nimbus-7 LIMS water vapor distributions, *J. Geophys. Res.*, in preparation, 1992.

Remsberg, E. E., J. M. Russell III, and C.-Y. Wu, An interim reference model for the variability of the middle atmosphere water vapor distribution, *Adv. Space Res., 10*, no. 6, 51-64, 1990.

Rind, D., E.-W. Chiou, W. Chu, J. Larsen, S. Oltmans, J. Lerner, M. P. McCormick, and L. McMaster, Positive water vapour feedback in climate models confirmed by satellite data, *Nature, 349*, 500-503, 1991.

Rosenfield, J. E., Radiative effects of polar stratospheric clouds during the Airborne Antarctic Ozone Experiment and the Airborne Arctic Stratospheric Expedition, *J. Geophys. Res.*, *97*, 7841-7858, 1992.

Schoeberl, M. R., L. R. Lait, P. A. Newman, and J. E. Rosenfield, The structure of the polar vortex, *J. Geophys. Res.*, *97*, 7859-7882, 1992.

Starr, D. O'C., and S. H. Melfi, eds., *The Role of Water Vapor in Climate, NASA Conference Publication 3120*, 60 pp., NASA, Washington D.C., July 1991.

Tuck, A. F., Synoptic and chemical evolution of the Antarctic vortex in late winter and early spring, 1987, *J. Geophys. Res.*, *94*, 11687-11737, 1989.

ACKNOWLEDGMENTS

Adrian Tuck read a draft of this chapter, and his comments are appreciated.

FIGURE CAPTIONS

Figure B-1. Zonal mean H_2O cross section from SAGE II for an average March (1986-88). Contour interval is 0.5 ppmv up to 6 ppmv, then at the spacing of 8, 10, 100, and 1000 ppmv.

Figure B-2. Zonal mean cross section of (LIMS minus SAGE II)/SAGE II H_2O for March. Negative (dashed) contours have an interval of 10%; positive (solid) contours have an interval of 20%.

Figure B-3. Zonal mean cross section of (model minus SAGE II) /SAGE II water vapor for March for the following models: a) AER, b) CALJPL, c) CAMED-theta, d) DUPONT, e) GSFC, f) ITALY, g) LLNL, h) MPI, i) MRI, j) NCAR, k) NOCAR, and l) WASH. Contour interval is as in B-2.

Figure B-4. Annual variation of zonal mean H_2O at $z^* = 20$ km from (a) SAGE II and the models (b) AER, (c) CALJPL, (d) CAMED, (e) DUPONT, (f) GSFC, (g) ITALY, (h) LLNL, (i) MRI, (j) NCAR, and (k) WASH. Contour interval is 0.5 ppmv.

Figure B-5. Annual variation of zonal mean H_2O at $z^* = 16$ km from SAGE II.

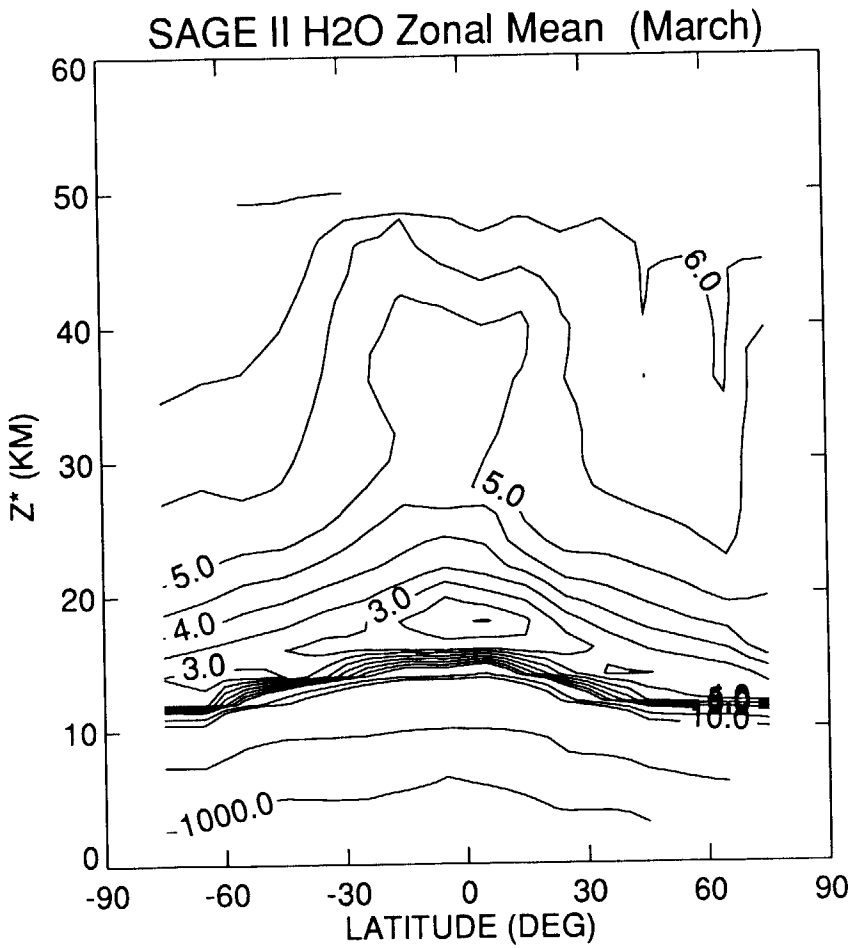

Figure B-1

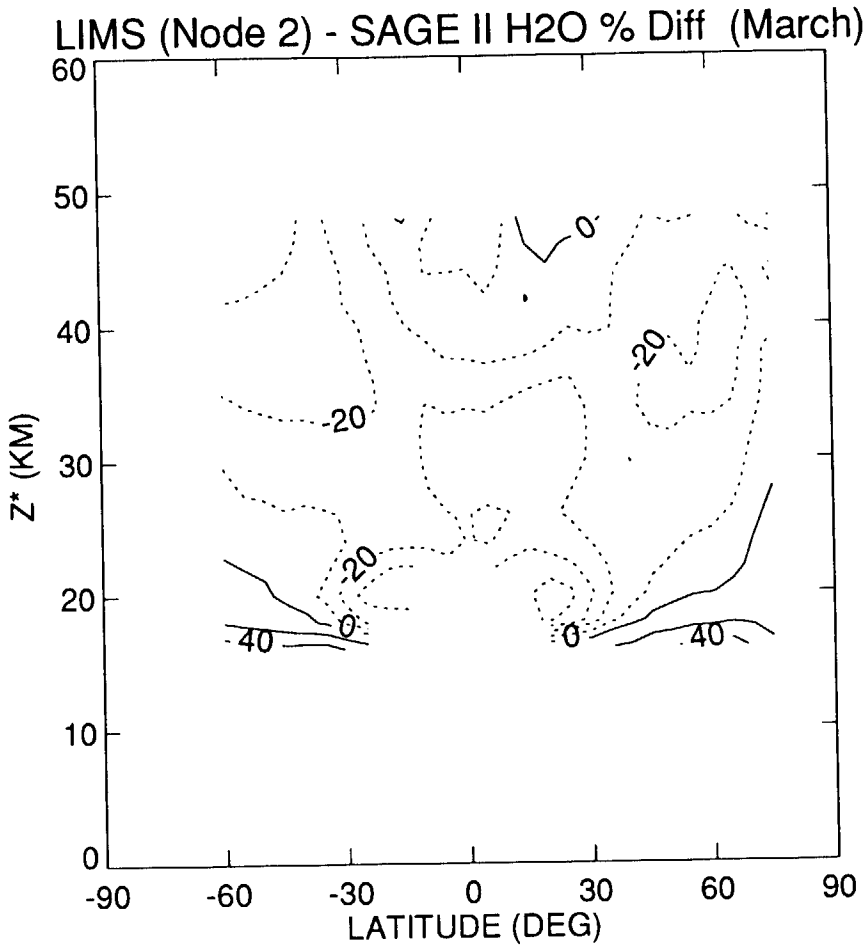

Figure B-2

Model - SAGE II H2O % Diff (March)

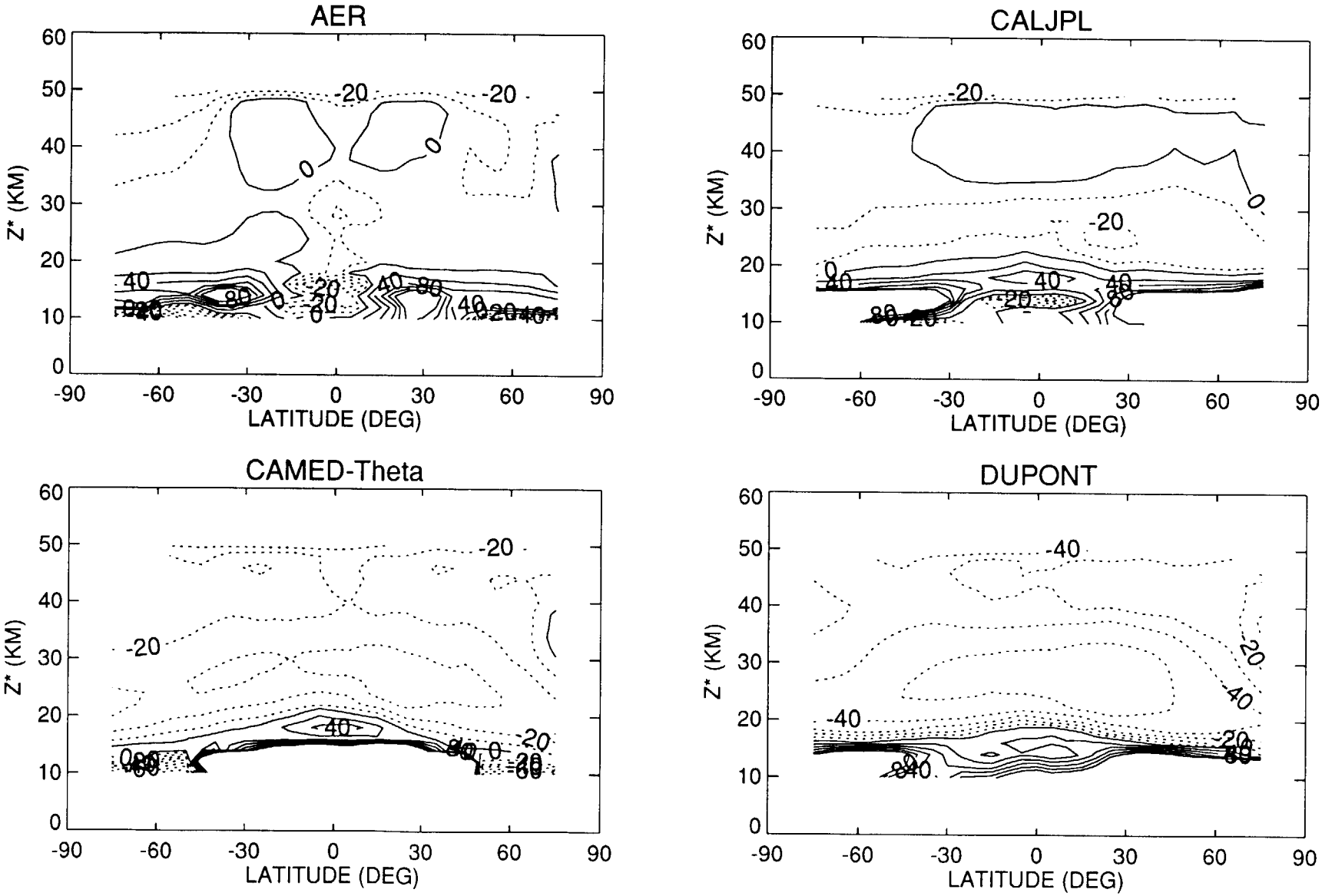

Figure B-3

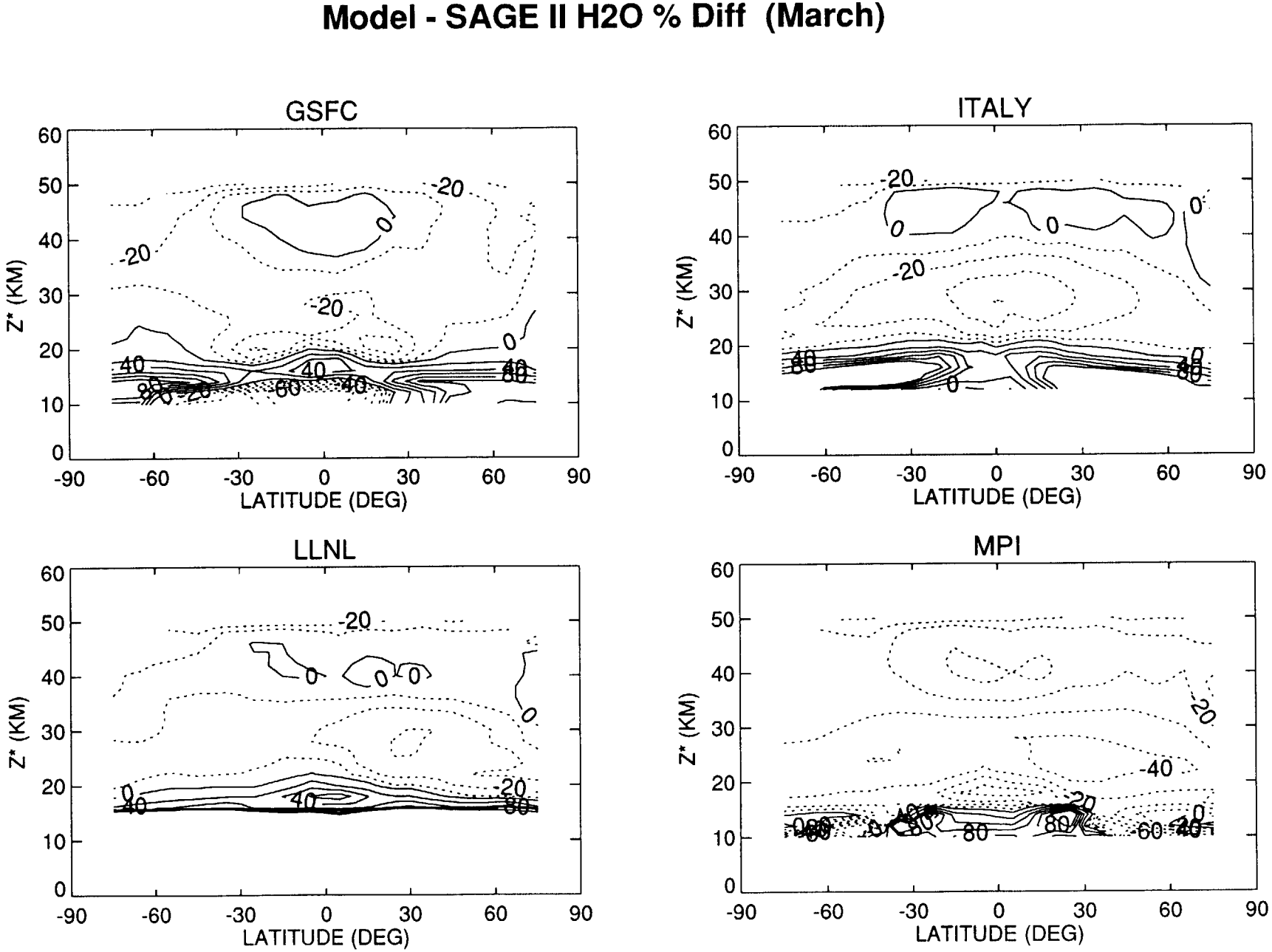

Figure B-3 (cont.)

Model - SAGE II H2O % Diff (March)

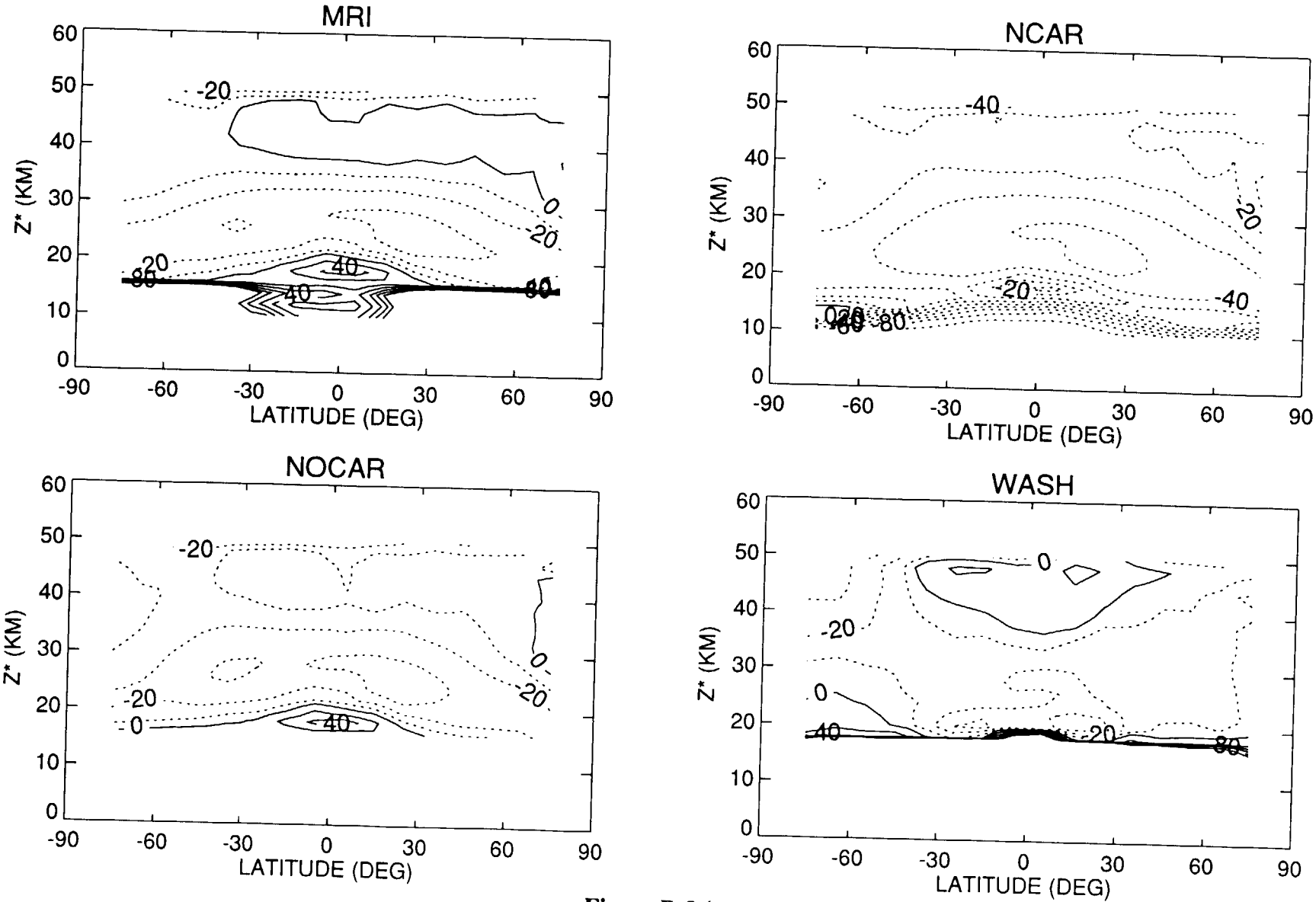

Figure B-3 (cont.)

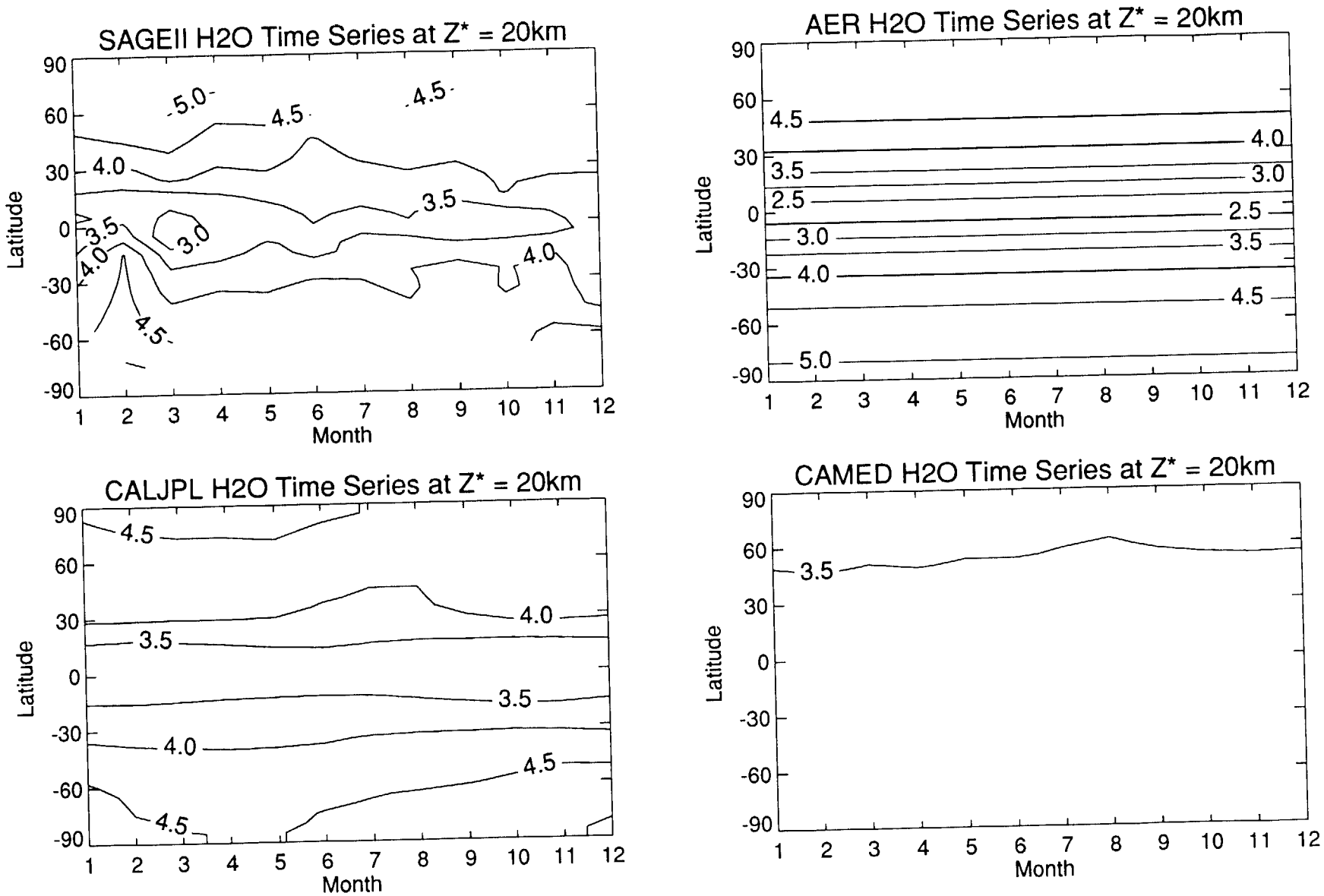
SAGEII H2O Time Series at Z* = 20km
AER H2O Time Series at Z* = 20km
CALJPL H2O Time Series at Z* = 20km
CAMED H2O Time Series at Z* = 20km
Latitude
Month
90
60
30
0
-30
-60
-90
1 2 3 4 5 6 7 8 9 10 11 12
5.0
4.5
4.0
3.5
3.0
2.5

Figure B-4

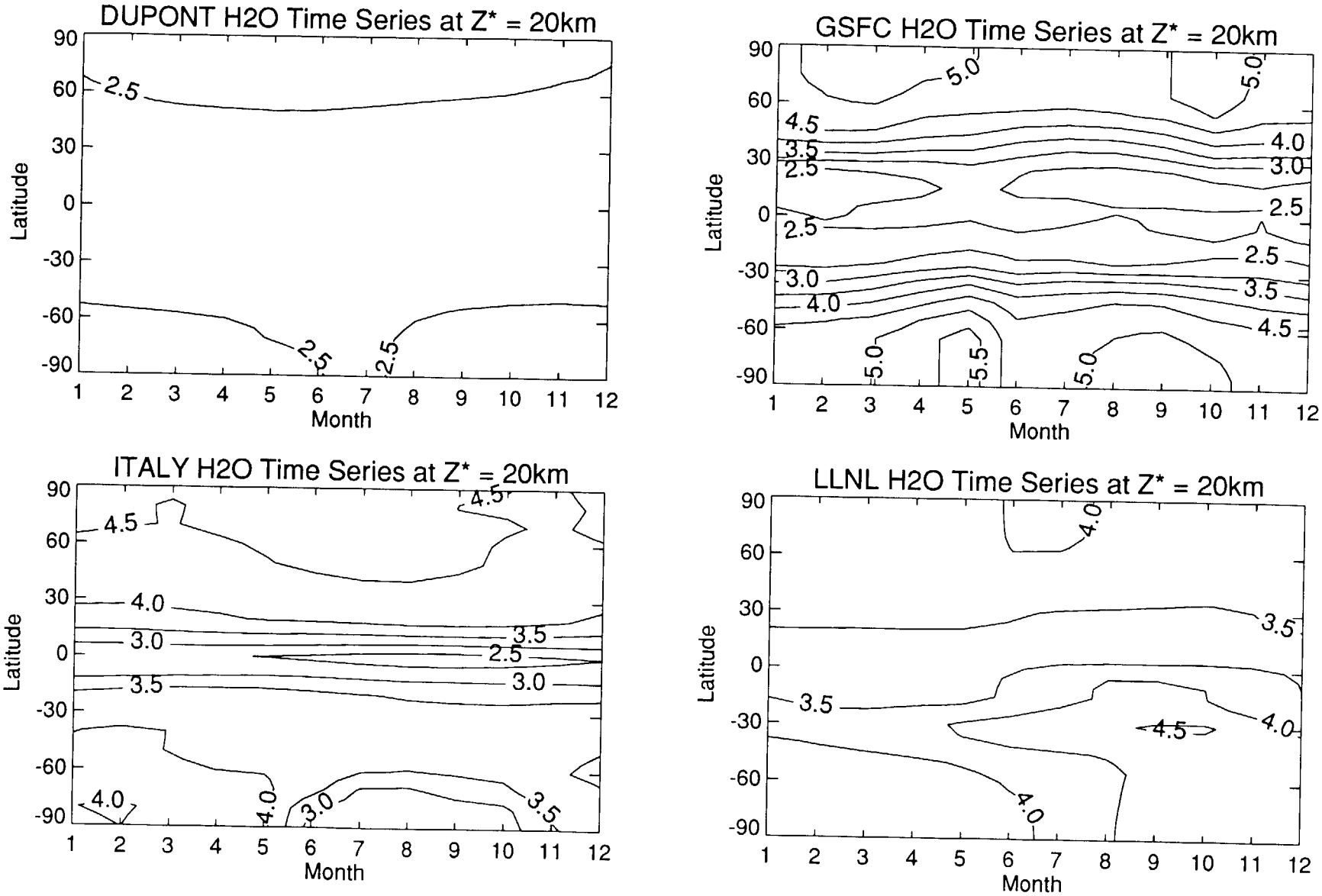

Figure B-4 (cont.)

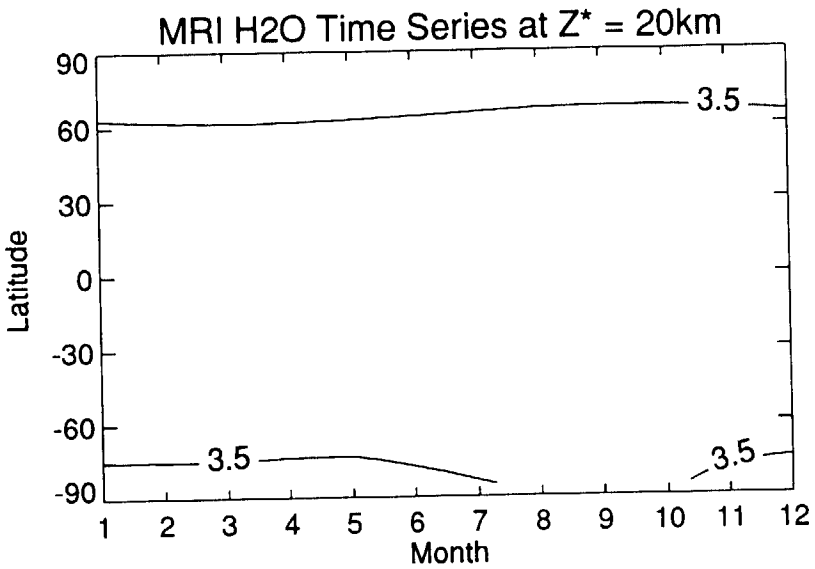

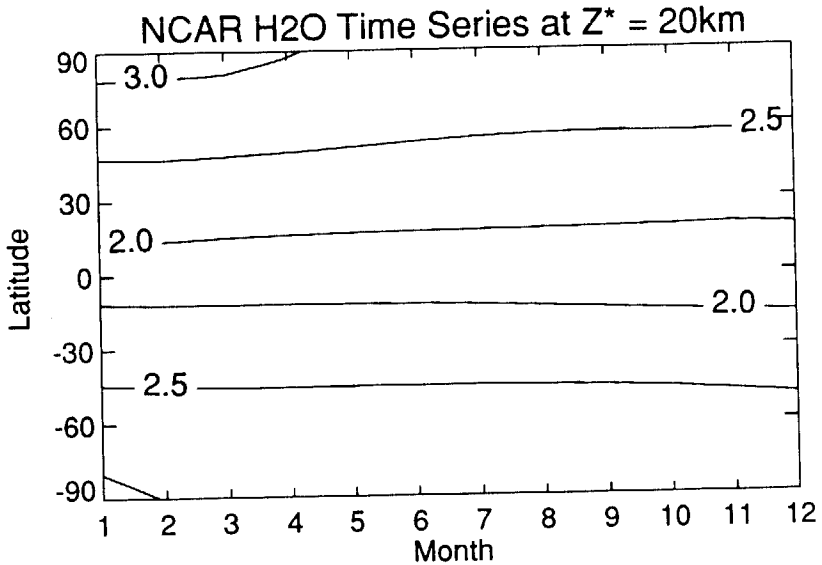

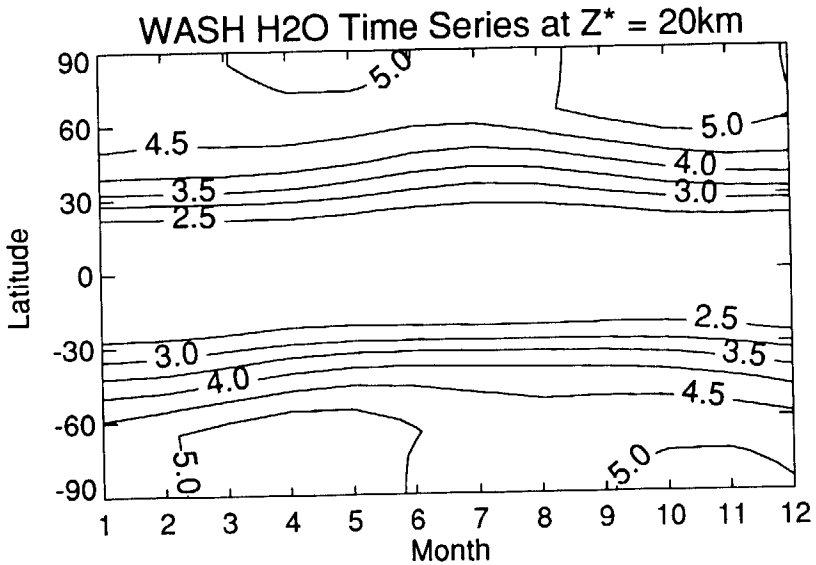

Figure B-4 (cont.)

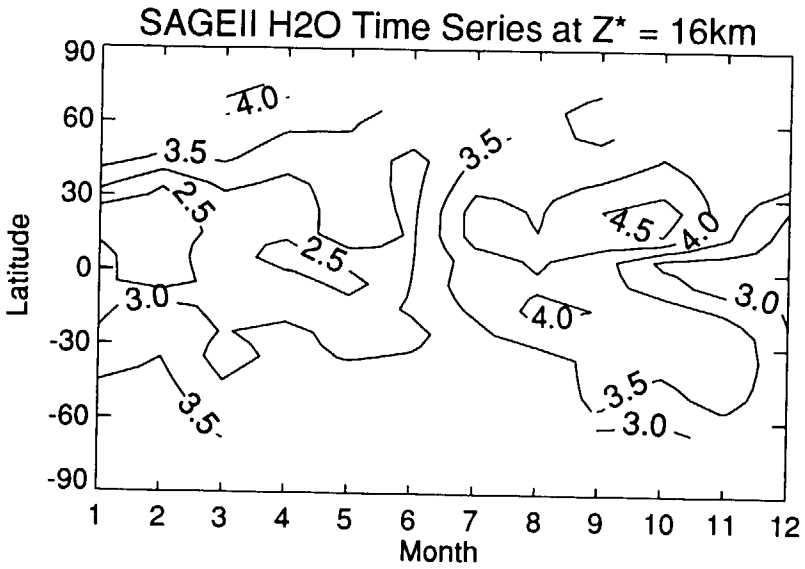
SAGEII H2O Time Series at Z* = 16km
Latitude
Month
90
60
30
0
-30
-60
-90
1
2
3
4
5
6
7
8
9
10
11
12
4.0
3.5
2.5
3.0
4.5

Figure B-5

C: Integrated Column Ozone

C: Comparison of Modeled and Measured Total Column Ozone

Paul A. Newman
NASA - Goddard Space Flight Center

INTRODUCTION

Two- and three-dimensional models constitute one of our most important tools for assessing anthropogenic trace gas impact on the stratosphere and mesosphere. These models incorporate all of the major stratospheric families of trace gasses, including O_x, NO_x, ClO_x, HO_x, and BrO_x. In addition, most of these models use sophisticated radiation packages, and are generally formulated using detailed dynamical transport (e.g., in the two-dimensional model, the residual circulation with prescribed or self-consistent mixing rates). With the exception of the GISS model, the models employed in this study are two-dimensional.

This comparison of models and data is performed to fulfill a number of tasks: 1) verify the collective accuracy of the models to represent the present total ozone distribution, 2) check temporal trends from the models, 3) identify individual model failures, and 4) assess the impact of various processes on model results.

The first task is perhaps the most difficult to assess, since most of the models use the total column ozone diagram as the primary model verification. In short, if task one is not fulfilled by a particular model, the model and its parameterizations are examined and re-worked (within limits) until a reasonable total column ozone diagram is produced. This model examination helps remove glaring errors and flawed parameterizations that impact total ozone, effectively producing model "tuning." This effective tuning precludes the use of total column ozone as a higher order model diagnostic. Nevertheless, this section will show detailed comparisons of models and observations which will provide some confidence in the models and will reveal subtle differences with the observational data.

The second task of verification of decadal model trends is a much more stringent test of the models. The models were run using both homogeneous and heterogeneous chemistry. Comparisons reveal that homogeneous chemistry alone does not produce a reasonable simulation of the observed 1980 to 1990 decadal trend.

The third task of identifying individual model failures will be discussed under Model Comparisons 1980. Individual comparisons of model data and Total Ozone Mapping Spectrometer (TOMS) data will be used to assess the capabilities of each model.

The final task of assessing the impact of various processes on model results is intermingled with the assessment of temporal trends in the model. In any case, it will be seen that models employing gas phase homogeneous chemical schemes alone are inadequate for properly simulating the present atmosphere. Heterogeneous chemistry on both the background sulfate layer and on polar stratospheric clouds is not a negligible process.

This section is divided into a number of segments. The introduction will list the models and the model runs used in this study. The second segment will look at a comparison of the 1980 model simulations to 1979-1980 TOMS data. The third segment will describe model trends and show comparisons to the TOMS trends, while the final segment will summarize the report.

Table C-1. Models Used in This Study for Comparison With the Data

AER	M. Ko, D. Weisenstein, J. Rodriguez, N.D. Sze Atmospheric and Environmental Research, Inc. Cambridge, MA	
CAMED	R. S. Harwood, J. Kinnersley University of Edinburgh Edinburgh EH9 3JZ, UK	J. A. Pyle University of Cambridge Cambridge CB2 1EP, UK
DUPONT	C. Miller, D. Fisher E.I. Du Pont de Nemours, Inc. Wilmington, DE 19880-0320	
GISS	M. Prather University of California, Irvine Irvine, CA 92717	
GSFC	C. H. Jackman, A. R. Douglass NASA/Goddard Space Flight Center Greenbelt, MD 20771	
ITALY	G. Pitari, E. Mancini, G. Visconti Universita` degli Studi L`Aquila 67101 Coppito (L`Aquila), Italy	
LLNL	D. Wuebbles, P. Connell, K. Grant, D. Kinnison, D. Rotman Lawrence Livermore National Laboratory Livermore, CA 94550	
MPI	C. Bruehl, P. J. Crutzen Max Planck Institute for Chemistry, D-6500 Mainz, Germany	
MRI	T. Sasaki Meteorological Research Institute Tsukuba, Ibaraki 305, Japan	
NCAR	C. Granier, G. Brasseur, I. Folkins, S. Walters National Center for Atmospheric Research, Boulder, Colorado Matt Hitchman University of Wisconsin, Madison, Wisconsin Anne Smith University of Michigan, Ann Arbor, Michigan	
OSLO	I. Isaksen, F. Stordal University of Oslo 0315 Oslo 3, Norway	
WASH	K. K. Tung, H. Yang, E. Olaguer University of Washington Seattle, WA	

MODELS AND DATA

Models

These models are generally two-dimensional, formulated using a transport circulation with two-dimensional mixing rates. The principal type of transport circulation used by the two-dimensional models is the residual circulation with prescribed or self-consistent mixing rates. Exceptions are the three-dimensional GISS model and the CAMED-theta model.

Discussion of Different Model Runs

There are four types of model runs used in this study for both of the years 1980 and 1990: A steady-state (SS) run, an aerosol lower-limit (LL) run, an aerosol upper-limit (UL) run, and a run with both upper-limit aerosols and polar stratospheric clouds (UL+PSC). The aerosol upper limit (UL) is outlined in Table 8.8 of WMO (1992), while the aerosol lower limit (LL) is the upper limit reduced by a factor of four. These limits approximately straddle the nonvolcanic loading of the stratosphere. While these aerosol loadings are less than what was encountered following the eruption of El Chichon in 1982, both 1980 and 1990 were relatively unperturbed by volcanic emissions. Hence, these aerosol loadings provide good limits on the true loading of the stratosphere under relatively clean conditions.

The NCAR, ITALY, and OSLO models include PSC parameterizations in addition to the heterogeneous chemistry on the background aerosol layer. The ITALY model (Pitari and Visconti, 1991; Pitari et al., 1992) uses a fixed size distribution for both type I and II PSCs. The PSCs are assumed to form in cold temperatures when the local mixing ratios of HNO_3 and H_2O are larger than saturation mixing ratios for NAT and water ice. The temperature dependence of saturation pressures is calculated using Poole and McCormick (1988). The amount of HNO_3 and H_2O exceeding the saturation value condenses instantaneously and these PSCs are removed through sedimentation. Aerosol evaporation takes place when gas phase HNO_3 and H_2O mixing ratios are lower than saturation.

The NCAR model also includes a PSC parameterization. Type I PSCs form in less than 1 time step when temperatures decrease below 195 K. Type II PSCs are present where the temperature drops below 191 K. These temperatures are higher than the thermodynamic ones, since two-dimensional model zonal average T is usually higher than the coldest air masses at a given latitude. Conversion of HCl and $ClONO_2$ into chlorine radicals takes place in less than a time step. Inside type II PSCs, dehydration and denitrification occur with a 5-day time constant. Where type I PSCs are present, no dehydration takes place, but a weak denitrification is assumed to occur, with a time constant of 30 days. When the sun returns to the polar regions, the classic catalysis and cycles involving Cl_2O_2 and BrO destroy ozone.

Total Ozone Data

Total ozone data are available from both ground-based Dobson sites and the TOMS aboard the Nimbus-7 satellite. TOMS data are the primary focus of this study, since the measurements show good direct agreement with the Dobson data and with the Dobson trends (*see* UNEP report, chapter 2; Stolarski et al., 1992). In addition to good comparisons with the Dobson data, TOMS data have full global coverage for the individual years of 1980 and 1990. The TOMS data have an estimated precision of 1.3%, with somewhat higher biases at high solar zenith angles (near the edge of polar night). Torres et al. (1992) estimate 30 DU errors for low ozone events at solar zenith angles large than 85 degrees.

MODEL COMPARISONS 1980

Model Standard

To facilitate the model comparisons, a model standard is defined as the average of all of the steady-state model runs. This standard is a sum of the AER, CAMED, DUPONT, GSFC, ITALY, LLNL, MRI, NCAR, and WASH models. Figure C-1 displays this standard alongside the TOMS total ozone plot of 1980 (an average of 1979 and 1980). The difference between the standard and TOMS is on the bottom of the figure. There are a number of salient features displayed in the TOMS observations. Among these features are: 1) the northern hemisphere total ozone maximum in March and April near the pole, 2) the northern hemisphere ozone minimum in August and September, 3) the tropical annual cycle (minimum in January-February, followed by a maximum in September-August), 4) The southern hemisphere ozone maximum at approximately 60S over the entire year, 5) the southern hemisphere annual cycle of ozone (minimum in March-April, maximum in September-October-November), and 6) the southern hemisphere polar low in early spring (August-September-October).

The model standard (top right Figure C-1) includes all of the salient features shown in the TOMS data. The northern hemisphere total ozone maximum appears in the spring, while a similar feature also appears in the southern latitudes. In general, there is good agreement between TOMS and the model standard.

While good agreement is generally apparent, a number of problems are still easily seen in direct comparisons of the model standard and TOMS. The most glaring problems in the model standard are: 1) the value of the ozone maxima in both hemispheres during late winter is too low, 2) the gradient between the tropical ozone values and the midlatitude ozone maxima is too weak, 3) the lack of a final warming in the southern hemisphere during November, and 4) the lack of latitudinal breadth of the low total ozone in the tropics.

The weakness of the total ozone maxima is seen in the difference between the standard and TOMS (bottom, Figure C-1). The northern hemisphere spring maxima in the TOMS data is on the order of 480 DU, whereas the maxima in the model standard is only 420 DU. In a similar fashion, the southern hemisphere spring maxima is greater than 400 DU, whereas the standard model is slightly in excess of 360 DU. The weakness of the midlatitude total ozone gradient is easily seen by comparing the closely packed contours in TOMS data between 30N and 50N during January and March, with the less tightly packed contours over the same region and time in the standard. The southern hemisphere final warming is observed in the increase in southern hemisphere polar total ozone from 280 DU to 360 DU between October and November. This final warming effect is not observed in the model standard. Finally, the lack of breadth of the tropical ozone minima is reflected by the positive differences in the sub-tropics in the difference plot.

Individual Model Comparisons

AER

The AER SS run is shown in Figure C-2; the difference between the SS run and TOMS is shown on the right of this figure. The AER model has all of the features shown in the standard, and has all of the problems also shown in the standard. Note that the northern hemisphere maximum during the spring is offset from the pole, and occurs approximately 1 month later than the TOMS maximum. The AER runs using aerosols show the same basic behavior.

CAMED

The CAMED SS run is shown in Figure C-3; the difference between the SS run and TOMS is shown on the right of this figure. As with the AER model the Cambridge model contains most of the features in the standard. Differences are approximately 20 DU over the tropical region, but are generally larger than 20 DU outside the tropics. As with the standard, the tropical low ozone region is rather narrow in comparison to TOMS. Again, the northern hemisphere spring maximum is too weak. In the northern hemisphere ozone values tend to fall off during the progression from spring to late summer. Generally, this falloff occurs at a more rapid rate in northern hemisphere polar latitudes, and more gradually in the midlatitudes. As a result, a midlatitude maximum develops. This development is observed in the standard model, as well as the CAMED model. However, in the CAMED model, this maximum shows a slow progression southward over the course of the summer (near 60N in July and at 45N in October), while in the TOMS data, this maximum is generally fixed near 60N. The CAMED runs using aerosols show the same basic behavior.

DUPONT

The DUPONT SS run is shown in Figure C-4; the difference between the SS run and TOMS is shown on the right of this figure. As with the previous models, the DUPONT model tends to produce the same features as the model standard. However, the DUPONT model underestimates total ozone by 5%-20%. If the DUPONT model was normalized to annual TOMS global ozone, it would still underestimate the northern hemisphere spring maximum and would not produce a southern hemisphere winter total ozone minimum.

GISS

The GISS model is the only three-dimensional model run included in this model assessment. The GISS SS run is shown in Figure C-5; the difference between the SS run and TOMS is shown on the right of this figure. While the GISS model tends to produce the same features as the model standard, it is biased low with respect to the TOMS data by 5%-20%. Normalizing to the annual TOMS global ozone would still lead to an underestimate of the northern hemisphere spring maximum, and would not produce a southern hemisphere winter total ozone minimum.

GSFC

The GSFC model (shown in Figure C-6) displays total ozone values in 1980 that are overall lower than the TOMS data. While the annual cycle in the northern polar region is approximately the correct amplitude, the mean is approximately 80 DU too low. The GSFC model again shows many of the problems generic to the model standard (i.e., northern hemisphere spring max too low, midlatitude gradients too weak, a poor representation of the southern hemisphere final warming, and a rather narrow tropical total ozone minimum).

ITALY

The ITALY model is displayed in Figure C-7. Two cases are included for the ITALY model: the gas phase steady state and the heterogeneous upper limit (UL) with polar stratospheric clouds (PSCs). A comparison of the SS run with the model standard reveals many of the problems associated with the other models: a weak northern hemisphere spring maximum, weak latitudinal total ozone gradients (particularly in the northern hemisphere winter-spring), a weak southern hemisphere spring maximum, a relatively poor representation of the southern hemisphere final warming, and a rather narrow tropical ozone minimum.

The UL+PSC case is shown at the bottom of Figure C-7. This run shows increased northern hemisphere and southern hemisphere spring column ozone amounts in comparison to the SS case when the $N_2O_5 + H_2O$ reaction alone is added. This is immediately evident by a comparison of the SS and UL+PSC runs during March-April at the northern latitudes (total ozone amounts of 420 and 440 DU, respectively). In the UL run without PSCs the southern hemisphere increase is also evident. Addition of PSCs leads to the development of a strong ozone minimum at southern polar latitudes during the October period (i.e., an ozone hole). The increase of total ozone at high latitudes in the UL+PSC case is probably a result of the suppression of the catalytic loss of ozone via NO_x, as NO_x is sequestered in HNO_3. Since concentrations of total inorganic chlorine in 1980 were still relatively low, the catalytic loss of ozone via Cl_x was unable to sufficiently compensate for the depressed NO_x levels, hence ozone concentrations increased.

LLNL

The LLNL model is shown in Figure C-8 for the SS case. The LLNL case is the only model that has total ozone greater than TOMS during the northern hemisphere spring in the polar and sub-polar region, albeit only marginally higher. While TOMS data average values greater than 480 DU, the LLNL case shows values slightly higher than 500 DU. The southern hemisphere case shows midlatitude total ozone values that are again slightly too large and high-latitude values that are much too large (i.e., there is a distinct lack of a south polar minimum). Peak TOMS total ozone values (400 DU) in the southern hemisphere occur in October at 55S, whereas the LLNL SS case shows peak values in excess of 420 DU during October at the South Pole.

MPI

The MPI time-dependent (TD) case in displayed in Figure C-9. As with the model standard, the MPI model underestimates the northern hemisphere and southern hemisphere spring maxima, and also underestimates the midlatitude gradient of total ozone. In addition, the southern hemisphere winter polar ozone minima is also poorly represented. However, the MPI model shows a rather broad tropical low ozone region in good agreement with TOMS.

MRI

The MRI SS case in shown in Figure C-10. The MRI model displays the major features observed in the TOMS data, including the spring maxima and a south polar minima. However, the MRI model underestimates the northern hemisphere and southern hemisphere spring maxima, underestimates the midlatitude gradient of total ozone and underestimates the width of the tropical ozone low. In addition, the southern hemisphere winter polar ozone minima is lowest during the March-April period.

NCAR

The NCAR SS run (top) is shown in Figure C-11. This run shows nearly identical behavior to the other models: a slight underestimate of the northern hemisphere spring maximum, an underestimate of the northern hemisphere winter-spring midlatitude gradient of total ozone, and a relatively narrow tropical minima. In the southern hemisphere the SS midlatitude maximum compares quite nicely to the TOMS data, but the south polar minimum is clearly too strong.

The NCAR heterogeneous UL run is shown in the bottom of Figure C-11. Differences between the SS and UL runs for 1980 show a decrease of the winter-spring high-latitude maxima, and the development of a strong southern hemisphere polar minima. Midlatitude values are comparable in both runs. The reduction of the spring maxima when aerosol heterogeneous chemistry is included is unique to the NCAR model. The other models which include aerosol

heterogeneous chemistry show increases of total ozone between the SS and heterogeneous runs when the $N_2O_5+H_2O$ reaction is added.

OSLO

Figure C-12 displays the OSLO model TD run. This TD run is lower than the TOMS data with the largest differences near the northern hemisphere and southern hemisphere spring maxima, with the exception of spring values, which are too high over the South Pole. The OSLO model does not show the distinctive southern hemisphere maxima near 55S in the spring, nor does it show the mid-winter minima over the polar region. The breadth of the tropical minima in the OSLO model is in good agreement with the TOMS data.

WASH

The WASH SS model run is shown in Figure C-13. The WASH model nicely captures the total ozone maxima in the northern hemisphere and southern hemisphere, produces a final warming in December, has a nice winter-to-spring polar ozone minima at the South Pole, has good latitudinal breadth in the tropical minima, and approximately captures the southern hemisphere midlatitude ozone gradient. However, the WASH model is similar to the other models with respect to the northern hemisphere midlatitude gradient (too weak) and the northern hemisphere and southern hemisphere high-latitude maxima (too weak).

MODEL TRENDS

TOMS

The TOMS trends are shown in Figures C-14. The left panel displays an average of 1990 and 1989 subtracted from an average of 1980 and 1979, while the right panel displays the trend from 1980 to 1990 using a statistical analysis for the full TOMS data set (Stolarski et al., 1992). Both calculations show insignificant trends (trends of approximately 3% are not significant) in the tropics, with rather large trends in the high latitudes during spring. The northern hemisphere spring TOMS trend is 6%-10%, while the southern hemisphere spring trend is in excess of 30%. Largest trends are generally found in the polar regions, with trends of 2%-6% in the midlatitudes. Only the northern hemisphere displays annual variability in long-term trends, with relatively weak trends in the northern hemisphere summer and fall.

Model Averages

To show the general results of the models, the model trends have been averaged into four groups: steady state (SS), heterogeneous lower limit (LL), heterogeneous upper limit (UL), and heterogeneous upper limit with PSCs (UL+PSC). These averages are displayed in Figure C-15.

The SS run (Figure C-15, top left panel) is averaged from the AER, CAMED, DUPONT, GSFC, LLNL, ITALY, MRI, NCAR, and WASH models. In general, these models and the time-dependent model runs (AER, MPI, MRI, and OSLO) show losses everywhere for the decade which are less than 2%, clearly much smaller than the trends shown in the TOMS data. The ITALY model produces the largest winter-spring losses at the high northern hemisphere and southern hemisphere latitudes of approximately 4%. The NCAR SS run shows losses of less than 1% in the northern hemisphere winter-spring polar regions, with wide areas of relatively insignificant ozone increases (less than 2 DU). The CAMED model also shows a region of increased ozone in the northern hemisphere polar region in the late winter to early spring of approximately 10-20 DU (2%-4%).

The LL run (Figure C-15, top right panel) is averaged from the AER, CAMED, DUPONT, GSFC, LLNL, ITALY, and NCAR models. These models show decadal losses that range from small (1%) up to 10%. The CAMED model produces losses in the polar northern hemisphere during late spring of up to 8%, while the ITALY model produces a more globally uniform loss of approximately 4%. The NCAR LL run shows February northern hemisphere polar losses of 8% and August southern hemisphere polar losses of 12%.

The UL run (Figure C-15, bottom left panel) is averaged from the AER, ITALY, and NCAR models. The AER and ITALY models are generally consistent, displaying high-latitude winter-spring losses of approximately 4%-6%, while the NCAR model shows 16% losses at high northern hemisphere latitudes in February, and 30% southern hemisphere polar losses in August and September. These large losses in the NCAR UL run are nearly double the predicted losses from the NCAR LL model run.

The UL+PSC run (Figure C-15, bottom right panel) is averaged from the ITALY, NCAR, and OSLO models. The ITALY model shows northern hemisphere winter-spring losses of approximately 4%, while the OSLO model shows 8% and the NCAR model shows 16%. In the southern hemisphere the ITALY model shows losses of 10% in September-October, while the NCAR model shows 30% losses and the OSLO model shows 10% losses in October.

Figure C-16 displays the three UL+PSC runs used in the Figure C-15 average. The ITALY model run (top left) is clearly too weak in the northern hemisphere winter-spring and close to correct in the southern hemisphere winter-spring, while the OSLO model (bottom left) produces reasonable northern hemisphere spring polar losses of 8% but weak southern hemisphere spring polar losses of only 10%. The NCAR model run (top right) is nearly correct in both hemispheres. Separate NCAR model runs with PSCs alone, and with heterogeneous processes on the aerosol background alone, reveals that most of the NCAR northern hemisphere losses are a result of the heterogeneous processes without PSCs (i.e., PSCs alone in the northern hemisphere produce small long-term trends). The southern hemisphere polar winter-spring losses in the NCAR model seem to be enhanced in the mid to late spring by the inclusion of PSCs. Hence, instead of 10%-15% losses in the southern hemisphere polar region as a result of the aerosols during October and November, the losses are increased to 20%-25% when PSCs are included.

Most of the model runs shown in this section do not represent the TOMS losses in a credible way. The closest approximation to the TOMS losses is seen in the heterogeneous UL+PSC model runs. The closest approach to the TOMS data is seen in the NCAR model runs. The NCAR UL+PSC model run is generally the best simulation of the TOMS losses in all of these representations.

SUMMARY

The models produce reasonable representations of total ozone for 1980. While 1990 data are not shown here, the same conclusion is generally applicable for 1990 data. Systemic problems in the model runs are weakness of the spring total ozone maxima in both hemispheres, weakness of the midlatitude total ozone gradient, poor representation of the southern hemisphere spring final warming, and tropical low ozone regions that are too latitudinally narrow. In addition to these problems the 1990 model runs generally have poor representations of the Antarctic ozone hole. Comparisons of most of the steady-state model runs to the heterogeneous model runs indicate that the inclusion of heterogeneous reactions acts to increase the column ozone. This increase by inclusion of heterogeneous reactions is generally true for both 1980 model runs and 1990 model runs. The increase is probably a result of the suppression of ozone loss via the reduction of NO_x from the $N_2O_5+H_2O$ heterogeneous reaction on the aerosol layer. The most radical departures

from this result are the NCAR model runs which show decreases of total ozone between their steady-state run and their heterogeneous run in both 1980 and 1990.

Total ozone trends from TOMS are 6%-10% at northern mid to high latitudes during the late winter and early spring. These trends are best represented by the model runs that include both aerosols and polar stratospheric clouds, although the model runs with the upper-limit aerosol chemistry also show reasonable agreement. However, largest northern hemisphere TOMS trends occur in the midlatitudes, whereas the UL+PSC model runs show largest trends near the North Pole.

Total ozone trends from TOMS are ~50% at southern high latitudes during the late winter and early spring. These trends are best represented by the model runs that include both aerosols and polar stratospheric clouds. However, while the model simulations produce large trends, they are still substantially smaller than the TOMS trends of 50%. The trend from the NCAR simulation is largest at 30% but is still too small.

REFERENCES

Pitari, G., and G. Visconti, Ozone trend in the northern hemisphere: A numerical study, *J. Geophys. Res., 96*, 10931, 1991.

Pitari, G., G. Visconti, and M. Verdecchia, Global ozone depletion and the Antarctic ozone hole, *J. Geophys. Res.*, in press, 1992.

Poole, L. R. and M. P. McCormick, Airborne lidar observations of Arctic polar stratospheric clouds: Indications of two distinct growth mode, *Geophys. Res. Lett., 15*, 21-23, 1988.

Stolarski, R., R. Bojkov, L. Bishop, C. Zerefos, J. Staehlin, J. Zawodny, Measured trends in ozone, *Science, 256*, 342-449, 1992.

Torres, O., Z. Ahmad, and J. R. Herman, Optical effects of polar stratospheric clouds on the retrieval of TOMS total ozone, *J. Geophys. Res., 97,* 13,015-13,024, 1992.

World Meteorological Organization (WMO), *Scientific Assessment of Ozone Depletion: 1991,* Global Ozone Research and Monitoring Project Report No. 25, WMO, Geneva, 1992.

FIGURE CAPTIONS

Figure C-1. Annual variation of column ozone: a) TOMS average for 1979/80, b) model average for 1980, and c) average model minus TOMS. Contour interval is 20 Dobson Units (DU).

Figures C-2 through C-6. 1980 ozone column: (left) model ozone, (right) model minus TOMS. (C-2) AER, (C-3) CAMED, (C-4) DUPONT, (C-5) GISS, and (C-6) GSFC.

Figure C-7. As in C-2, but for ITALY model: (top) gas phase chemistry; (bottom) heterogeneous plus gas phase chemistry.

Figures C-8 through C-10. As in C-2, but (C-8) LLNL, (C-9) MPI, and (C-10) MRI.

Figure C-11. As in C-7, but for NCAR model.

Figures C-12 through C-13. As in C-2, but (C-12) OSLO and (C-13) WASH.

Figure C-14. Percentage change in column ozone: (left) TOMS average, 1990 minus 1980; (right) decadal trend in TOMS ozone.

Figure C-15. Decadal ozone trend from model averages: (a-top left) gas phase chemistry; (b-top right) gas phase plus background aerosol chemistry; (c-bottom left) gas phase plus perturbed aerosol chemistry; (d-bottom right) gas phase, perturbed aerosol and PSC chemistry.

Figure C-16. As in Figure C-15d, but for each of the three models in the average.

O3 Column 1980 (Dobson Units)

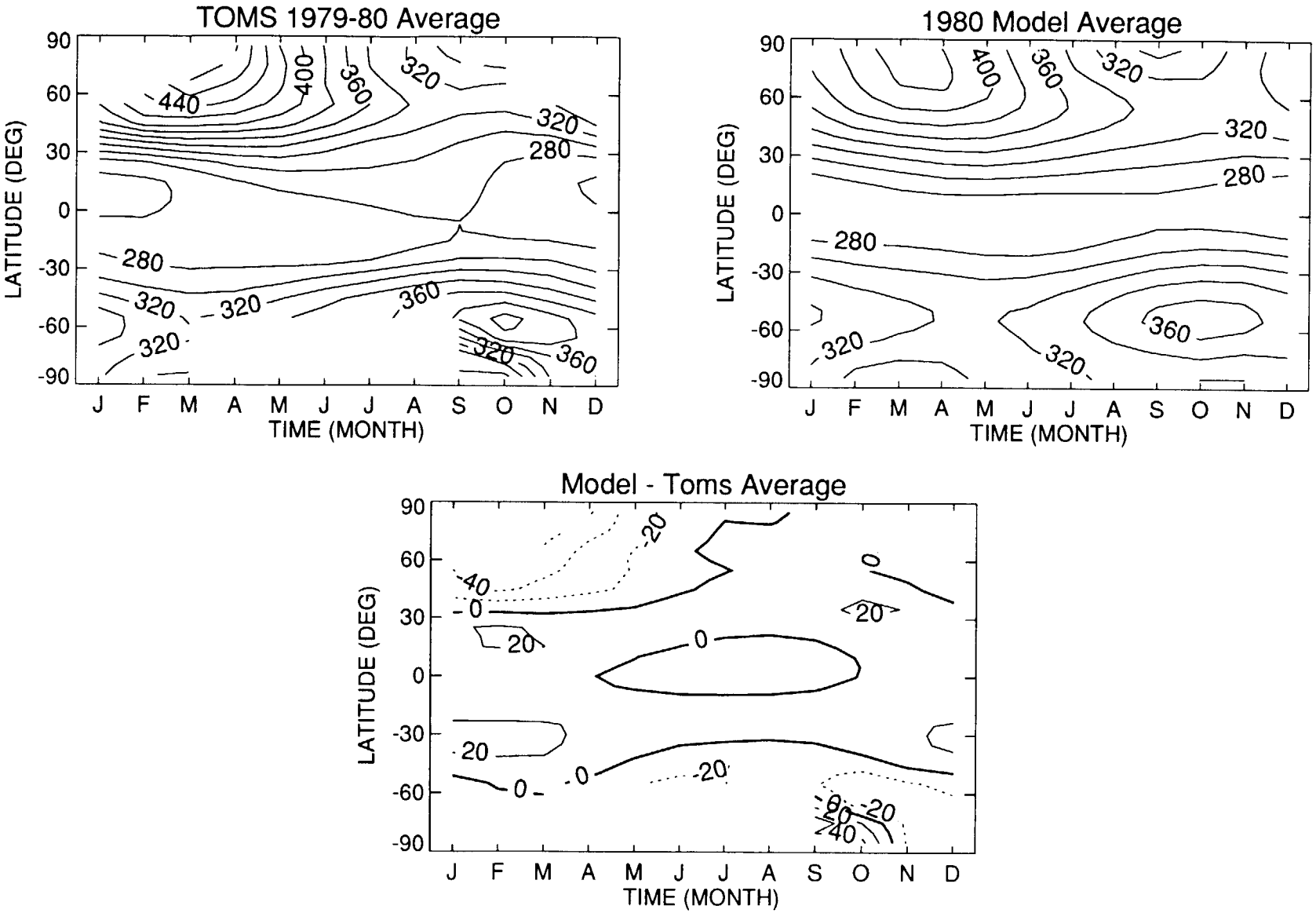

Figure C-1

O3 Column 1980 (Dobson Units)

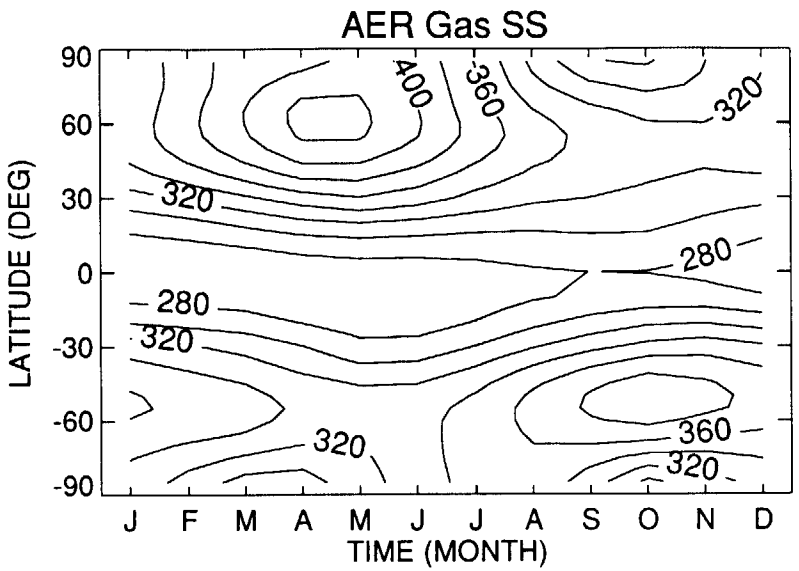

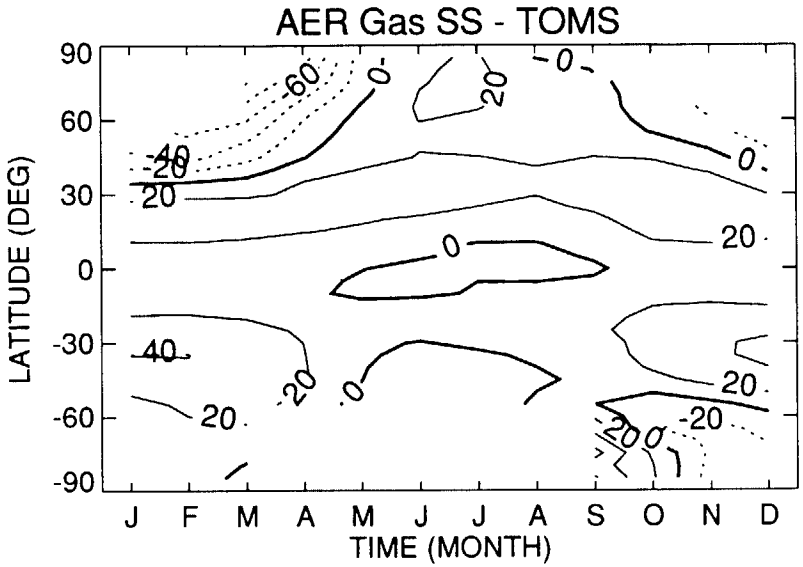

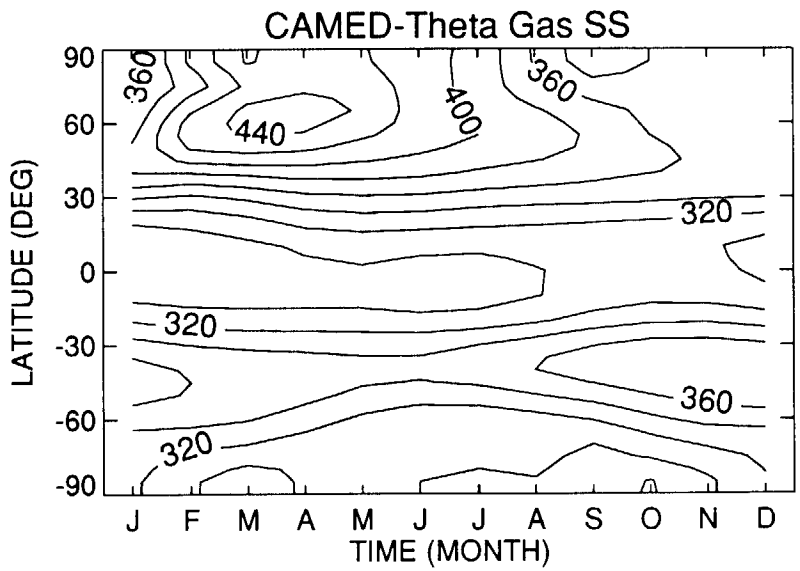

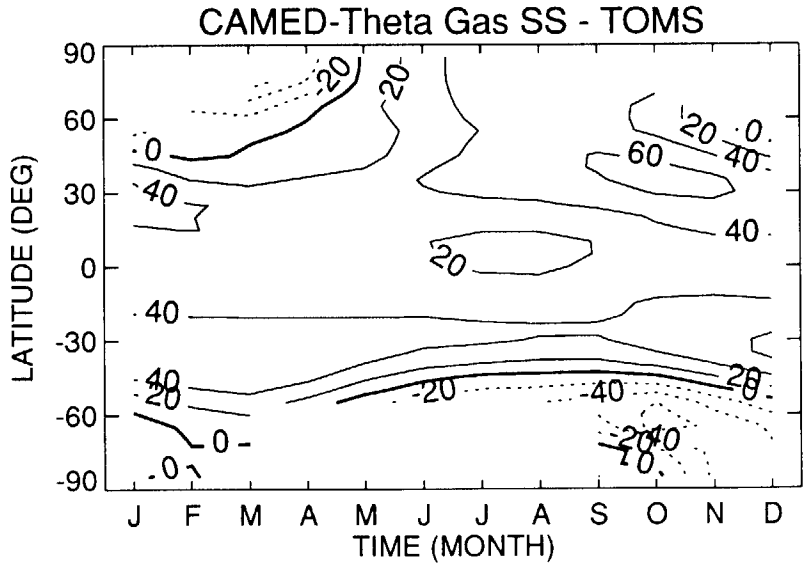

Figure C-2 (top, left and right) **Figure C-3 (bottom, left and right)**

O3 Column 1980 (Dobson Units)

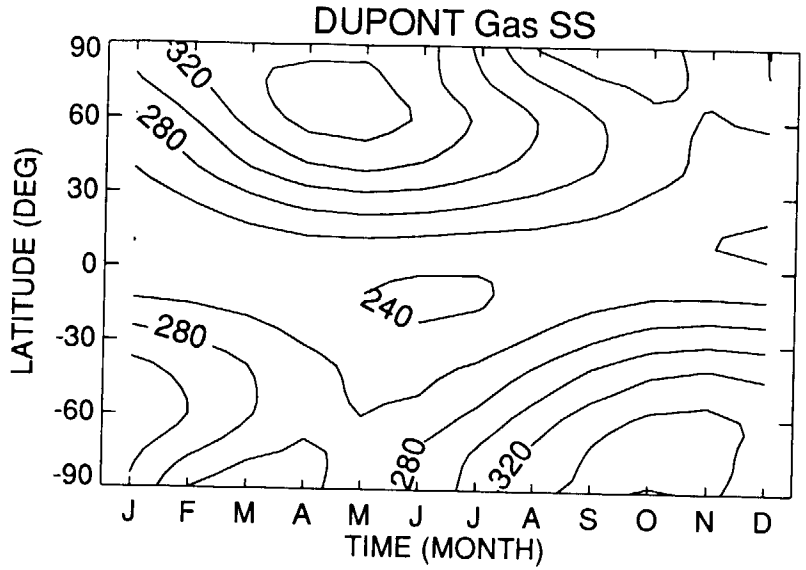

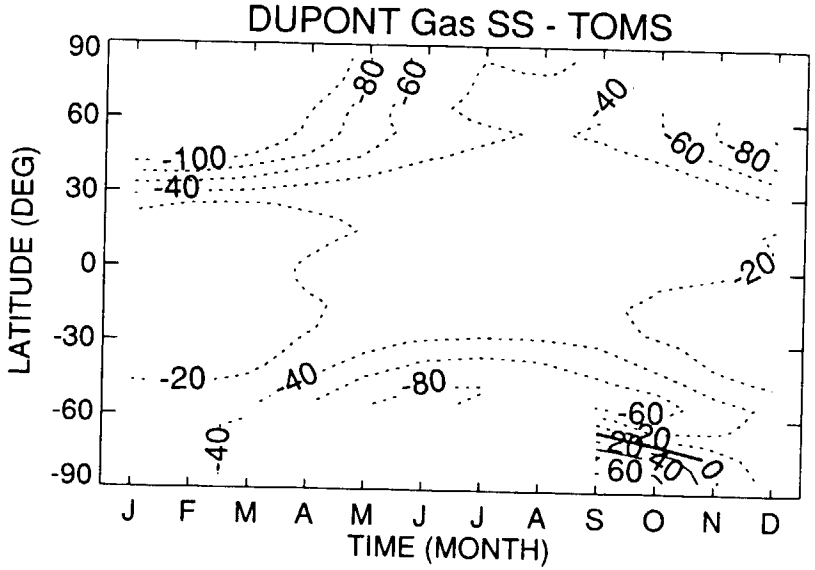

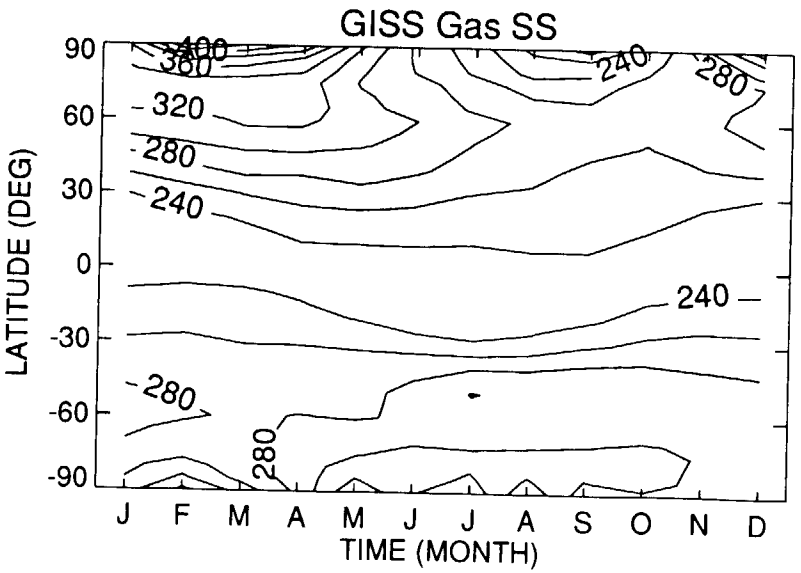

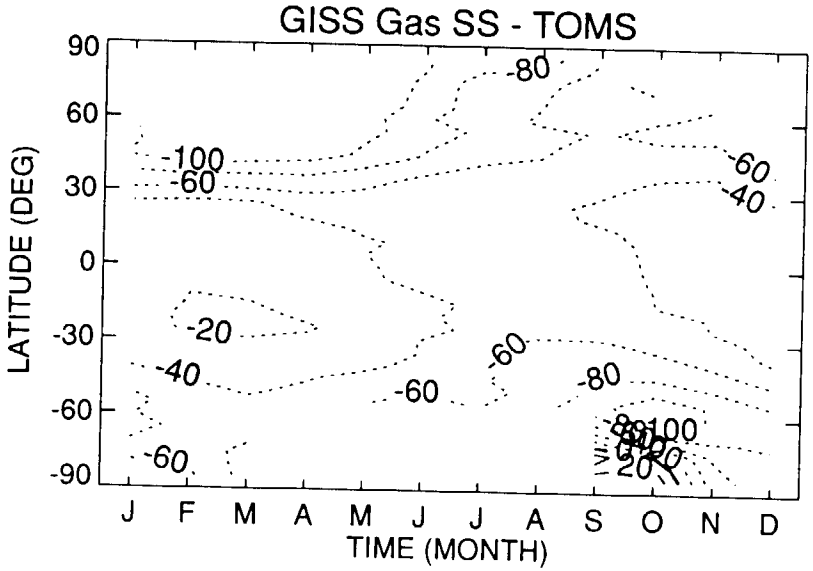

Figure C-4 (top, left and right) **Figure C-5 (bottom, left and right)**

O3 Column 1980 (Dobson Units)

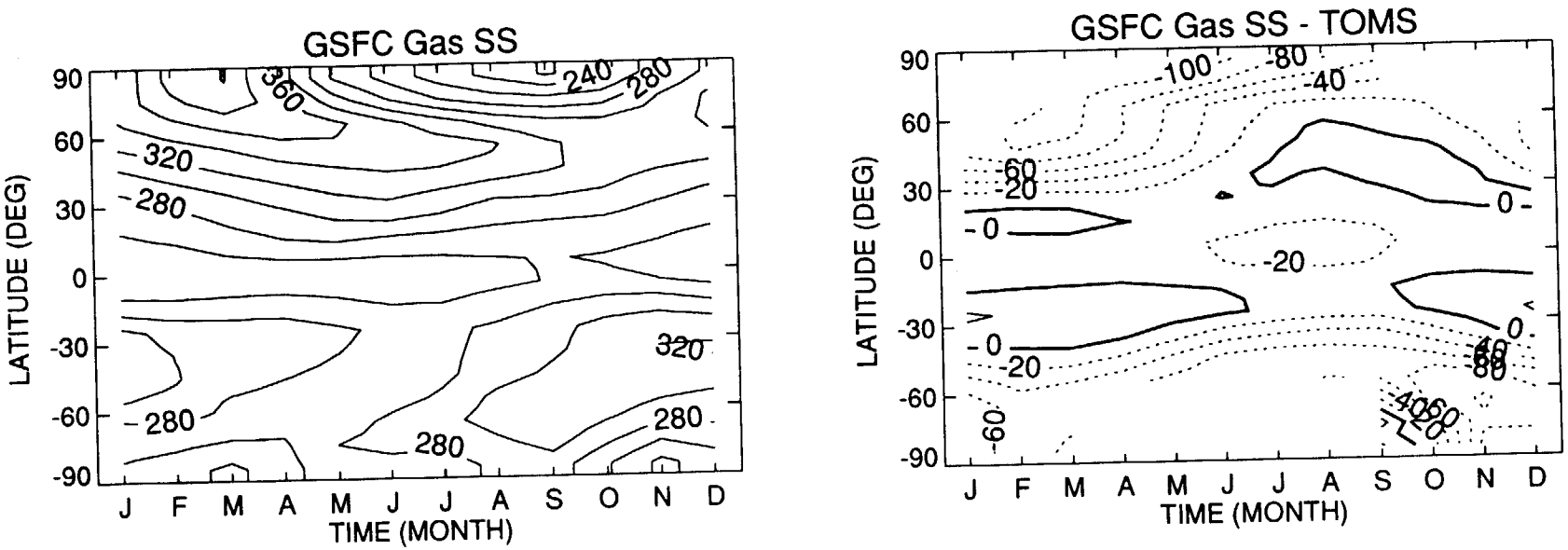

Figure C-6

O3 Column 1980 (Dobson Units)

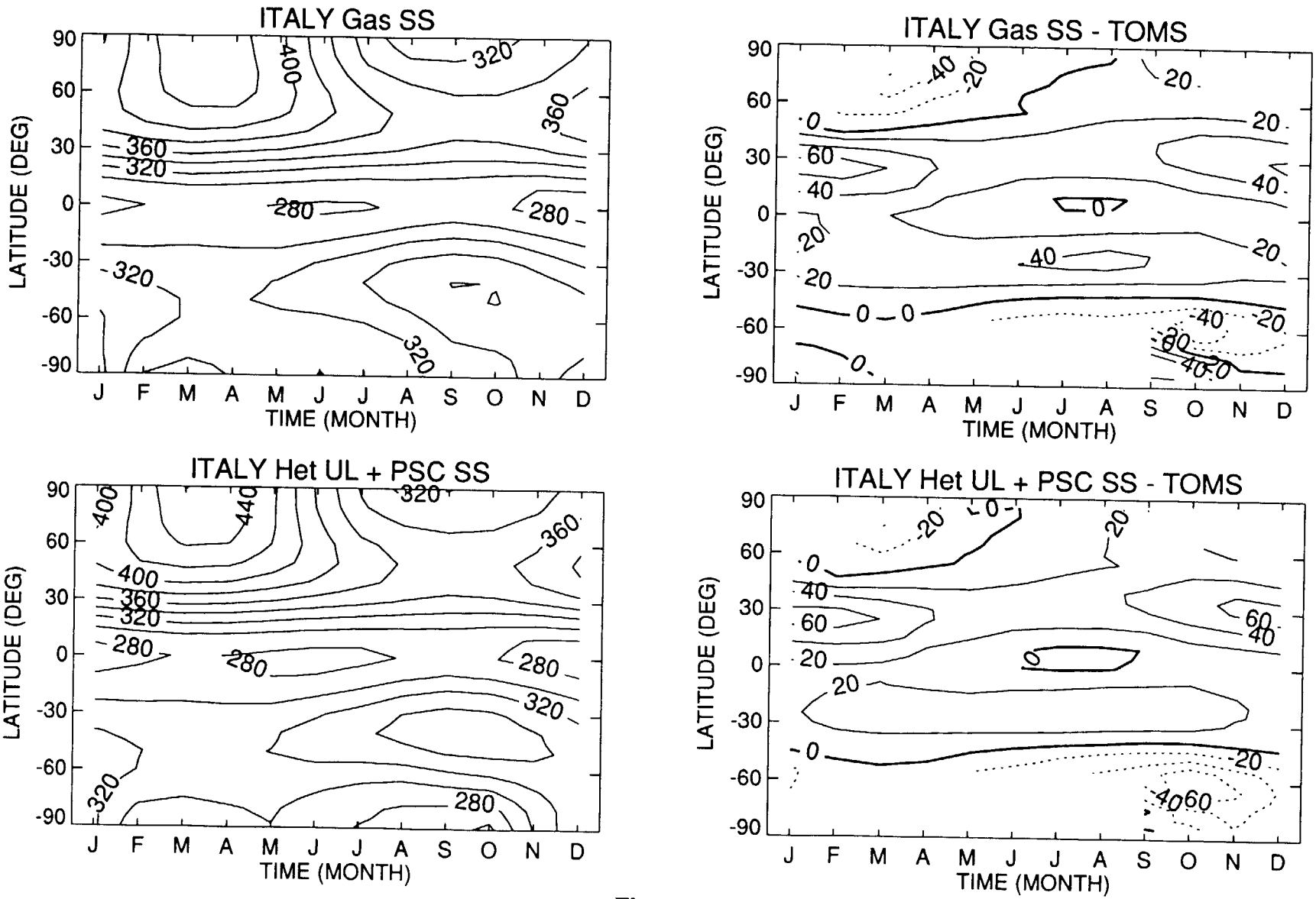

Figure C-7

O3 Column 1980 (Dobson Units)

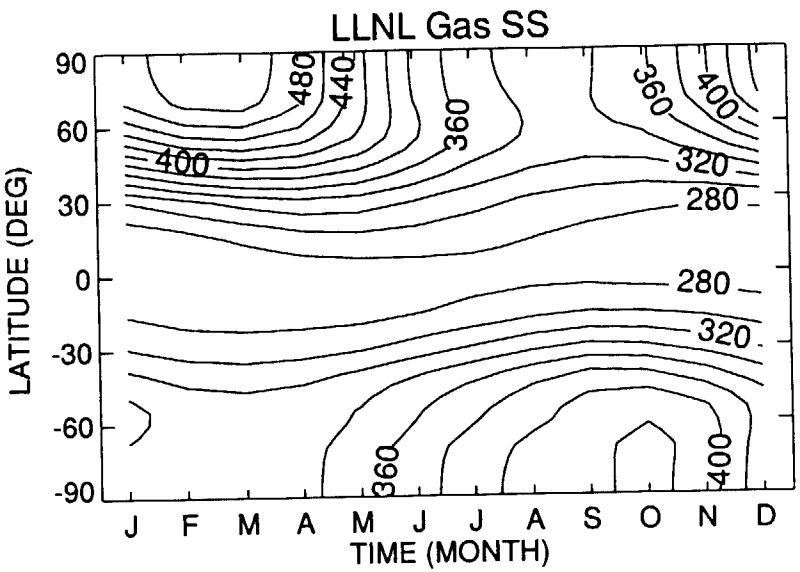

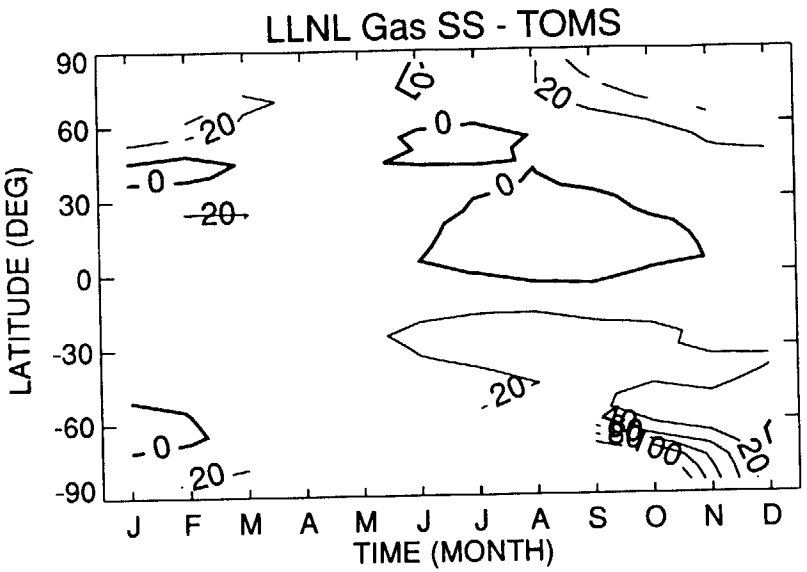

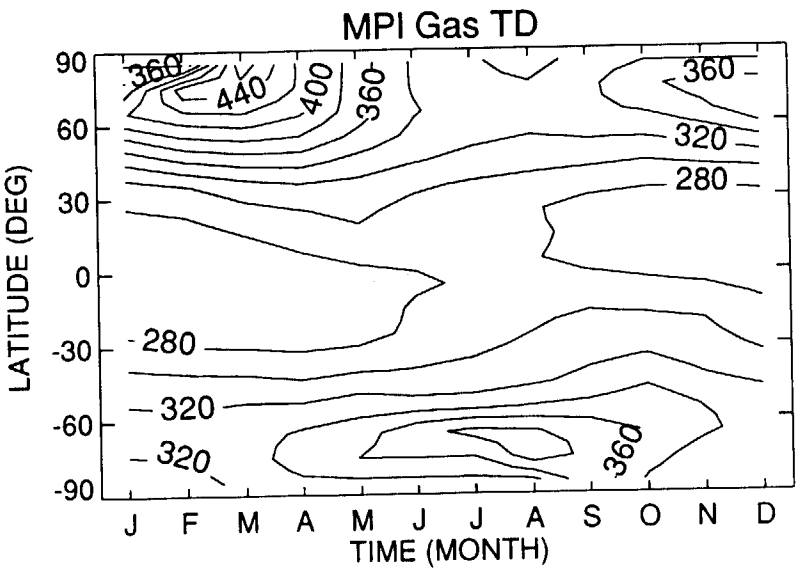

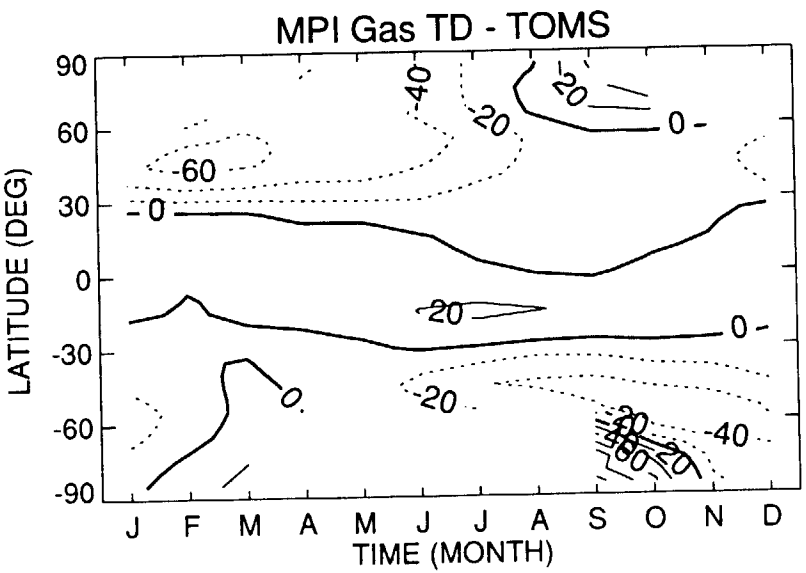

Figure C-8 (top, left and right)

Figure C-9 (bottom, left and right)

O3 Column 1980 (Dobson Units)

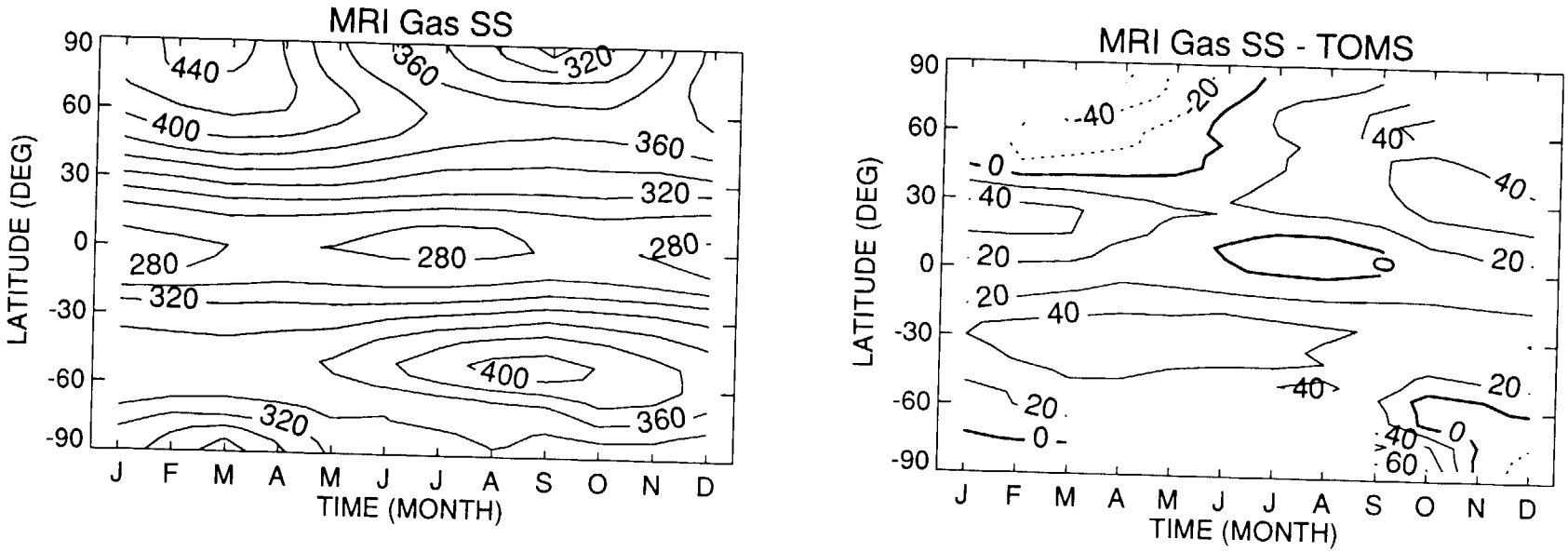

Figure C-10

O3 Column 1980 (Dobson Units)

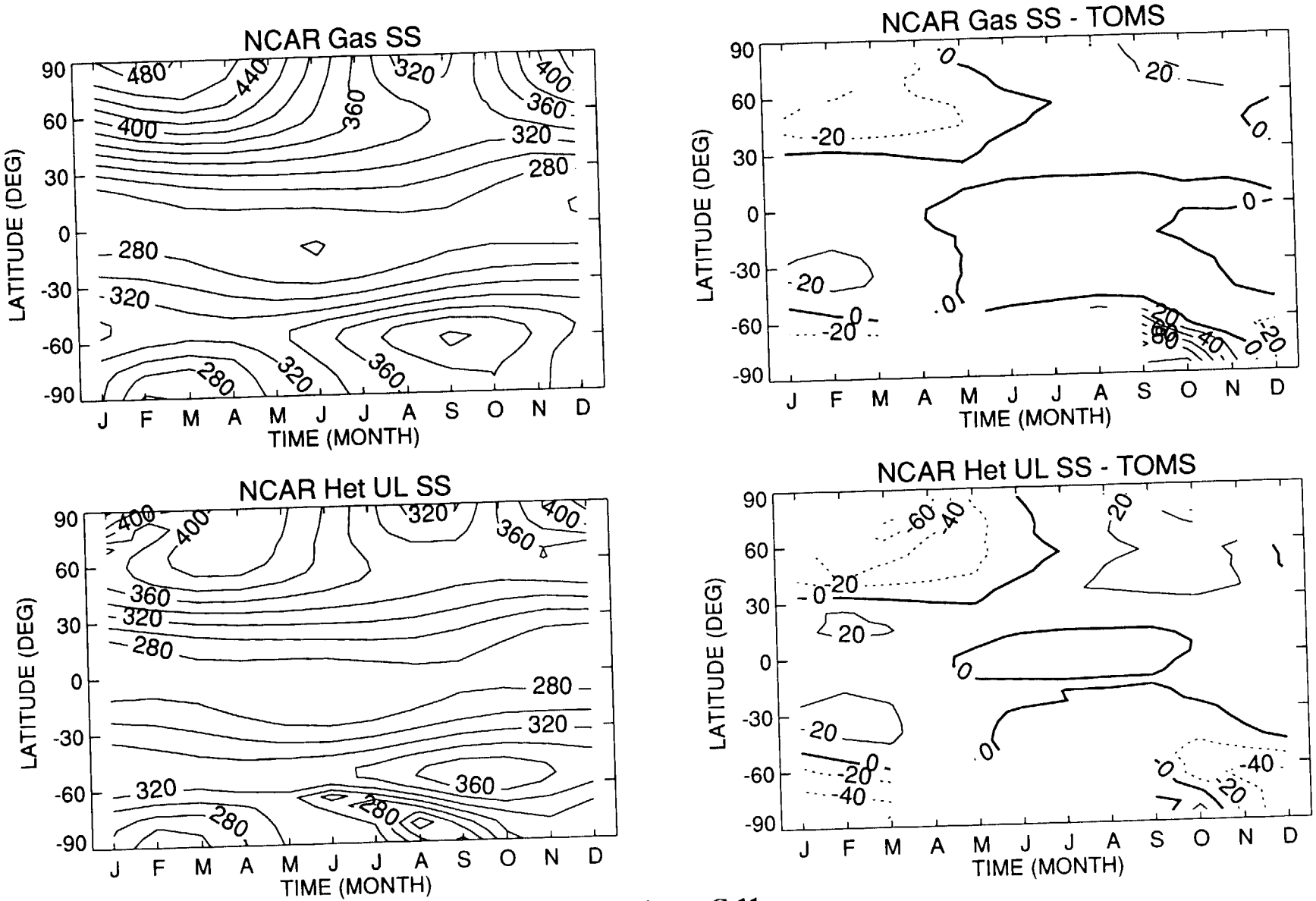

Figure C-11

O3 Column 1980 (Dobson Units)

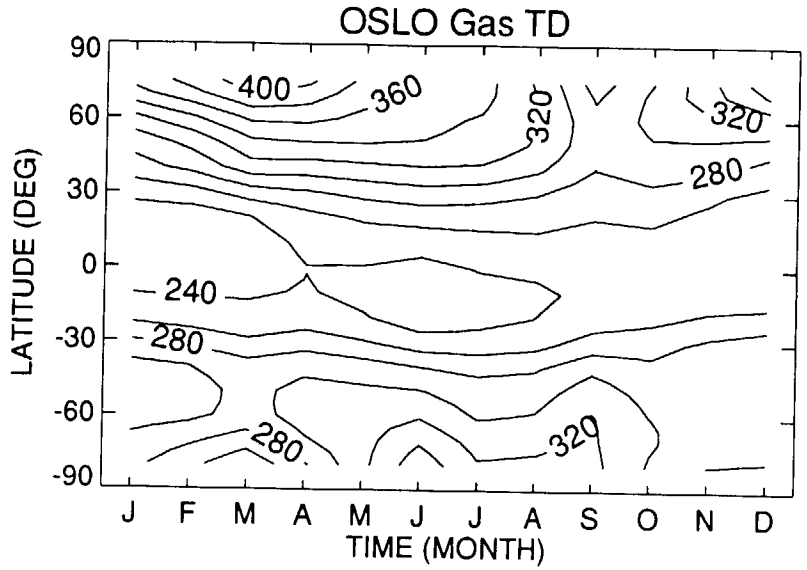

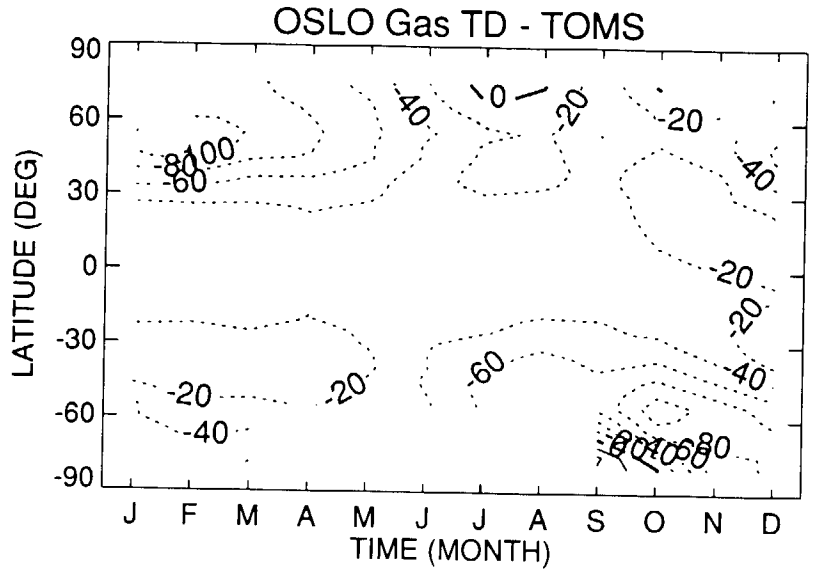

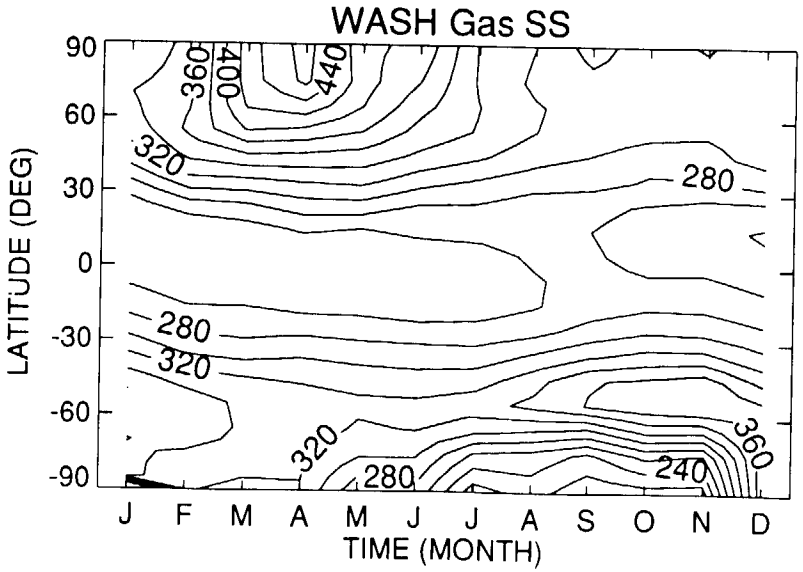

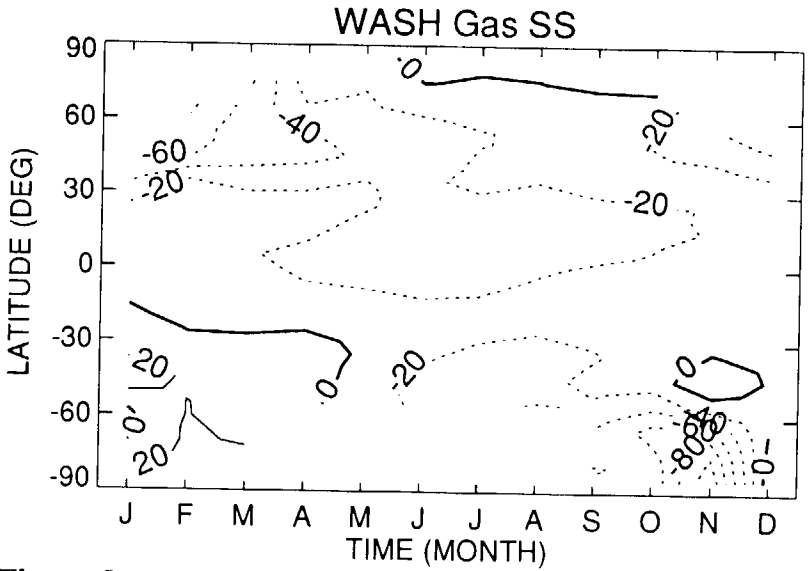

Figure C-12 (top, left and right) **Figure C-13 (bottom, left and right)**

O3 Column (% Change)

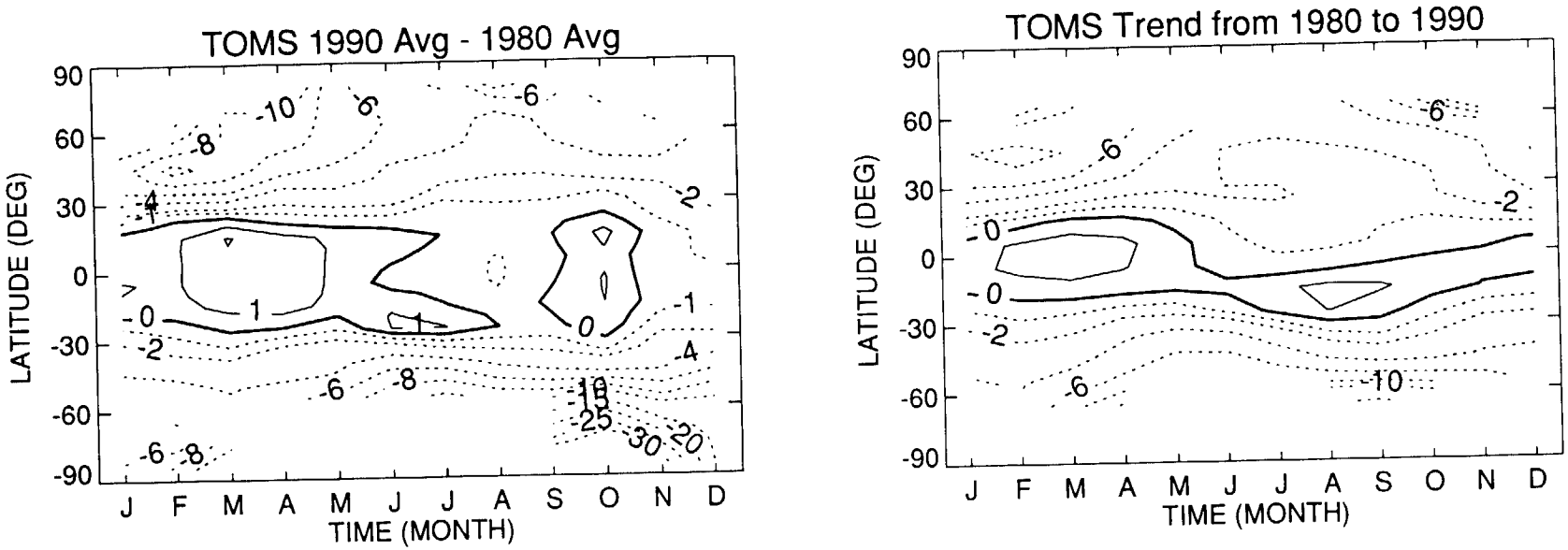

Figure C-14

O3 Column (% Change)

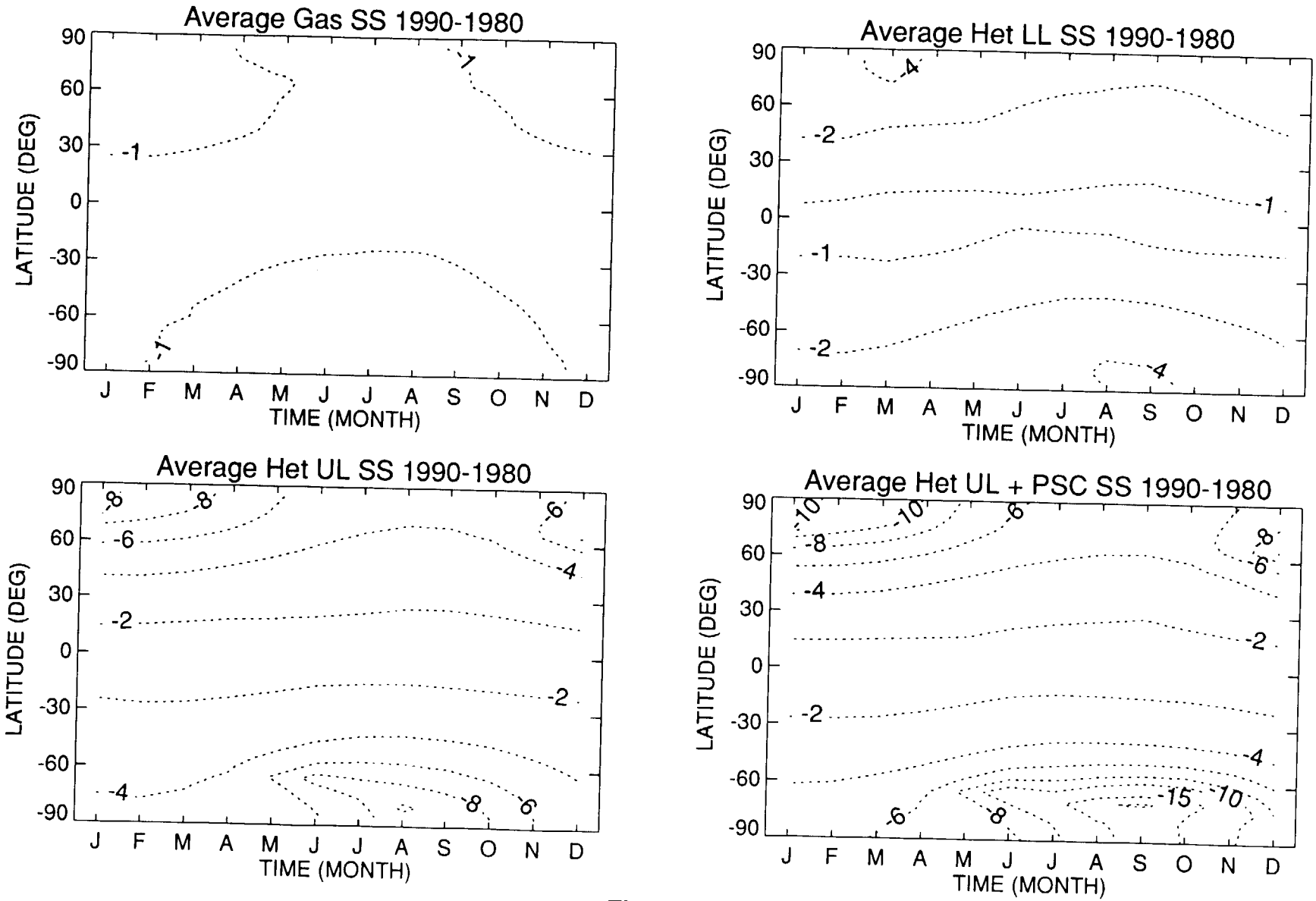

Figure C-15

O3 Column 1990-1980 (% Change)

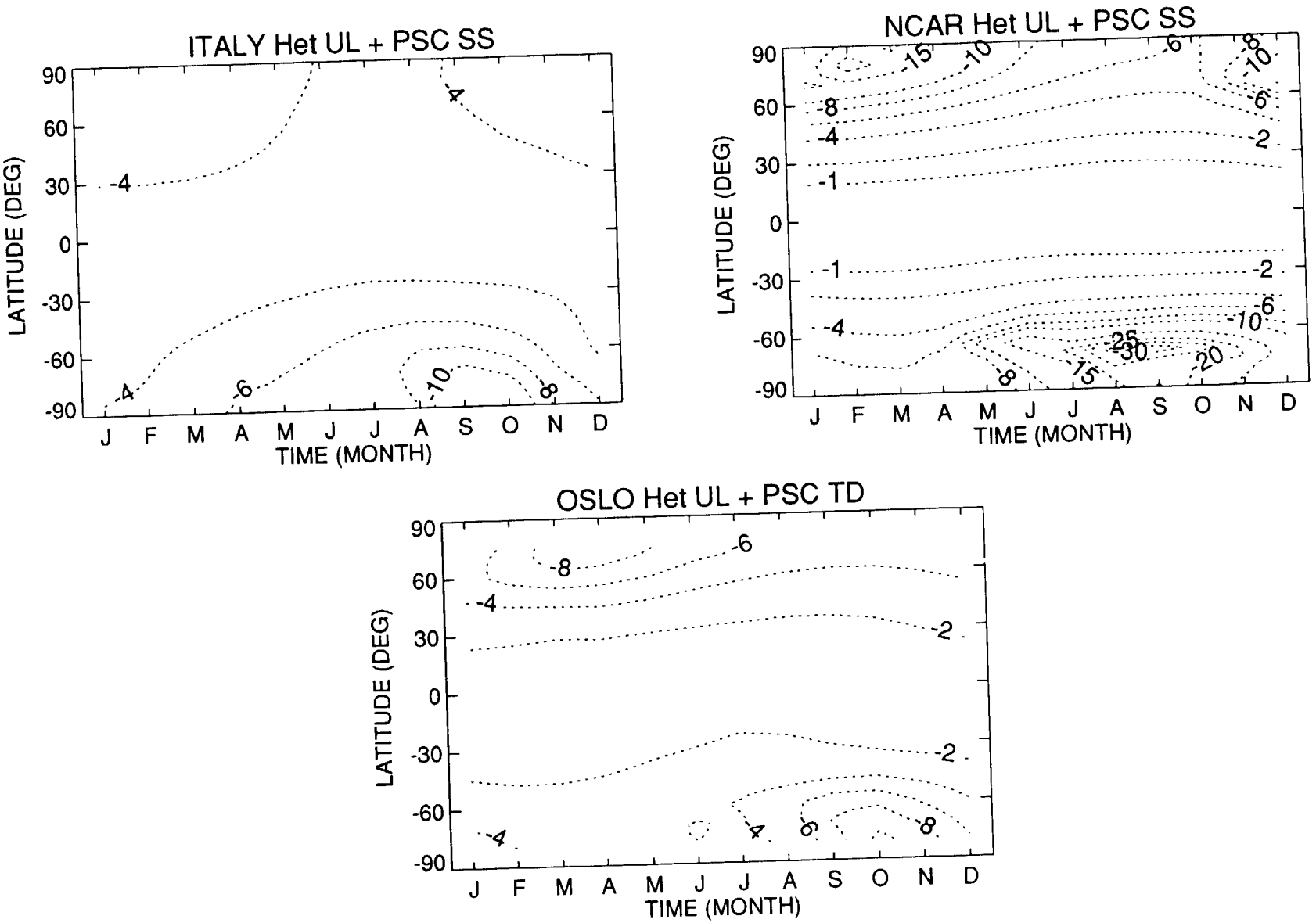

Figure C-16

D: Ozone Profiles

D: Ozone Profile Comparisons

Richard McPeters
NASA-Goddard Space Flight Center

INTRODUCTION

Because the ultimate objective of the High Speed Research Program (HSRP) atmospheric effects (AESA) program is the prediction of the effects of atmospheric perturbations on ozone, the ability of the various models to predict correctly the distribution and time dependence of ozone is particularly important. In section C the ability of the models to derive total column ozone accurately was examined; in this section we examine the ability of the models to produce the vertical distribution of ozone correctly, a much more stringent test of model accuracy. It is quite possible for a model that correctly matches the observed total column ozone to have serious errors in the vertical distribution of ozone because of flaws in the implementation of the dynamics of the lower stratosphere, for instance. The models will be evaluated through comparison with a "1980" reference ozone profile derived from measurements made by the Solar Backscattered Ultraviolet (SBUV) instrument on the Nimbus-7 satellite and through comparison with average Stratospheric Aerosol and Gas Experiment (SAGE II) profiles. This strategy for model evaluation should be accepted with two cautions: first, as will be discussed, there is certainly some level of uncertainty in the measured profiles used to create the reference, and second, one would not expect the models to agree exactly with any particular 2-year average because of the effects of atmospheric variability.

OBSERVATIONAL REFERENCE DATA

Data from the Total Ozone Mapping Spectrometer (TOMS) on Nimbus-7 show that, after accounting for solar cycle changes, there was a significant ozone depletion between 1980 and 1990, with the strongest decrease occurring between 1980 and 1985 (Stolarski et al., 1991). These conclusions are supported by ozonesonde measurements (Staehelin and Schmid, 1991) and by SAGE II measurements (McCormick et al., 1992). There is no good evidence for significant ozone depletion prior to 1980, except possibly in the Antarctic in spring (Angell and Korshover, 1983; Farman et al., 1985). Consequently, we have chosen to use 1980 as the "normal" observational reference period for model comparison for the ozone profiles.

Version 6 data from the SBUV on Nimbus-7 were used to define the ozone reference profile. SBUV provided near global coverage of ozone from November 1978 through February 1987, at which point chopper wheel synchronization problems began to introduce "noise" into the albedo measurement. In the version 6 processing time dependent instrument errors resulting from degradation of the diffuser plate were corrected. Another significant improvement in the version 6 SBUV algorithm is that data from SAGE II were used to define the a priori profile climatology for the 10-125 mb altitude region. We believe that the SAGE data are the best and most extensive available for defining the shape of the ozone profile in the lower stratosphere, the area most critical for the HSRP evaluation. Data from SAGE II are available from 1985 through 1991. Because the SAGE ozone measurement uses the occultation technique, the measurement point sweeps through latitudes from 80S through 80N over a period of about a month as the sunset/sunrise points shift with the drifting orbit. The version 6 SBUV data combine the strengths of SBUV–the very extensive and uniform sampling–with the strengths of SAGE–high accuracy and good vertical resolution in the lower stratosphere. Because accurate data from SBUV were not available after 1987, the present study limits itself to comparison with a 1980 reference and does not evaluate trends in the ozone profiles (though SAGE II or SBUV/2 data could be used for this purpose in future studies).

SBUV inherently has about 8 km vertical resolution above the ozone maximum and only about 15 km resolution in the 10-25 km region. (SBUV provides very little information from the lowest 10 km of the troposphere). The SBUV measurements of the backscattered albedo–the ratio of backscattered radiance to incident solar irradiance–determine the average amount of ozone in the 15-30 km region; the a priori climatology (the SAGE data) determines the shape of the profile within that altitude range. The use of SAGE climatology in the SBUV algorithm does not imply that SAGE and SBUV are required to agree in the lower stratosphere.

The ozone reference consists of monthly average ozone profiles for 10-degree latitude zones from 80S to 80N. Since scattered sunlight is used to measure ozone, no data are available from SBUV at high latitudes in the winter (polar night). A 2-year average, 1979 and 1980, was used to create the "1980" reference in order to minimize the effect of the quasi-biennial oscillation (QBO) in the tropics, an effect generally not included in the model calculations. SBUV retrieval is done internally in Umkehr layers (approximately 5 km thick). A spline fit of layer ozone versus log pressure was done to produce column ozone and ozone mixing ratio at the 2 km z^* levels required for comparison with the models.

Figure D-1 (top) shows the seasonal behavior of the SBUV reference ozone as a function of latitude for two altitudes – 20 km and 30 km. For comparison, SAGE II data averaged for the 1985-1990 period are also shown (middle). Though SAGE latitude coverage is somewhat less, the agreement in ozone morphology is generally quite good, not only in the features of the seasonal variation but even in the absolute ozone levels, except in the tropics where SBUV-measured ozone is somewhat less than SAGE-measured ozone. Some common features of the models can be examined in an average of nine of the models, also shown in Figure D-1 (bottom). Results of individual model comparisons will be discussed in detail in the next section, but in general the models correctly produce the overall features of the seasonal ozone variation, including the basic latitudinal variation and the seasonal behavior at high latitudes. While ozone in the equatorial zone at 20 km is somewhat too high and the latitudinal gradient is somewhat underestimated, this probably does not represent a serious problem given the steep gradient in ozone with altitude in this region.

Figure D-2 is a plot of the height-latitude cross section of the percent difference (SAGE II–SBUV) / SBUV for four representative months - January, April, July, and October. In this and comparisons to follow, altitudes below 15 km are not shown because of the lack of validity of the SBUV reference in the troposphere. The figure shows that SBUV and SAGE agree generally to the ±10% level, with the principal area of disagreement being in the tropics in the 15-25 km region. SAGE measurements are about 20% higher than SBUV at 20 km but about 20% less than SBUV at 15 km. Part of this difference could be due to time difference - SBUV data are from 1979-1980, while SAGE data are from 1985-1990. While neither SBUV data nor SAGE data are of the highest quality in the low-altitude region, we would estimate that the reference model should be considered valid at 20 km to the ±20%-30% level of accuracy, and valid to the ±50% level even at 15 km.

Figure D-3 is a similar plot, but shows the difference between balloon measurements (ECC sondes) and the SBUV reference. Considerably more variability is seen, largely because the ECC sonde data set is very limited, consisting of profiles measured sporadically at only nine sites over the period 1979-1988. The comparison cannot be considered conclusive, but the agreement between 15 and 30 km is generally to the ±40% level, and is consistently worse only in the 15-20 km region near the equator.

Based on these measurement comparisons, we would conclude that the 1979-1980 SBUV reference profile correctly represents the ozone distribution to the 10%-20% accuracy level in the 30-50 km region and to the 30%-50% accuracy level even in the 15-25 km region.

MODEL COMPARISONS WITH DATA

An extensive series of model calculations was done for comparison with the 1980 observational reference profiles, including runs that considered gas phase chemistry only (GAS) and runs that included heterogeneous chemistry for various levels of aerosol loading. To limit somewhat the scope of the comparisons we will examine only the heterogeneous lower-limit (HET-LL) model results (for GISS and WASH only the GAS results are currently available). The HET-LL result probably comes closest to representing normal non-volcanic conditions and is most appropriate for comparison with the 1980 reference. The results of the gas phase and HET-LL calculations are generally very similar when ozone is examined (this may not be true of other species). Figure D-4 shows the similarity of the GAS and HET-LL results by plotting the height-latitude cross sections of the percent difference between the model calculation and the reference profile. For both the GSFC July runs (left) and the NCAR January runs (right), the results of the gas phase calculations are almost identical to the results of the HET-LL calculations.

Figures D-5a through D-5l show the comparisons between observation and calculation for 12 different models. Each figure shows the height-latitude cross section of the difference (in percent) between the HET-LL model calculation and the reference profile for four different months: January, April, July, and October. Shown (in alphabetical order) are model comparisons for AER, CAMED, DUPONT, GISS, GSFC, ITALY, LLNL, MRI, MPI, NCAR, NOCAR, and WASH.

In the upper stratosphere, 35-50 km, almost all of the models underestimate ozone by 20%-40%. This underestimation is well known and is a problem of long standing. The SAGE average ozone in the upper stratosphere is also less than the SBUV reference, sometimes by as much as 20%. This could be due in part to real ozone change between 1980 (SBUV) and 1985-1990 (SAGE); both Umkehr and SBUV show trends at 45 km that amount to about 7% per decade. The NOCAR and ITALY models have the best agreement with observation in the upper stratosphere - the NOCAR model underestimates ozone by 0%-20%, while the ITALY model slightly overestimates ozone. The CAMED, GISS, and NCAR models have disagreements in the 10%-30% range.

In the middle stratosphere, 25-35 km, all the models predict ozone to much better accuracy, generally agreeing with the reference profile to within about ±20% except near the winter terminator.

The biggest variance among the models is seen in the lower stratosphere, the 15-25 km region. The disagreement mostly occurs in the equatorial region; at mid and high latitudes agreement is generally to within ±20% or so. The AER, LLNL, MPI and MRI models overestimate ozone at 20 km in the tropics by 20%-80%, but are in better agreement near 15 km. The GSFC model at 20 km overestimates ozone by only 20%-40% , but has large disagreements exceeding 80% at lower altitudes between 30S and the equator. The CAMED and ITALY models overestimate ozone throughout the 15-25 km region by 40%-100% with the largest disagreements at the lowest altitudes. The GISS model appears to contain a wave structure such that it overestimates by 40% at 23 km, is in agreement at 20 km, and overestimates by 60%-100% at 15 km. The DUPONT, NCAR, and NOCAR models agree best with the reference profile in the tropical lower stratosphere, agreeing to within 0%-20% near 20 km, and agreeing to within 40%-60% even at 15 km. At 20 km the SAGE-based SBUV profile should be accurate to within ±20%-30%, and while neither SAGE nor SBUV is capable of good accuracy at 15 km in the tropics, disagreements approaching 100% should not be ignored, even though the actual amount of ozone at this altitude is small.

PROFILE SHAPE EVALUATION

It is difficult to evaluate how realistic the profile shapes produced by the models are based only on the height-latitude cross section of the model-reference difference. Since a large percent difference in ozone at 15 km may represent a very small error in actual ozone, it is instructive to look at actual ozone profiles. Figures D-6a through D-10c are plots of ozone mixing ratio versus altitude for the same four months as before for five latitude zones: 15S-15N (D-6a-c), 40N-55N (D-7a-c), 40S-55S (D-8a-c), 65N-80N (D-9a-c), and 65S-80S (D-10a-c). In each case profiles from nine of the models are plotted along with the SBUV and SAGE II profiles (separated into parts a, b, and c for clarity). A plot of mixing ratio emphasizes features of the ozone distribution between 25 and 45 km at the expense of details in the lowest stratosphere. Both the SBUV reference profile and the SAGE average profile are plotted for low latitudes and middle latitudes; insufficient data were available from SAGE at high latitudes. Despite the time difference of the observational data, SAGE and SBUV data are generally consistent, though SAGE data tend to peak 2-4 km lower in altitude than SBUV data.

Figures D-6a-c show that all the models reproduce the mixing ratio profile quite well in the equatorial zone, 15S-15N, though peaking 1-2 km lower than SAGE and 2-4 km lower than the SBUV reference profile. ITALY smoothes through the mixing ratio peak more than the other models, while GSFC has too sharp a peak.

At middle latitudes, 40-55 degrees north (D-7a-c) and south (D-8a-c), the models reproduce the magnitude of the reference profile well in summer but peak at an altitude about 5 km too low. For the winter profiles the ITALY, CAMED, GISS, NCAR, and NOCAR models agree well with the reference. In the southern hemisphere the ITALY and NCAR models most nearly match the winter profile shape. The AER, DUPONT, GSFC, LLNL, and MRI models tend to be too low in magnitude and peak at a significantly lower altitude.

Not unexpectedly, the comparisons are most erratic at high latitudes in winter. With the exception of the ITALY and GISS models, all the models tend to peak at much too low an altitude in the 65- to 80-degree zones (Figures D-9a-c and Figures D-10a-c). They tend to peak near 25 km and then decrease at higher altitudes in a fairly flat distribution, while the SBUV reference has a broad peak maximizing near 40 km. The CAMED model is unusual, producing a double peak in winter: one peak near 25 km and a second peak near 42 km. Part of the reason for the large discrepancy could be that the measured data for this zone in winter come mostly from near 65 degree latitude, because higher latitudes are in darkness and ozone measurement is not possible.

In summer most of the models agree much better with the reference profile, though, as at other latitudes, peaking a few kilometers too low. The LLNL, MPI, MRI, NCAR and WASH models peak at an altitude significantly too low even in summer.

The spring comparisons are intermediate. In the northern hemisphere most models derive approximately the correct altitude for the peak but significantly underestimate its magnitude (LLNL, MRI, AER, GSFC, and DUPONT). Two models, ITALY and NCAR, overestimate the peak. In the southern hemisphere in the fall only ITALY reproduces the observed high altitude peak near 45 km. The other models have relatively flat peaks lower down, similar to their behavior in winter.

CONCLUSIONS

We have used a 2-year average (1979 and 1980) of reprocessed SBUV ozone data to establish a "1980" reference ozone profile. We believe that this reference, which uses SAGE II profiles for its a priori profile shape, correctly represents the ozone distribution to the 10%-20% accuracy level

in the 30-50 km region, and to the 30%-50% accuracy level in the 15-25 km region. Ozone calculated by each of the models was compared with this ozone reference profile to assess the accuracy of the models' ozone computation. In the upper stratosphere, 35-50 km, most of the models consistently underestimate ozone by 20%-40%. Only the ITALY model agrees with observation near 50 km. In the middle stratosphere, 25-35 km, all the models predict ozone to much greater accuracy, generally agreeing with the reference profile to within about ±20% except near the winter terminator. The largest percent differences from the reference occur in the equatorial region in the 15-25 km region, with disagreements from 60% to more than 100%. The DUPONT, NCAR, and NOCAR models agree best with the reference profile in the tropical lower stratosphere, agreeing to within 0%-20% near 20 km and agreeing to within 40%-60% even at 15 km.

Overall the models correctly produce the shape of the mixing ratio profile in the equatorial regions and at higher latitudes in summer, though they persistently generate a mixing ratio peak a few kilometers lower than is observed by SBUV or SAGE. At higher latitudes in other seasons the models tend to peak at significantly too low an altitude, too low by about 5 km at middle latitudes and too low by as much as 10 km at high latitudes. Model performance is poorest at high latitudes in winter where all the models except the ITALY and GISS models peak at much too low an altitude. The models peak near 25 km, while the SBUV reference has a broad peak maximizing near 40 km.

REFERENCES

Angell, J., and J. Korshover, Global variation in total ozone and layer-mean ozone: an update through 1981, *J. Climate Appl. Meteor.*, *22*, 1611-1627, 1983.

Farman, J., B. Gardiner, and J. Shanklin, Large losses of total ozone in Antarctica reveal seasonal ClO_x/NO_x interaction, *Nature*, *315*, 207-210, 1985.

McCormick, M.P., R. Veiga, and W.P. Chu, Stratospheric ozone profile and total ozone trends derived from SAGE I and SAGE II data, *Geophys. Res. Lett.*, *19*, 269-271, 1992.

Staehelin, J., and W. Schmid, Trend analysis of tropospheric ozone concentrations utilizing the 20-year data set of ozone balloon soundings over Payerne (Switzerland), *Atmos. Envir.*, *25a*, 1739-1749, 1991.

Stolarski, R.S., P. Bloomfield, R. McPeters, and J. Herman, Total ozone trends deduced from Nimbus-7 TOMS data, *Geophys. Res. Lett.*, *18*, 1015-1018, 1991.

FIGURE CAPTIONS

Figure D-1. A plot showing the seasonal behavior of the SBUV reference ozone (top), average SAGE II ozone for 1985-1990 (middle), and an average of nine of the models (bottom), as a function of latitude for two altitudes – 20 km and 30 km.

Figure D-2. A height-latitude cross section of the percent difference between SAGE II and SBUV for four representative months – January, April, July, and October. In this and comparisons to follow, altitudes below 15 km are not shown because of the lack of validity of the SBUV reference in the troposphere.

Figure D-3. A plot similar to Figure D-2 but of the difference between balloon measurements (ECC sondes) and the SBUV reference. The ECC sonde data set is very limited, consisting of profiles measured sporadically at only nine sites over the period 1979-1988.

Figure D-4. A comparison showing the similarity of the gas phase calculations and the heterogeneous lower-limit (HET-LL) calculations. Height-latitude cross sections of the percent difference between the model calculation and the reference profile for the GSFC model July runs (left) and the NCAR January runs (right) are shown.

Figures D-5a - 5l. Comparisons between the ozone reference and the calculation results for each of twelve different models (shown in alphabetical order). Each figure shows the height-latitude cross section of the difference (in percent) between the HET-LL model calculation and the reference profile for four different months: January, April, July, and October. The GISS, MPI, and WASH models are not SS Het LL cases.

Figures D-6a - D-10c. Plots of ozone mixing ratio versus altitude for January, April, July, and October for 5 latitude zones: 15S-15N (D-6a-c), 40N-55N (D-7a-c), 40S-55S (D-8a-c), 65N-80N (D-9a-c), and 65S-80S (D-10a-c). In each case profiles from eleven of the models are plotted along with the SBUV and SAGE II profiles (separated into parts a, b and c for clarity).

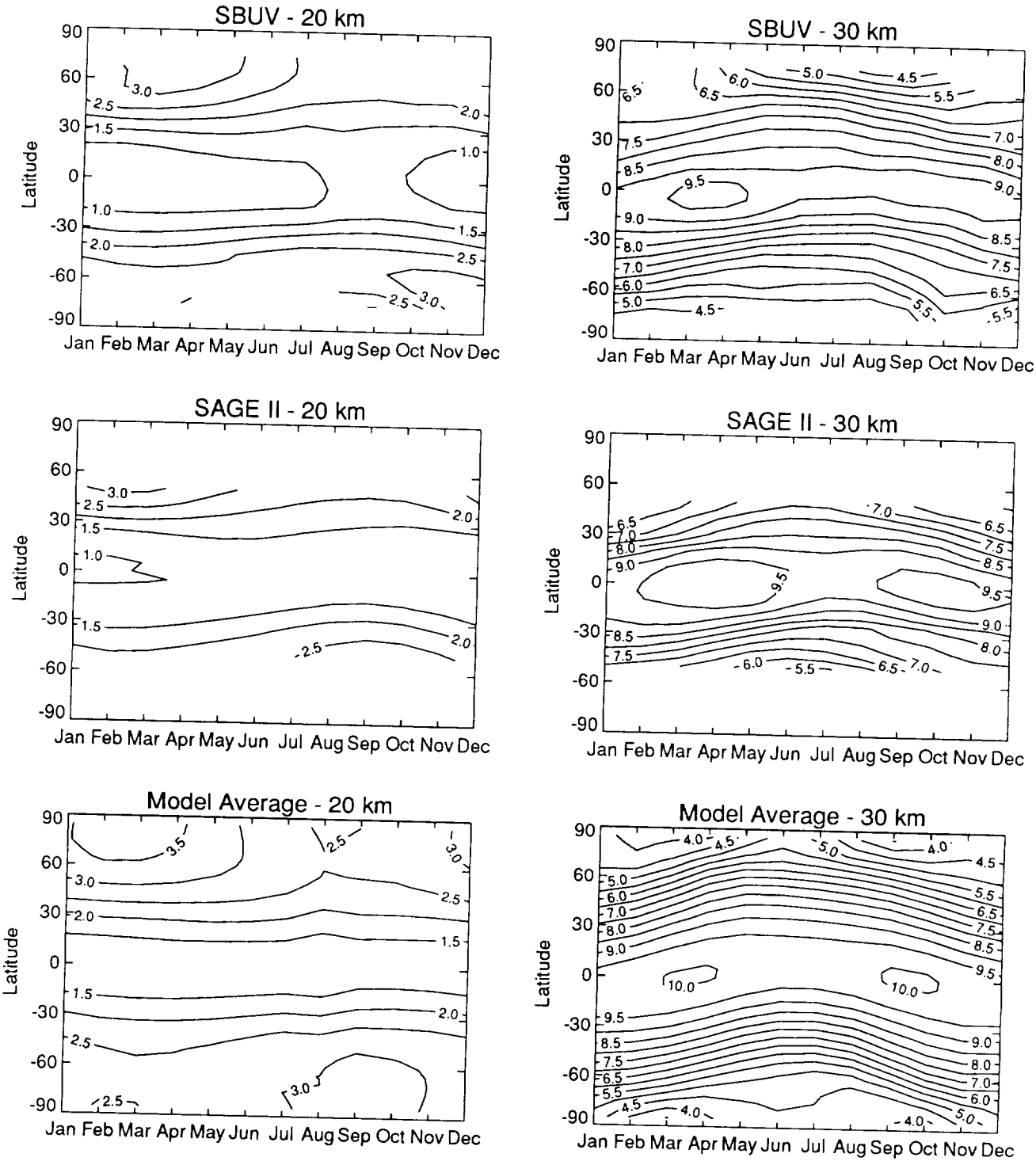
SBUV - 20 km
SBUV - 30 km
SAGE II - 20 km
SAGE II - 30 km
Model Average - 20 km
Model Average - 30 km
Latitude
90
60
30
0
-30
-60
-90
Jan Feb Mar Apr May Jun Jul Aug Sep Oct Nov Dec

Figure D-1

O3 (SAGE II - SBUV) Percent Difference

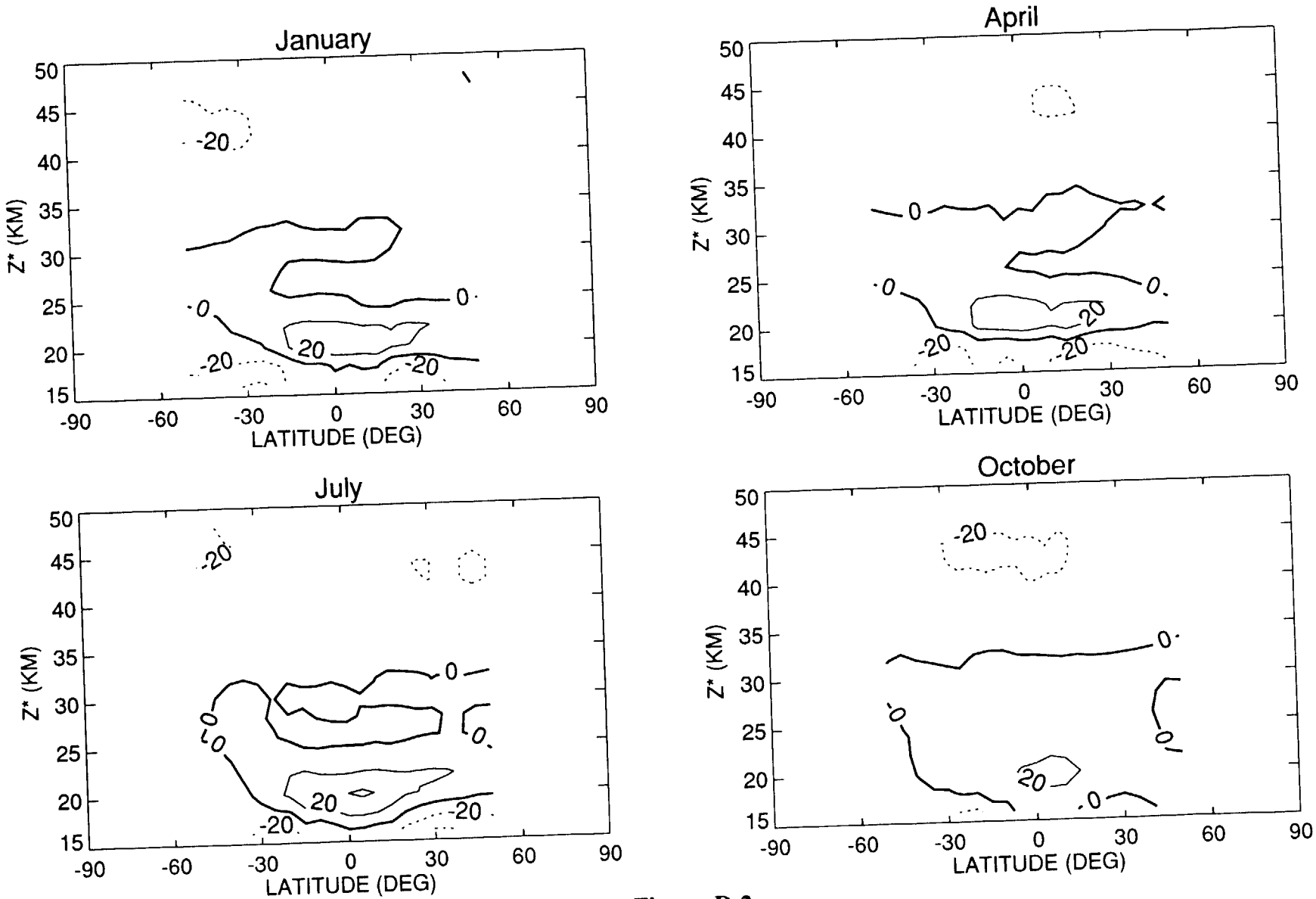

Figure D-2

O3 (ECC - SBUV) Percent Difference

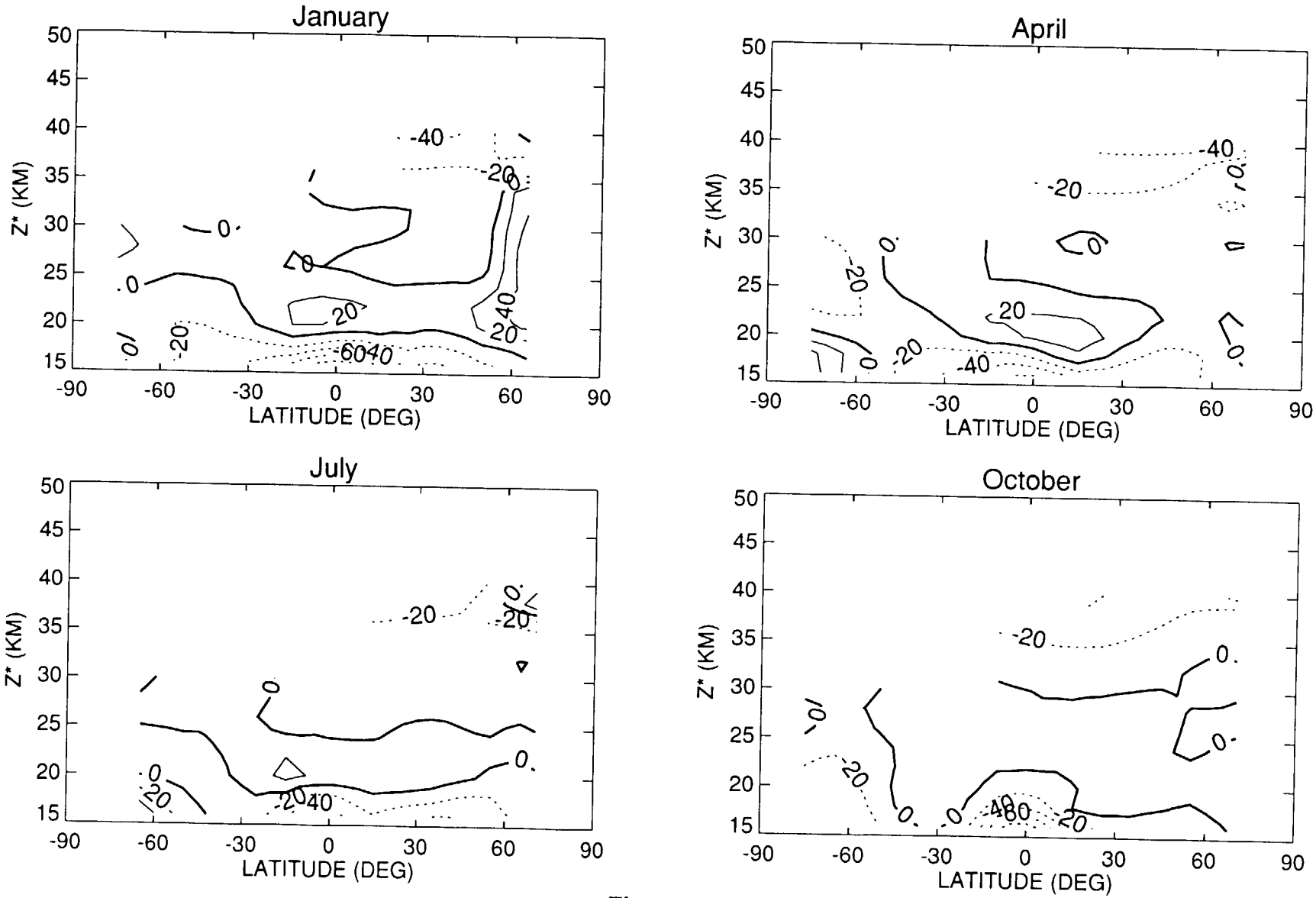

Figure D-3

O3 (Model - SBUV) Percent Difference

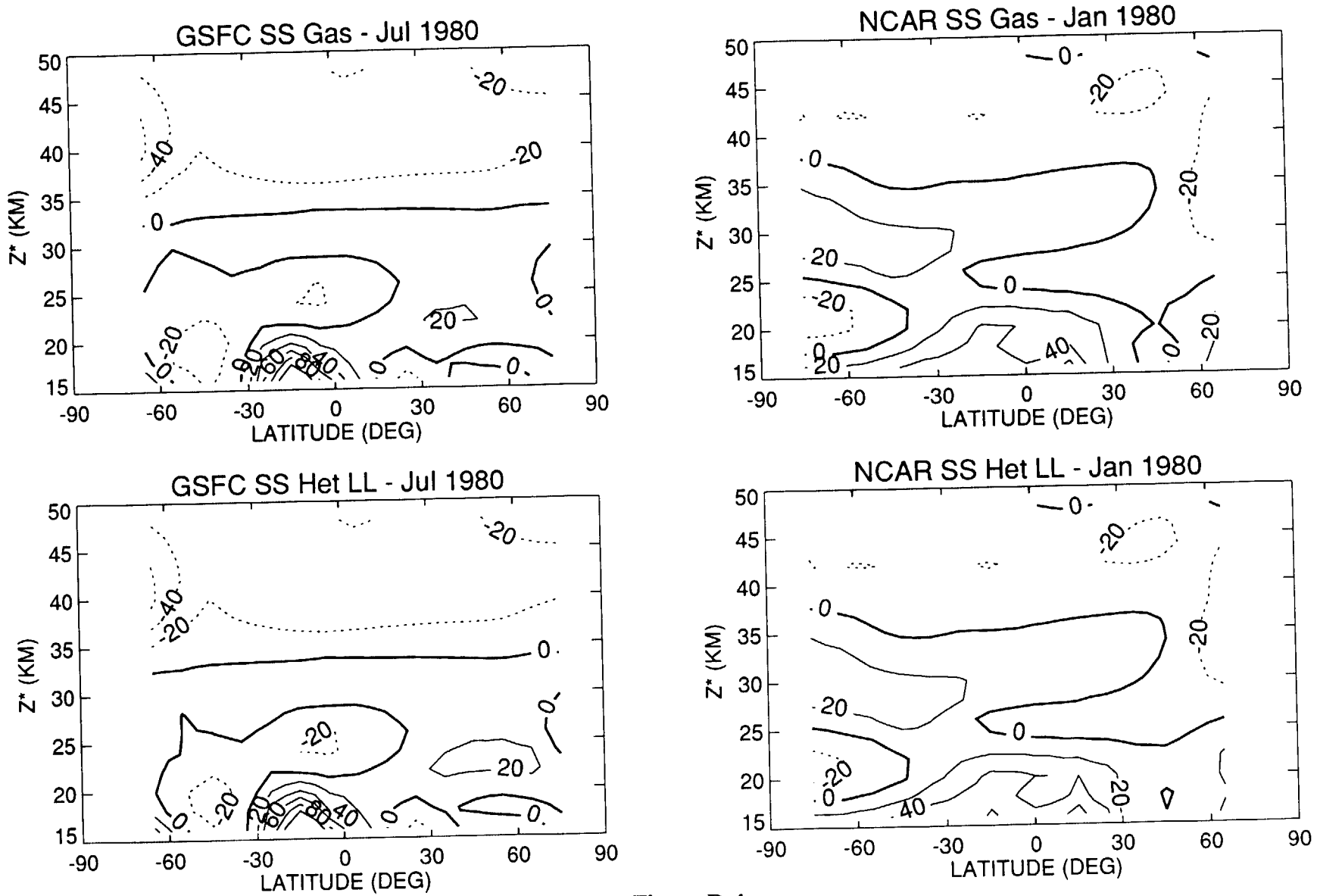

Figure D-4

O3 (Model - SBUV) Percent Difference

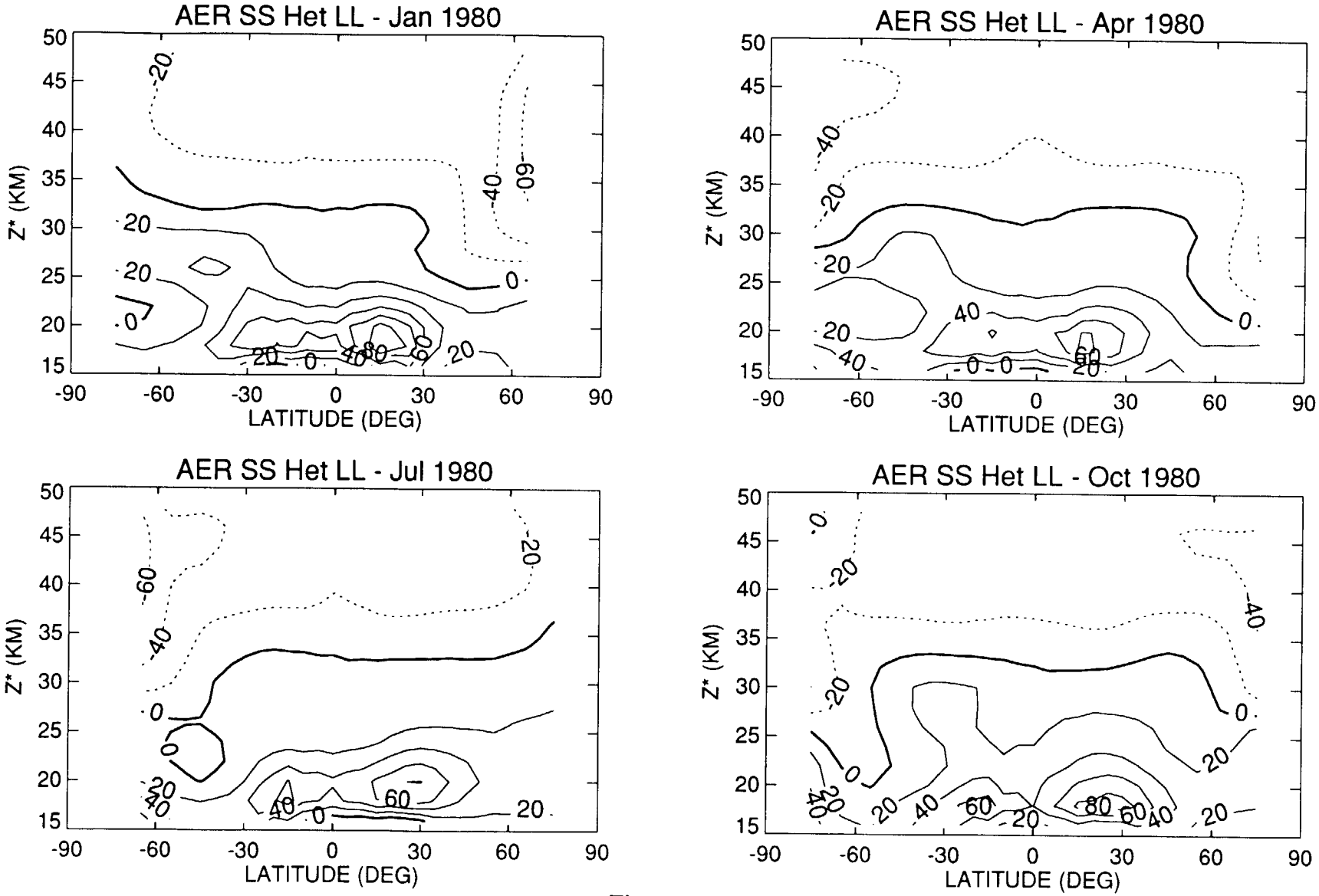

Figure D-5 a

O3 (Model - SBUV) Percent Difference

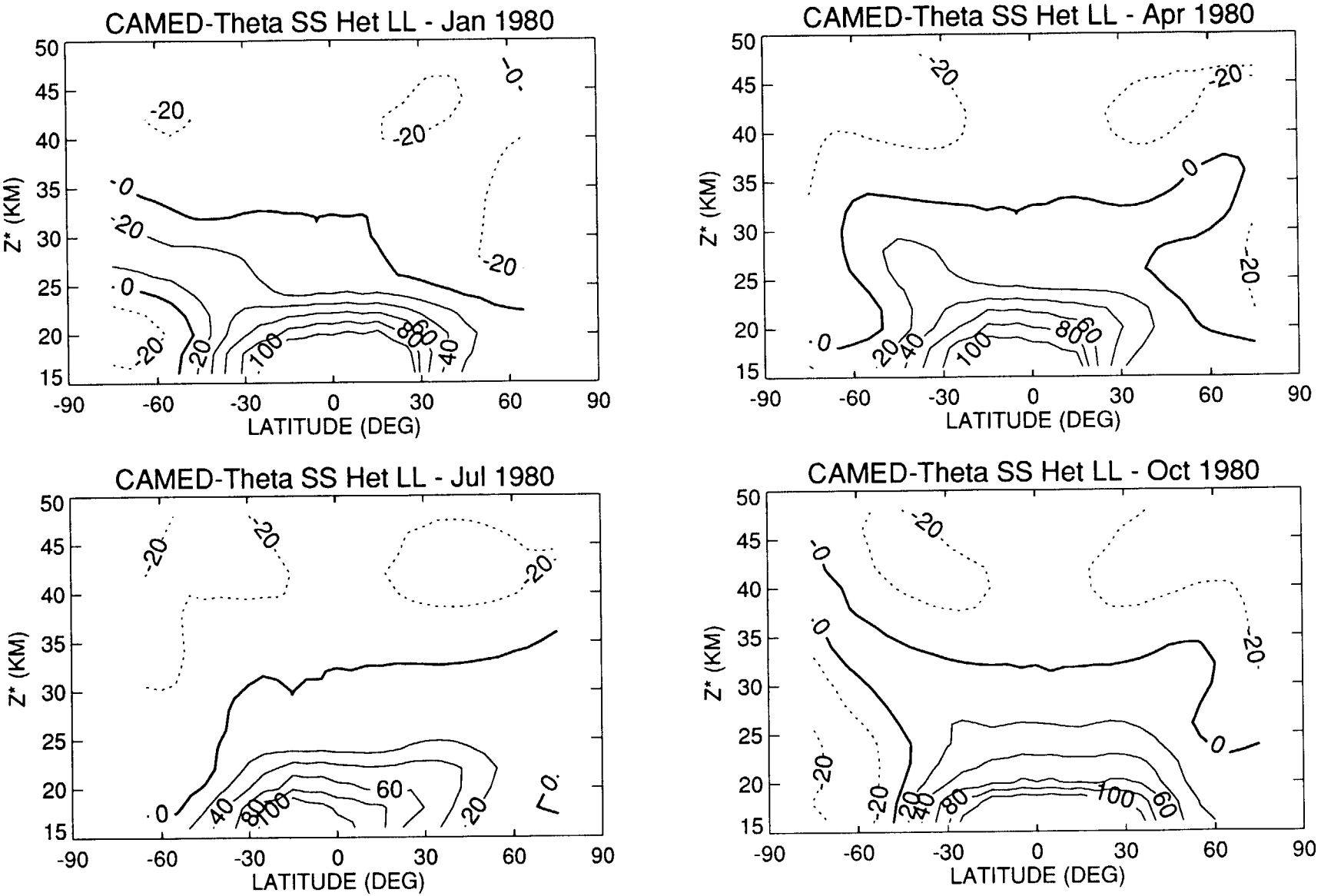

Figure D-5 b

O3 (Model - SBUV) Percent Difference

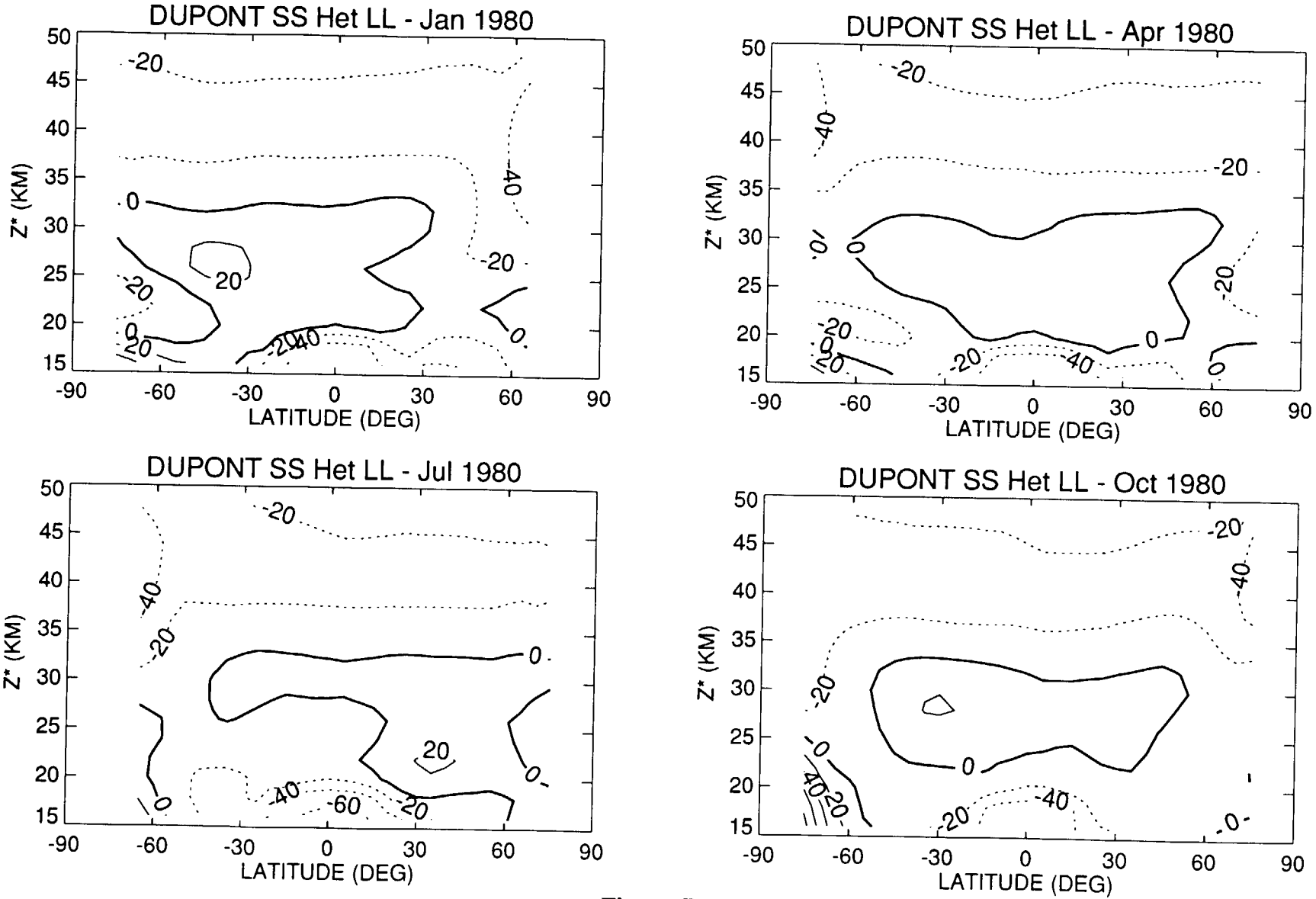

Figure D-5 c

O3 (Model - SBUV) Percent Difference

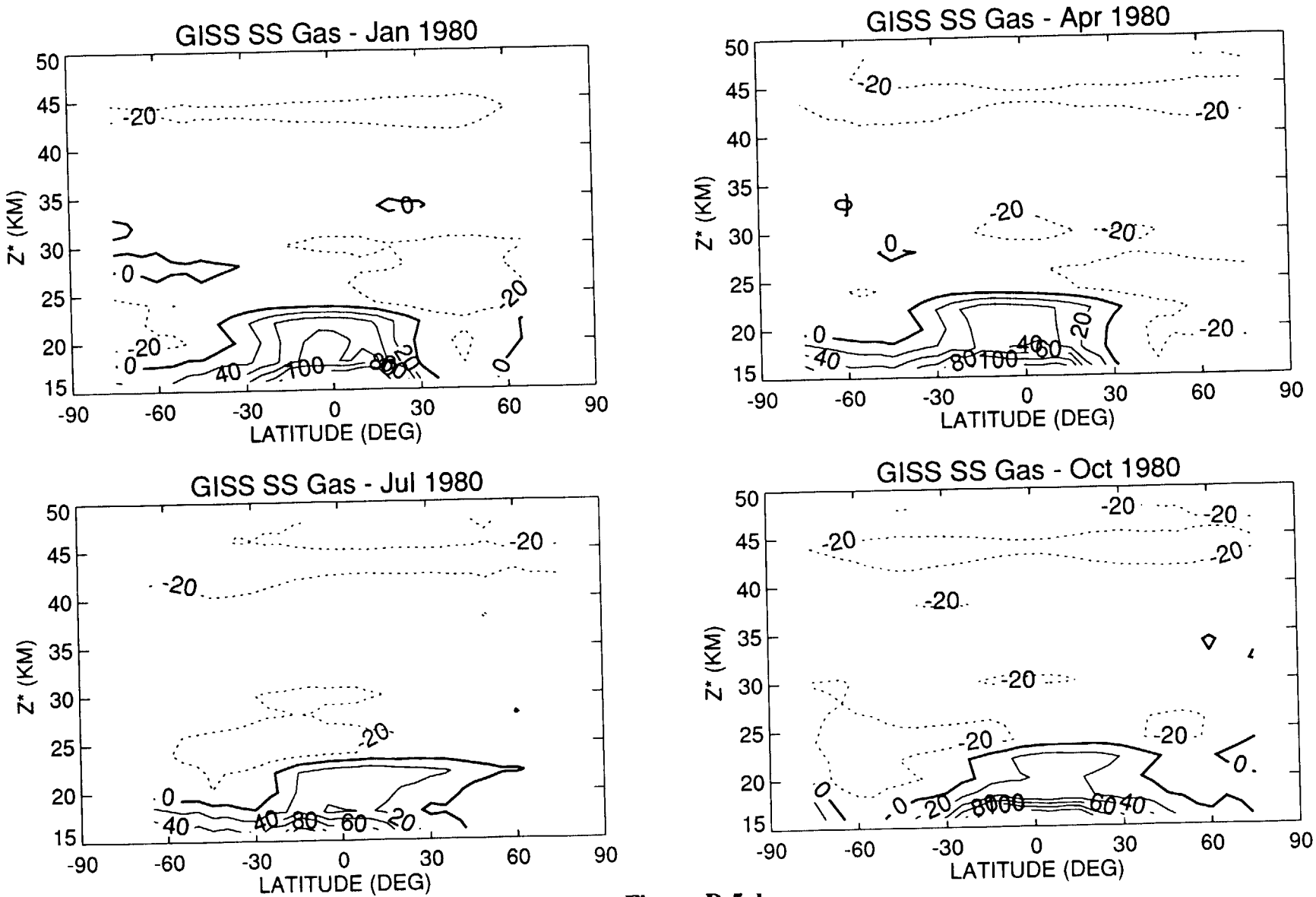

Figure D-5 d

O3 (Model - SBUV) Percent Difference

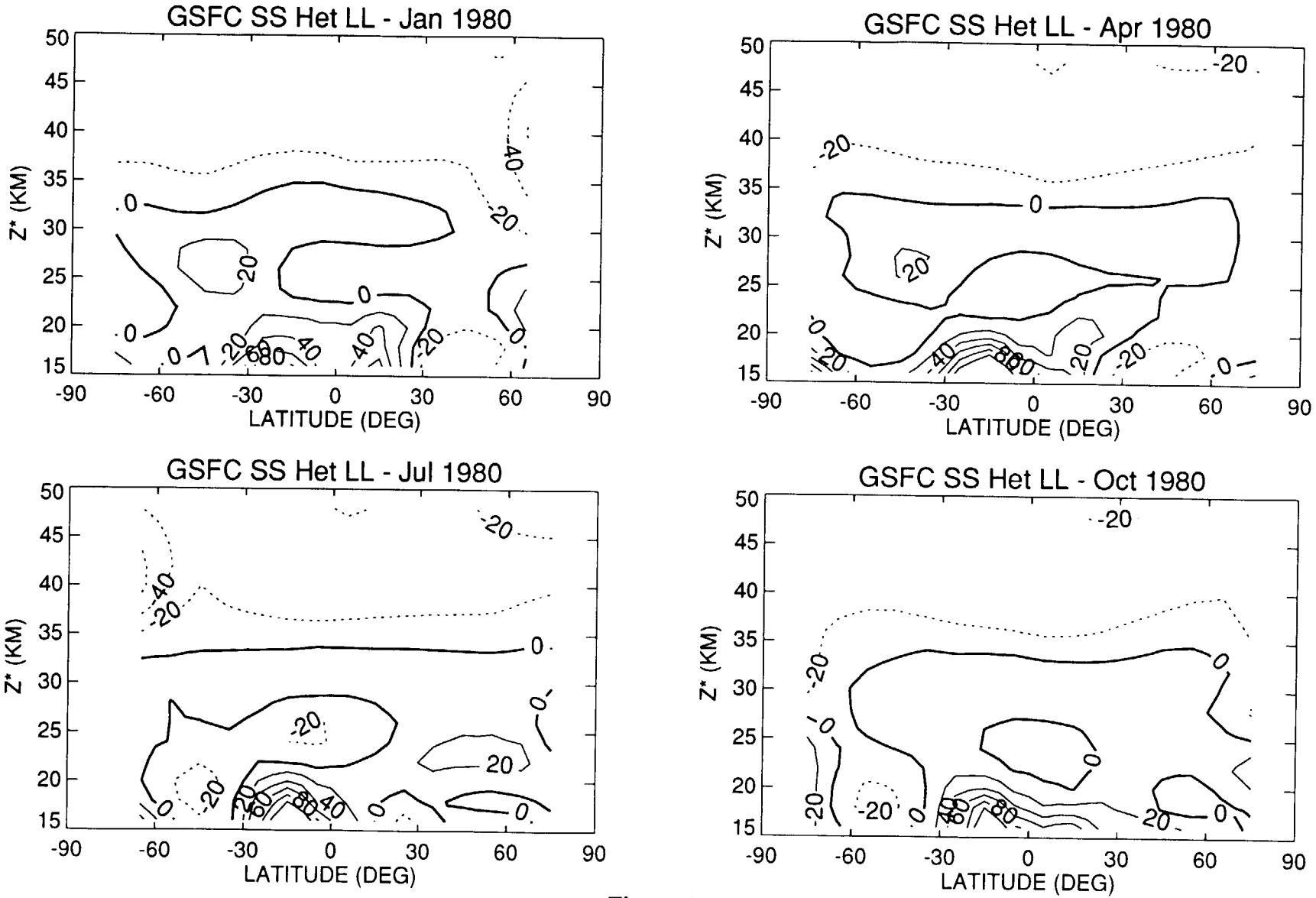

Figure D-5 e

O3 (Model - SBUV) Percent Difference

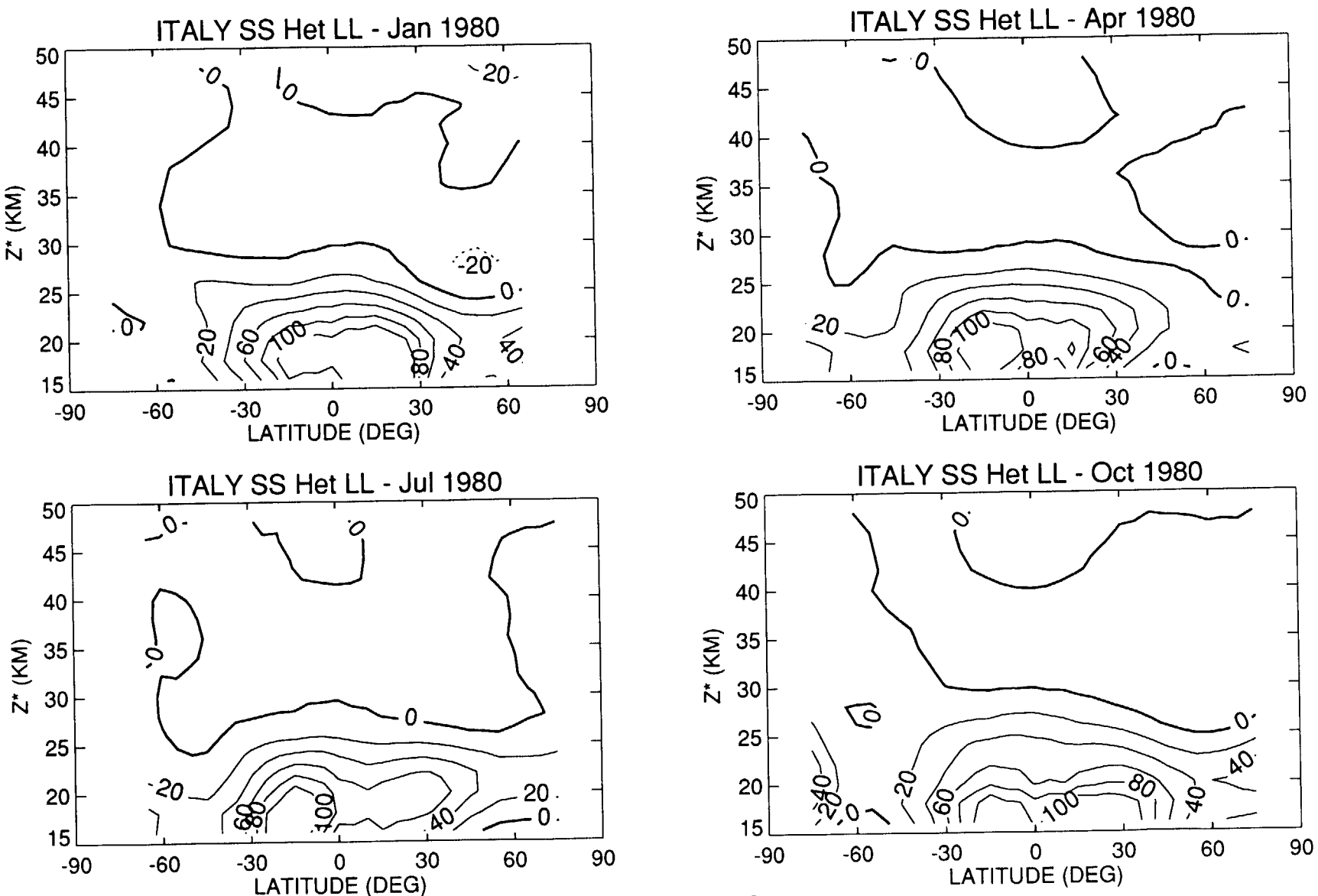

Figure D-5 f

O3 (Model - SBUV) Percent Difference

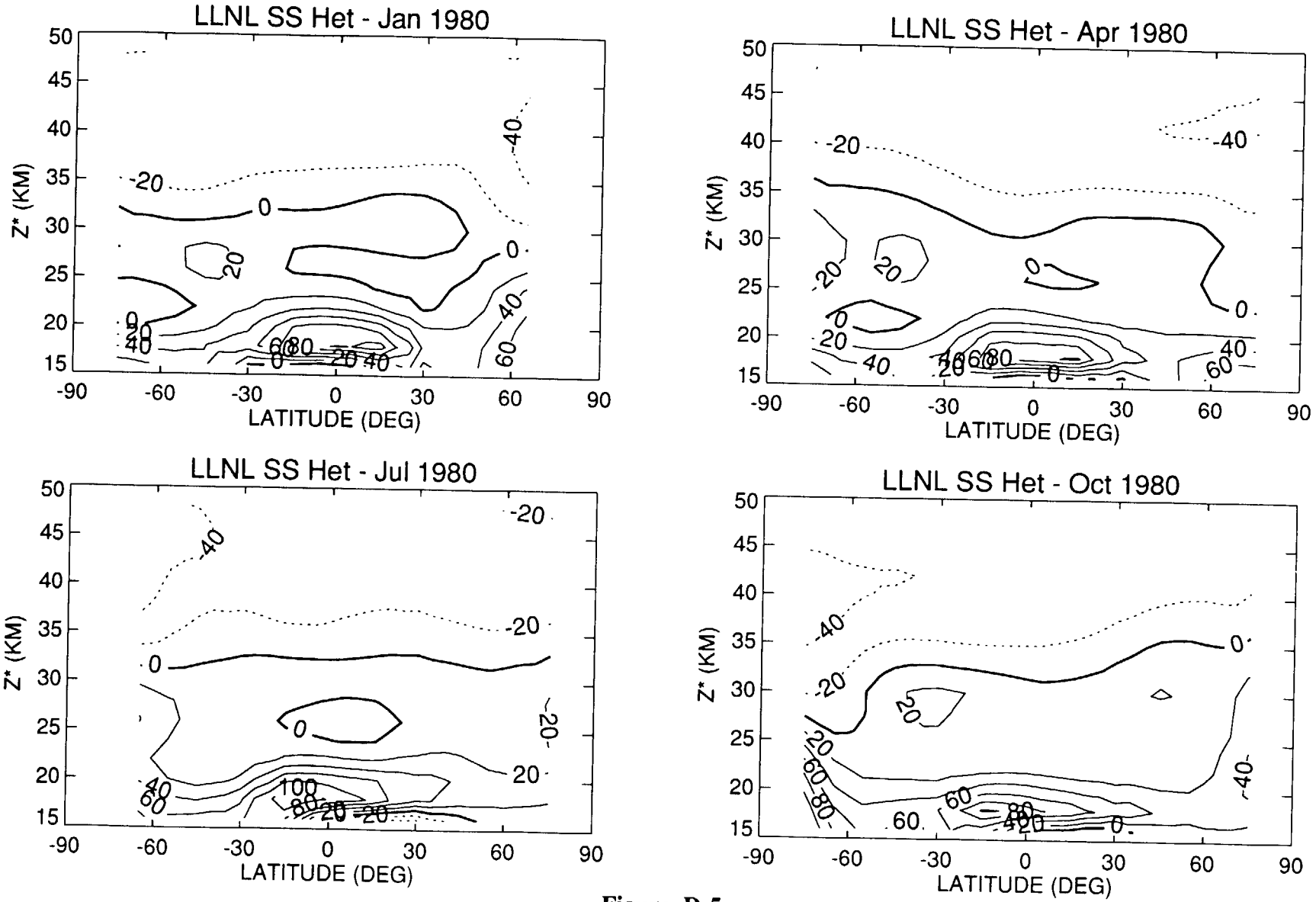

Figure D-5 g

O3 (Model - SBUV) Percent Difference

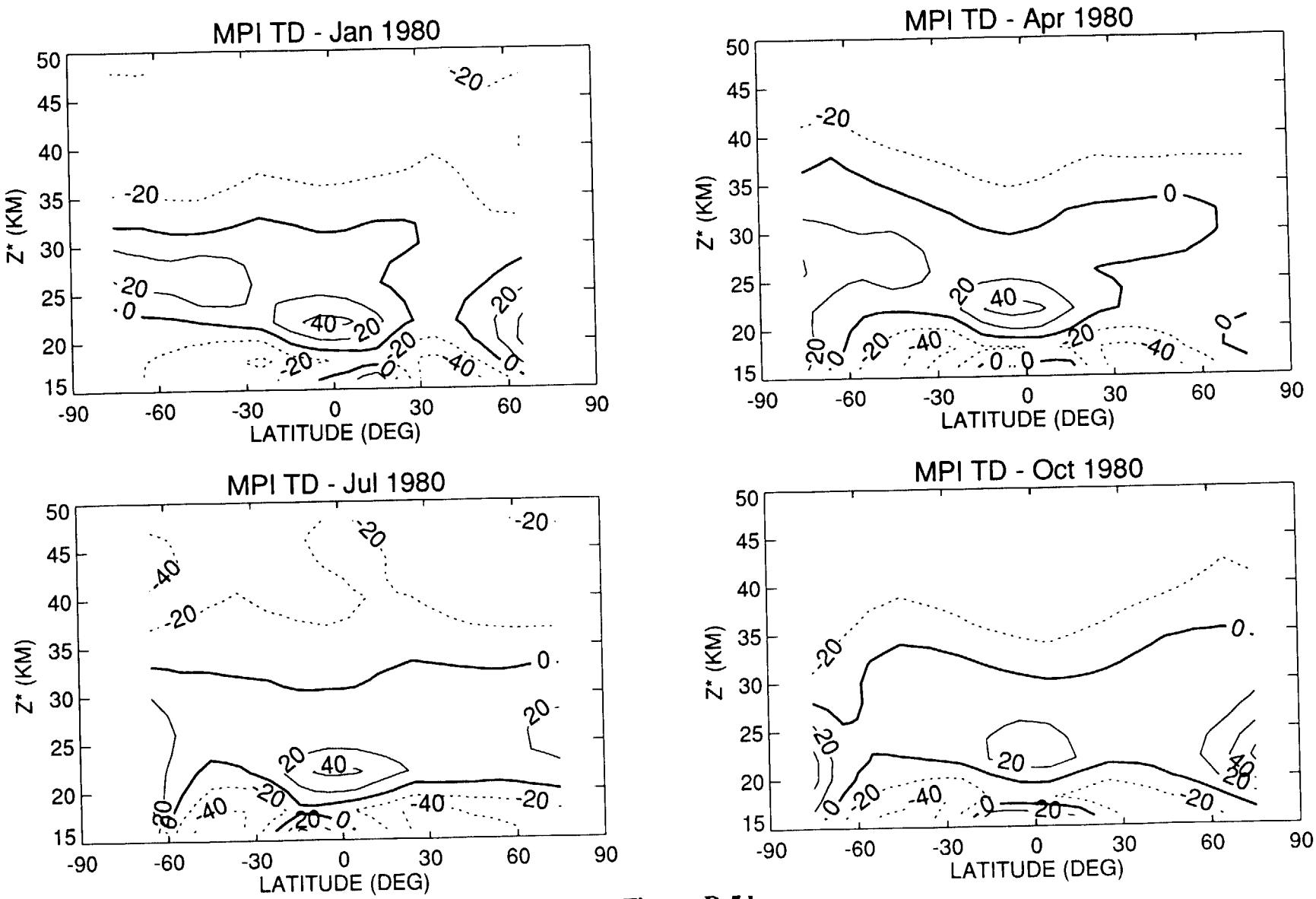

Figure D-5 h

O3 (Model - SBUV) Percent Difference

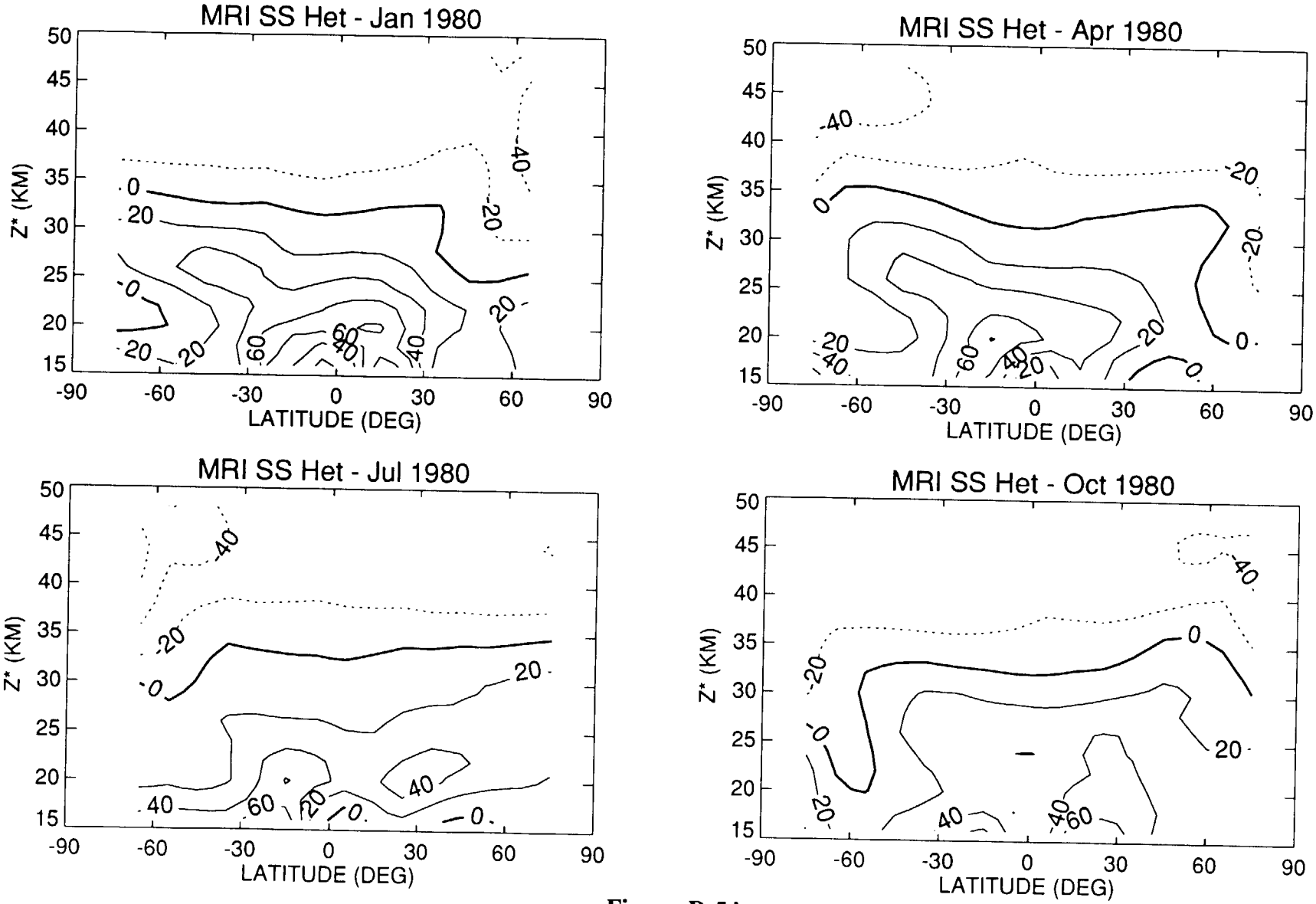

Figure D-5 i

O3 (Model - SBUV) Percent Difference

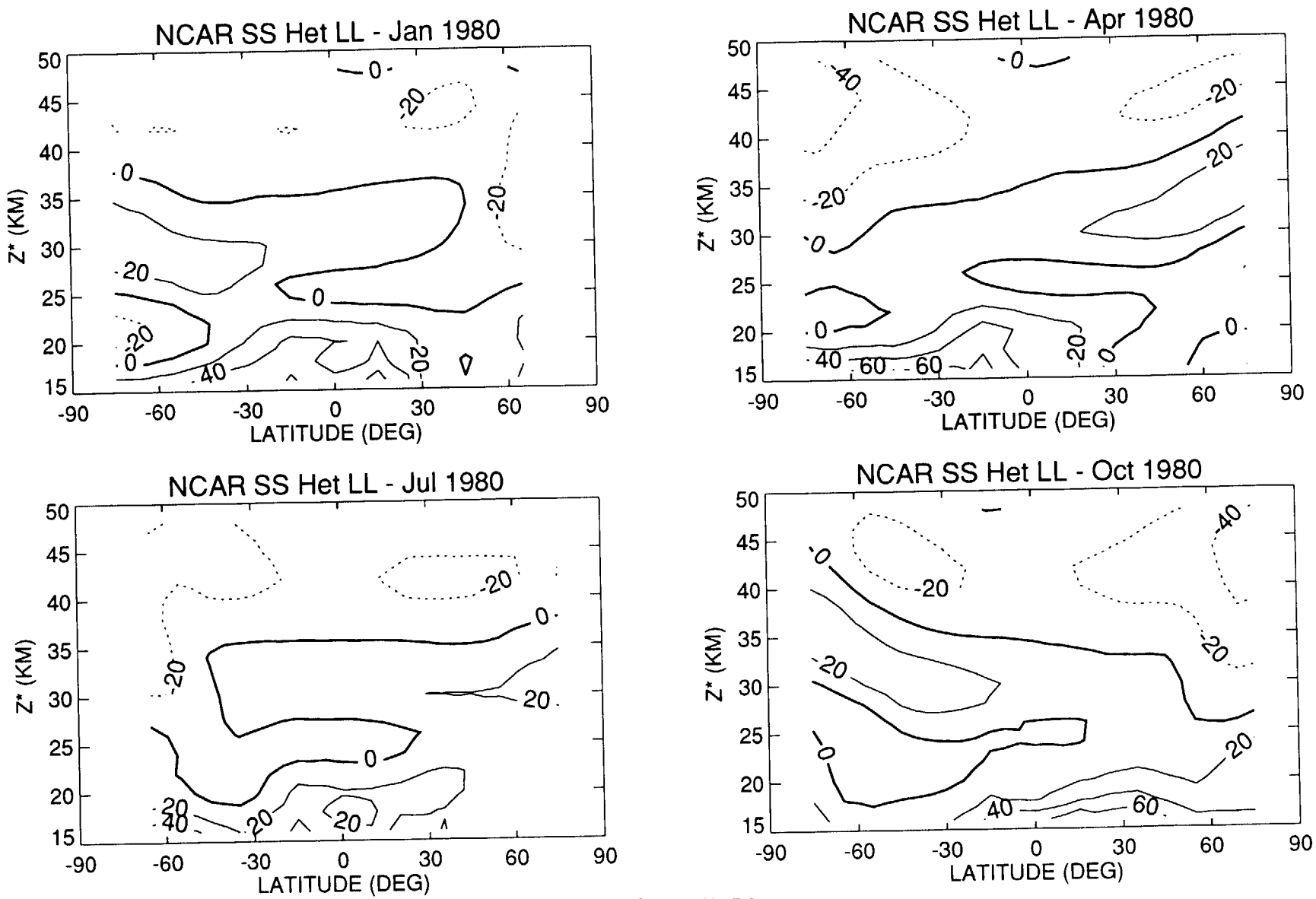

Figure D-5 j

O3 (Model - SBUV) Percent Difference

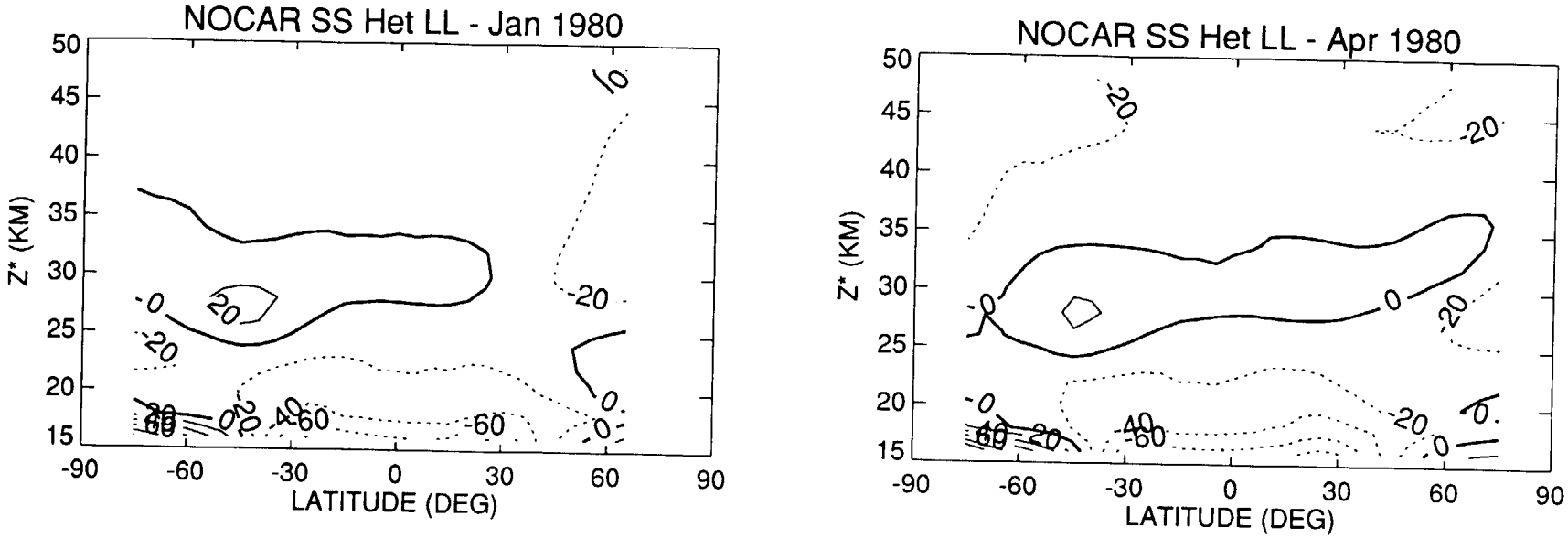

Figure D-5 k

O3 (Model - SBUV) Percent Difference

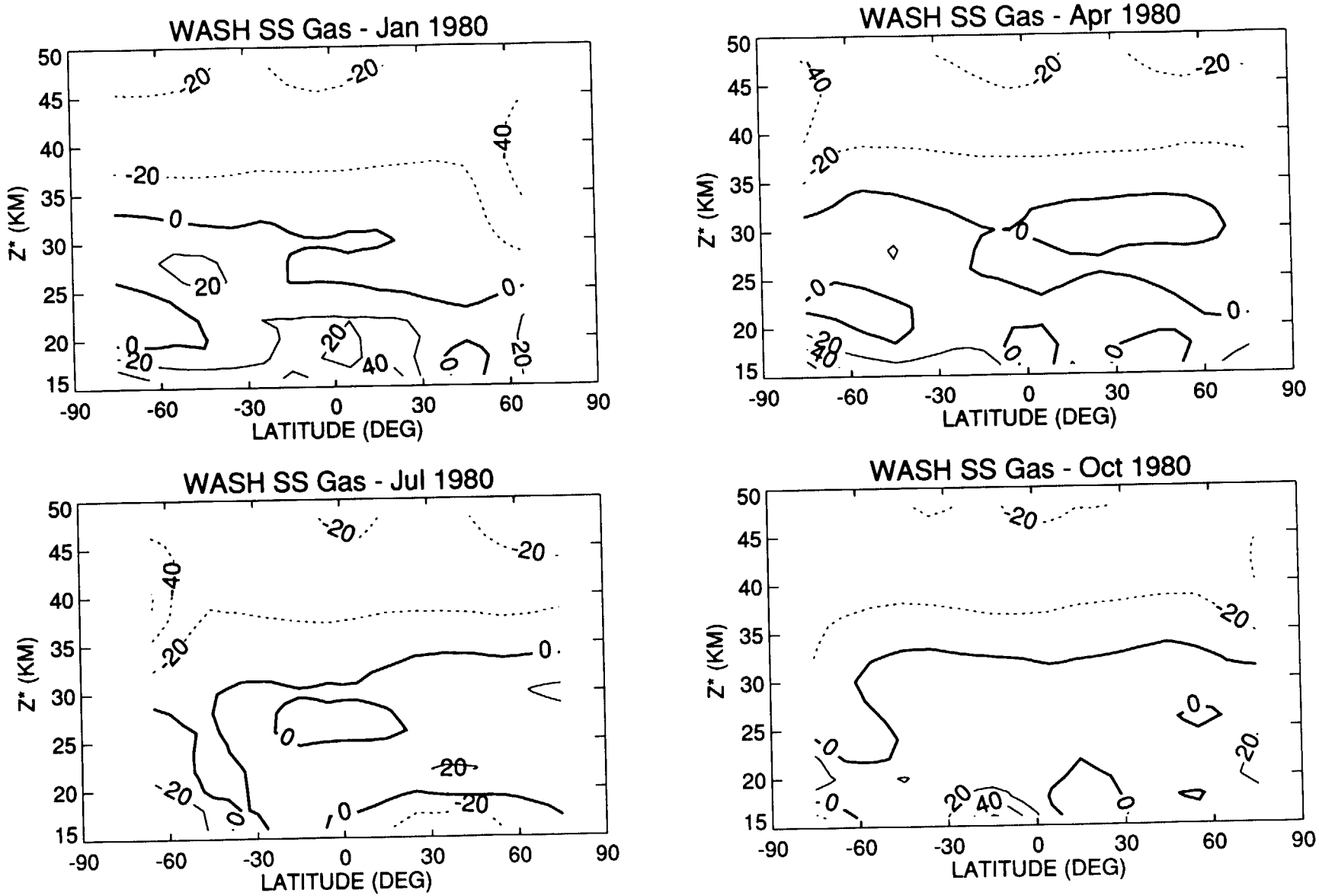

Figure D-5 1

O3 Average from 15S to 15N

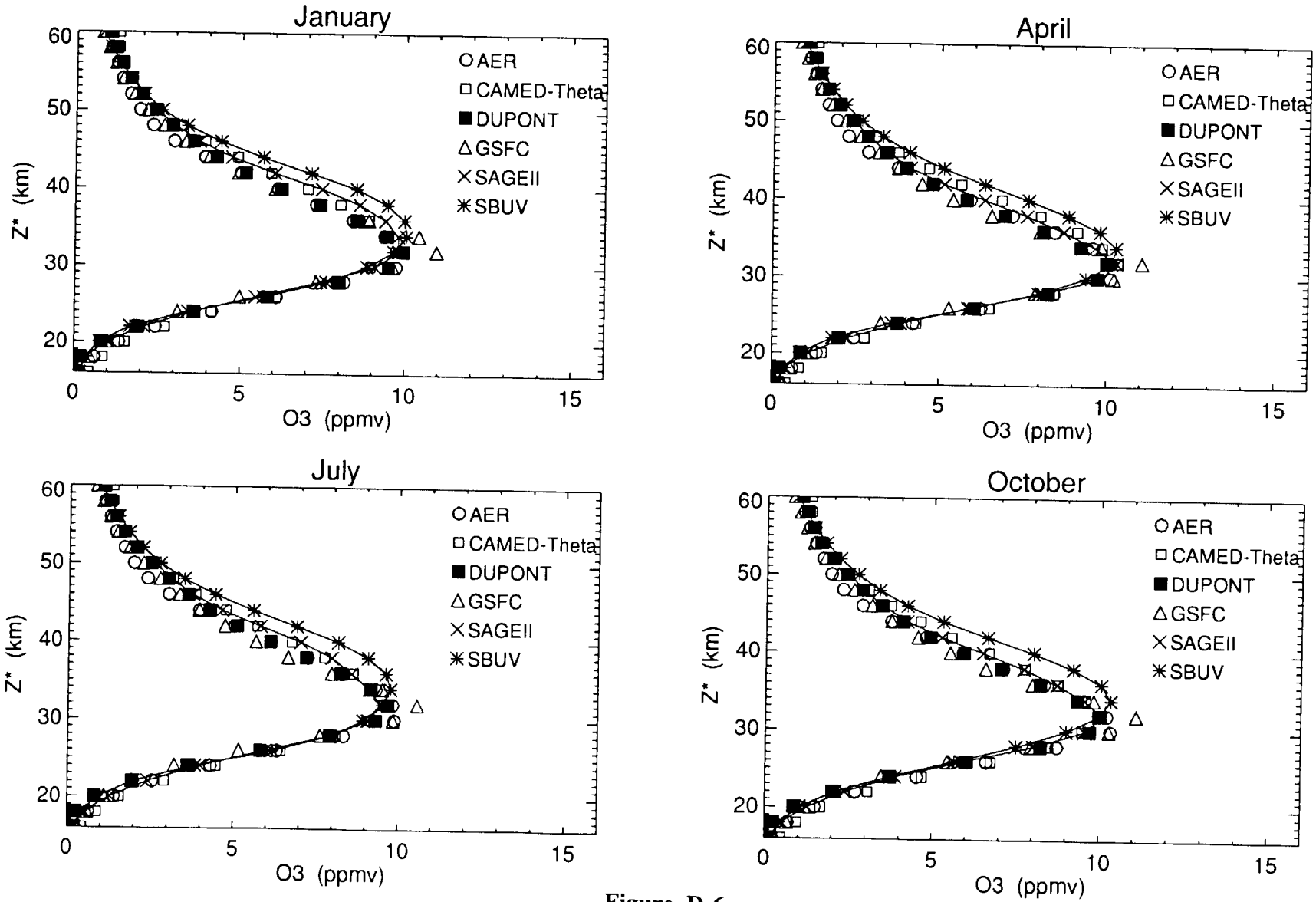

Figure D-6 a

O3 Average from 15S to 15N

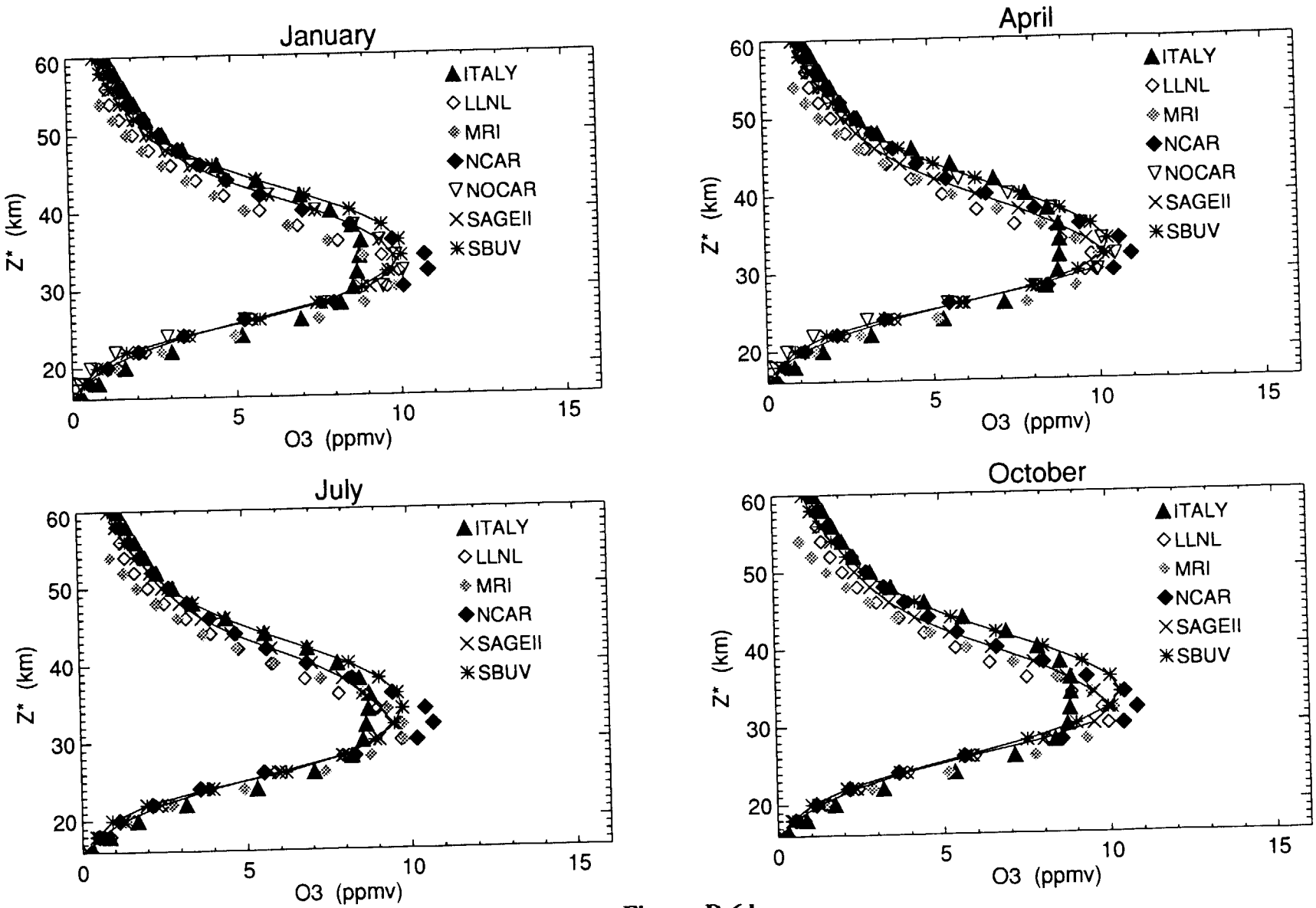

Figure D-6 b

O3 Average from 15S to 15N

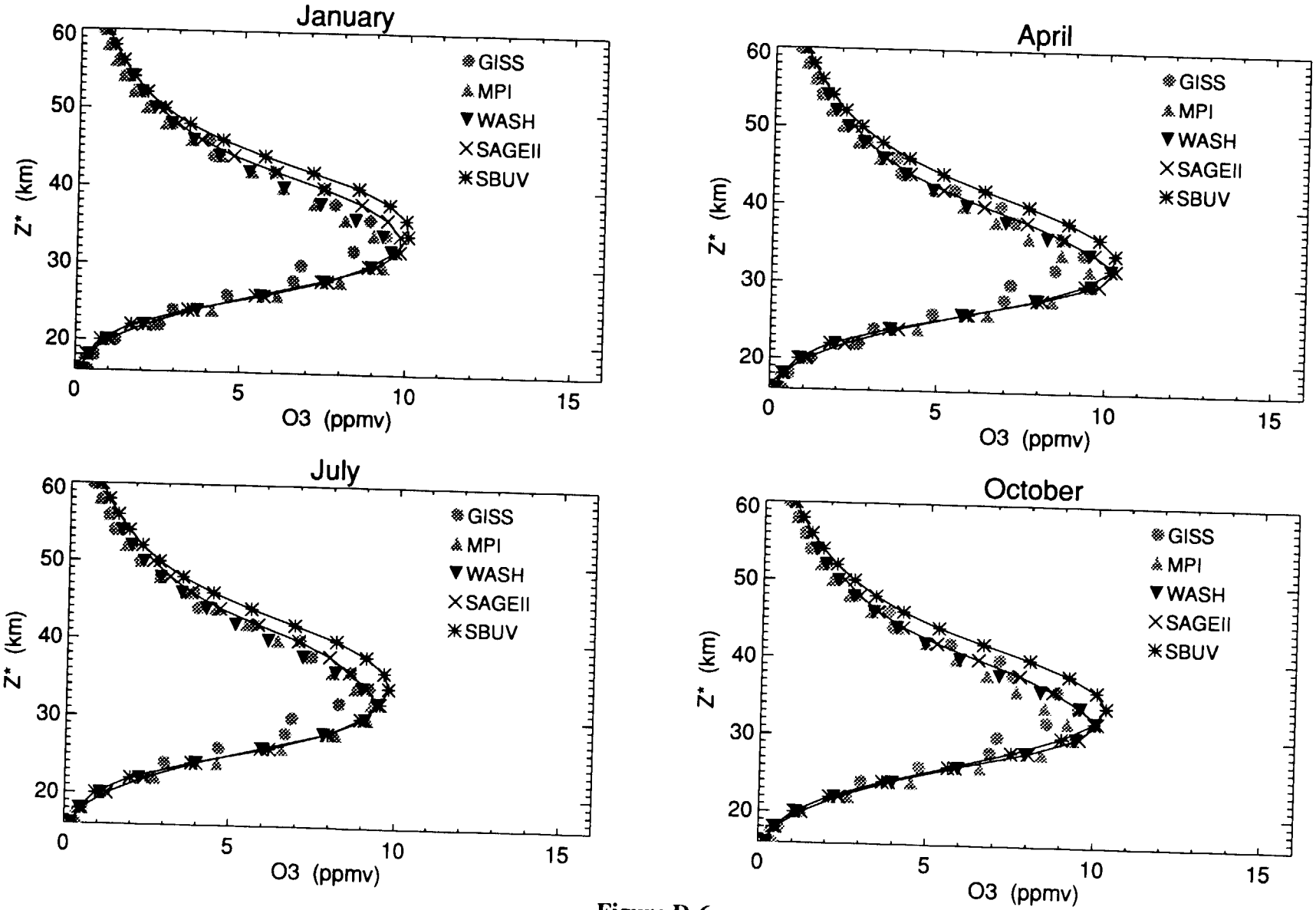

Figure D-6 c

O3 Average from 40N to 55N

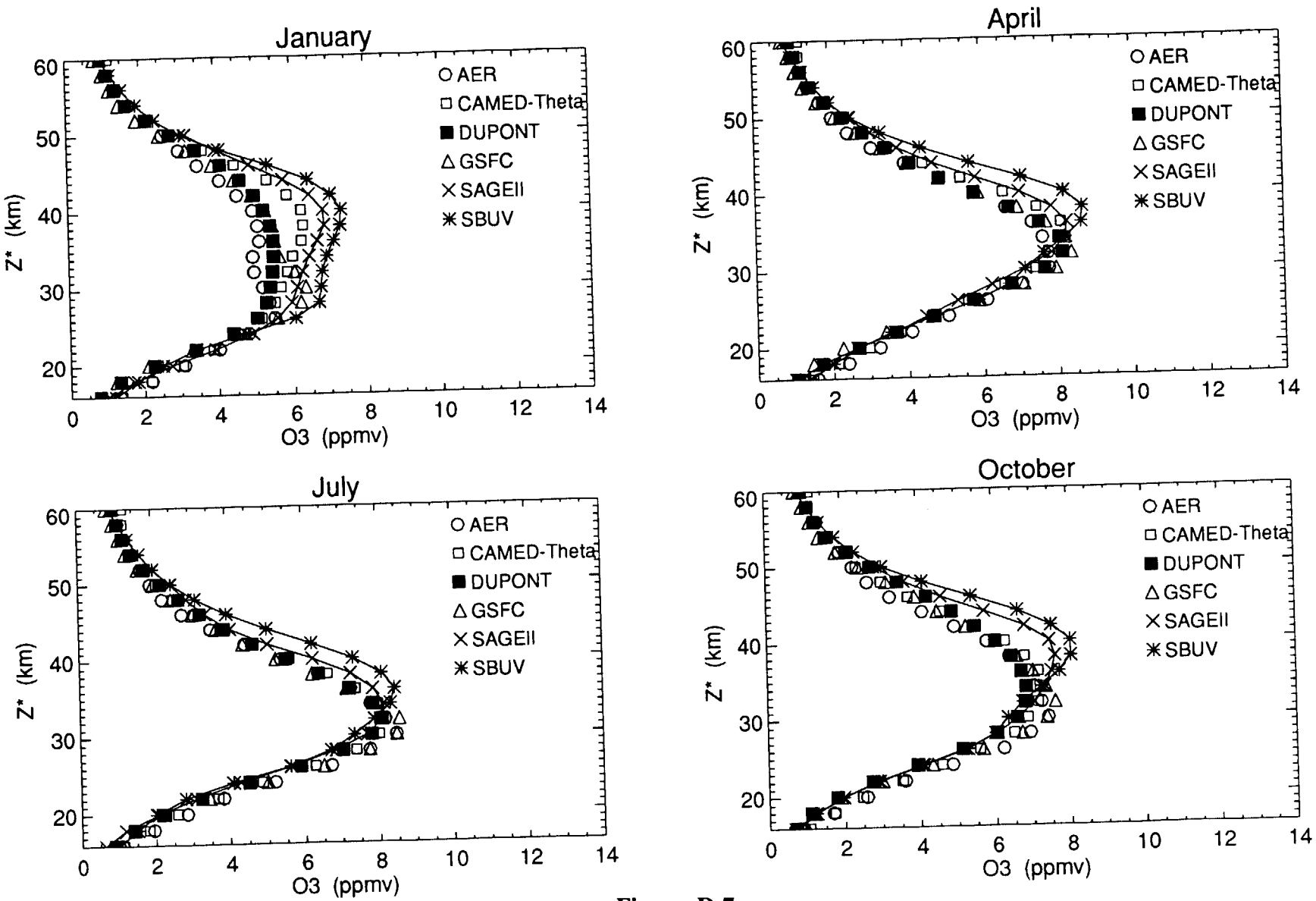

Figure D-7 a

O3 Average from 40N to 55N

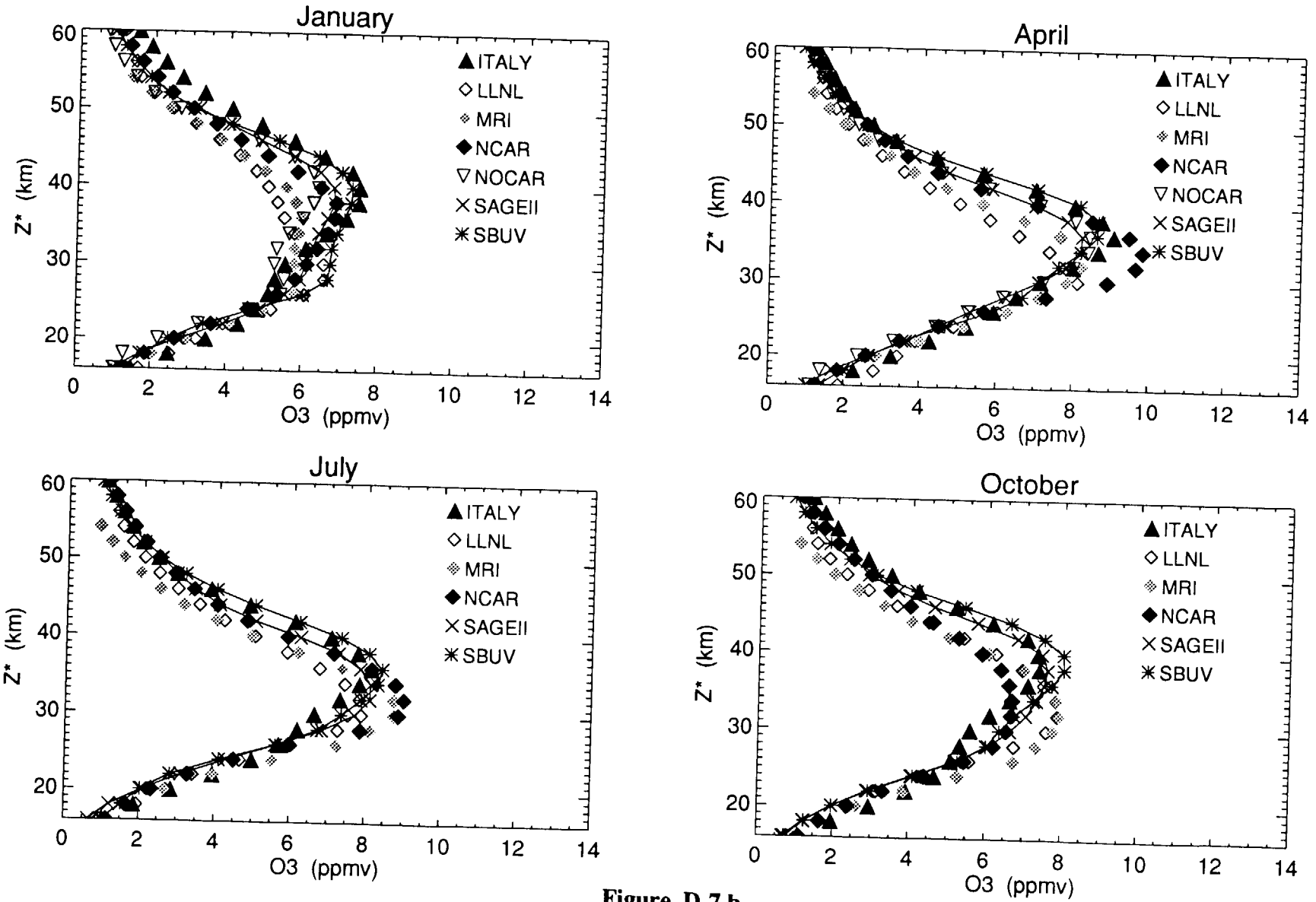

Figure D-7 b

O3 Average from 40N to 55N

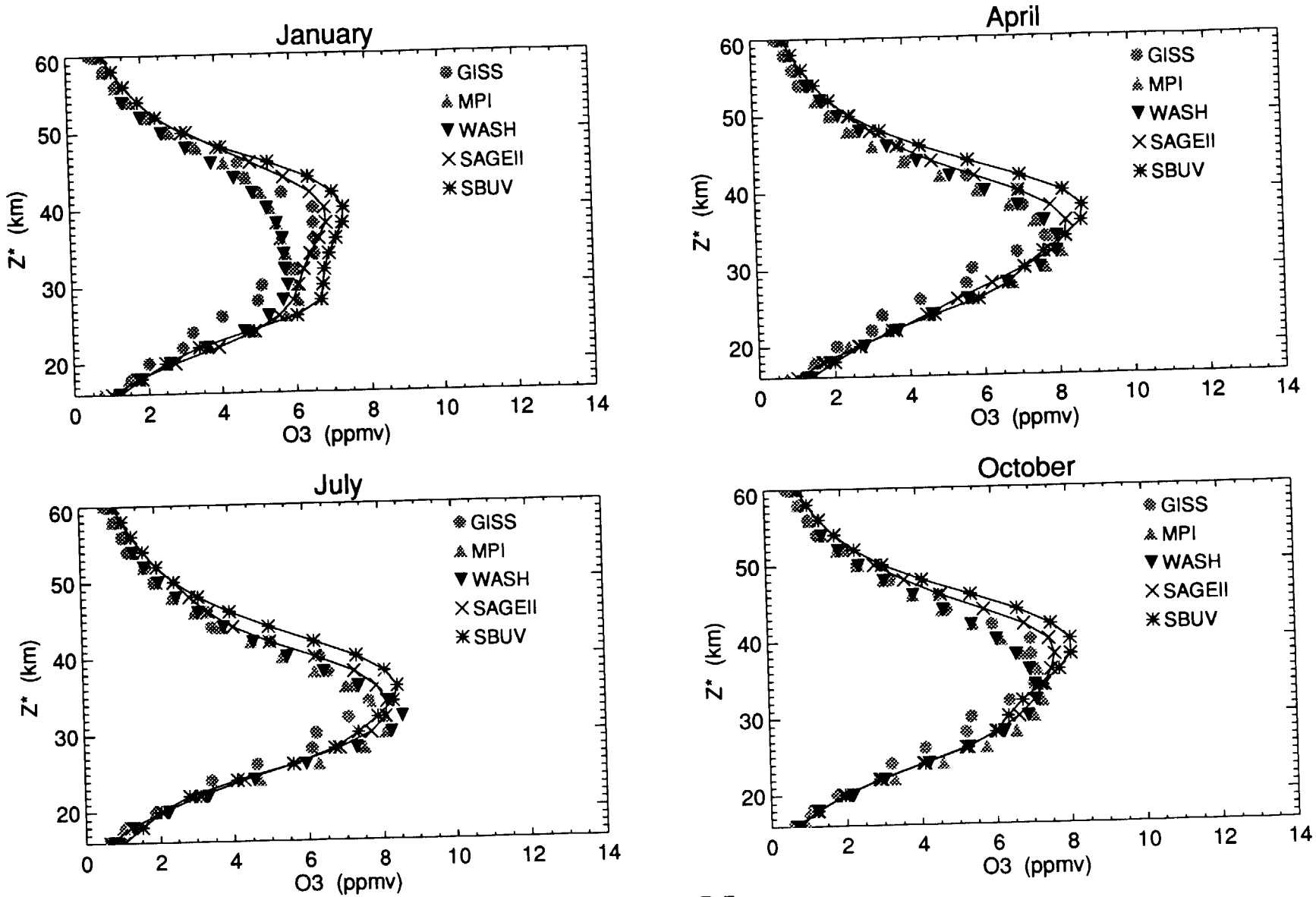

Figure D 7 c

O3 Average from 55S to 40S

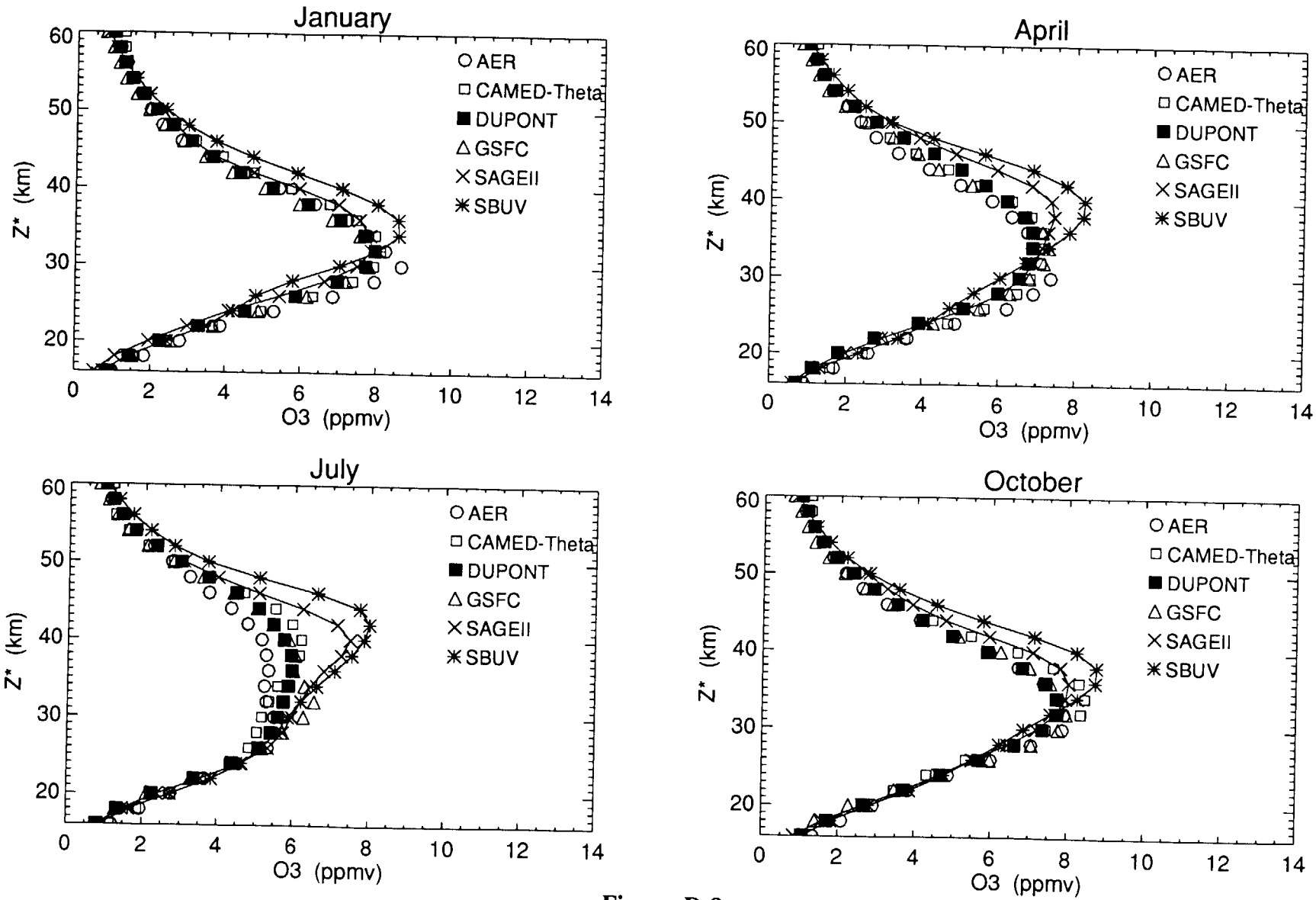

Figure D-8 a

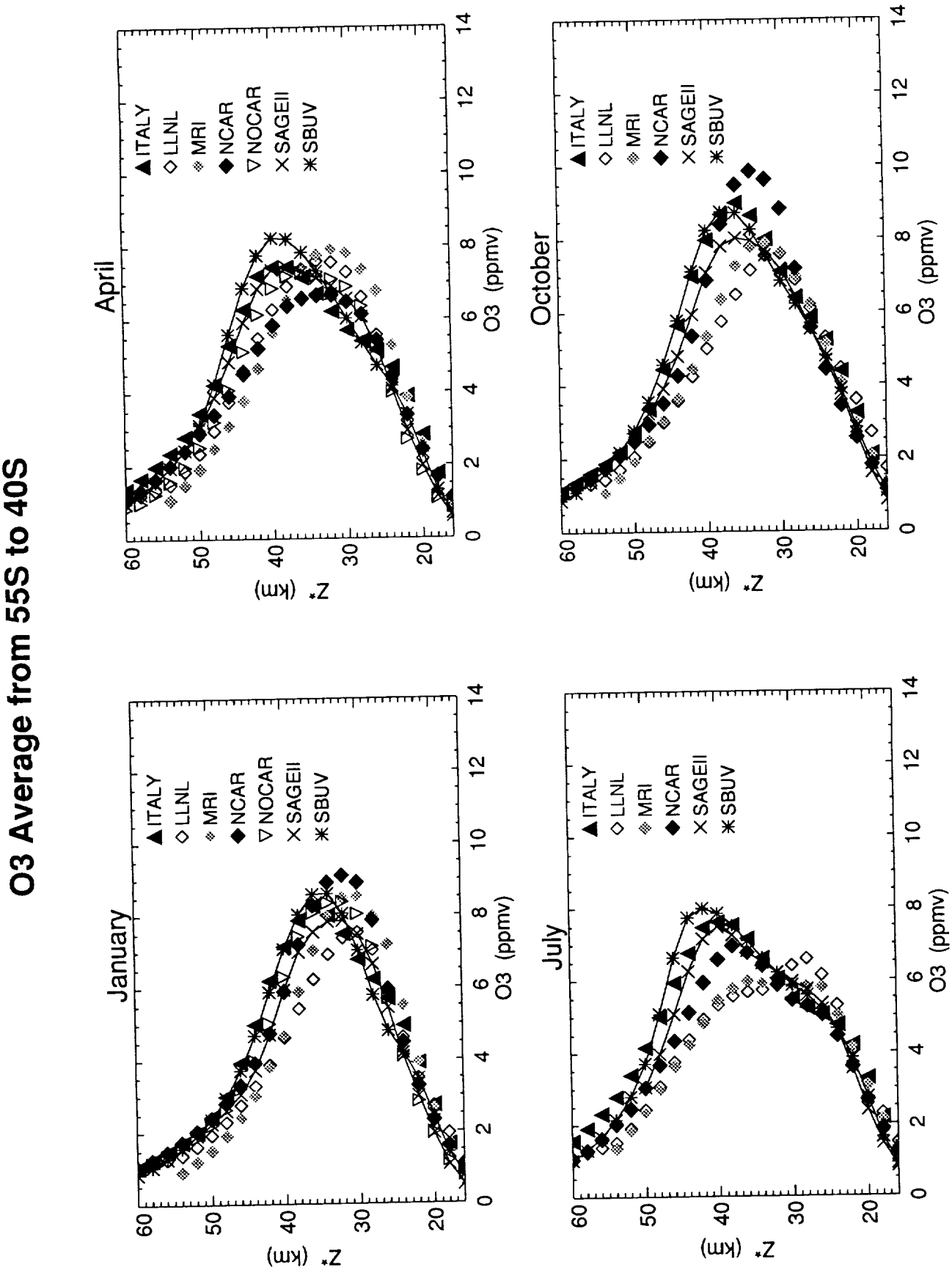
O3 Average from 55S to 40S
January
April
July
October
ITALY
LLNL
MRI
NCAR
NOCAR
SAGEII
SBUV
Z* (km)
O3 (ppmv)

Figure D-8 b

O3 Average from 55S to 40S

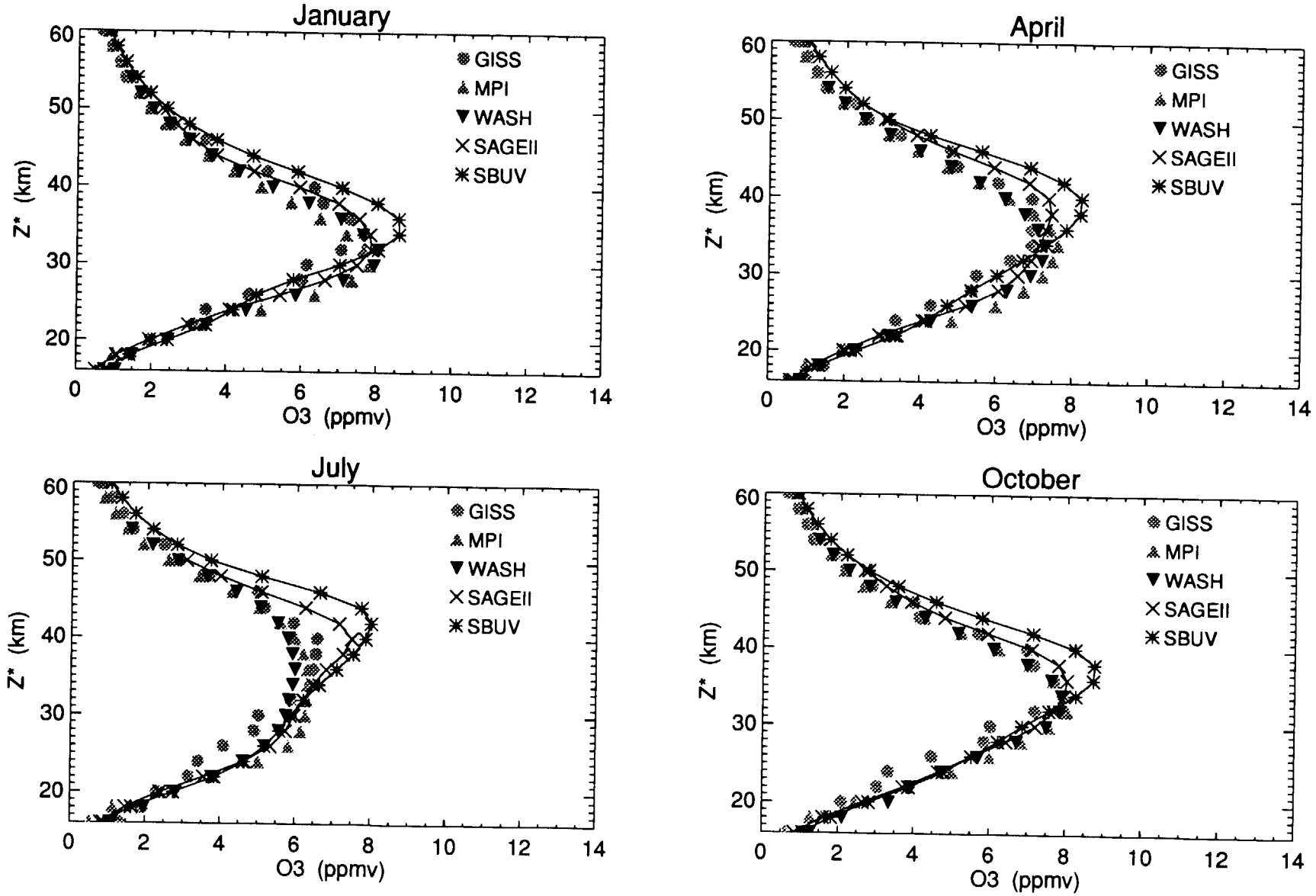

Figure D-8 c

O3 Average from 65N to 80N

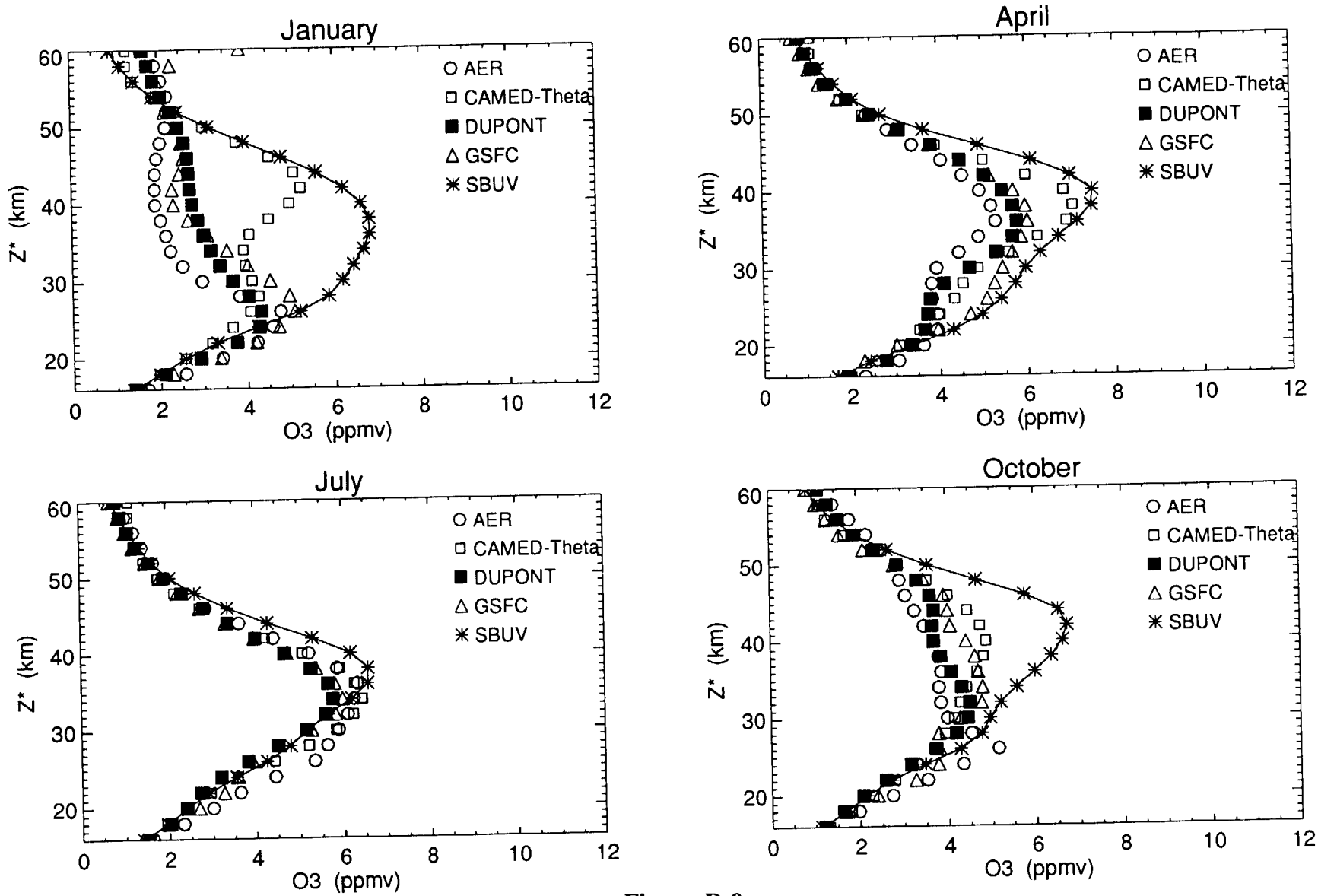

Figure D-9 a

O3 Average from 65N to 80N

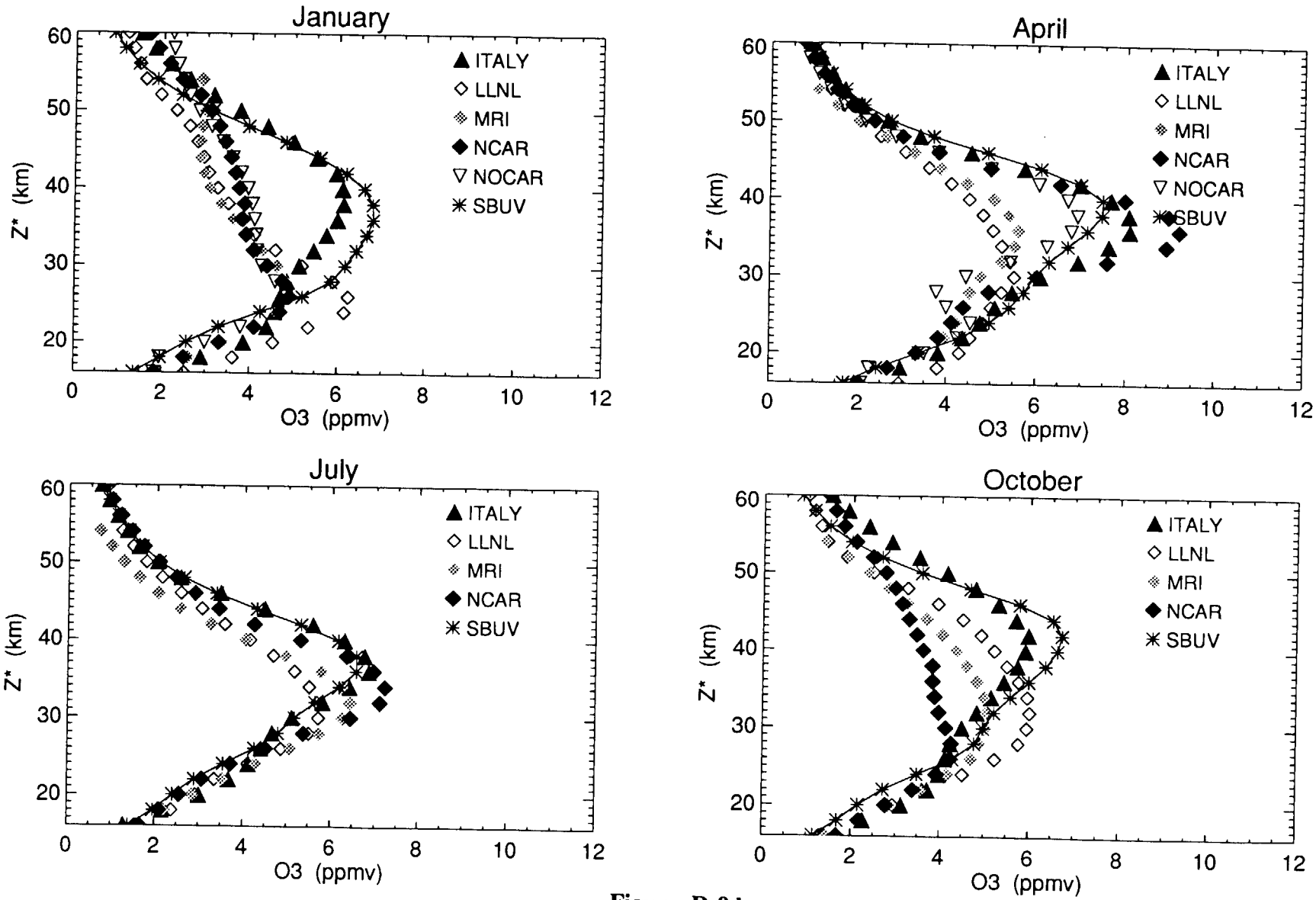

Figure D-9 b

O3 Average from 65N to 80N

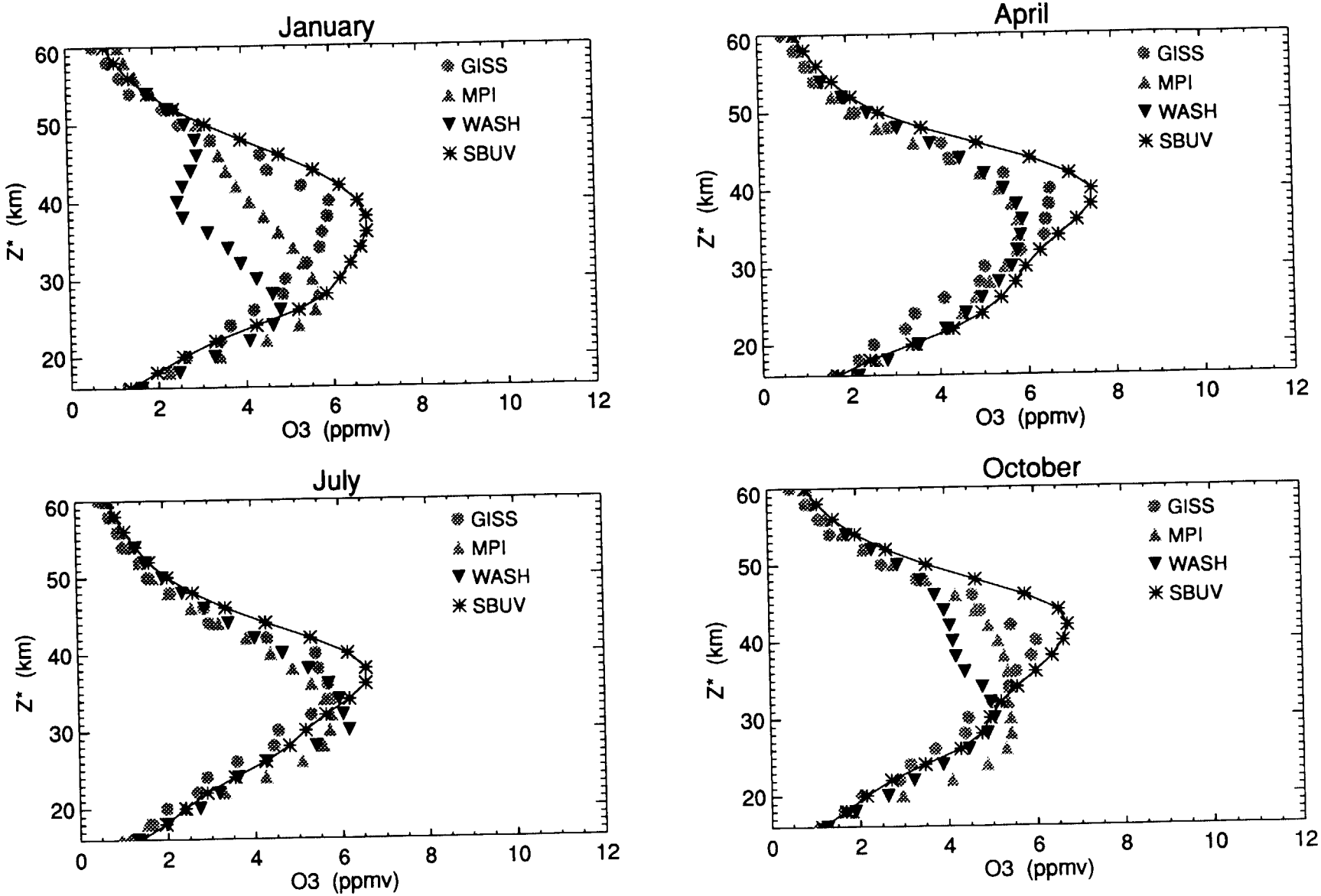

Figure D 9 c

O3 Average from 80S to 65S

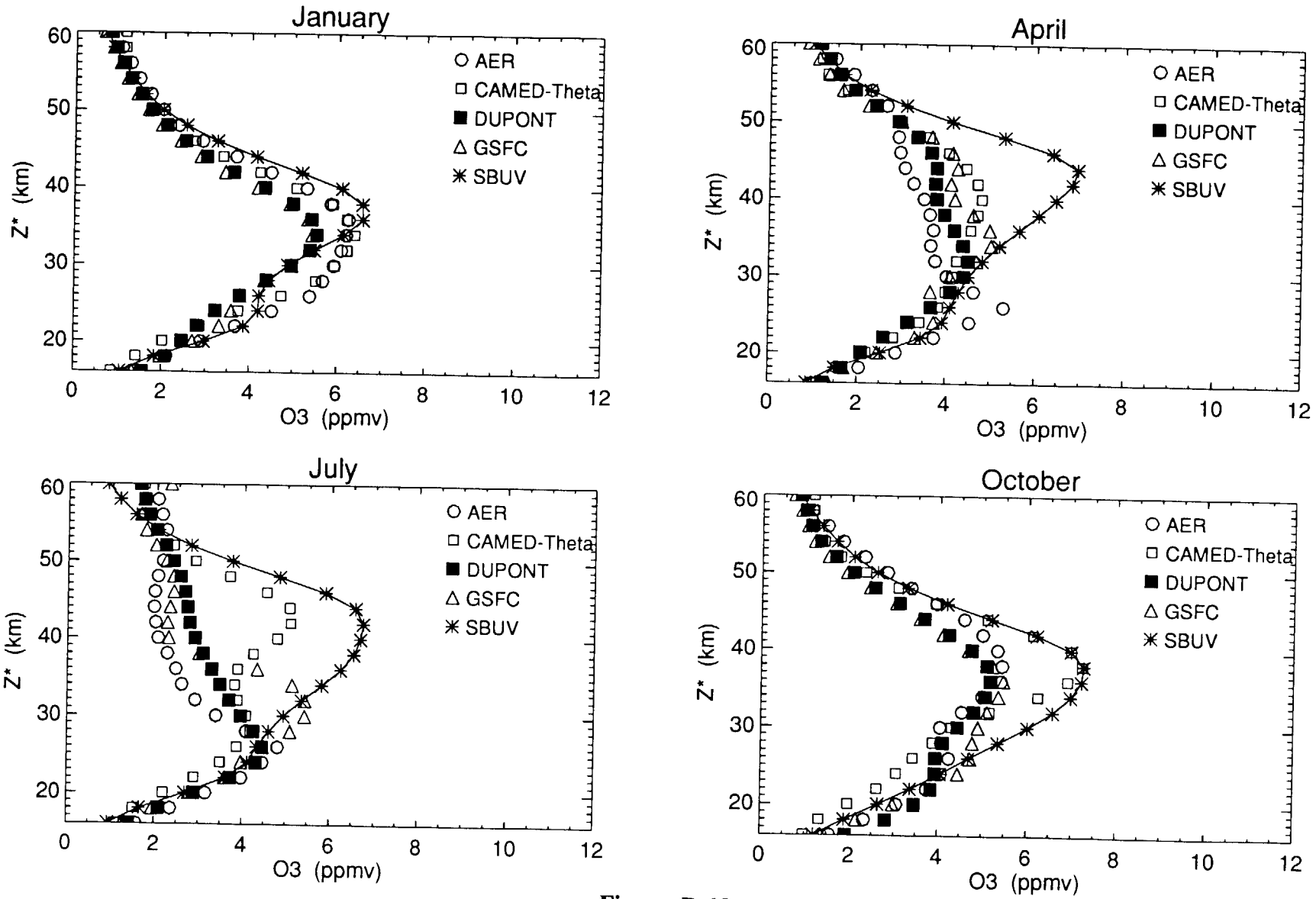

Figure D-10 a

O3 Average from 80S to 65S

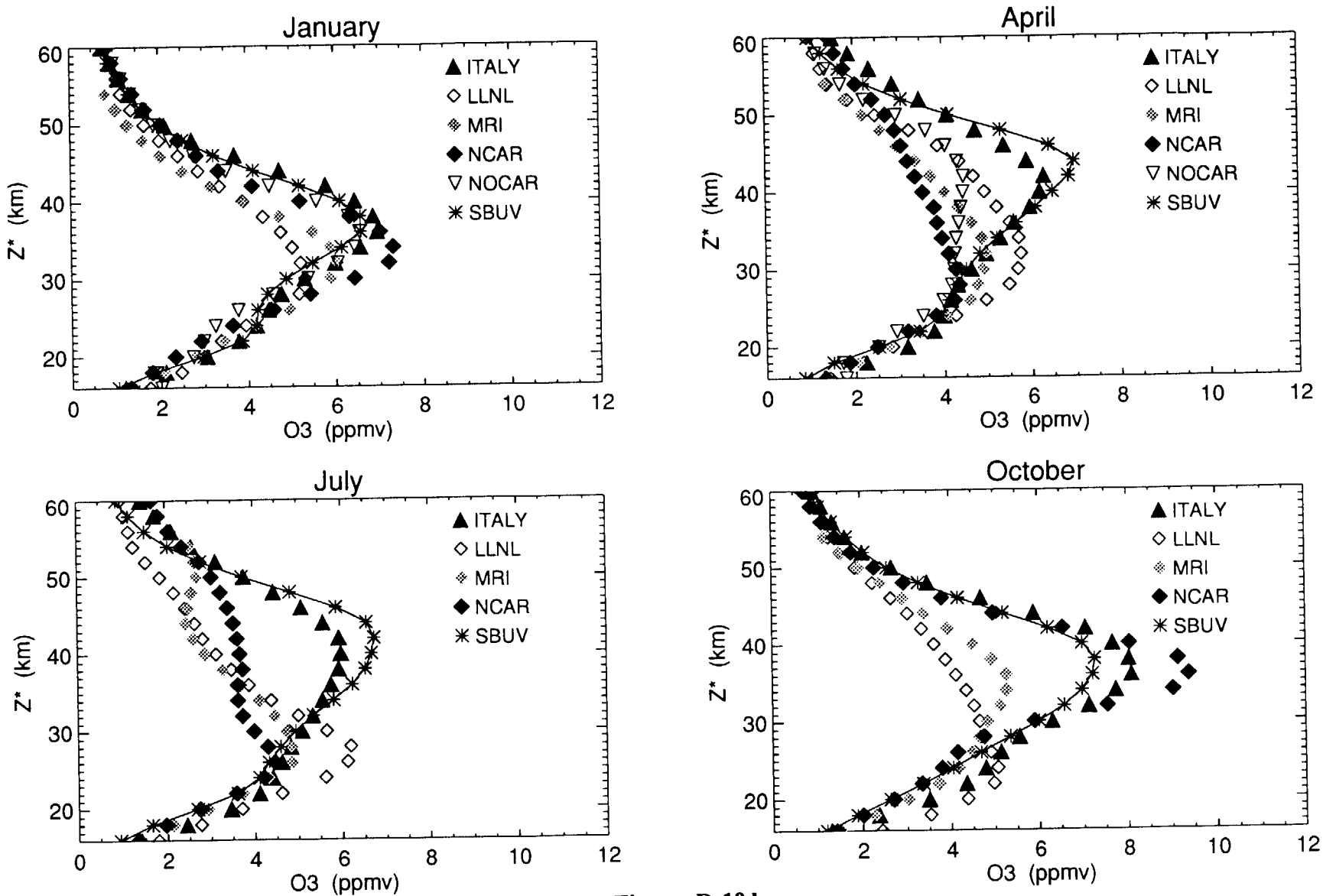

Figure D-10 b

O3 Average from 80S to 65S

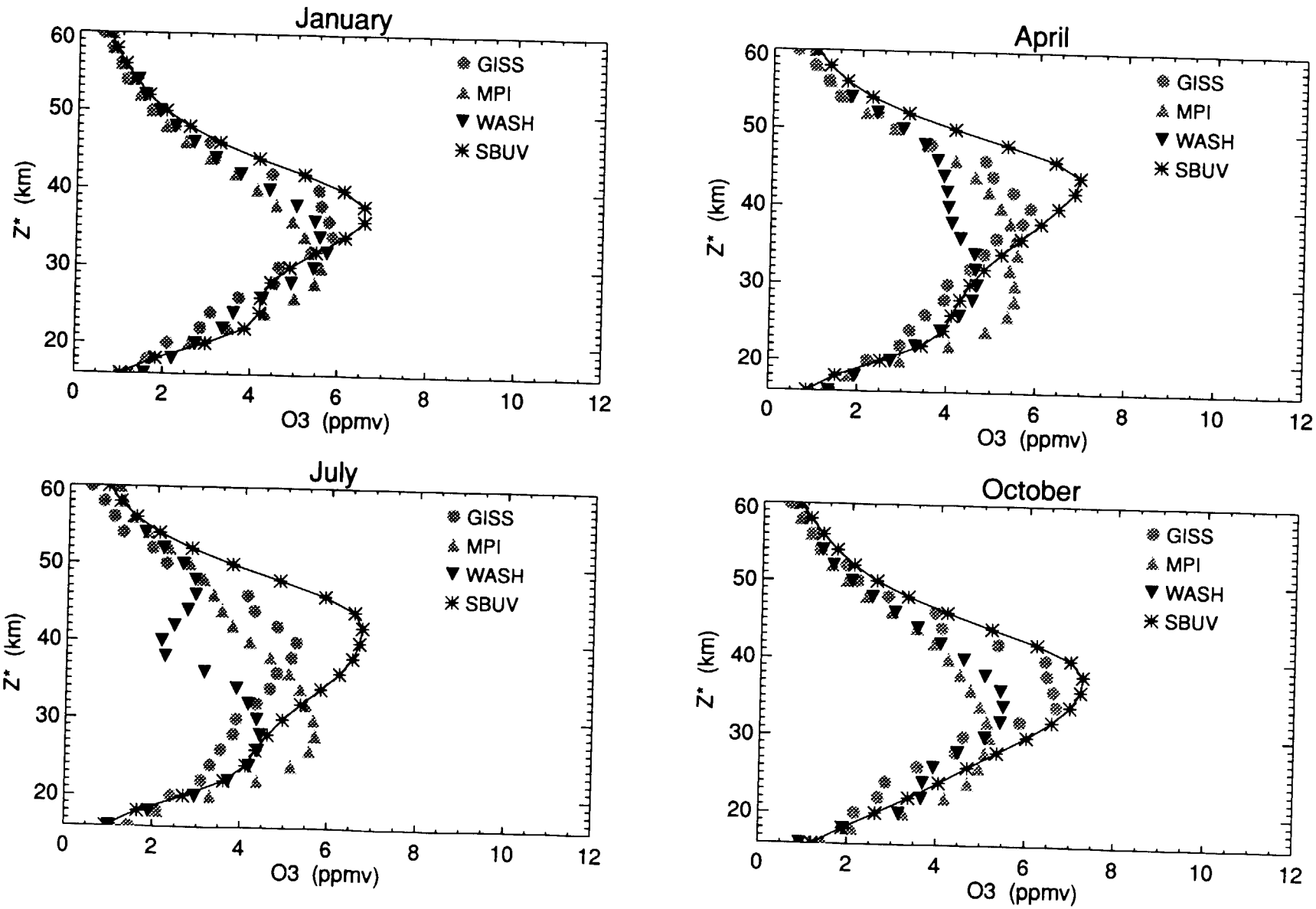

Figure D 10 c

E: Global Distributions of N_2O and CH_4

E: Large-Scale Structures in N_2O and CH_4

E. Remsberg and W. Grose
NASA-Langley Research Center

INTRODUCTION

Distributions of N_2O and CH_4 represent excellent tracers of transport for the lower stratosphere. N_2O is produced predominantly by microbial action in soil. It is destroyed in the stratosphere primarily through photolysis

$$N_2O + h\nu \rightarrow N_2 + O,$$

and provides a source of most of the stratospheric odd-nitrogen by

$$N_2O + O \rightarrow 2NO.$$

Photolytic rates tend to increase rapidly with altitude, and the N_2O lifetime decreases from about 50 years at 25 km to 2 months at 40 km (Figure 5.32 in Brasseur and Solomon, 1984).

Methane, like N_2O, is produced at the Earth's surface by a variety of processes. It has a lifetime of about 10 years at 25 km, decreasing more slowly to about 4 months at 40 km (Figure 5.12 in Brasseur and Solomon, 1984). It is destroyed primarily by reaction with OH

$$CH_4 + OH \rightarrow CH_3 + H_2O,$$

and secondarily by reaction with excited oxygen atoms

$$CH_4 + O \rightarrow CH_3 + OH$$

and

$$CH_4 + O \rightarrow CH_2O + H_2.$$

It can also react with chlorine atoms to yield

$$CH_4 + Cl \rightarrow CH_3 + HCl.$$

Chemical loss processes are significant for both CH_4 and N_2O in the stratosphere, though the rates are quite different. There is a close analogy between these species and the X1/X2 tracer simulation study in section O. Traditionally CH_4 and especially N_2O data have been used to validate both the model transport and chemistry, although comparisons with Stratospheric and Mesospheric Sounder (SAMS) data are not strictly independent tests of the circulation (WMO, 1982; 1985). More recently, isolines of N_2O have served as a useful coordinate for evaluating diabatic transport processes in the polar stratosphere (e.g., Proffitt et al., 1992; Schoeberl et al., 1989).

This section contains model comparisons with representative balloon and satellite data. Comparisons with the aircraft data from Airborne Antarctic Ozone Expedition (AAOE) and Airborne Arctic Stratospheric Expedition (AASE) are reported as part of section H. Furthermore, because N_2O is the primary source of NO_y in the stratosphere, the comparisons for N_2O will be important in evaluating differences in total odd nitrogen in models, particularly in the lower stratosphere–20 to 35 km. Differences in the N_2O distributions between models will be related to differences in model NO_y (see sections F, G, and H).

DATA SETS

During the 1970s and early 1980s, our knowledge of variations of N_2O and CH_4 was obtained from balloon-borne instruments. A number of comparisons were reported in Hudson and Reed (1979) and WMO (1982; 1985); we are using those same data sets for this Workshop. Individual balloon profiles should be more representative of a zonal average during late spring, summer, and early autumn. We have focused on model comparisons in May with the JPL measurements in Texas (32N) (Farmer et al., 1980) and the comparisons in June with measurements from the Julich (KFA) group taken in southern France (44N) (Volz et al., 1981; Schmidt et al., 1984). The in situ mixing ratios were obtained by gas chromatographic analyses of either grab samples or cryogenically cooled air samples. Their measurement accuracy is of the order 5%. The KFA profiles labeled BI9 and BI10 have been removed from our data base because of inconsistencies in the laboratory standards used to analyze them (U. Schmidt, personal communication, 1992). The infrared measurements of Farmer et al. have an accuracy of 10% to 30%. Shapes of the vertical profiles are particularly trustworthy because the concentration values are highly precise (of the order 5% or better). Of course, there can be significant differences between individual profiles if they are obtained for different seasons or if they are affected by the local transport of air from nearby latitudes.

Schmidt et al. (1991) report profiles near Kiruna, Sweden (68N) during January and February from 1987 to 1990. These profiles decrease rapidly with altitude and are considered typical of those species' distributions near the winter polar vortex.

We also considered comparisons for several Antarctic profiles during September and October of 1986 and 1987. They include results from the ground-based Mark IV Fourier transform infrared (FTIR) spectrometer (Toon et al., 1989), the airborne tunable laser absorption spectrometer (ATLAS) measurements on board the ER-2 (Loewenstein et al., 1989), and the ground-based microwave measurements by Parrish et al. (1988). All measurements were obtained in the polar vortex, which was fairly symmetric at the time. The ATLAS data are highly precise and also accurate to about 10%. The FTIR and microwave results were determined by obtaining an assumed N_2O profile that best fit the spectra measured by those instruments. Generally, the profiles obtained with the ground-based instruments are of lower vertical resolution and have somewhat lower accuracy than results from the ATLAS instrument.

The N_2O and CH_4 profiles from ATMOS at 28N and 48S during May 1985 are available from Gunson et al. (1990), and they are used in the comparisons. The uncertainty in those profiles is of the order 10%.

Most model comparisons have been conducted against the satellite distributions of N_2O and CH_4 from the Nimbus 7 SAMS experiment (Jones and Pyle, 1984), as archived at the National Space Sciences Data Center (NSSDC). The basic zonal mean profile data are reported at four pressure levels for N_2O (22.68 mb or about 26 km, 6.83 mb or about 35 km, 2.06 mb or about 43 km, and 0.62 mb or about 51.4 km) and at five pressure levels for CH_4 (the top level being 0.19 mb or about 60 km). Systematic error at 22.68 mb is about 50%, most of which is due to an estimated temperature bias of the order $\pm$ 2 K. Remsberg and Bhatt (1992) present evidence to suggest that the SAMS temperatures are too cold by 2 to 4 K at about 7 to 15 mb in April. Such a bias causes an overestimate of N_2O and CH_4 through the SAMS retrieval algorithm. Temperature biases are only of the order 1 K in the upper stratosphere, so the SAMS species results ought to be much more accurate there. Therefore, when the SAMS profile data are interpolated to z* levels between 26 and 35 km, any biases at 26 km will affect the interpolated results. This may explain a long-standing discrepancy between SAMS and balloon profiles of N_2O (Jones and Pyle, 1984).

The presence of occasional biases in the archived SAMS data below 35 km was noted in a 3-year time series (1979-1981) versus latitude plot of N_2O for z* = 30 km. Rapid changes were apparent in some regions, which did not seem entirely physical. A second version of the processed N_2O and CH_4 profiles was obtained from SAMS investigators at Oxford University (A. Dudhia, private communication, 1992), but those data also contain some clearly spurious points. Stanford and Ziemke (1991) removed these points from that version and then created a 3-year time series of the data. They also applied a low-pass filter to the time series. A comparison of their time series with that obtained from the archived SAMS data set yields very similar results for all but the 22-mb level. Therefore, we elected to use the generally available, originally archived SAMS data, but we are most confident of the more precise and accurate data at the interpolated z* levels between 35 and 51 km.

Examples of SAMS time series plots for N_2O are given in Figures E-1 and E-2 for z* = 36 and 44 km, respectively. Methane results are given in Figures E-3 and E-4. The time period of these data is 1979 through 1981. No methane data were available for September 1980. In general, there is continuity in the isoline patterns, and the effects of a semi-annual variation is apparent in the fields between ± 30 degrees latitude. There is also a direct correlation between features of the N_2O and CH_4 time series (*see also,* Stanford et al., 1992). These results are consistent with the precision estimates (of the order 5% to 20%) reported for the SAMS zonal mean cross sections by Jones and Pyle (1984).

MODEL/DATA COMPARISONS

Twelve models reported results for N_2O and eleven for CH_4 for a 1980 scenario (either steady-state gas phase–(SG) or lower-limit heterogeneous phase–(HetLL or SH)). CH_4 distributions were not reported for the GISS model.

Model comparisons with selected profiles are presented first. Figure E-5 contains N_2O results for May around 30N. The measured data are repeated in each of the four panels. The 12 models are divided such that results from three different models are shown in each panel. The balloon profile is that of Farmer et al. (1980), and it extends down to about 24 km. The Atmospheric Trace Molecule Spectroscopy (ATMOS) profile from Gunson et al. (1990) has a significant minimum near 30 km, which is believed to be due to meridional transport of lower N_2O values from higher latitudes–most likely related to the semi-annual oscillation and/or the final warming event that occurred several months earlier. SAMS N_2O for May from two years (1979, 1980) is shown. Below 35 km there is a divergence of the two SAMS profiles; part of that difference may be due to systematic biases for the retrieved SAMS data at 26 km. However, some of the difference may be real. For example, there was a significant amount of planetary wave activity for the northern hemisphere winter of 1978/79, and Solomon et al. (1986) showed that this leads to an upward acceleration of the tropical branch of the mean meridional circulation. The winter of 1979/1980 was relatively quiet by comparison. Furthermore, the quasi-biennial oscillation (QBO) was in its easterly phase during 1978/1979, and Trepte and Hitchman (1992) report a "lofting" and divergence of equatorial air for the midstratosphere in that situation. Thus, the May 1979 and 1980 N_2O profiles from SAMS may represent a typical range of observed N_2O values. The model results ought to fall within or very close to that range.

There is a large spread among the models in Figure E-5 between 15 and 35 km, where both differences in model transport and chemistry are critical. The model curves are bounded by CALJPL (strong vertical gradient) and by GSFC, LLNL, GISS, NOCAR, and NCAR (weaker vertical gradient). According to results in sections A (net circulation) and O (X1/X2 tracer study), both the GSFC and NOCAR models have the most vigorous net upward transport at low to middle latitudes (short tracer lifetimes)–in agreement with the findings here. AER, CAMED, and WASH have a weaker Brewer/Dobson circulation, and they generally fit the 1980 SAMS

data and the balloon profile. On the other hand, the CALJPL model has a relatively short lifetime for its X1/X2 tracer study, yet it has the steepest vertical N_2O gradient in Figure E-5. This discrepancy is due to a photodissociation rate for N_2O that is too large (Y. Yung, private communication, 1992).

Figure E-6 contains the CH_4 comparisons for May at 30N. First, there are some significant differences among the data. The 2 years of SAMS methane diverge below 35 km. The ATMOS data have a relative minimum near 32 km, and it is correlated with the relative minimum in N_2O in Figure E-5. Below that altitude ATMOS agrees with the Farmer et al. (1980) profile, while above 35 km it agrees with the SAMS data. Data differences at 30 to 35 km may be an indicator of the real interannual variability to be expected from this tracer. Generally, the models predict too much CH_4 at 30 km, perhaps because OH is too low. More likely it is an indication that the net upward transport in the lower stratosphere is too strong in spring. Alternatively, maybe the north/south exchange of air at midlatitudes is not correct for winter/spring. Model/data differences due to transport are in accord with the results of the carbon-14 dispersion experiment in section I. The DUPONT, LLNL, and MRI models give the more reasonable CH_4 profiles. The ITALY model at 20 km has an apparent source of CH_4, but not N_2O, in the lower stratosphere (*see* Figure E-5).

Figure E-7 contains N_2O comparisons for June at about 45N. The KFA balloon data are for 44N and the NOAA balloon data are from Laramie (41N) (Goldan et al., 1980). The corrected NOAA data are used here (Goldan et al., 1981). The KFA balloon data near 15 km are higher than the 300 ppbv prescribed for the model runs for the troposphere in 1980. As before, the NOCAR, GSFC, and GISS models have the weakest vertical gradient. The 1979 SAMS data support a gradual decrease. The balloon data and 1980 SAMS data support a more rapid N_2O decrease between 20 and 30 km. CALJPL agrees with the balloon data here. (Note that the NOAA balloon data have an "open diamond" symbol in all four panels; the LLNL model also has open diamonds but is only in panel E-7c.)

Figure E-8 shows methane results for June at 45N (c.f., Figures E-5 through E-7). AER and CAMED yield the best fit. The CALJPL profile contains too much CH_4 at the higher altitudes, perhaps because there is too little OH available. The LLNL result is too large above 50 km, most likely due to approximations at the upper boundary of their model. Generally, all of the models look good at 20 km.

Figure E-9 displays N_2O profiles for September at 45N. As in June, effects of planetary waves on the N_2O distribution should be insignificant in September, and the balloon data ought to be an excellent approximation to a zonal mean value. The 1979 SAMS data are clearly wrong at 28 km; they are of the order 315 ppbv. This means that our z* interpolations between 36 and 28 km are also questionable for September 1979, so we cannot rely on comparisons with these 1979 SAMS data. The model profiles agree with the other data between 20 and 30 km with the possible exceptions of the GISS, GSFC, and NOCAR results.

Figure E-10 shows low latitude results for N_2O for March. Balloon data are from NOAA flights from Panama in 1977 and from Brazil in 1978 and 1979 (Goldan et al., 1980). The SAMS N_2O profiles are nearly identical for 1979/1980, but again the values at 28 km are too large. Near 35 km there is better agreement between SAMS and the balloon data. Model comparisons with these data represent a stringent test of the strength of both the mean circulation between 20 and 30 km and the photolytic destruction of N_2O above that. Generally, the models are in very good agreement with the data. N_2O from CALJPL has a steep gradient between 20 and 35 km (see comments about Figure E-5). The ITALY model has its maximum N_2O level near the tropical tropopause (*see also* Figures E-6 and E-11).

Figure E-11 has methane comparisons for September at the equator. SAMS data are for 1979 and 1981, since no data were taken for September 1980. The 1979 SAMS data have a region of near constant mixing ratio between 35 and 42 km, increasing to about 1.3 ppmv at 30 km. The 1981 SAMS data decrease more smoothly with height. There is considerable variability among the model profiles. GSFC has a minimum at 45 km that is not seen in its N_2O for March in Figure E-10. This implies that their monthly circulations lead to quite different species distributions in March versus September.

Figure E-12 contains N_2O data at 68N from Schmidt et al. (1991) from several years in the late 1980s, but we are still comparing them with the model calculations for 1980. A 2.5% increase in N_2O over this decade is not significant for these comparisons. The decrease of N_2O with altitude observed from the balloons is perhaps more representative of distributions in the polar vortex rather than the zonal mean for February. The SAMS data should be more representative of zonal average values. SAMS results for 1979/80 are very similar above 35 km. The larger values for 1979 may be explained by the strong poleward mixing that winter. Meridional gradients of N_2O become pronounced in polar winter, so some of the SAMS/model differences in the midstratosphere may be due to the differing latitudes (SAMS at 65N; model at 70N). Generally, the model/data comparisons are very good from 10 to 25 km. There are some clear differences among the models at 30 km with CAMED, AER, DUPONT, and ITALY having the smallest N_2O. Many of the models have less than 10 ppbv at 35 km, while the SAMS data are near 40 ppbv. Model/data agreement at 35 km is best for CALJPL, GISS, NOCAR, WASH, and LLNL. Obviously, there are important differences in transport (both advection and mixing) among the various models for February.

Finally, the N_2O profile comparisons are completed with results near 75S in September (Figure E-13). It is clear that the observed N_2O gradient is steeper than from any of the models. Stronger diabatic descent would improve the comparisons. In this regard, the DUPONT, ITALY, LLNL, NOCAR, and CALJPL models already yield a reasonably good match to the data. Also it is possible that the measured data are more representative of the center of the polar vortex, while the models give a better estimate of the September zonal mean for 75S.

CORRELATION DIAGRAMS FROM SAMS DATA

The Nimbus-7 SAMS data contain many averaged profiles each month. Although the CH_4 and N_2O data are not obtained simultaneously (N_2O measurements are taken one day; CH_4 the next), their monthly zonal means are derived from sets of profiles of CH_4 and N_2O that are representative of atmospheric variations on that time scale. The slope of the correlation of CH_4 and N_2O for values near their tropospheric concentrations is approximately proportional to the ratio of the fluxes of each of these gases into the stratosphere, i.e., their mean stratospheric lifetime. Figures E-14 through E-16 contain correlation plots for March and December of 1979, 1980, and 1981 based on the SAMS data after vertical interpolation. The straight line is an estimate of the ratio of the lifetime of N_2O to that of CH_4, as obtained from section H in the caption of Figure H-1. (Section H has the correlation diagram for the balloon and aircraft data.) The only difference is that model CH_4 in the present section is for 1980, whereas the reference line in section H is for 1990. Therefore, the straight line fit was determined assuming that CH_4 was multiplied by 0.9 (a change of 10% per decade of time). Figure E-17 contains the results from the original SAMS data for 1981, prior to the vertical interpolation to z* intervals of 2 km.

The spread in the data in Figures E-14 to E-16 is less in 1979 than in 1980 or 1981–scatter being more pronounced at the higher mixing ratios (lower in the stratosphere). Furthermore, some data appear erroneous. There are CH_4 points that are greater than 1.6 ppmv, the tropospheric value, for December 1980/1981 and March 1981. Likewise there are N_2O points near 300 ppbv, which is its average tropospheric value at that time. We note that N_2O values

above about 150 ppbv, for example, occur below 35 km on the monthly zonal mean cross-section plots (not shown) and that points below that altitude are obtained by the interpolation between the 22.7- and 6.8-mb levels. Because systematic errors have a significant effect on the values at 22.7 mb, any quantitative correlations obtained from N_2O greater than about 150 ppbv are also less accurate. A similar comment applies to SAMS CH_4 values that are greater than about 1.1 ppmv. The strikingly different behavior of the N_2O-CH_4 correlations between 1979 and 1980 demonstrates an obvious problem with the measurements (versus a difference in "winter" transport), since a change in meridional mixing would not be able to do this.

The data are plotted for three latitude zones in Figures E-14 through E-16. Generally, the stratospheric loss frequency of a molecule of N_2O is faster than that of CH_4, and hence the slope of the correlation plots in Figures E-14–E-16 is shallow, intersecting zero-N_2O before zero-CH_4. In the upper stratosphere, the final loss of the last 0.5 ppmv of CH_4 occurs when most all of the N_2O is destroyed (*see also* model correlations in Figure E-18). A most interesting feature of the correlations is the departure from linearity. More effort is needed to fully explain this characteristic of the plots. Figure E-4 shows that the CH_4 mixing ratio does not drop below about 0.7 ppmv at low latitudes until the air parcels have ascended to 44 km. It is the tropical upper stratosphere and lower mesosphere where CH_4 undergoes a rapid chemical loss rate.

CORRELATION DIAGRAMS FROM MODELS

Figures E-18a–18k are the correlation diagrams from each model for a March 1980 simulation. The straight line is the same reference used for the SAMS correlations. The diagrams are similar between all the models. Differences are apparent in the spread (or dispersion) of points and overall shapes for each of the model diagrams. For example, the CALJPL and WASH models exhibit almost no spread, while NCAR and ITALY have the greatest spread. Points are clearly differentiated by latitude in the ITALY model. Most models display a nearly linear correlation between N_2O and CH_4 at high concentrations, becoming curved at low N_2O. Some curvature is apparent in the SAMS March 1980 correlation as well. The CALJPL model deviates most from a linear tendency.

It is noteworthy that the CALJPL correlation diagram in Figure O-6 of section O displays a curvature that is in rough agreement with the other models in that section. Since model transport should be the same for both the E and O experiments, we conclude that the chemical loss rates are different for the two experiments. A careful examination of these puzzling results revealed an error in the rate of loss of N_2O in the CALJPL model. The photodissociation coefficients were found to be too large.

Some guidance on model performance was sought by comparing model correlation diagrams with the March results from the 3 years of SAMS data. There is a degree of dispersion in the SAMS result, and there is a clear separation for the points at low versus mid and high latitudes. These characteristics are most apparent in the NCAR, ITALY, GSFC, CAMED-theta, and NOCAR models. The AER, DUPONT, MRI, and LLNL models show less spread and less differentiation with latitude, but their overall shapes are similar to that in the SAMS diagram. Of course, the observed scatter in the SAMS diagram is most certainly not geophysical, but may be a result of its random data errors; the SAMS results are not highly precise (Jones and Pyle, 1984). Finally, the WASH and CALJPL models display almost no spread or latitude differentiation. The clearest discriminator based on the SAMS data is the difference in the correlation as a function of latitude. A better understanding of this characteristic is needed before we can use it to evaluate model performance.

CONCLUSIONS

Balloon profiles of N_2O and CH_4 are accurate though there is some question about how representative they are for a zonal mean, especially in winter at middle and high latitudes. Therefore, we have focused on those profiles from spring through autumn at low and middle latitudes.

Because of year-to-year variations in planetary wave activity and in the QBO effects, model comparisons should be conducted against data taken from several years in order to be more representative. The comparisons at 45N are generally good for May, June, and September. The effective upward transport at 30N seems to be too strong at 20 to 35 km for most models. There are significant differences between the models at low latitudes, but more data are needed to discriminate among them. Model performance is generally very good at 15 to 20 km for February at 70N and September at 75S. High-latitude performance is not as good between 25 and 35 km, where isentropic mixing and diabatic descent are significant processes in model transport.

In the critical region of 15 to 25 km, our somewhat limited N_2O and CH_4 comparisons with profiles favor the MRI, LLNL, DUPONT, AER, CAMED, and WASH models for low and mid latitudes. The DUPONT, ITALY, NOCAR, CALJPL, and LLNL models gave the best overall match at high latitudes. In the upper stratosphere the comparisons between the N_2O/CH_4 correlation diagrams from SAMS and from models tend to favor the NCAR, ITALY, GSFC, CAMED, and NOCAR models. Overall though, no model is judged unsatisfactory based on the SAMS comparisons.

More profile data are needed between 15 and 35 km, where the N_2O and CH_4 mixing ratios are decreasing at clearly different rates. The aircraft campaigns provide precise, simultaneous data between 10 and 20 km for correlation diagrams and they do so over a wide range of conditions in the lower stratosphere. The SAMS results are a valuable data source above 35 km. Simultaneous and more precise profiles of CH_4 and N_2O are still needed for all these regions, and it is hoped that UARS, SPADE, and ATMOS II will provide more results in the near future.

ACKNOWLEDGMENTS

Drs. Brian Connor and Ulrich Schmidt read the draft copy of this chapter, and their comments are appreciated. Prof. John Stanford and Jerry Ziemke of Iowa State University and Dr. Clive Rodgers and Anu Dudhia of Oxford University assisted with interpretations of the quality of the SAMS data sets.

REFERENCES

Brasseur, G., and S. Solomon, *Aeronomy of the Middle Atmosphere*, D. Reidel Publ. Co., 441 pp., 1984.

Farmer, C. B., O. F. Raper, B. D. Robbins, R. A. Toth, C. Muller, Simultaneous spectroscopic measurements of stratospheric species: O_3, CH_4, CO, CO_2, N_2O, H_2O, HCl, and HF at northern and southern mid-latitudes, *J. Geophys. Res.*, *85*, 1621-1632, 1980.

Goldan, P. D., W. C. Kuster, D. L. Albritton, and A. L. Schmeltekopf, Stratospheric $CFCl_3$, CF_2Cl_2, and N_2O height profile measurements at several latitudes, *J. Geophys. Res.*, *85*, 413-423, 1980.

Goldan, P. D., W. C. Kuster, A. L. Schmeltekopf, F. C. Fehsenfeld, and D. L. Albritton, Correction of atmospheric N_2O mixing-ratio data, *J. Geophys. Res.*, *86*, 5385-5386, 1981.

Gunson, M. R., C. B. Farmer, R. H. Norton, R. Zander, C. P. Rinsland, J. H. Shaw, and B.-C. Gao, Measurements of CH_4, N_2O, CO, H_2O, and O_3 in the middle atmosphere by the atmospheric trace molecule spectroscopy experiment on Spacelab 3, *J. Geophys. Res.*, *95*, 13867-13882, 1990.

Hudson, R. D., and E. I. Reed, eds., *The Stratosphere: Present and Future, NASA Reference Publication 1049*, NTIS, Washington, D.C., 432 pp., 1979.

Jones, R. L., and J. A. Pyle, Observations of CH_4 and N_2O by the Nimbus 7 SAMS: A comparison with in situ data and two-dimensional numerical model calculations, *J. Geophys. Res.*,. *89*, 5263-5279, 1984.

Loewenstein, M., J. R. Podolske, K. R. Chan, and S. E. Strahan, Nitrous oxide as a dynamical tracer in the 1987 airborne Antarctic ozone experiment, *J. Geophys. Res.*, *94*, 11589-11598, 1989.

Parrish, A., R. L. deZafra, M. Jaramillo, B. Connor, P. M. Solomon, and J. W. Barrett, Extremely low N_2O concentrations in the springtime stratosphere at McMurdo Station, Antarctica, *Nature*, *332*, 53-55, 1988.

Proffitt, M. H., S. Solomon, and M. Loewenstein, Comparison of 2-D model simulations of ozone and nitrous oxide at high latitudes with stratospheric measurements, *J. Geophys. Res.*, *97*, 939-944, 1992.

Remsberg, E. E., and P. P. Bhatt, The accuracy of temperature distributions used to derive the net transport for a zonally averaged model, accepted for *Proceedings of the International Ozone Symposium*, Charlottesville, VA, 1992.

Schmidt, U., R. Bauer, A. Khedim, E. Klein, G. Kulessa, and C. Schiller, Profile observations of long-lived trace gases in the Arctic vortex, *Geophys. Res. Letts.*, *18*, 767-770, 1991.

Schmidt, U., A. Khedim, D. Knapska, G. Kulessa, and F. J. Johnen, Stratospheric trace gas distributions observed in different seasons, *Adv. Space Res.*, *4*, 131-134, 1984.

Schoeberl, M. R., L. R. Lait, P. A. Newman, R. L. Martin, M. H. Proffitt, D. L. Hartmann, M. Loewenstein, J. Podolske, S. E. Strahan, J. Anderson, K. R. Chan, and B. Gary, Reconstruction of the constituent distribution and trends in the Antarctic polar vortex from ER-2 flight observations, *J. Geophys. Res.*, *94*, 16815-16846, 1989.

Solomon, S., J. T. Kiehl, R. R. Garcia, and W. Grose, Tracer transport by the diabatic circulation deduced from satellite observations, *J. Atmos. Sci.*, *43*, 1603-1617, 1986.

Stanford, J. L., J. R. Ziemke, and S. Y. Gao, Stratospheric circulation features deduced from SAMS constituent data, *J. Atmos. Sci.*, in press, 1992.

Stanford, J. L., and J. R. Ziemke, CH4 and N_2O photochemical lifetimes in the upper stratosphere: In situ estimates using SAMS data, *Geophys. Res. Letts.*, *18*, 677-680, 1991.

Toon, G. C., C. B. Farmer, P. W. Schaper, J.-F. Blavier, and L. L. Lowes, Ground-based infrared measurements of tropospheric source gases over Antarctica during the 1986 Austral spring, *J. Geophys. Res.*, *94*, 11613- 11624, 1989.

Trepte, C. R., and M. H. Hitchman, Tropical stratospheric circulation deduced from satellite aerosol data, *Nature*, *355*, 626-628, 1992.

Volz, A., U. Schmidt, J. Rudolph, D. H. Ehhalt, F. J. Johnen, and A. Khedim, Vertical profiles of trace gases at mid latitudes, Jul-Report 1742, Kernforschungsanlage Julich GmbH, D-5170 Julich, FRG, 1981.

World Meteorological Organization (WMO), *Atmospheric Ozone 1985, Vol. II, Report No. 16*, WMO, Geneva, 1985.

World Meteorological Organization (WMO), *The Stratosphere 1981: Theory and Measurements*, *Report No. 11*, R. Hudson, ed., WMO, Geneva, 1982.

FIGURE CAPTIONS

Figure E-1. Time series plot (1979-1981) of Nimbus-7 SAMS N_2O at z* = 36 km.

Figure E-2. As in Figure E-1, but at z* = 44 km.

Figure E-3. As in Figure E-1, but for SAMS CH_4.

Figure E-4. As in Figure E-3, but at z* = 44 km.

Figure E-5. N_2O profile comparisons at 30N for May. Models are (a) AER, CALJPL, CAMED; (b) DUPONT, GISS, GSFC; (c) ITALY, LLNL, MRI; and (d) NCAR, NOCAR, WASH.

Figure E-6. As in Figure E-5, but for CH_4.

Figure E-7. As in Figure E-5, but at 45N for June.

Figure E-8. As in Figure E-7, but for CH_4.

Figure E-9. As in Figure E-5, but at 45N for September.

Figure E-10. As in Figure E-5, but at equator for March.

Figure E-11. As in Figure E-10, but for CH_4 for September.

Figure E-12. As in Figure E-5, but at 70N for February.

Figure E-13. As in Figure E-5, but at 75S for September.

Figure E-14. Correlation diagrams of SAMS CH_4 versus N_2O for December and March 1979 for three latitude zones.

Figure E-15. As in Figure E-14, but for 1980.

Figure E-16. As in Figure E-14, but for 1981.

Figure E-17. As in Figure E-16, but derived from SAMS data prior to vertical interpolation.

Figure E-18. CH_4/N_2O correlation diagrams for March from the 1980 SG simulation from each model: a) AER, b) CALJPL, c) CAMED-theta, d) DUPONT, e) GSFC, f) ITALY, g) LLNL, h) MRI, i) NCAR, j) NOCAR, and K) WASH.

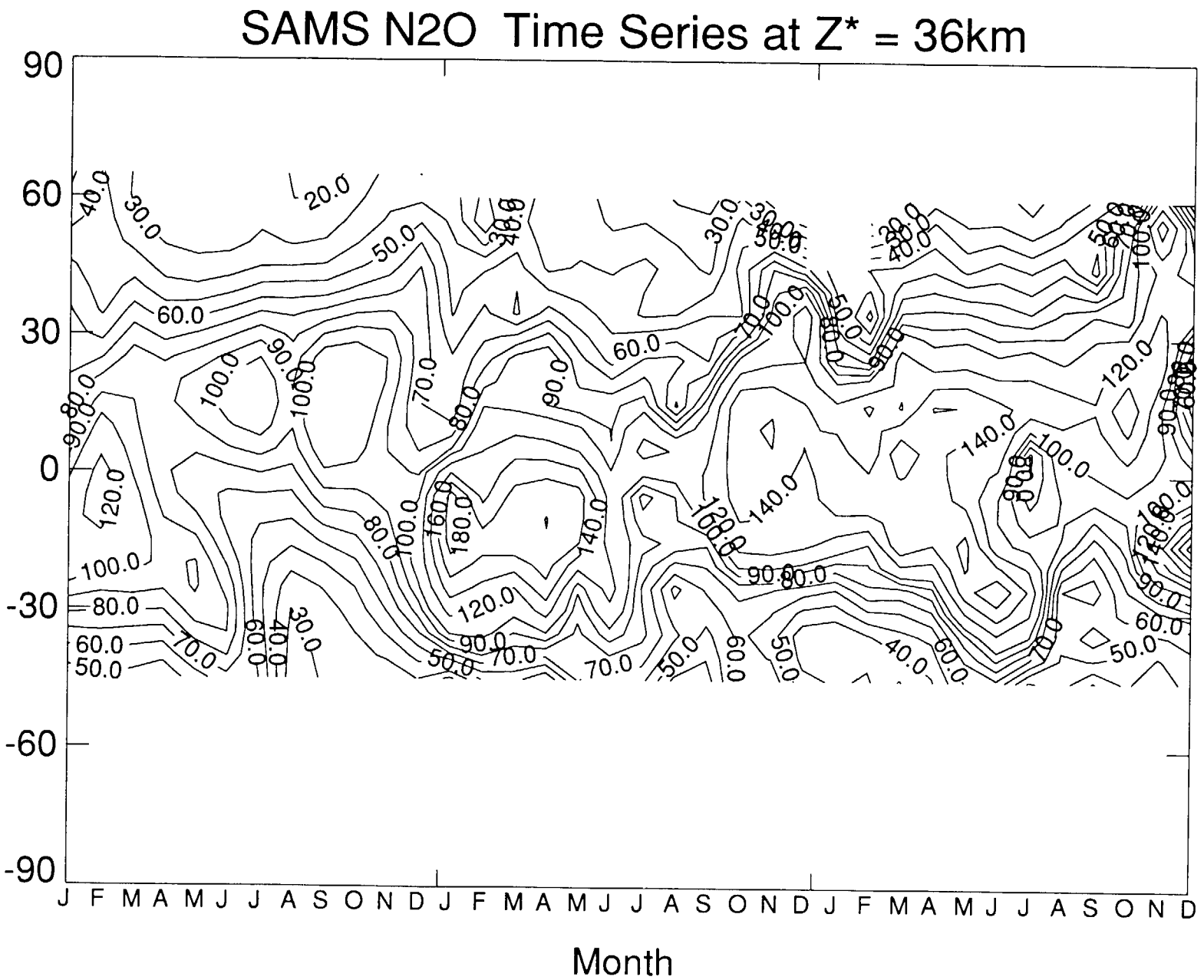
SAMS N2O Time Series at Z* = 36km
Latitude
90
60
30
0
-30
-60
-90
J F M A M J J A S O N D J F M A M J J A S O N D J F M A M J J A S O N D
Month

Figure E-1

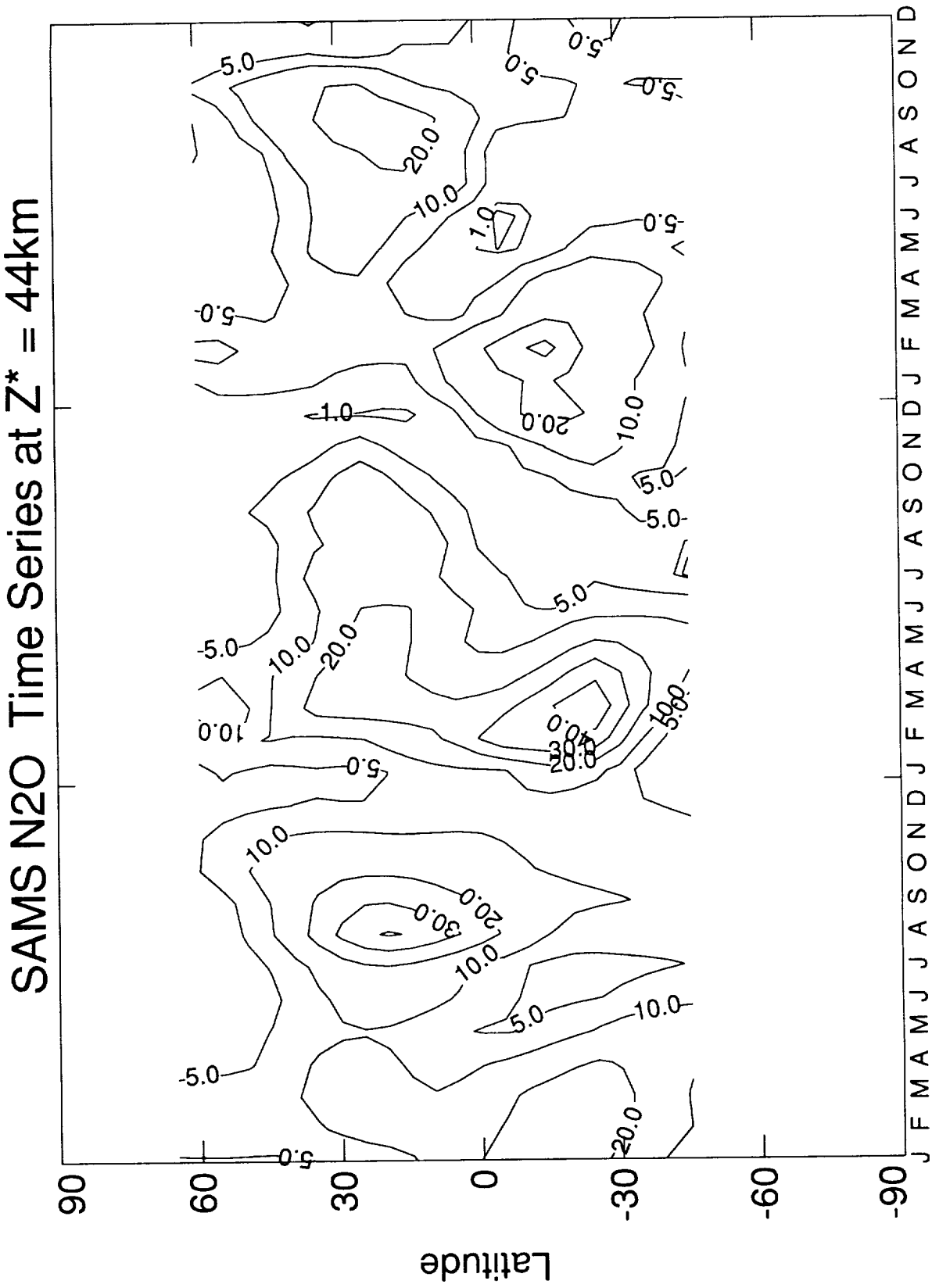
SAMS N2O Time Series at Z* = 44km
Latitude
90
60
30
0
-30
-60
-90
Month
J F M A M J J A S O N D J F M A M J J A S O N D J F M A M J J A S O N D

Figure E-2

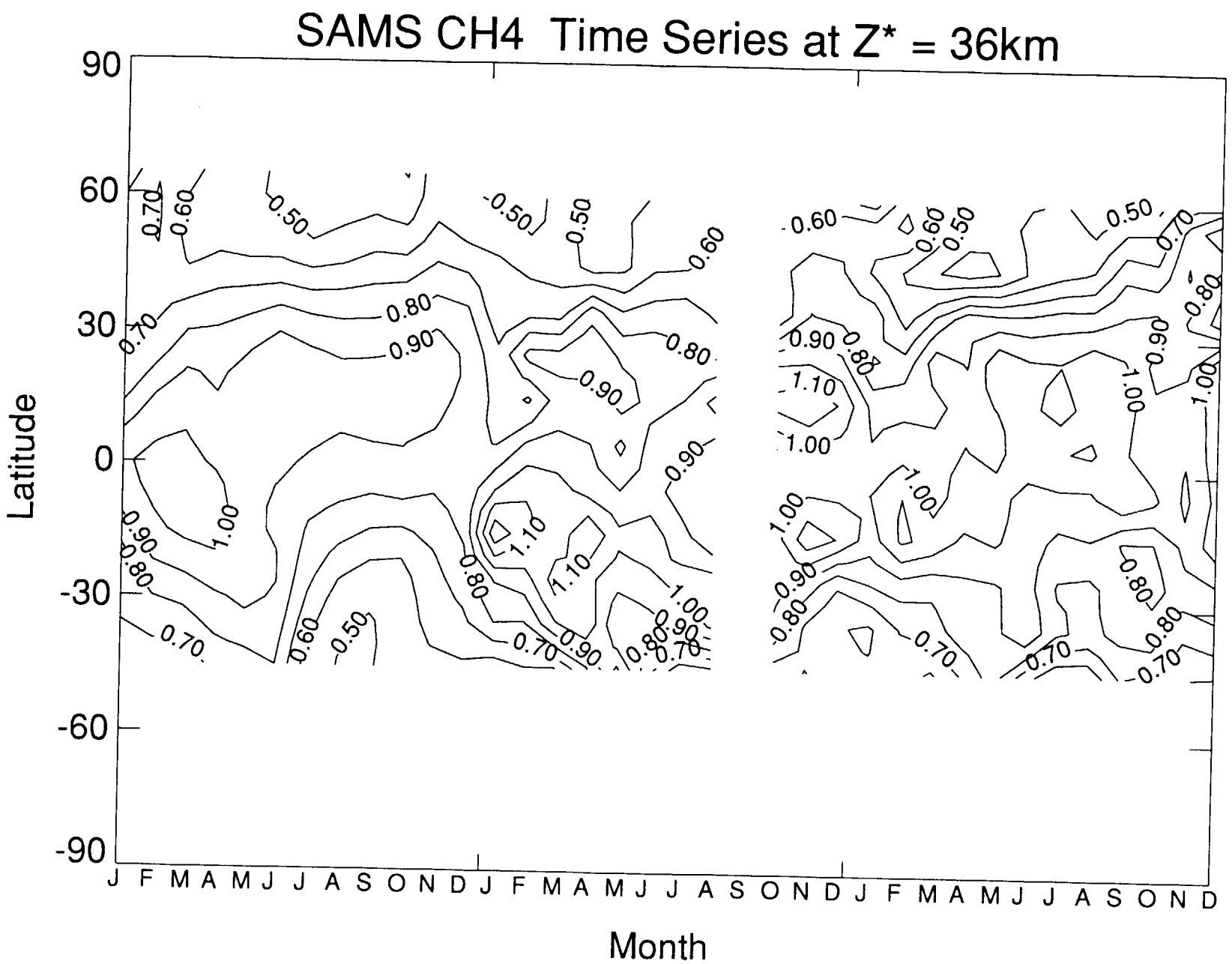
SAMS CH4 Time Series at Z* = 36km
Latitude
90
60
30
0
-30
-60
-90
J F M A M J J A S O N D J F M A M J J A S O N D J F M A M J J A S O N D
Month

Figure E-3

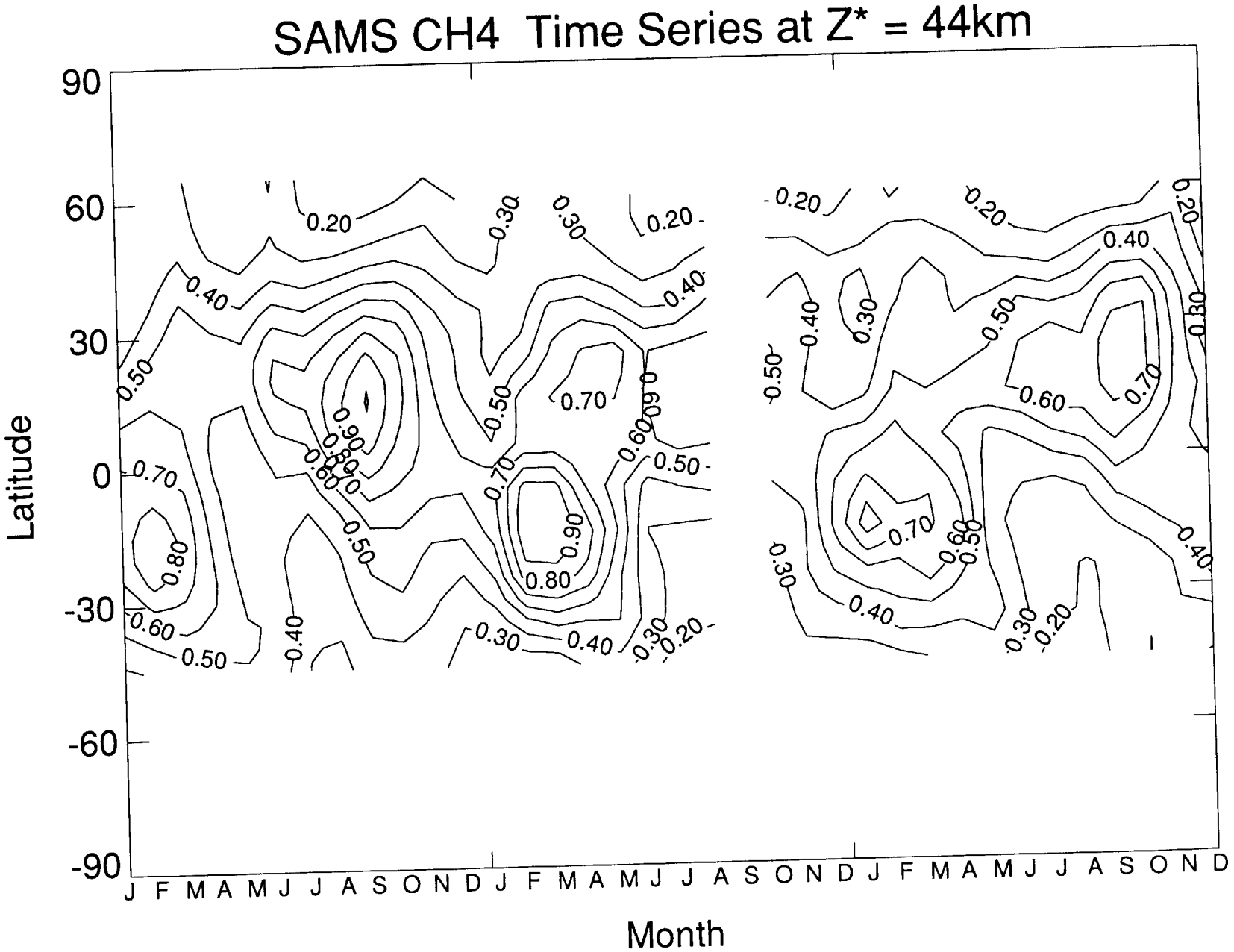
SAMS CH4 Time Series at Z* = 44km
Latitude
90
60
30
0
-30
-60
-90
J F M A M J J A S O N D J F M A M J J A S O N D J F M A M J J A S O N D
Month

Figure E-4

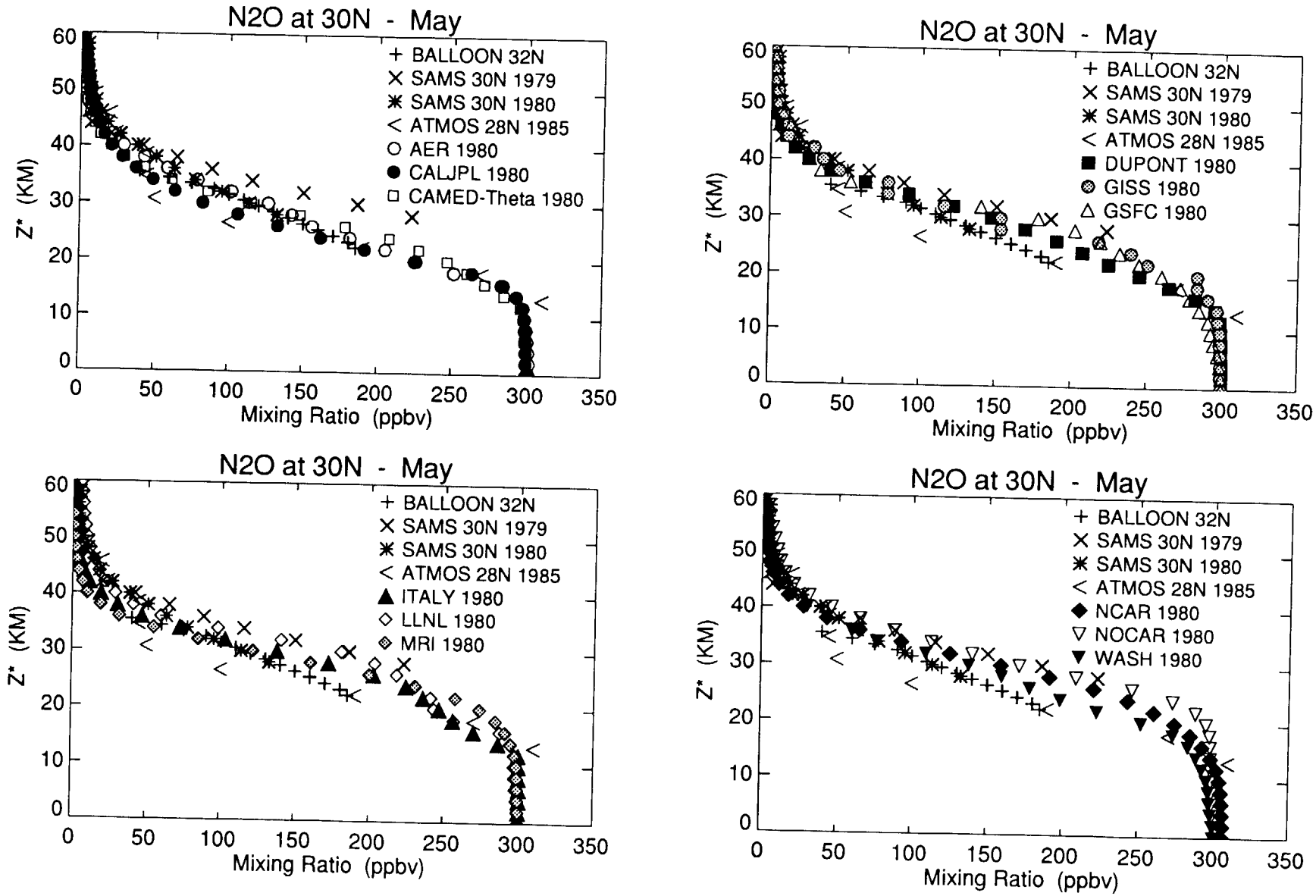
N2O at 30N - May
+ BALLOON 32N
× SAMS 30N 1979
✳ SAMS 30N 1980
< ATMOS 28N 1985
○ AER 1980
● CALJPL 1980
□ CAMED-Theta 1980
Z* (KM)
Mixing Ratio (ppbv)
N2O at 30N - May
+ BALLOON 32N
× SAMS 30N 1979
✳ SAMS 30N 1980
< ATMOS 28N 1985
■ DUPONT 1980
◎ GISS 1980
△ GSFC 1980
Z* (KM)
Mixing Ratio (ppbv)
N2O at 30N - May
+ BALLOON 32N
× SAMS 30N 1979
✳ SAMS 30N 1980
< ATMOS 28N 1985
▲ ITALY 1980
◇ LLNL 1980
◈ MRI 1980
Z* (KM)
Mixing Ratio (ppbv)
N2O at 30N - May
+ BALLOON 32N
× SAMS 30N 1979
✳ SAMS 30N 1980
< ATMOS 28N 1985
◆ NCAR 1980
▽ NOCAR 1980
▼ WASH 1980
Z* (KM)
Mixing Ratio (ppbv)

Figure E-5

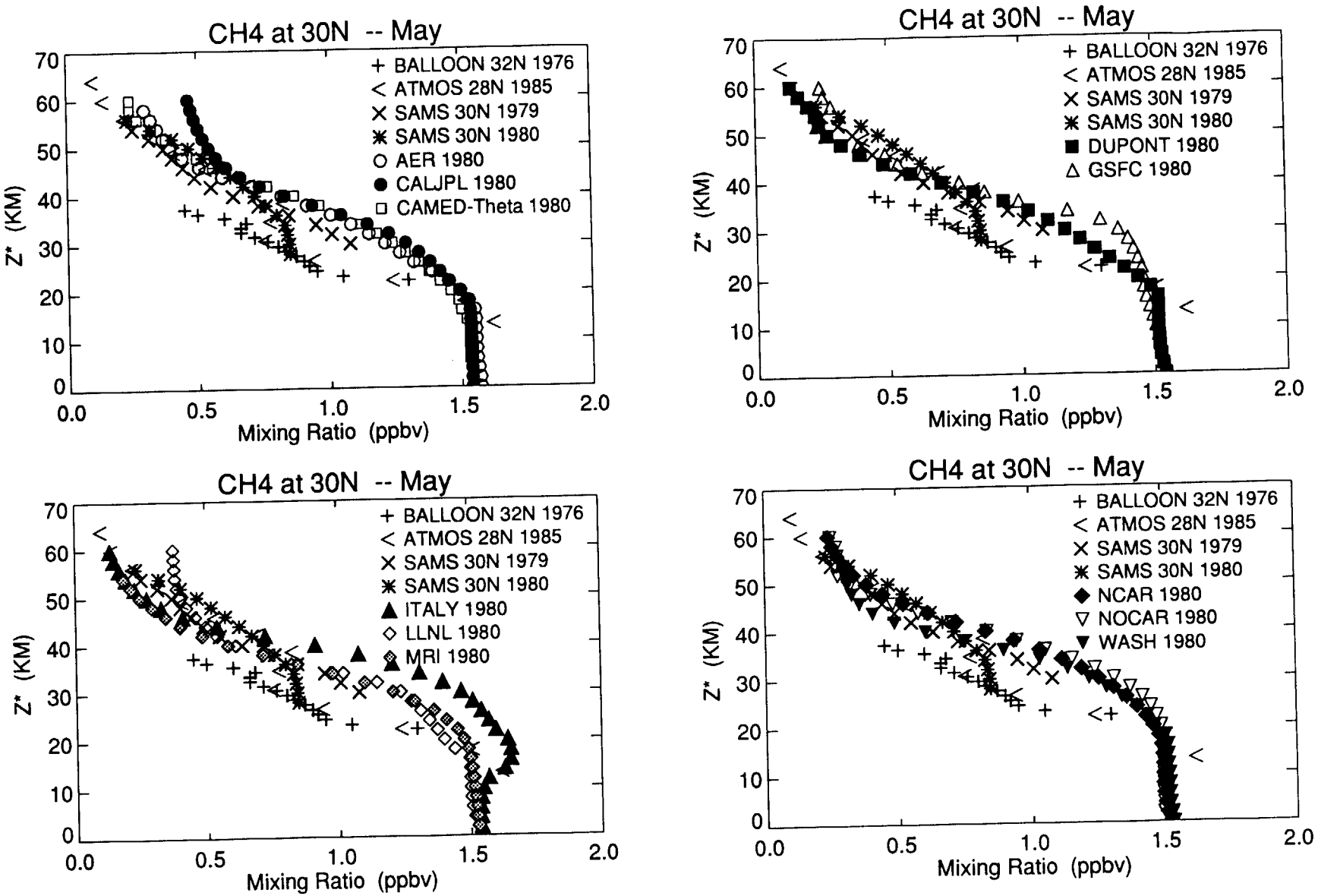
CH4 at 30N -- May
+ BALLOON 32N 1976
< ATMOS 28N 1985
X SAMS 30N 1979
* SAMS 30N 1980
O AER 1980
● CALJPL 1980
□ CAMED-Theta 1980
Z* (KM)
Mixing Ratio (ppbv)
CH4 at 30N -- May
+ BALLOON 32N 1976
< ATMOS 28N 1985
X SAMS 30N 1979
* SAMS 30N 1980
■ DUPONT 1980
△ GSFC 1980
Z* (KM)
Mixing Ratio (ppbv)
CH4 at 30N -- May
+ BALLOON 32N 1976
< ATMOS 28N 1985
X SAMS 30N 1979
* SAMS 30N 1980
▲ ITALY 1980
◇ LLNL 1980
MRI 1980
Z* (KM)
Mixing Ratio (ppbv)
CH4 at 30N -- May
+ BALLOON 32N 1976
< ATMOS 28N 1985
X SAMS 30N 1979
* SAMS 30N 1980
◆ NCAR 1980
▽ NOCAR 1980
▼ WASH 1980
Z* (KM)
Mixing Ratio (ppbv)

Figure E-6

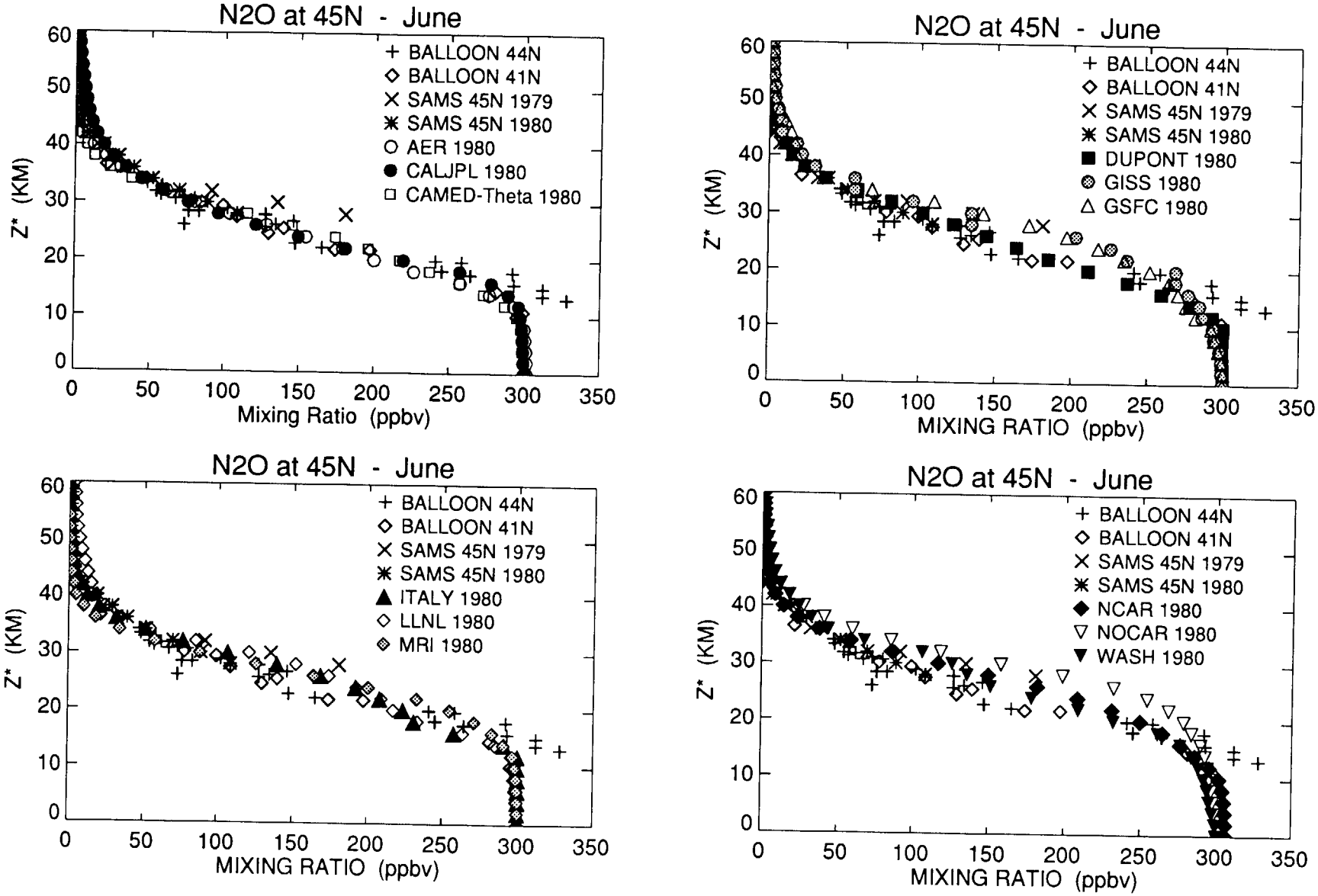
N2O at 45N - June
Z* (KM)
Mixing Ratio (ppbv)
+ BALLOON 44N
◇ BALLOON 41N
× SAMS 45N 1979
✳ SAMS 45N 1980
○ AER 1980
● CALJPL 1980
□ CAMED-Theta 1980
N2O at 45N - June
Z* (KM)
MIXING RATIO (ppbv)
+ BALLOON 44N
◇ BALLOON 41N
× SAMS 45N 1979
✳ SAMS 45N 1980
■ DUPONT 1980
◍ GISS 1980
△ GSFC 1980
N2O at 45N - June
Z* (KM)
MIXING RATIO (ppbv)
+ BALLOON 44N
◇ BALLOON 41N
× SAMS 45N 1979
✳ SAMS 45N 1980
▲ ITALY 1980
◇ LLNL 1980
◈ MRI 1980
N2O at 45N - June
Z* (KM)
MIXING RATIO (ppbv)
+ BALLOON 44N
◇ BALLOON 41N
× SAMS 45N 1979
✳ SAMS 45N 1980
◆ NCAR 1980
▽ NOCAR 1980
▼ WASH 1980

Figure E-7

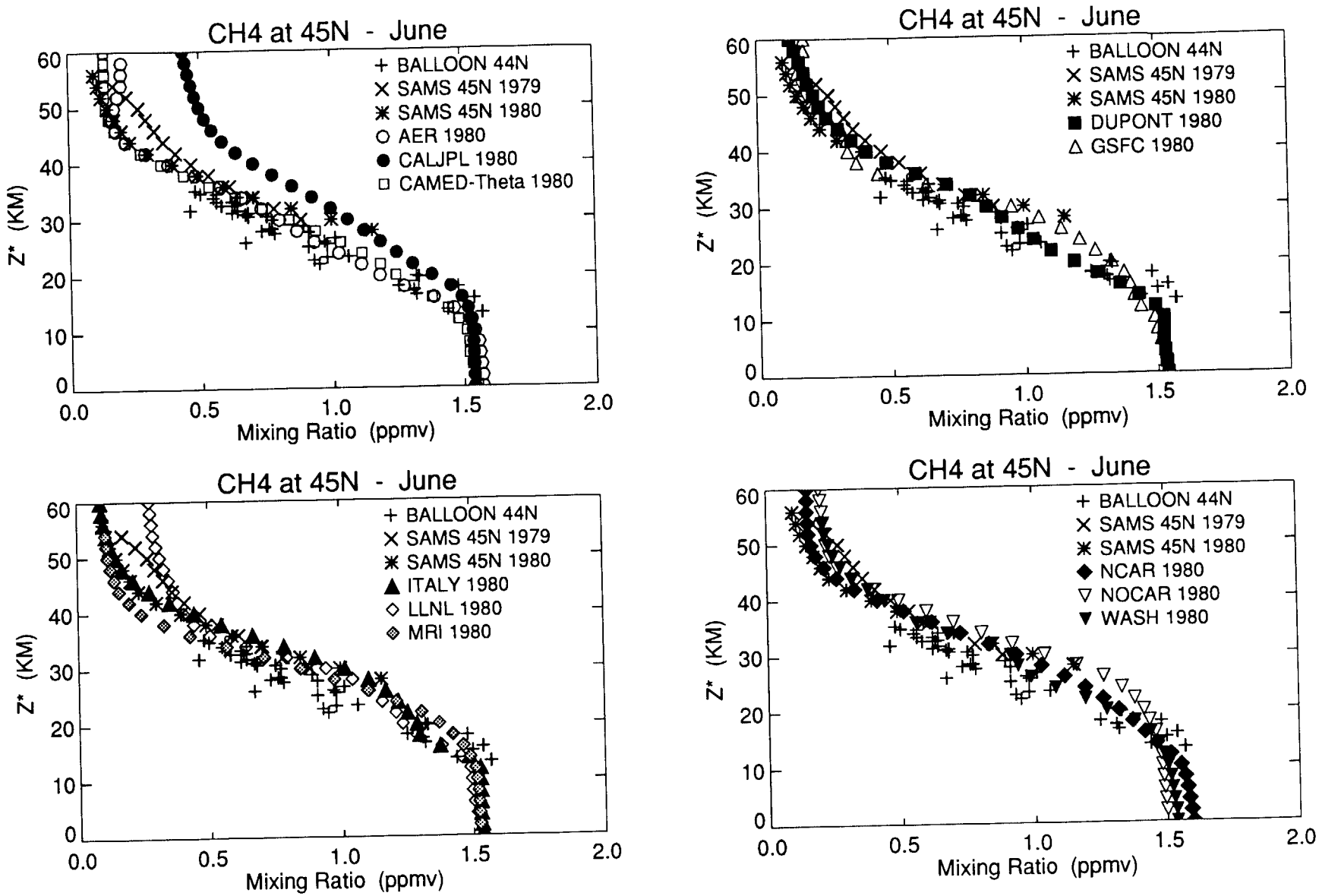
CH4 at 45N - June
+ BALLOON 44N
× SAMS 45N 1979
✳ SAMS 45N 1980
○ AER 1980
● CALJPL 1980
□ CAMED-Theta 1980
Z* (KM)
Mixing Ratio (ppmv)
CH4 at 45N - June
+ BALLOON 44N
× SAMS 45N 1979
✳ SAMS 45N 1980
■ DUPONT 1980
△ GSFC 1980
Z* (KM)
Mixing Ratio (ppmv)
CH4 at 45N - June
+ BALLOON 44N
× SAMS 45N 1979
✳ SAMS 45N 1980
▲ ITALY 1980
◇ LLNL 1980
◈ MRI 1980
Z* (KM)
Mixing Ratio (ppmv)
CH4 at 45N - June
+ BALLOON 44N
× SAMS 45N 1979
✳ SAMS 45N 1980
◆ NCAR 1980
▽ NOCAR 1980
▼ WASH 1980
Z* (KM)
Mixing Ratio (ppmv)

Figure E-8

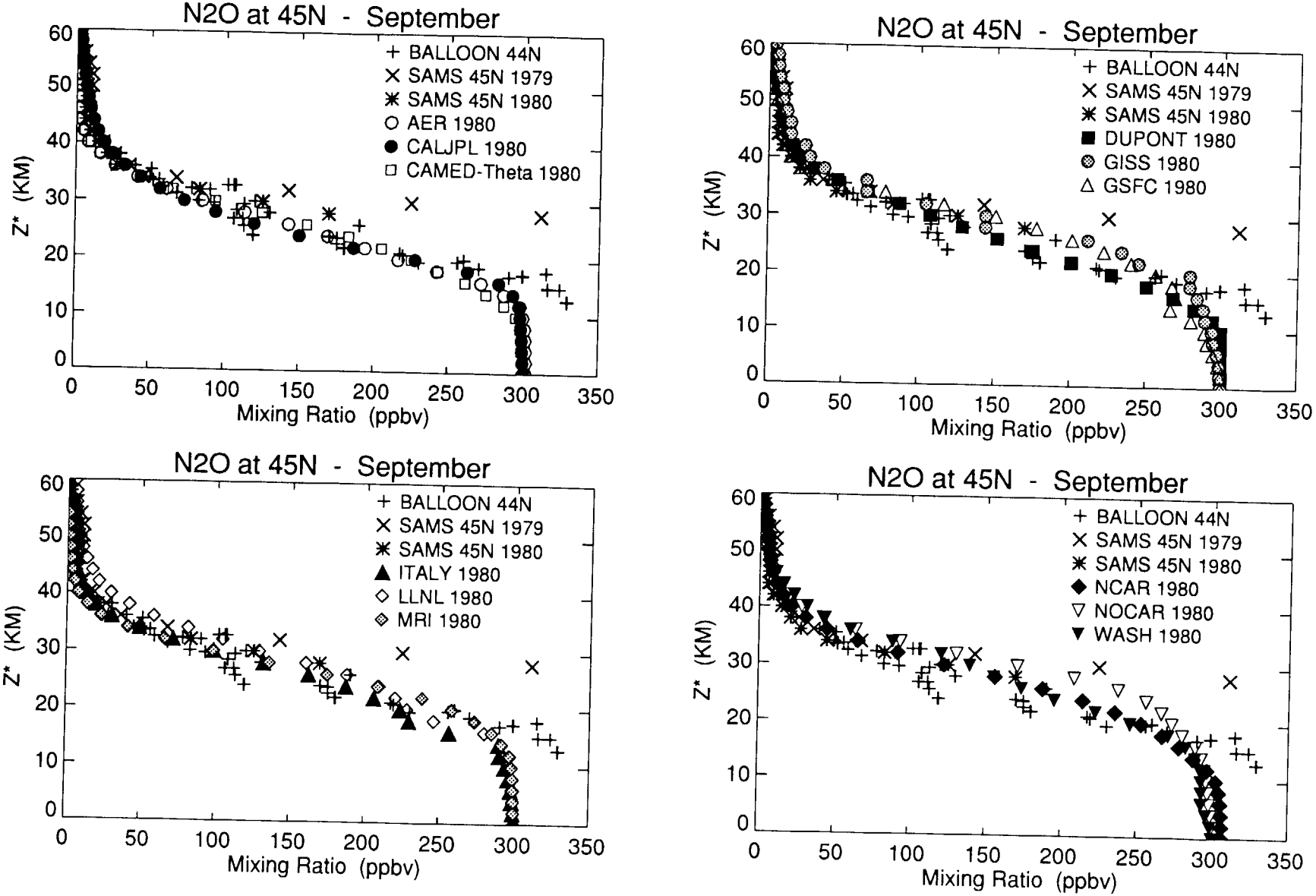
N2O at 45N - September
+ BALLOON 44N
× SAMS 45N 1979
✳ SAMS 45N 1980
○ AER 1980
● CALJPL 1980
□ CAMED-Theta 1980
Z* (KM)
Mixing Ratio (ppbv)
N2O at 45N - September
+ BALLOON 44N
× SAMS 45N 1979
✳ SAMS 45N 1980
■ DUPONT 1980
⊗ GISS 1980
△ GSFC 1980
Z* (KM)
Mixing Ratio (ppbv)
N2O at 45N - September
+ BALLOON 44N
× SAMS 45N 1979
✳ SAMS 45N 1980
▲ ITALY 1980
◇ LLNL 1980
◈ MRI 1980
Z* (KM)
Mixing Ratio (ppbv)
N2O at 45N - September
+ BALLOON 44N
× SAMS 45N 1979
✳ SAMS 45N 1980
◆ NCAR 1980
▽ NOCAR 1980
▼ WASH 1980
Z* (KM)
Mixing Ratio (ppbv)

Figure E-9

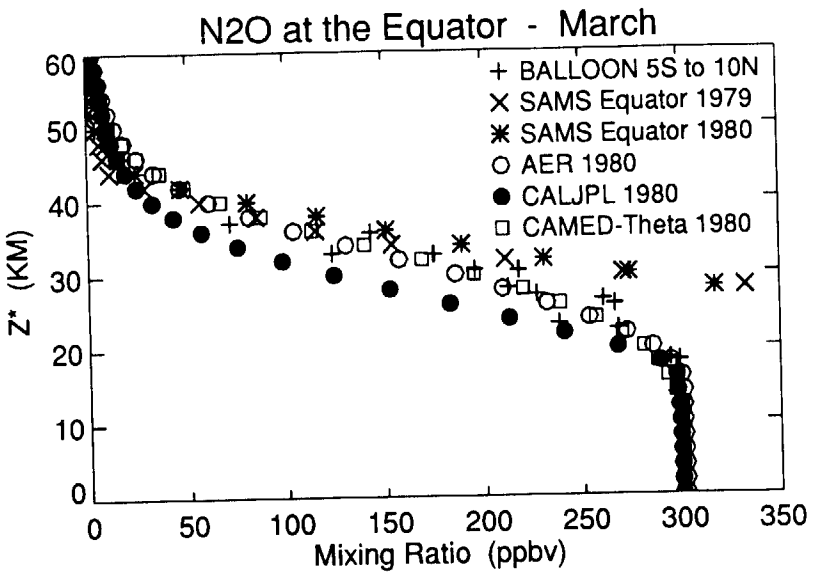
N2O at the Equator - March
+ BALLOON 5S to 10N
× SAMS Equator 1979
✳ SAMS Equator 1980
○ AER 1980
● CALJPL 1980
□ CAMED-Theta 1980
Z* (KM)
Mixing Ratio (ppbv)

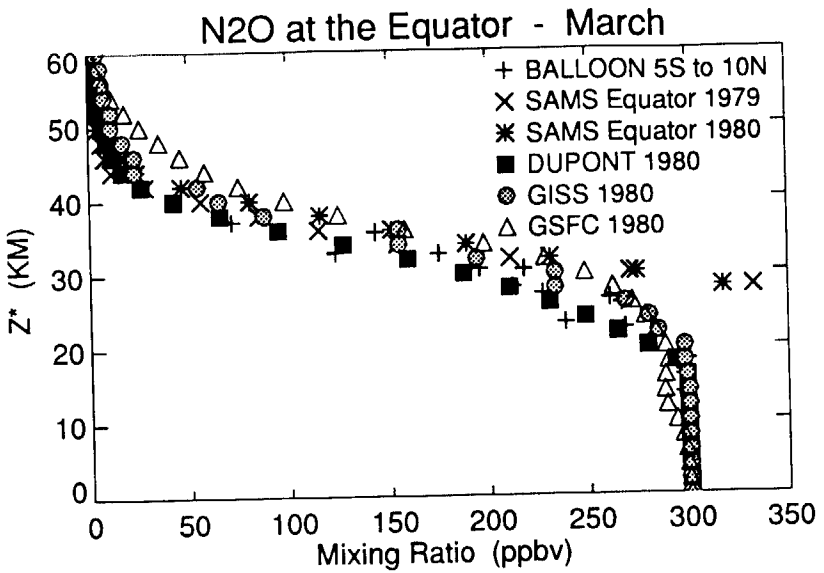
N2O at the Equator - March
+ BALLOON 5S to 10N
× SAMS Equator 1979
✳ SAMS Equator 1980
■ DUPONT 1980
⊗ GISS 1980
△ GSFC 1980
Z* (KM)
Mixing Ratio (ppbv)

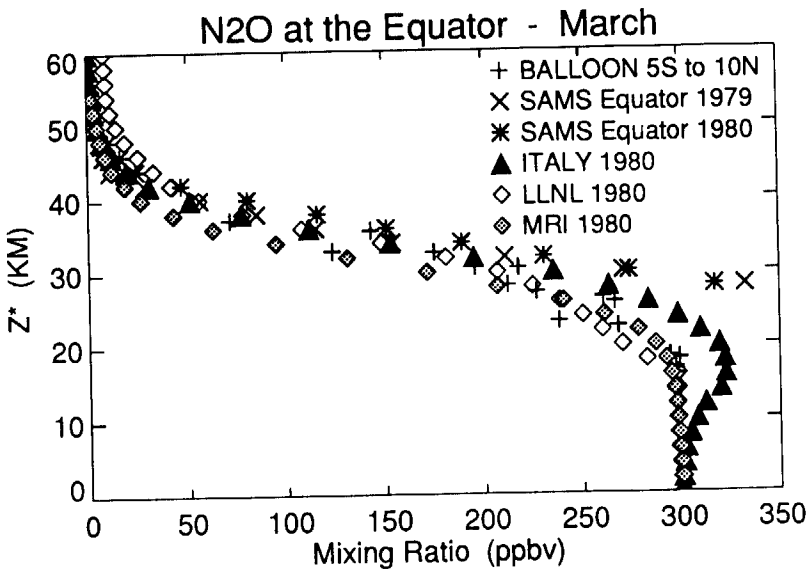
N2O at the Equator - March
+ BALLOON 5S to 10N
× SAMS Equator 1979
✳ SAMS Equator 1980
▲ ITALY 1980
◇ LLNL 1980
◈ MRI 1980
Z* (KM)
Mixing Ratio (ppbv)

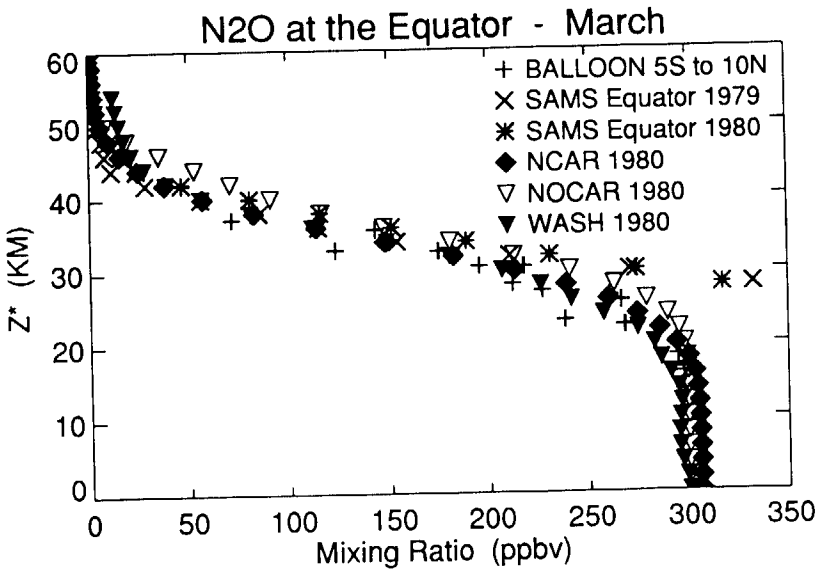
N2O at the Equator - March
+ BALLOON 5S to 10N
× SAMS Equator 1979
✳ SAMS Equator 1980
◆ NCAR 1980
▽ NOCAR 1980
▼ WASH 1980
Z* (KM)
Mixing Ratio (ppbv)

Figure E-10

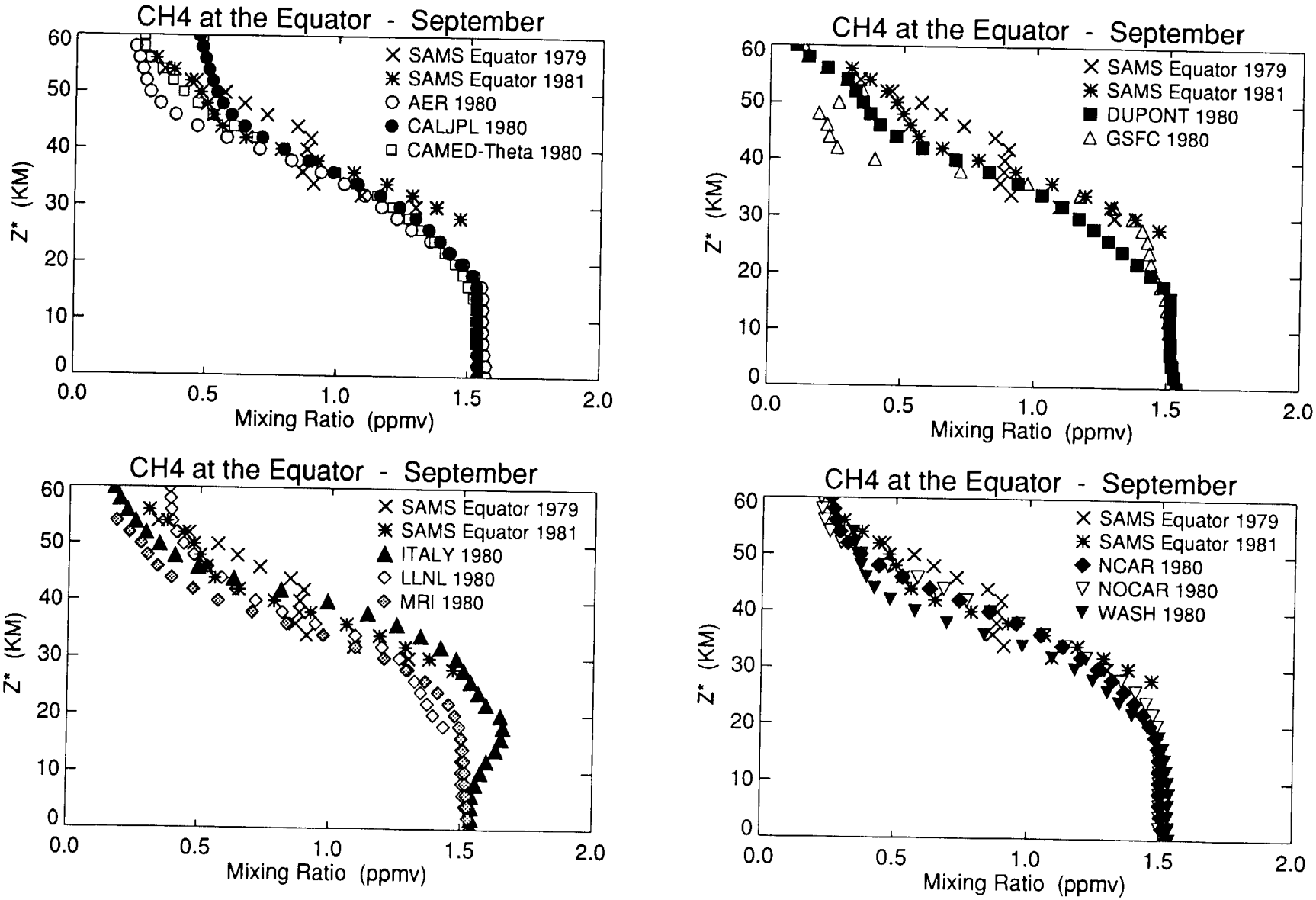
CH4 at the Equator - September
SAMS Equator 1979
SAMS Equator 1981
AER 1980
CALJPL 1980
CAMED-Theta 1980
Z* (KM)
Mixing Ratio (ppmv)
CH4 at the Equator - September
SAMS Equator 1979
SAMS Equator 1981
DUPONT 1980
GSFC 1980
Z* (KM)
Mixing Ratio (ppmv)
CH4 at the Equator - September
SAMS Equator 1979
SAMS Equator 1981
ITALY 1980
LLNL 1980
MRI 1980
Z* (KM)
Mixing Ratio (ppmv)
CH4 at the Equator - September
SAMS Equator 1979
SAMS Equator 1981
NCAR 1980
NOCAR 1980
WASH 1980
Z* (KM)
Mixing Ratio (ppmv)

Figure E-11

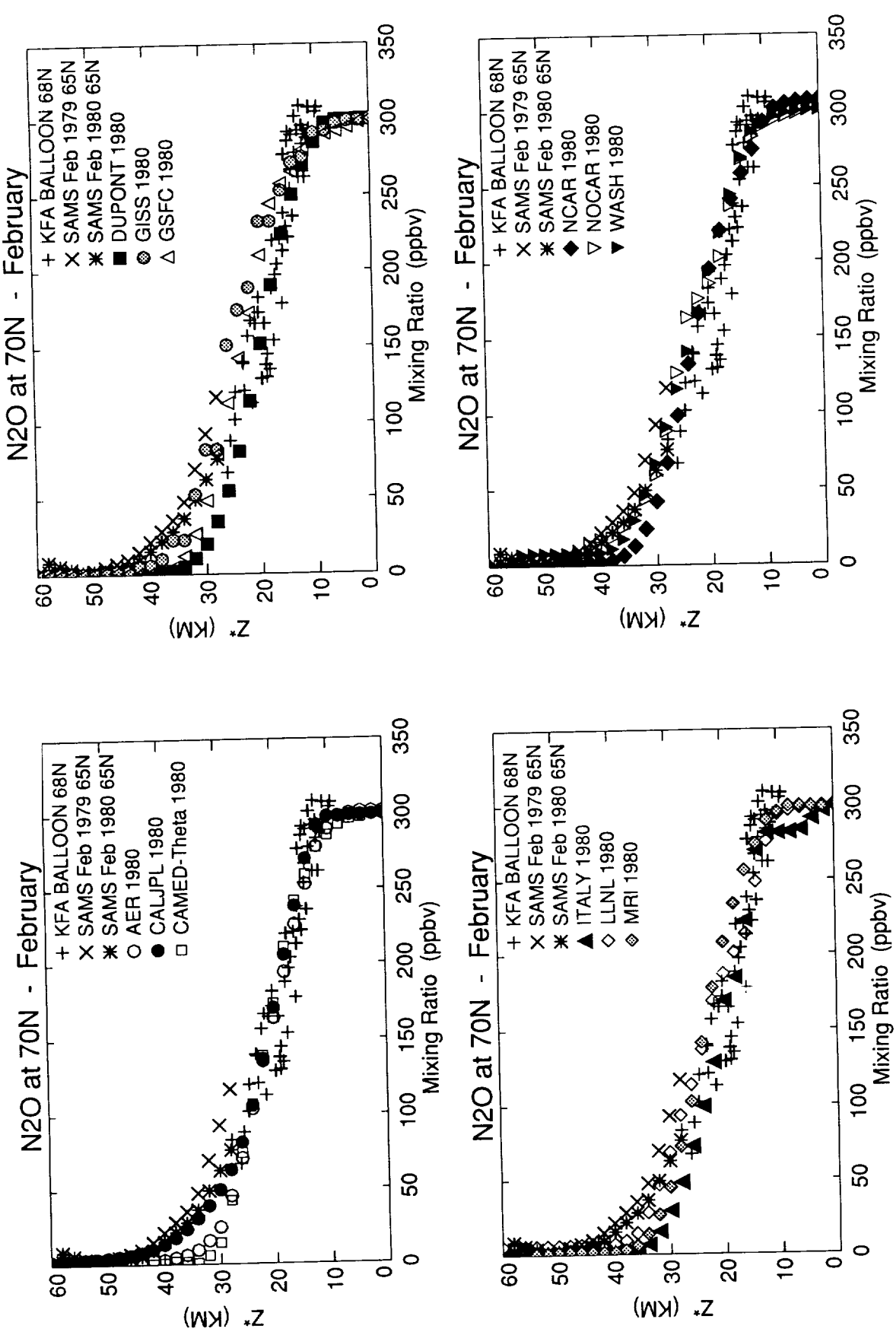
N2O at 70N - February
+ KFA BALLOON 68N
X SAMS Feb 1979 65N
* SAMS Feb 1980 65N
■ DUPONT 1980
⊗ GISS 1980
△ GSFC 1980
Z* (KM)
Mixing Ratio (ppbv)
N2O at 70N - February
+ KFA BALLOON 68N
X SAMS Feb 1979 65N
* SAMS Feb 1980 65N
◆ NCAR 1980
▽ NOCAR 1980
▼ WASH 1980
Z* (KM)
Mixing Ratio (ppbv)
N2O at 70N - February
+ KFA BALLOON 68N
X SAMS Feb 1979 65N
* SAMS Feb 1980 65N
○ AER 1980
● CALJPL 1980
□ CAMED-Theta 1980
Z* (KM)
Mixing Ratio (ppbv)
N2O at 70N - February
+ KFA BALLOON 68N
X SAMS Feb 1979 65N
* SAMS Feb 1980 65N
▲ ITALY 1980
◇ LLNL 1980
◈ MRI 1980
Z* (KM)
Mixing Ratio (ppbv)

Figure E-12

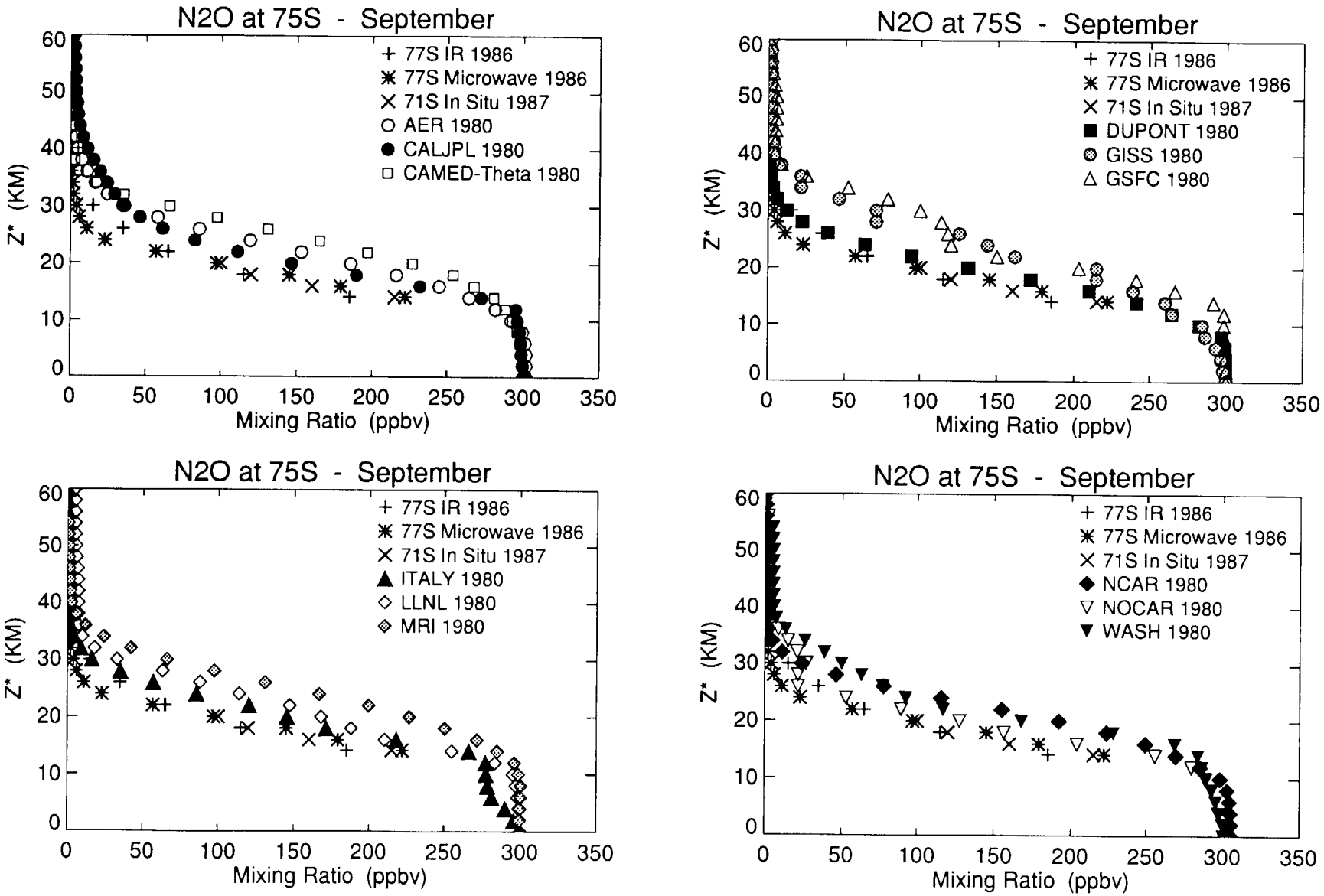
N2O at 75S - September
+ 77S IR 1986
* 77S Microwave 1986
X 71S In Situ 1987
O AER 1980
● CALJPL 1980
□ CAMED-Theta 1980
Z* (KM)
Mixing Ratio (ppbv)
N2O at 75S - September
+ 77S IR 1986
* 77S Microwave 1986
X 71S In Situ 1987
■ DUPONT 1980
GISS 1980
△ GSFC 1980
Z* (KM)
Mixing Ratio (ppbv)
N2O at 75S - September
+ 77S IR 1986
* 77S Microwave 1986
X 71S In Situ 1987
▲ ITALY 1980
◇ LLNL 1980
MRI 1980
Z* (KM)
Mixing Ratio (ppbv)
N2O at 75S - September
+ 77S IR 1986
* 77S Microwave 1986
X 71S In Situ 1987
◆ NCAR 1980
▽ NOCAR 1980
▼ WASH 1980
Z* (KM)
Mixing Ratio (ppbv)

Figure E-13

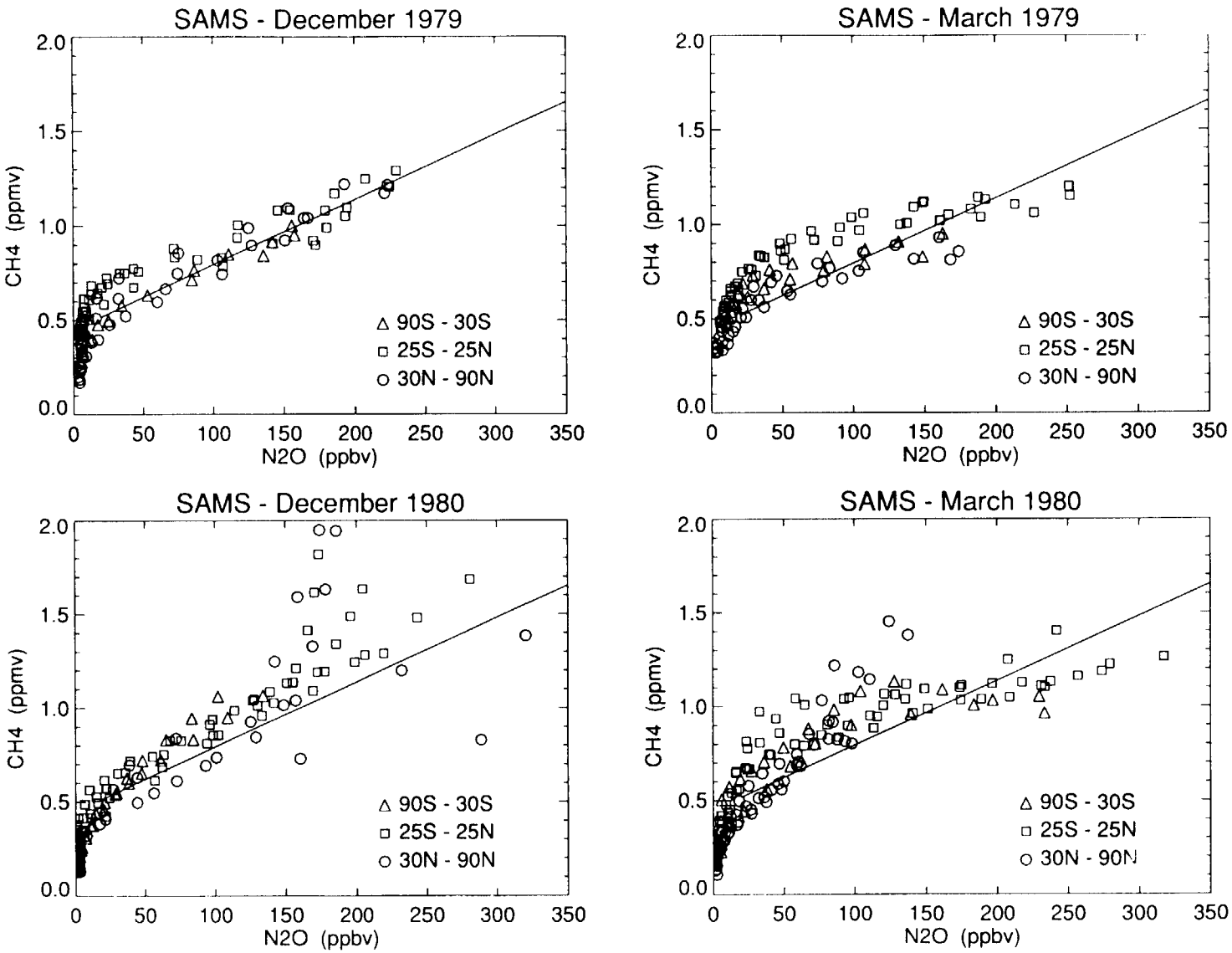

Figure E-14 (top, left and right) **Figure E-15 (bottom, left and right)**

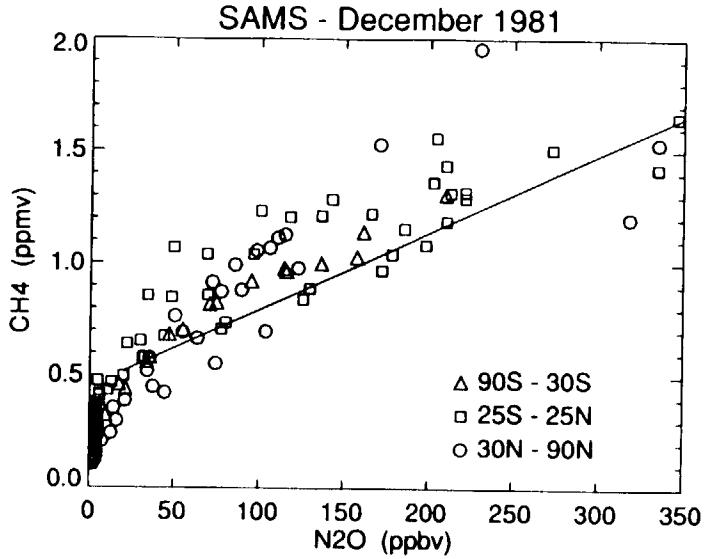

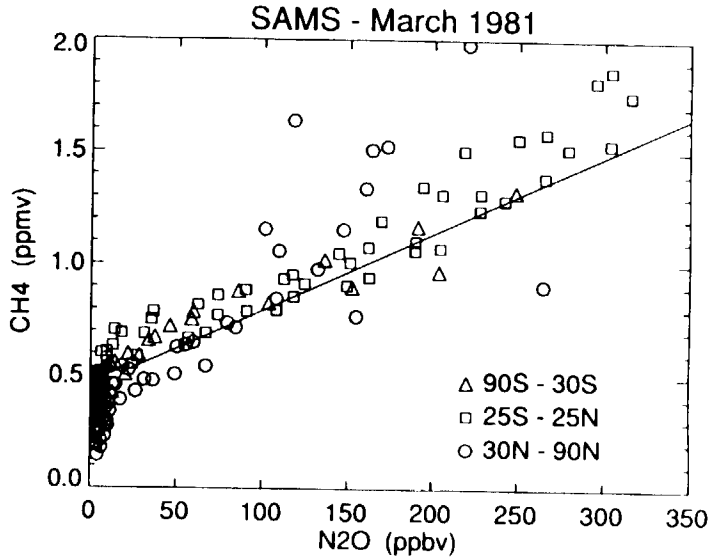

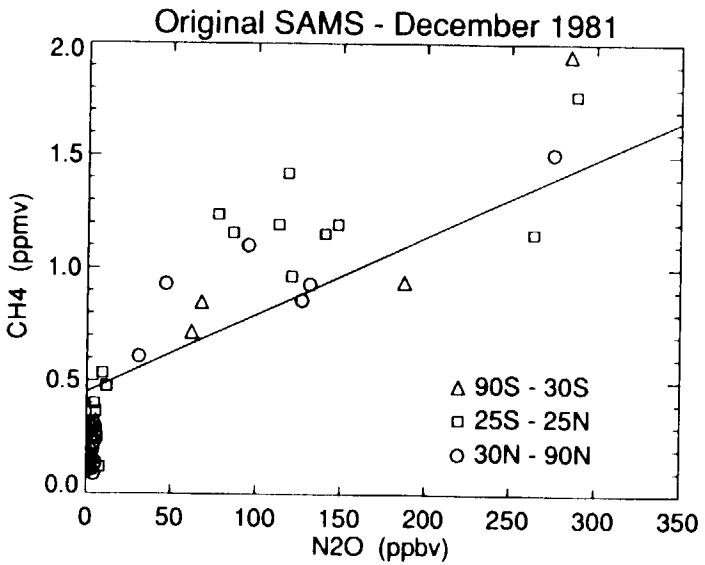

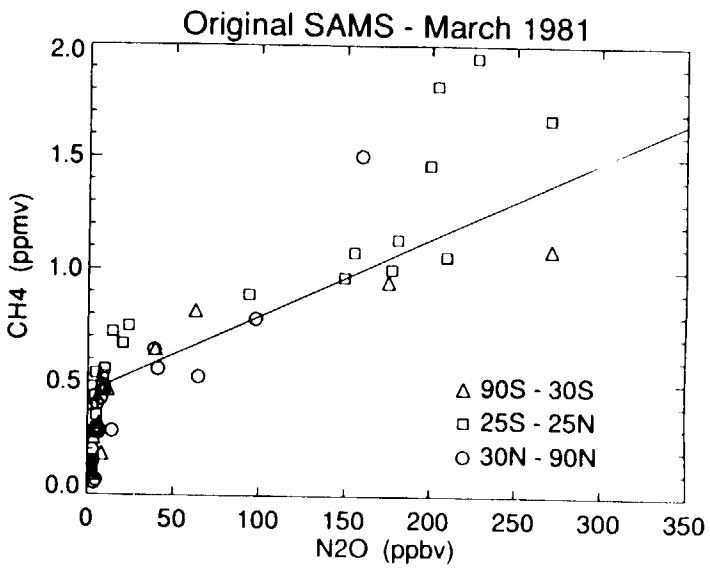

Figure E-16 (top, left and right) **Figure E-17 (bottom, left and right)**

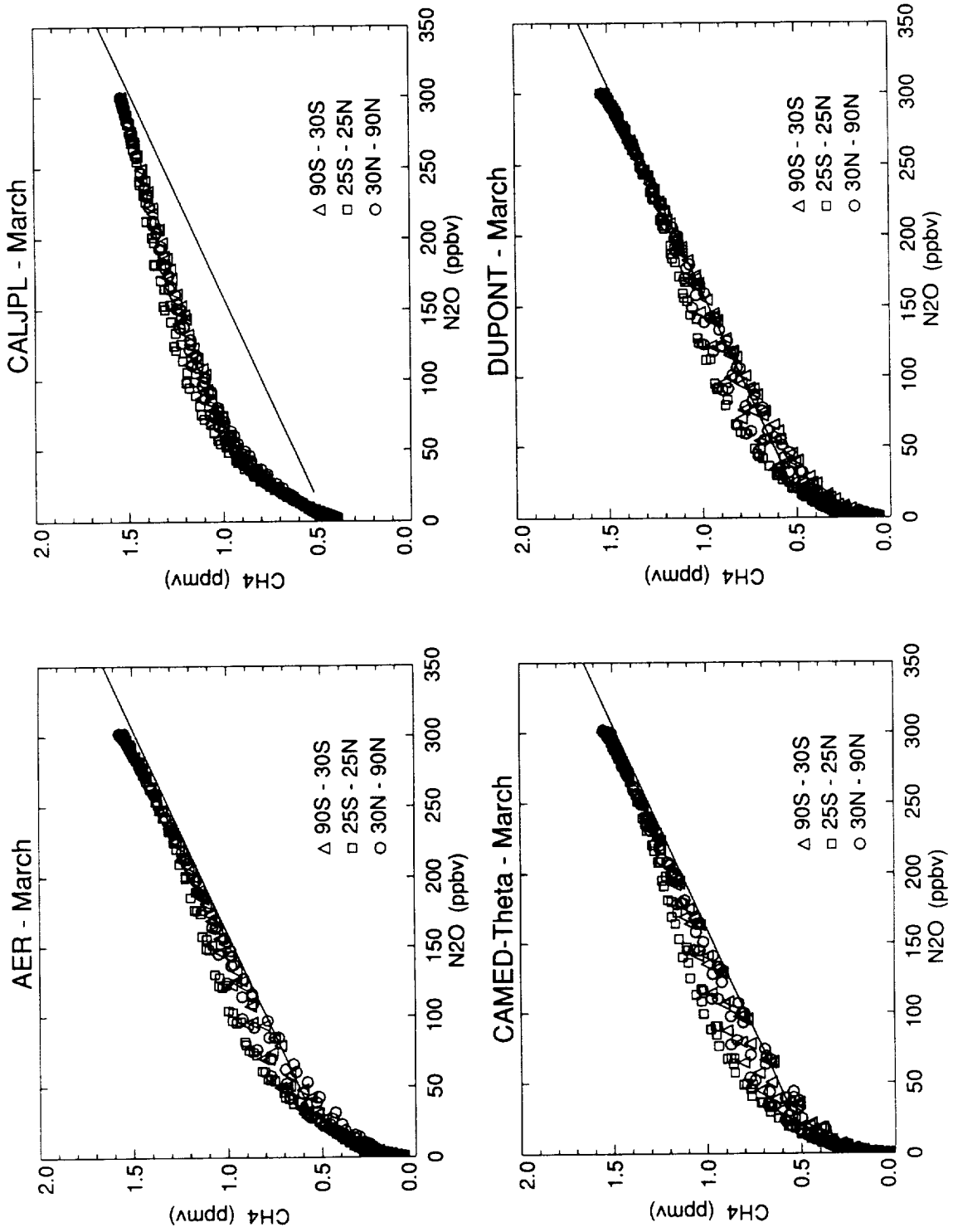
CALJPL - March
DUPONT - March
AER - March
CAMED-Theta - March
CH4 (ppmv)
N2O (ppbv)
△ 90S - 30S
□ 25S - 25N
○ 30N - 90N
0.0
0.5
1.0
1.5
2.0
0
50
100
150
200
250
300
350

Figure E-18

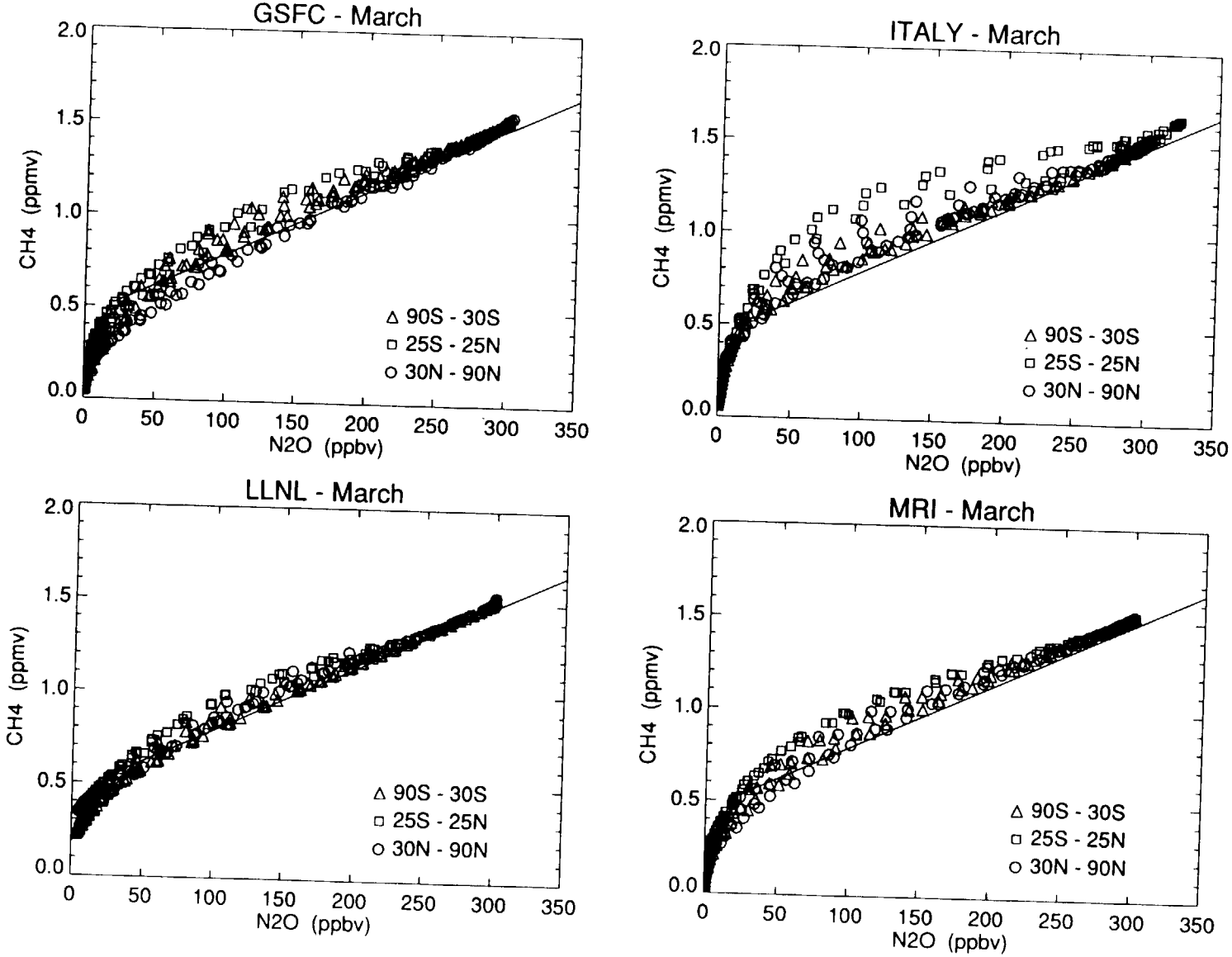

Figure E-18 (cont.)

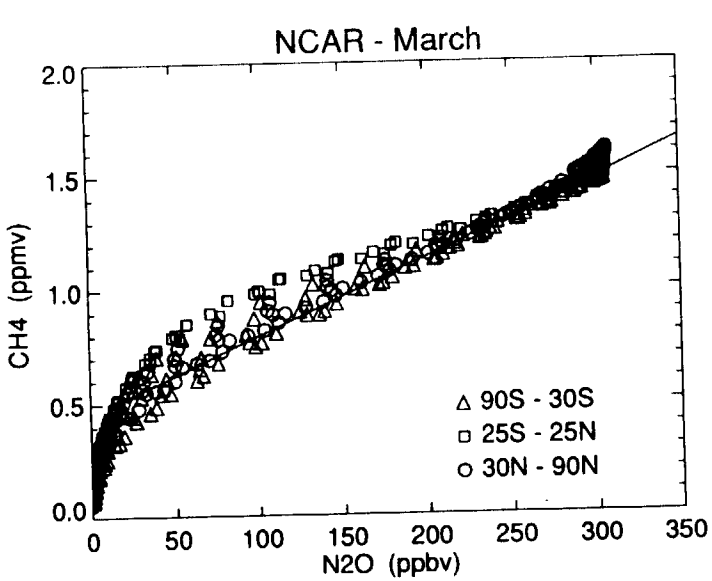

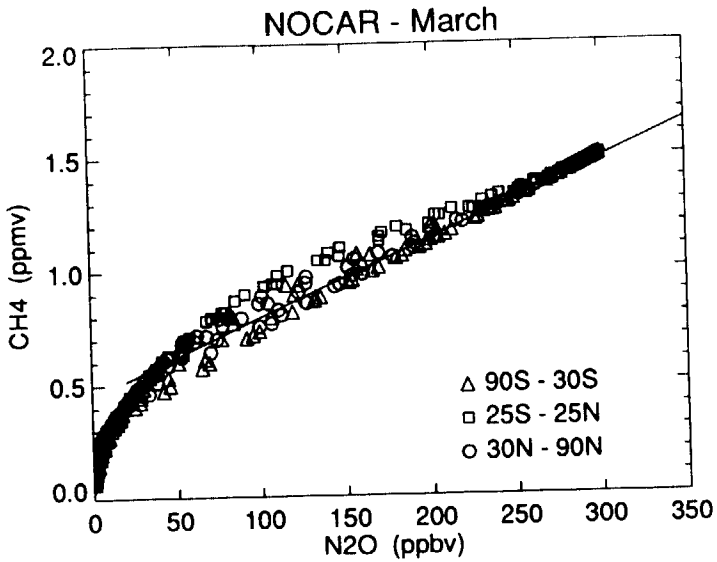

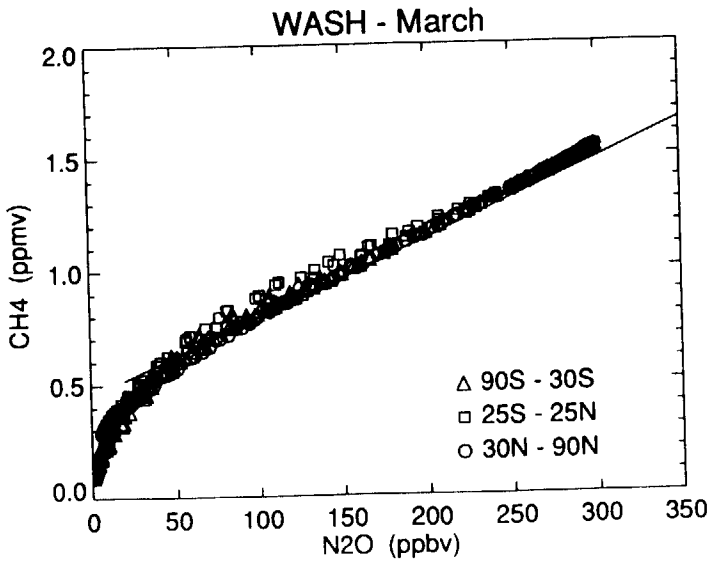

Figure E-18 (cont.)

F: Abundances and Distribution of NO_y Species

F: Abundances and Distribution of NO_y Species

J. M. Zawodny
NASA-Langley Research Center

INTRODUCTION

Experiment F is an intercomparison of model NO_2, HNO_3, and NO_y distributions among themselves and with existing satellite measurements and climatologies. These three species span a large range of lifetimes, from the diurnal variations of NO_2, to the HNO_3 variability on a monthly scale, to the seasonal transport of NO_y. The NO_2 comparisons are primarily a test of the chemistry in the models. In contrast, the NO_y variations and differences among the models are mostly due to dynamical differences, although the absolute abundances of NO_y in each model will depend on the relative chemical rates for N_2O loss and the amount of NO_y loss above 40 km (see section K). The HNO_3 distributions are sensitive to both chemistry and dynamics.

The models used in this experiment are described in detail elsewhere in this report; only those aspects of and differences between the models relevant to this experiment are discussed in this section. Unlike previous reports, this report includes observed species abundances and distributions received primarily from satellite-based observing systems. Specifically, this section includes NO_2 and HNO_3 measurements from the LIMS instrument from the 1978-1979 time period and NO_2 observations from 1984-1991 from SAGE II. No direct measurements of NO_y exist on a global scale with which the models can be compared; however, a useful lower limit of NO_y can be derived from the combined LIMS HNO_3 and nighttime NO_2 data sets. There are in situ NO_y measurements from aircraft for altitudes below 20 km, and these are discussed in section H.

Also not found in previous reports is the inclusion of heterogeneous processes in most models, defined here as being reactions of N_2O_5 and $ClONO_2$ on sulfuric acid aerosols. Most of the model runs generated for this intercomparison were performed two ways: with gas phase chemistry only or with gas phase plus heterogeneous reactions. These different chemistries produce significant changes in the model partitioning of NO_y. In each of the intercomparisons that follow, we will attempt to assess the performance of each type of chemistry. Table F-1 lists the modeling groups that submitted results to all or part of this experiment.

NO_2 RESULTS

Satellite measurements of NO_2 have been made, in a quasi-continuous fashion, since 1978 when the LIMS instrument began 7 months of operation. SAGE I made NO_2 measurements from early-1979 through mid-1981. Then Solar Mesospheric Explorer (SME) followed in 1982 and operated through 1986. Since 1984, the SAGE II instrument has continued with these measurements. Due to the brevity of the measurements or interferences from aerosols, only the SAGE II measurements are well suited to providing a measure of the "typical" seasonal distribution of stratospheric NO_2. With over 7 years of data, the SAGE II data set can be used to extract a mean seasonal cycle, removing a large part of the interannual variability. In addition, the SAGE II data have undergone extensive validation (Cunnold et al., 1991). The SAGE measurements are thought to have an accuracy of 15% for a single profile (random component) and a comparable overall uncertainty (systematic component).

The SAGE II data do not provide daily global coverage. The measurements "sweep" from one latitude extreme (50S-80S) to the other (50N-80N) in a period of about a month. The latitudes from 50S to 50N are sampled on roughly a monthly basis. Poleward of this, the

sampling pattern develops gaps in the winter and summer months. An additional difficulty in comparing these data with model data is that the SAGE measurements are made at local sunset, a time that assessment models normally do not simulate. Each of these problems can be circumvented though, as we will show below. The SAGE II NO_2 profiles extend over the altitude range from 20 to 40 km, and have been validated over the range from 25 to 38 km.

Table F-1. Contributions to Experiment F

Group	NO_2g 80-90	NO_2h 80-90	HNO_3g 80-90	HNO_3h 80-90	NO_yg 80-90	NO_yh 80-90
AER	s -	s -	x -	x -	x x	x x
CAMED	d d	d d	x x	x x	x x	x x
duPont	d -	d -	x x	x x	- x	- x
GSFC	d d	d d	x x	x x	x x	x x
Italy	x x	x x	x x	x x	x x	x x
LLNL	n n	n n	x -	x -	x x	x x
NCAR	x x	x x	x x	x x	x x	x x
WASH	x x	- -	x x	- -	x x	- -

x– contributed and 24-hr average NO_2
s– sunset NO_2; d– daytime average
- – did not contribute
n– local noon NO_2

Categories followed by a "g" indicate gas phase chemistry only.
Categories followed by a "h" indicate chemistry, including heterogeneous reactions as well as gas phase ones.
80 or 90 refers to year 1980 or 1990 submission.

As shown in Table F-1, the model submissions to this part of the experiment fall into four categories: local sunset, local noon, daytime average, and 24-hour average. Local sunset models (AER) are, of course, an appropriate match for the measurements and additional interpretation is unnecessary. For all other intercomparisons, potentially compromising assumptions must be made. Future intercomparisons of species with strong diurnal variability should be done with model results calculated at the appropriate local time. For this work, the following arguments will be made. At nonpolar latitudes (50S-50N), the local noon values are roughly proportional to the sunset values with the constant of proportionality, JNO_2@noon/JNO_2@sunset, not varying strongly with season. The noon to sunset ratio is somewhat smaller in the winter at the higher latitudes, due to incomplete N_2O_5 photolysis. A similar argument can be applied to the daytime average models. The effect of incomplete photolysis of N_2O_5 can cause some difficulties near 30 km. Above that altitude, the N_2O_5 photolysis is quite rapid. Below that, it is so slow as to become a negligible factor, since the thermal decomposition of N_2O_5 dominates the steady-state values. Unfortunately, similar arguments cannot be made in the case of the 24-hour average models. A simple example demonstrates why this is so. Let us suppose that at some altitude, the NO_2 mixing ratio jumps from a value of 1 ppbv during the day to a value of 2 ppbv at sunset, remaining at that value until sunrise. At equinox, the daily mean value is 1.5 ppbv. However, at solstice, the ratio of day to night is no longer unity and the daily mean value would shift away from 1.5 in a linear fashion according to the ratio of day to night. Therefore, even though there does not exist an annual cycle in the NO_2 mixing ratio at any particular local time, the daily average NO_2 will have a clear cycle present. In reality, the sunset (rise) jump in NO_2, due to its (lack of) photolysis to produce NO, can be quite large at high altitudes, but at the lowest altitudes this jump in NO_2 could be small. Generally the effect will be to increase the apparent seasonal cycle in NO_2. The resulting error introduced by these assumptions should not significantly alter the interpretation and results of this NO_2 intercomparison since differences at the several tens of percent are being discussed.

To avoid the potential sampling problem with the SAGE data, we adopted the following method of intercomparison. The first six and a half years of SAGE II NO_2 data were separated into 10-degree-wide latitude bands for each z* level, thus creating a set of time series. As was done in Zawodny and McCormick (1991), each of these time series was fit via linear regression to provide estimates of the mean, semiannual, and annual amplitudes and phases (sinusoidal variations) along with longer period terms to allow for the interannual variability related to the quasi-biennial oscillation (QBO). This method is very effective in reproducing observed variations (see Figure F-1). This same technique, without the longer period terms, was applied to the model data sets as well.

Because of the anticipated differences in the mean NO_2 fields in the model and measurement data sets, the amplitudes of the annual and semiannual components were expressed as a percentage of the mean value for each time series. Over the range of NO_y values dealt with here the ratio of NO_2 to NO_y is independent of the NO_y abundance (linear in NO_y). Therefore, the primary reason for differences in the mean NO_2 fields is that the NO_y fields differ. So by expressing the seasonal amplitudes in terms of percentages of the mean field, the NO_y differences divide out; however, the small (10%) NO_y seasonal variability does remain.

Figure F-2 shows the mean NO_2 mixing ratio fields and Figure F-3 the amplitudes of the semiannual and annual components from the SAGE II measurements. There is a maximum in the mean mixing ratio (Figure F-2a), which is in excess of 7 ppbv at 35 km and a slight tendency for more NO_2 in the southern hemisphere. In the lower stratosphere (22 km), the distribution has a distinct minimum at the equator which is about a factor of two less than that at midlatitudes. The semiannual variability is typically less than 5% (10% p-p) except at low altitudes at middle latitudes and near the equator. The equatorial amplitude can be quite large and may be due to the semiannual forcing of the dynamics. The semiannual component (not shown) is somewhat stronger at the southern middle latitudes than it is in the north. The latitude-altitude plot of the amplitude of the annual component (Figure F-3a) shows a great deal of structure and strong gradients, both with altitude and latitude. There is a prominent region of low annual variability (10% or less) near the mixing ratio peak. This region is asymmetric about the equator, extending over a narrower range of altitudes but to higher latitudes in the south as compared with the north. At the middle latitudes, the isopleths are nearly vertical between 30 and 40 km with the values in the southern hemisphere about 5% larger than those in the north. Below 30 km, the gradients steepen, reaching a maximum in the amplitude of the annual component near 23 km. In the lower stratosphere, the region of variability in excess of 20% ranges into the subtropics.

Five modeling groups contributed non-24-hour average NO_2 results to this experiment (AER, CAMED, DUPONT, GSFC, and LLNL). Based on the arguments made previously, all five were treated as being directly comparable to the SAGE II measurements as far as altitude and latitude gradients are concerned. All but LLNL had mean NO_2 mixing ratio fields that were very similar to the SAGE II values. Figure F-2 contrasts the model means against the measurements and each other. Unlike the others, the LLNL has a peak at 40 km, which is in excess of 10 ppbv. A similar difference will also be evident in the NO_y discussion. We will begin this intercomparison between models and measurements by considering the gas-phase-only results.

Because of the lack of structure in the semiannual amplitude field, we will proceed to the results for the annual variations. Figure F-3 displays the latitude-altitude contours of the amplitude of the annual component of the NO_2 mixing ratio seasonal variability from the five models mentioned above. All models have a region of minimal variability in the equatorial region. While the DUPONT model does not show a strong asymmetry about the equator, due to the fact that the southern hemispheric circulation is a mirror image of the north with a 6-month lag, the others do reproduce the general features seen in the SAGE II data. In particular, the CAMED model has a striking resemblance to the SAGE II data, although the pattern of minimal

variability is located at a slightly higher altitude in the CAMED model than is found in SAGE. At the middle latitudes, the models again qualitatively reproduce what is seen in the SAGE data. At the high altitudes, the large variations are confined to the high latitudes and are similar in magnitude to the SAGE II data (20%-25%). In the lower stratosphere, the region of large variability in the models extends to the subtropics, but is at a much reduced amplitude (about half) and appears at a lower altitude (18 km vs 23 km). In general, the models seem to have the basic climatology qualitatively correct, but the magnitude of the variability in the lower stratosphere is not as great in the models as is observed in the measurements.

The results from a 24-hour average model, such as NCAR (not shown), are drastically different from a daytime result. At the highest altitudes, the NO/NO_2 ratio can approach or exceed 10. Consequently, the annual cycle in the length of night drives the 24-hour average model annual cycle in NO_2 to very large amplitudes. In the lower stratosphere the NO abundances are comparable to NO_2. Here the changing night/day ratio is forcing the annual cycle out of phase with the chemistry. The long nights in winter, when NO_2 is usually at minimal values, cause the 24-hour average results to be artificially high (compared to a daytime model). The result is that the 24-hour average models cannot be compared with the sunset measurements.

When heterogeneous reactions on sulfate aerosols is included in the models, large changes in the NO_2 mixing ratios occur in the region below 30 km. As can be seen in Figures F-4 and F-5, the mean changes very little from the gas-phase-only model except in the lower stratosphere where the heterogeneous chemistry lowers the amount of NO_2 substantially. Additionally, the amplitudes of the annual component in the NO_2 mixing ratios increase by a factor of 2 to 3. This brings them into much better agreement with the SAGE II observational results and, in some cases, it may actually cause them to overshoot. Also when these reactions are included, the altitude of the peak amplitude moves up into better agreement with SAGE. As we will see in the section on HNO_3, the temperature sensitivity of the aerosol surface area density along with the reaction rates (sticking coefficients) is such that in winter the NO_x is converted to HNO_3. This makes the low winter values even lower and extends these low values to higher altitudes than is seen in the gas-phase-only results. In response, the HNO_3 winter values increase.

HNO_3 RESULTS

No widespread measurements of the HNO_3 global distribution have been made since the 7 months of LIMS operation during 1978-1979. The brief period of LIMS data does cover an equinox and a solstice so that there is some information on the seasonal variability of the stratospheric HNO_3 abundance. However, the lack of a multiyear data set for HNO_3 leaves no way of assessing whether small differences between models and observation are due to interannual variability. If the interannual variability of HNO_3 is similar to NO_2, it could be as large as 30% from year to year. The large number of observations from LIMS allows the monthly mean distribution to have a small random error component. Gille et al. (1984) have evaluated the systematic errors in the LIMS HNO_3 measurements and found them to be accurate to within 41% and 29% at 50 and 10 mb, respectively. The LIMS measurements cover the altitude range from slightly in excess of 40 km down to 15/21 km in the mid/tropical latitudes. Figure F-6 presents the LIMS monthly mean HNO_3 mixing ratio for December 1978 and March 1979. Peak HNO_3 mixing ratios occur at 24 km at middle latitudes rising to 28 km near the equator. The bulk of the HNO_3 is found away from the tropics where mixing ratios reach values of 6 ppbv in summer and over 10 ppbv in winter. Due to the long photolysis lifetime of HNO_3, the distribution at equinox has values at the spring pole which are larger than those in the fall hemisphere. The equatorial maximum at 28 km is a factor of 2 or 3 less than what is found at middle latitudes.

As will be seen, there is a large variance among the model HNO_3 distributions. It is useful to consider a mean model that is defined as the average of all models and that also shows the average seasonal variation. As before, the models were run twice, including heterogeneous reactions in the second run. The latitude-altitude cross sections of the mean model for December and March are also presented in Figure F-6 c-d for the gas-phase-only case and Figure F-6 e-f when heterogeneous reactions are added. When the December and March models are compared to the LIMS values, we see that the mean model is in excellent agreement with the LIMS observations in the summer (December south) and fall (March south) hemispheres. However, the spring and winter model results for the hemispheres severely underestimate the HNO_3 mixing ratios. When the heterogeneous chemistry is added, the winter and spring hemispheres come into considerably better agreement, perhaps now overestimating the observed HNO_3 abundances.

For later diagnostic purposes, the December and March differences ([Model - LIMS] / LIMS) between each model (with heterogeneous reactions) and the LIMS measurements are presented in Figure F-7. Briefly, the CAMED model had the highest levels of HNO_3 found in the troposphere, DUPONT and LLNL had the highest levels in the upper stratosphere, and the highest amounts of HNO_3 in the middle and lower stratosphere were found in the NCAR model. Model-to-observation differences in the hundreds of percent are not uncommon, but in the lower stratosphere models are generally within 50% of the measurements.

NO_y RESULTS

Direct satellite observations of NO_y are not possible. At best, an estimate of a lower limit to the NO_y distribution can be obtained by summing together distributions of the component gases in the NO_y family. In the stratosphere, the bulk of NO_y is in the form of NO, NO_2, and HNO_3. At night most of the NO_y is in the form of HNO_3, NO_2, and N_2O_5. The only simultaneous nighttime measurements of HNO_3 and NO_2 are those made by LIMS. As discussed previously there are some limitations in using this data set, but it is still a valuable intercomparison to make. The LIMS "psuedo-NO_y" (LIMS nighttime NO_2 + HNO_3) distributions for December and March are shown in Figure F-8. The pseudo-NO_y is seen to peak around 40 km (a little lower near the poles) at a value slightly in excess of 18 ppbv. This peak is prominently displaced into the southern hemisphere in both months. There is a clear equatorial minimum in the lower and middle stratosphere. In an absolute sense, the LIMS NO_2 plus HNO_3 has an accuracy of 33% and 20% at 30 and 3 mb, respectively (Remsberg, personal communication).

As with the HNO_3 model results, the monthly model NO_y distributions have been averaged to form a mean model. The December and March latitude distributions of the mean model also appear in Figure F-8. The mean model reaches a peak NO_y mixing ratio of slightly more than 17 (18) ppbv in December (March) at an altitude of 40 to 42 km. Again as seen in the LIMS data, the altitude of the peak decreases towards the poles. While there is some indication of more NO_y in the southern hemisphere (except September), the hemispheric difference is not as large as LIMS suggests. The mean model has an equatorial minimum and, in general, shows much less latitudinal structure than do the LIMS data. This is of little consequence, since 7 months of LIMS data cannot be used to assess the interannual variability, a likely cause of the structure observed. In northern spring, the LIMS psuedo-NO_y distribution has a rather broad peak and a strong latitude gradient near the peak. The mean model does not capture this feature. Again this may be peculiar to this particular year.

The individual model NO_y fields vary a great deal from one to the other. The CAMED, MRI, and ITALY models have very similar distributions (although ITALY tends to peak at lower altitude) to what was seen in the mean model. Both LLNL and WASH better reproduce the hemispheric asymmetry, but differ by 25%-30% at the peak. The NCAR model also has a fair degree of asymmetry, but it is in an opposite sense to the others or to LIMS. Perhaps the most

interesting model NO_y results were submitted by GSFC. Their model generates structure that the other models do not generate and that, in the lower stratosphere, looks like what is seen in the LIMS data. GSFC also has unusually high peak NO_y mixing ratios, nearly 40% above the mean model. For comparison with the findings from the HNO_3 section, the difference for each model from the observations of NO_y is provided in Figure F-9. While the amplitude of the differences between the two are different for NO_y, they have a very similar structure in the lower stratosphere to those seen in the HNO_3 comparison (Figure F-7). Because of the steep gradient in NO_y below 35 km, the NO_y distribution in this region is very sensitive to differences in vertical transport between the models (*see* Net Circulation in section A).

When the mean model is compared with the LIMS estimate of a NO_y lower limit, several things become apparent (Figures F-8e and 8f). Most obvious is the "bulls eye" centered on the equator at 30 km showing the LIMS pseudo-NO_y up to 40% less than the mean model. At 30 km, the QBO component of the zonal wind was at its easterly peak value during March of 1979 (WMO, 1986). The expected QBO perturbation in NO_y of 12% (Chipperfield and Gray, 1992) or the observed 20% perturbation in NO_2, an NO_y proxy (Zawodny and McCormick, 1991), would result in an NO_y minimum. Since the models do not simulate the QBO dynamics (nor the semiannual oscillation [SAO] for that matter), a 40% difference in NO_y is not beyond reason. As noted earlier, the LIMS NO_y is typically larger than the models in the midstratosphere and upper stratosphere in the southern hemisphere. There is no clear indication that the models have an NO_y deficit with respect to the LIMS data. Model-to-model differences are large, and the magnitude of the deficit is neither significantly nor consistently larger than the LIMS measurements uncertainties.

CONCLUSIONS

Care must be taken when comparing measurements and model results for species that have significant diurnal variability. With some care and caution, the SAGE II sunset measurements can be compared with sunset, noon, or daytime average model results. Additionally, the NO_y differences must be considered. When effects of the differing model NO_y fields are removed from the NO_2 data, the models reproduce the observed seasonal variations only when heterogeneous chemistry is included. Otherwise, the annual variability is underestimated by a factor of 2 or 3.

The model HNO_3 distributions closely agree with observations in the summer and fall hemispheres. This agreement falls out automatically from the observations and the model predictions that HNO_3 is the primary NO_y constituent in the lower stratosphere. The inclusion of heterogeneous chemistry is required to bring the winter and spring predictions into agreement with the LIMS measurements. Particularly in the troposphere and upper stratosphere, there is large model-to-model variability. The model-to-model differences in lower-stratospheric NO_y are quite similar to the differences seen in the HNO_3 comparison, as demonstrated in section O. Therefore, the primary reason for the lack of agreement between the models in the lower stratosphere is due to the differing NO_y distributions.

There is a great deal of difference between the model NO_y fields. At the altitude extremes (troposphere and upper stratosphere) model-to-model differences may be in excess of 300%. In the midstratosphere and lower stratosphere, however, the models rarely vary by more than 50%. This is still a large variance, but there is currently no way of determining who is right or wrong. There is also an indication of a model NO_y deficit in the lower stratosphere, but the magnitude of the deficit is not beyond the uncertainties in the LIMS NO_y proxy. Additionally, the presence of what appears to be large interannual variability due to the QBO and SAO in the NO_y data confirms the need to revisit this NO_y analysis when several years of suitable data become available.

The inclusion of heterogeneous chemistry in the models significantly improves the agreement between the models and the observations. In some instances, this additional chemistry over-corrects the prior deficiencies. Further progress can only come from a more complete intercomparison with observations, preferably multiyear data sets, of N_2O_5 and $ClONO_2$ in addition to HNO_3 and NO_2.

REFERENCES

Chipperfield, M. P., and L. J. Gray, Two-dimensional model studies of the interannual variability of trace gases in the middle atmosphere, *J. Geophys. Res., 97*, 5963-5980, 1992.

Cunnold, D. M., J. M. Zawodny, W. P. Chu, J. P. Pommereau, F. Goutail, J. Lenoble, M. P. McCormick, R. E. Veiga, D. Murcray, N. Iwagami, K. Shibasaki, P. C. Simon, and W. Peetermans, Validation of the SAGE II NO_2 measurements, *J. Geophys. Res., 96*, 12913-12925, 1991.

Gille, J. C., J. M. Russell, III, P. L. Bailey, E. E. Remsberg, L. L. Gordley, W. F. J. Evans, H. Fischer, B. W. Gandrud, A. Girard, J. E. Harries, and S. A. Beck, Accuracy and precision of the nitric acid concentrations determined by the Limb Infrared Monitor of the Stratosphere Experiment on NIMBUS 7, *J. Geophys. Res., 89*, 5179-5190, 1984.

World Meteorological Organization (WMO), *Atmospheric Ozone 1985, Global Ozone Research and Monitoring Project,* Report No. 16, WMO. Geneva, 1986.

Zawodny, J.M., and M.P. McCormick, Stratospheric Aerosol and Gas Experiment II measurements of the quasi-biennial oscillations in ozone and nitrogen dioxide, *J. Geophys. Res., 96*, 9371-9377, 1991.

FIGURE CAPTIONS

Figure F-1. The 31.5 km SAGE II time series for daily mean NO_2 in the latitude band from 10S to the equator (dots). The lines represent two different ways of modeling the QBO.

Figure F-2. Latitude-height contours of annual mean NO_2 mixing ratio (ppbv) from a) SAGE II, and gas phase models from b) AER, c) CAMED, d) DUPONT, e) GSFC, and f) LLNL.

Figure F-3. Latitude-height contours of the amplitude of the annual component of the NO_2 variability expressed as a percentage of the mean NO_2. Panel a) is the observed SAGE II field. The rest are Gas Phase models from b) AER, c) CAMED, d) DUPONT, e) GSFC, and f) LLNL.

Figure F-4. Same as Figure F-2 except b through f are for model runs with heterogeneous reactions included.

Figure F-5. Same as Figure F-3 except b through f are for model runs with heterogeneous reactions included.

Figure F-6. Latitude-height contours of the nitric acid mixing ratio in (ppbv) observed by LIMS during December (a) and March (b). The model results for the same months appear in panels c and d. Panels e and f are the HNO_3 fields when the models include heterogeneous reactions.

Figure F-7. Contours of the difference in HNO_3 fields between models (with heterogeneous reactions) and LIMS ((Model - LIMS)/LIMS in percent) for both December and March. Panels a-b are for AER, c-d are CAMED, e-f are DUPONT, g-h are GSFC, i-j are ITALY, k-l are LLNL, m-n are MRI, o-p are from NCAR, and q-r are from WASH.

Figure F-8. Latitude-height contours of the sum of HNO_3 and nighttime NO_2 mixing ratios in (ppbv) observed by LIMS during December (a) and March (b). The model NO_y results for the same months appear in panels c and d. Panels e and f are the NO_y fields when the models include heterogeneous reactions.

Figure F-9. Contours of the difference between model NO_y (with heterogeneous reactions) and LIMS "psuedo-NO_y" ((model - LIMS)/LIMS in percent) for both December and March. Panels a-b are for AER, c-d are CAMED, e-f are GSFC, g-h are ITALY, i-j are LLNL, k-l are MRI, m-n are NCAR, and o-p are for WASH.

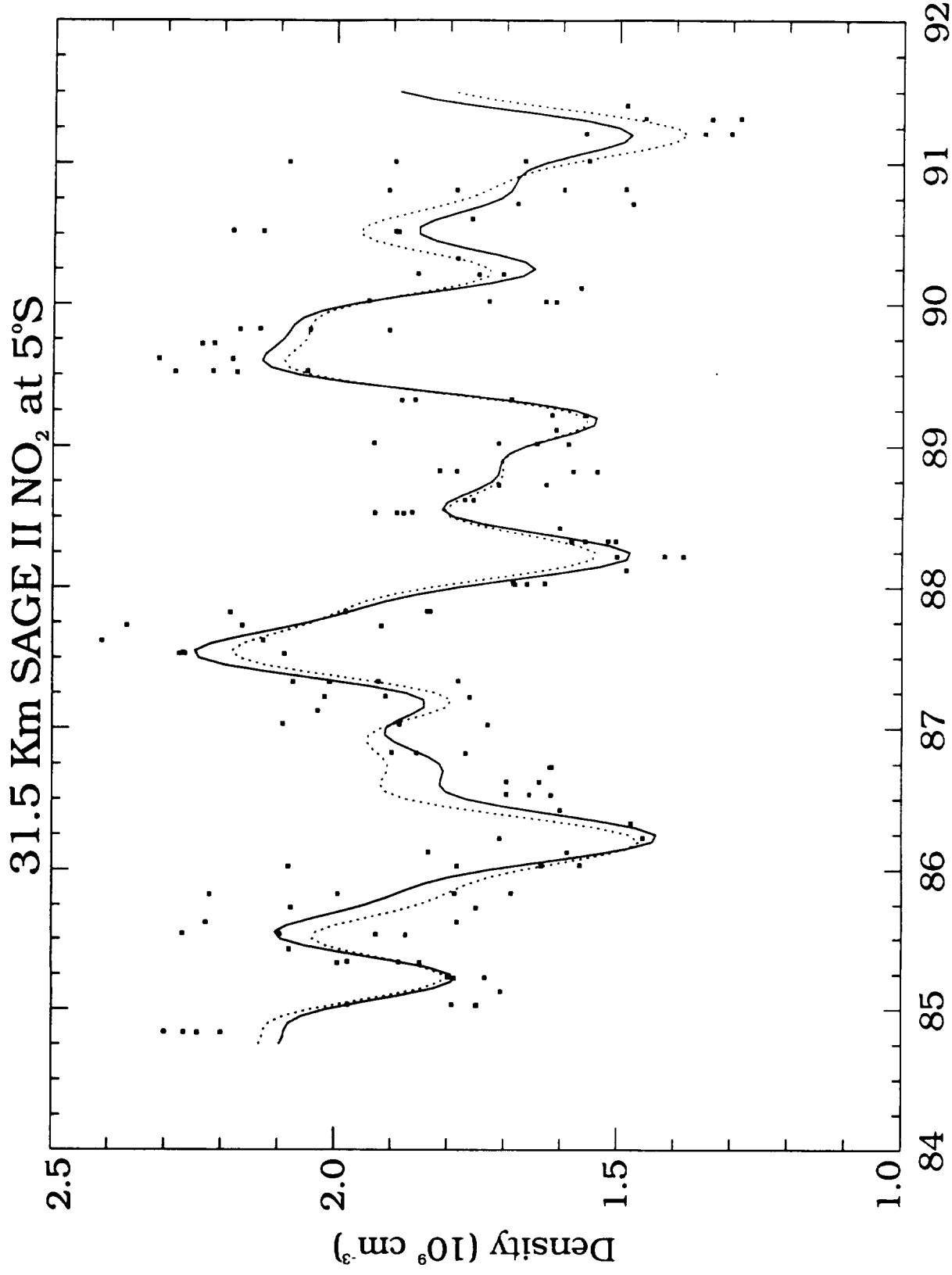
31.5 Km SAGE II NO_2 at 5°S
Density (10^9 cm^{-3})
2.5
2.0
1.5
1.0
84
85
86
87
88
89
90
91
92
Time (yr)

Figure F-1

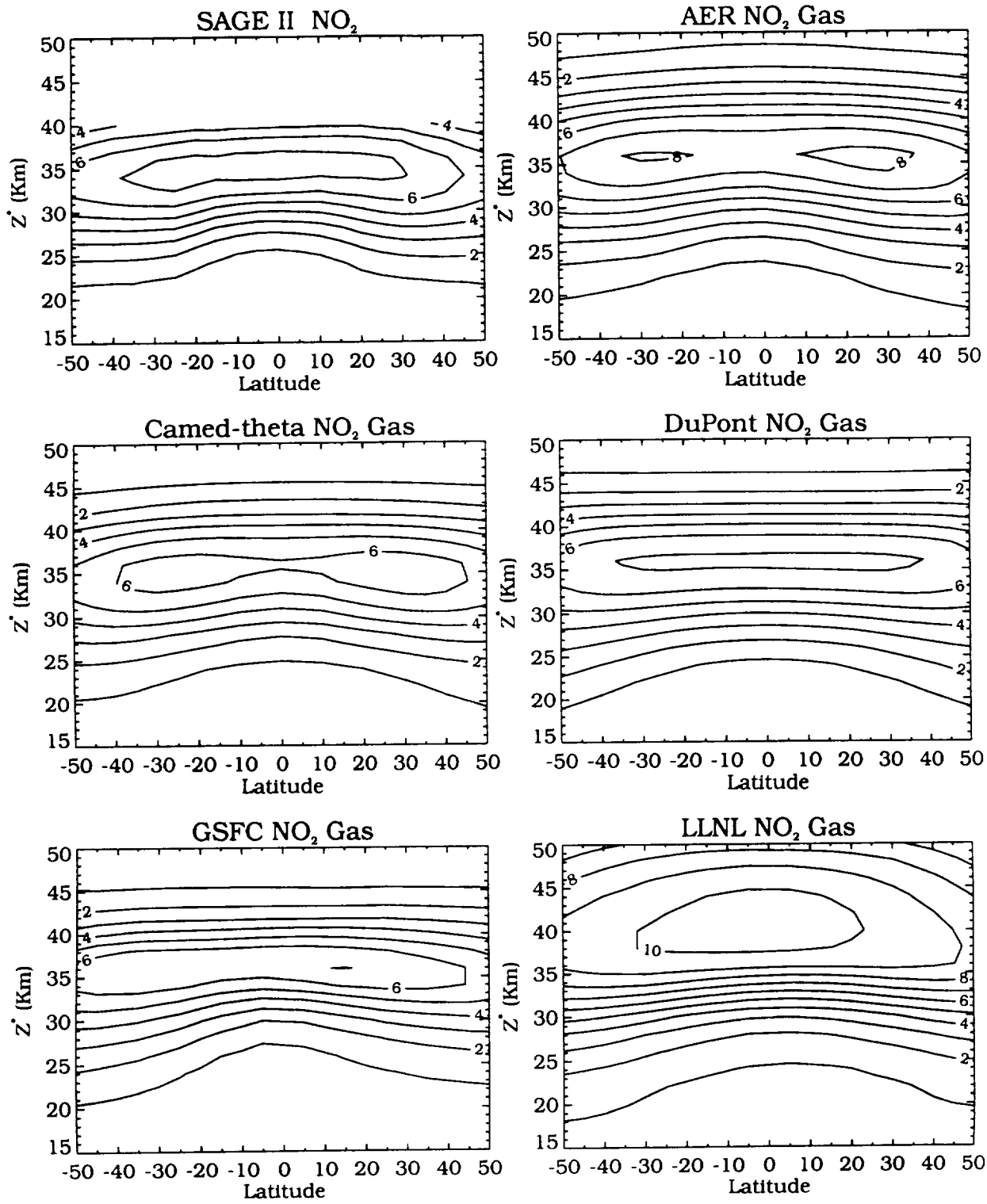
SAGE II NO2
AER NO2 Gas
Camed-theta NO2 Gas
DuPont NO2 Gas
GSFC NO2 Gas
LLNL NO2 Gas
Z* (Km)
Latitude
50
45
40
35
30
25
20
15
-50 -40 -30 -20 -10 0 10 20 30 40 50

Figure F-2

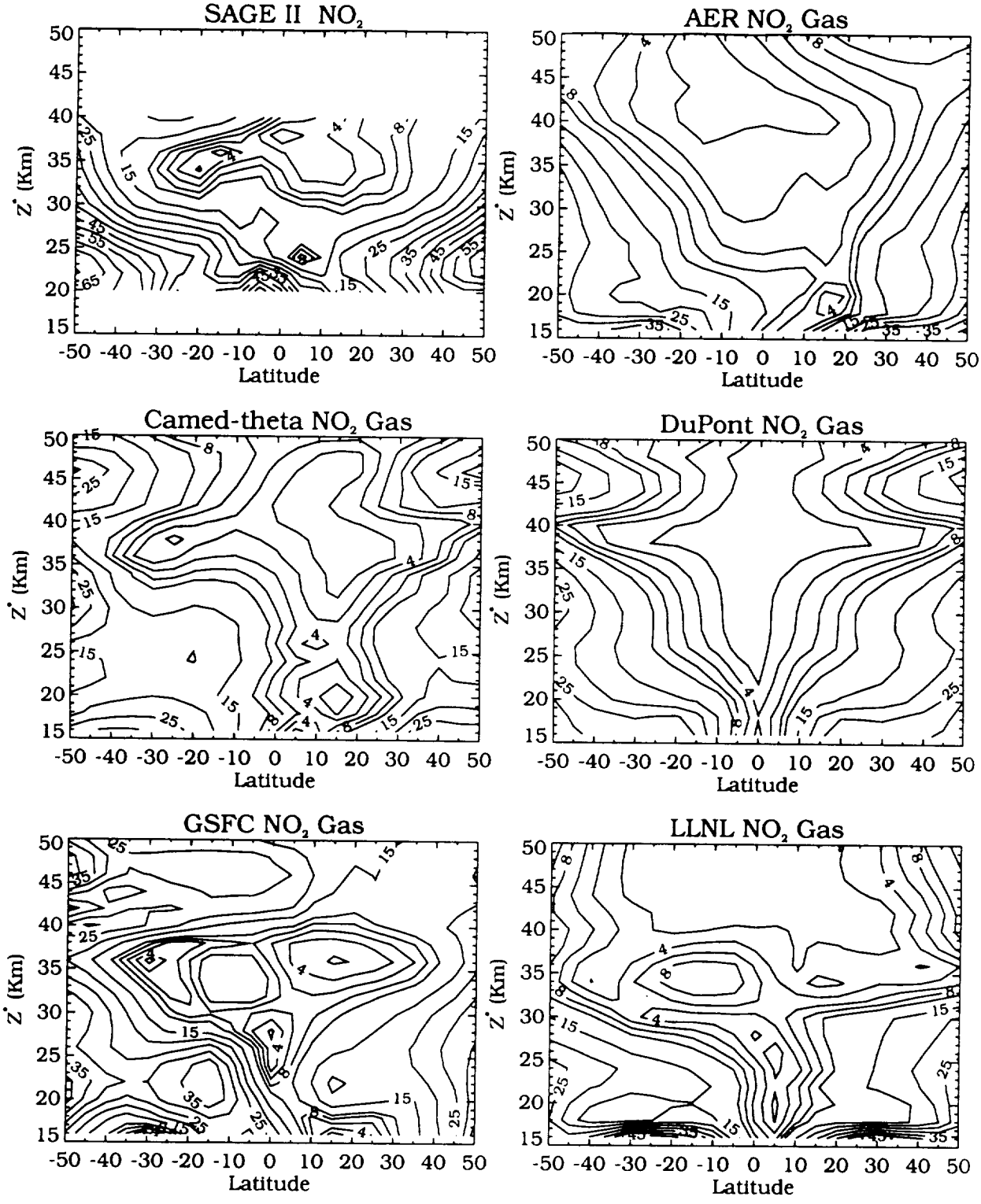
SAGE II NO2
AER NO2 Gas
Camed-theta NO2 Gas
DuPont NO2 Gas
GSFC NO2 Gas
LLNL NO2 Gas
Z* (Km)
Latitude
-50 -40 -30 -20 -10 0 10 20 30 40 50

Figure F-3

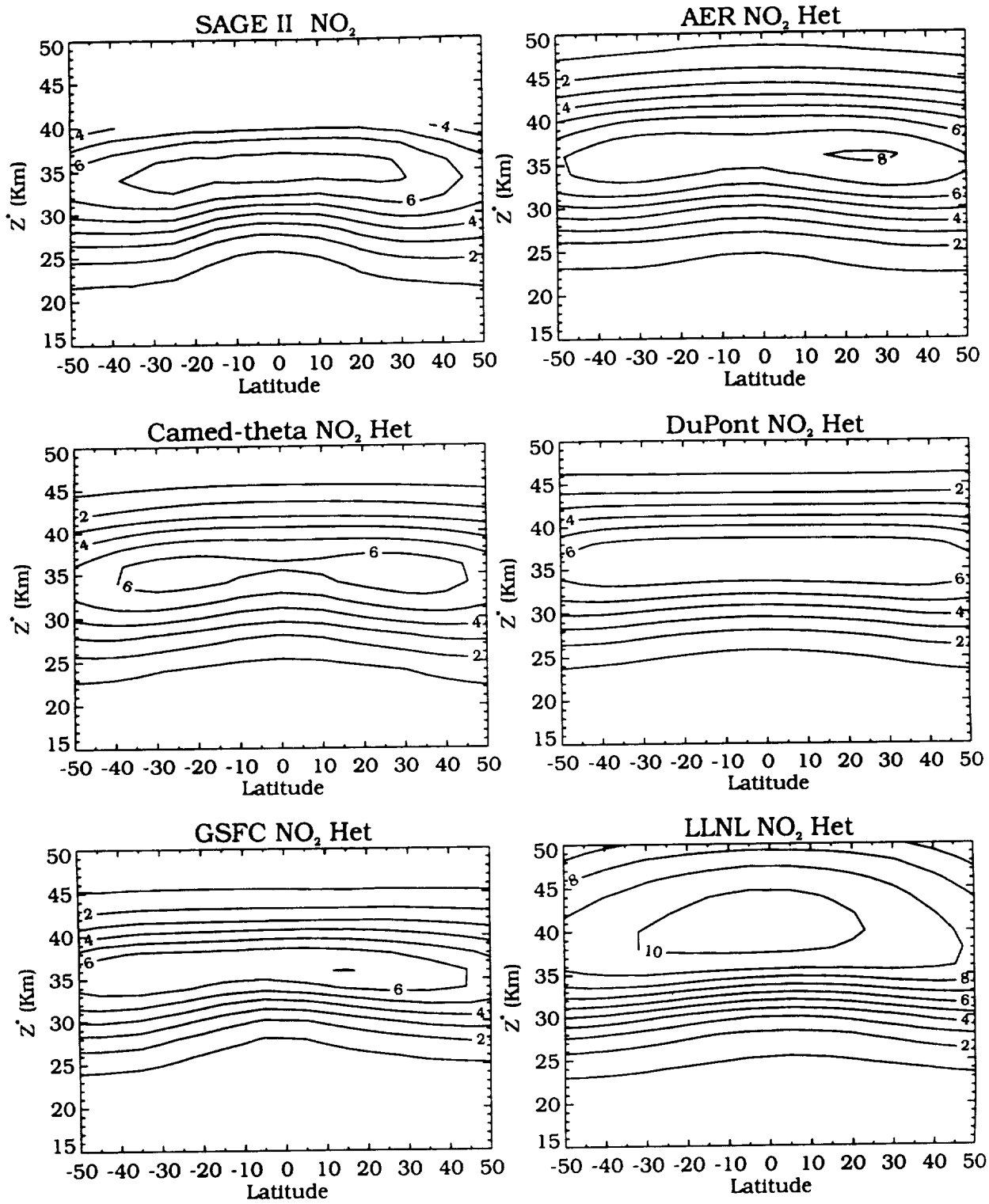
SAGE II NO2
AER NO2 Het
Camed-theta NO2 Het
DuPont NO2 Het
GSFC NO2 Het
LLNL NO2 Het
Z* (Km)
Latitude
50
45
40
35
30
25
20
15
-50 -40 -30 -20 -10 0 10 20 30 40 50
2
4
6
8
10

Figure F-4

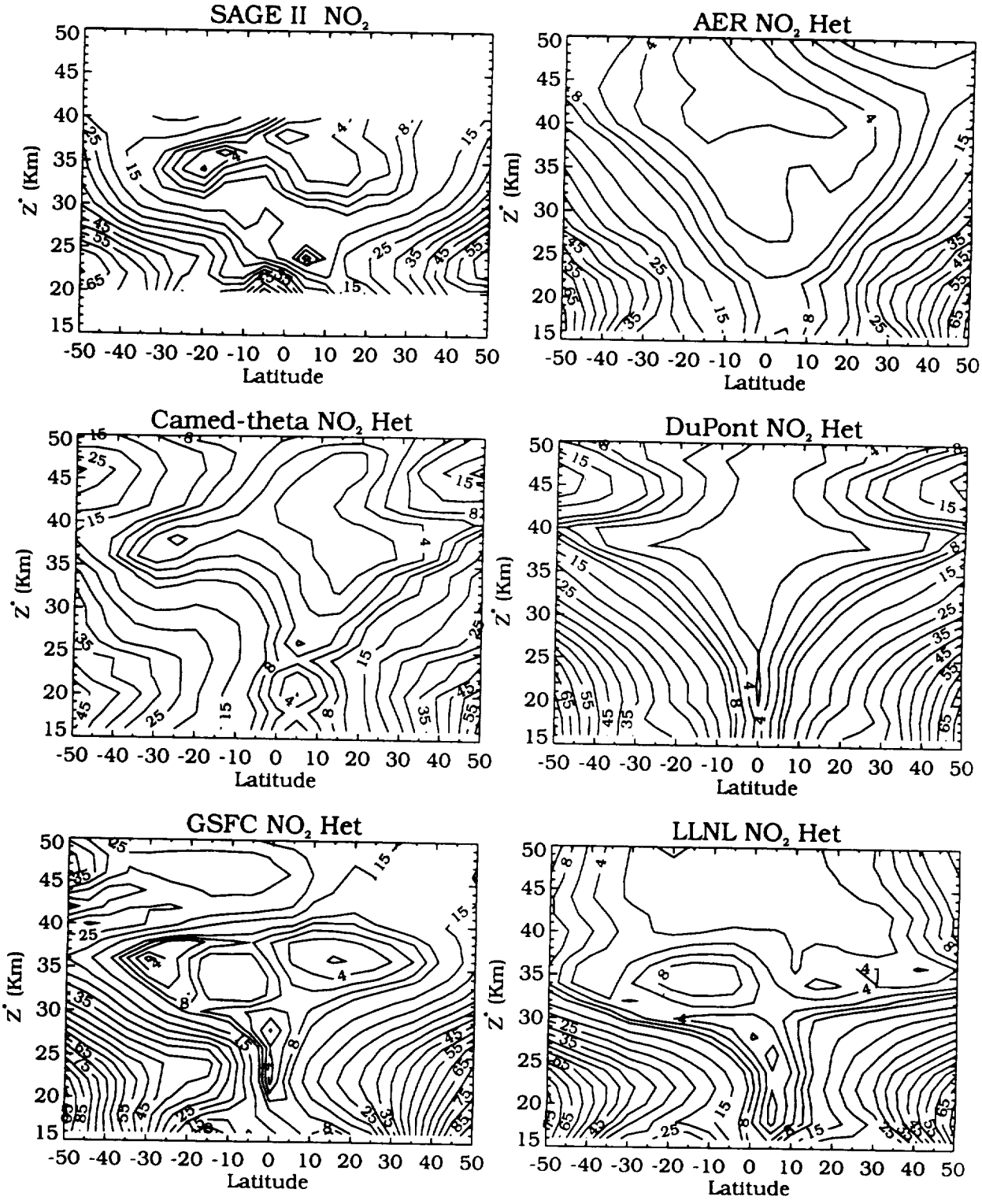
SAGE II NO2
AER NO2 Het
Camed-theta NO2 Het
DuPont NO2 Het
GSFC NO2 Het
LLNL NO2 Het
Z* (Km)
Latitude
50
45
40
35
30
25
20
15
-50 -40 -30 -20 -10 0 10 20 30 40 50

Figure F-5

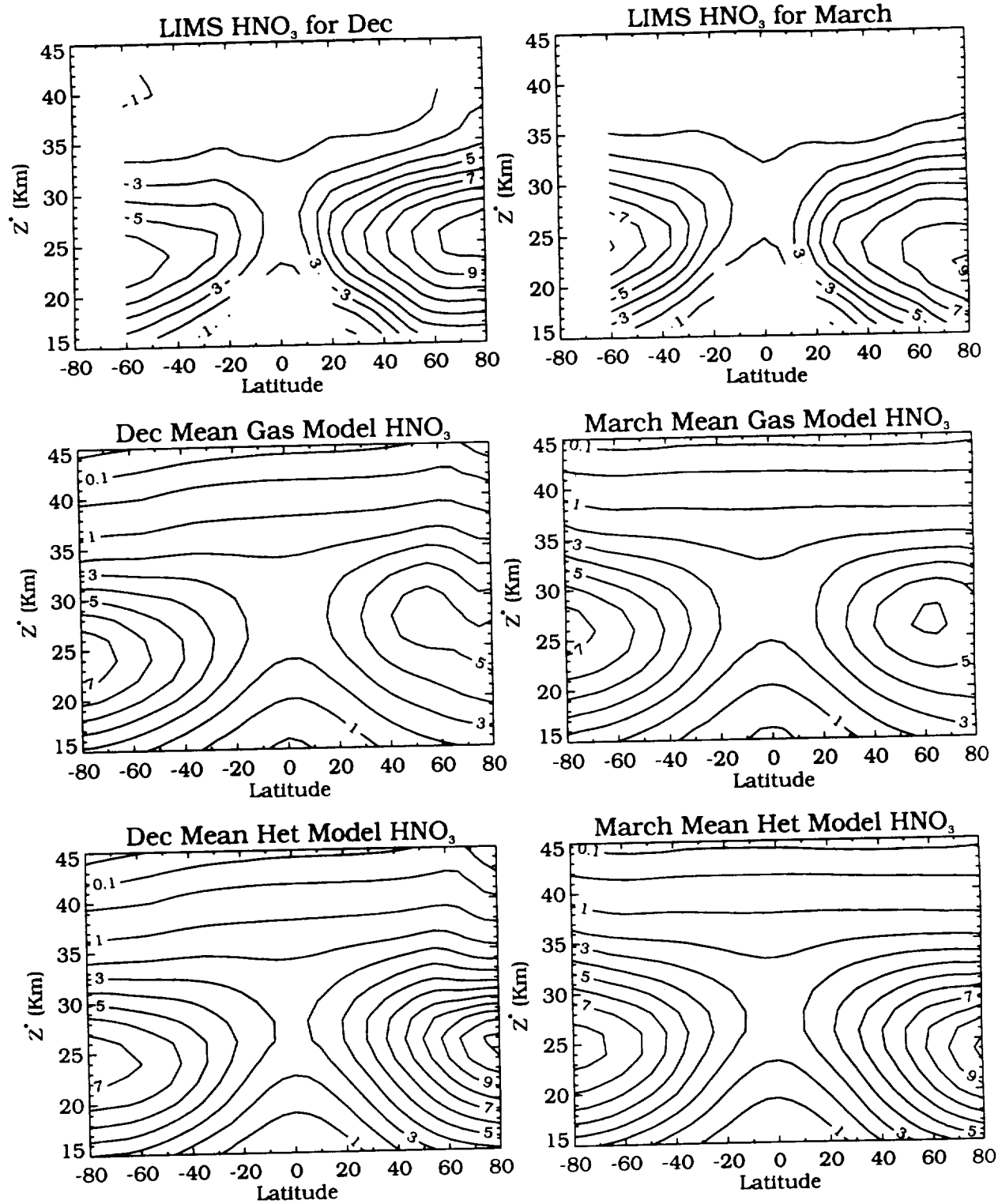
LIMS HNO3 for Dec
LIMS HNO3 for March
Dec Mean Gas Model HNO3
March Mean Gas Model HNO3
Dec Mean Het Model HNO3
March Mean Het Model HNO3
Z* (Km)
Latitude

Figure F-6

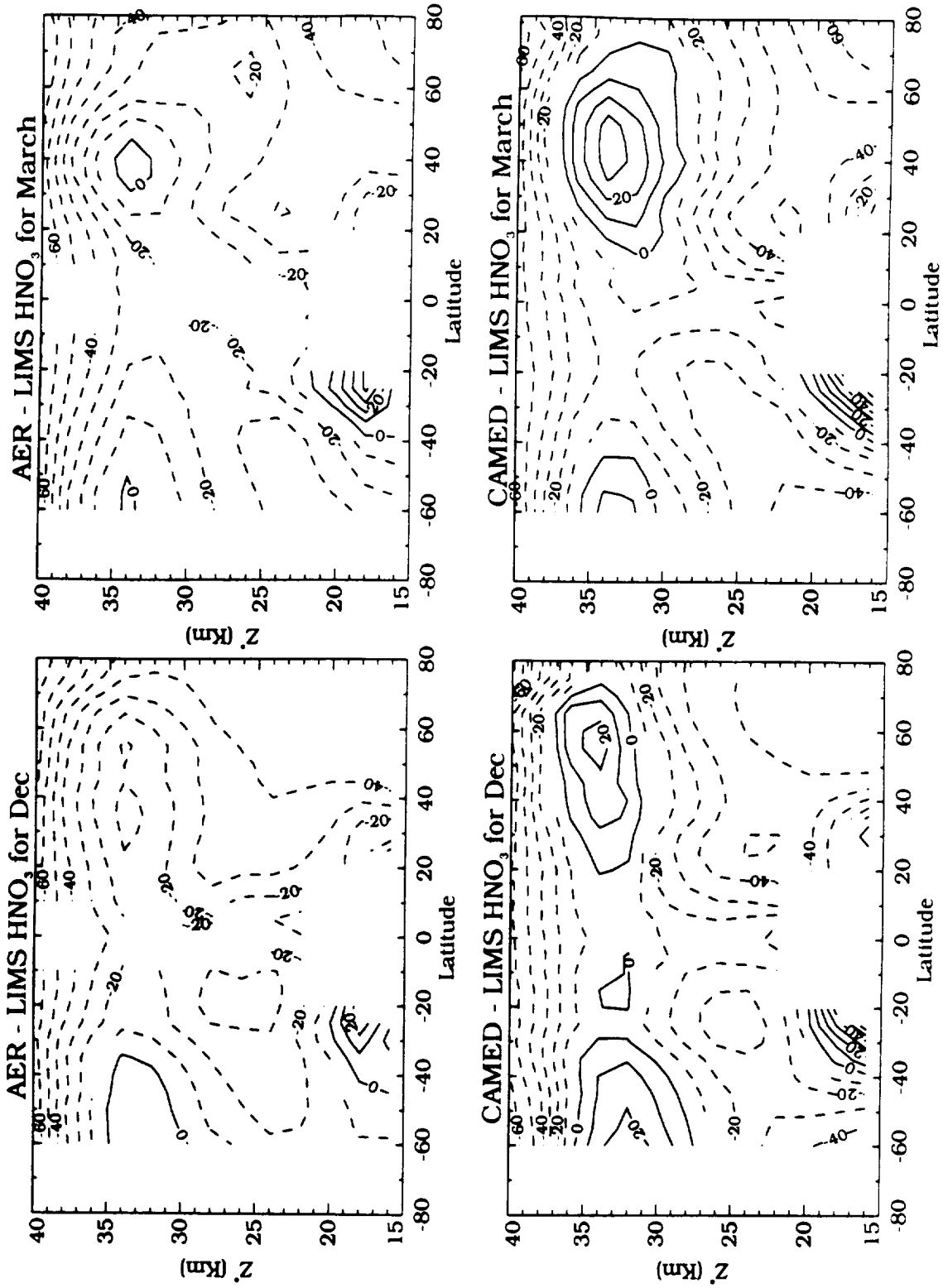
AER - LIMS HNO3 for March
CAMED - LIMS HNO3 for March
AER - LIMS HNO3 for Dec
CAMED - LIMS HNO3 for Dec
Z* (Km)
Latitude

Figure F-7

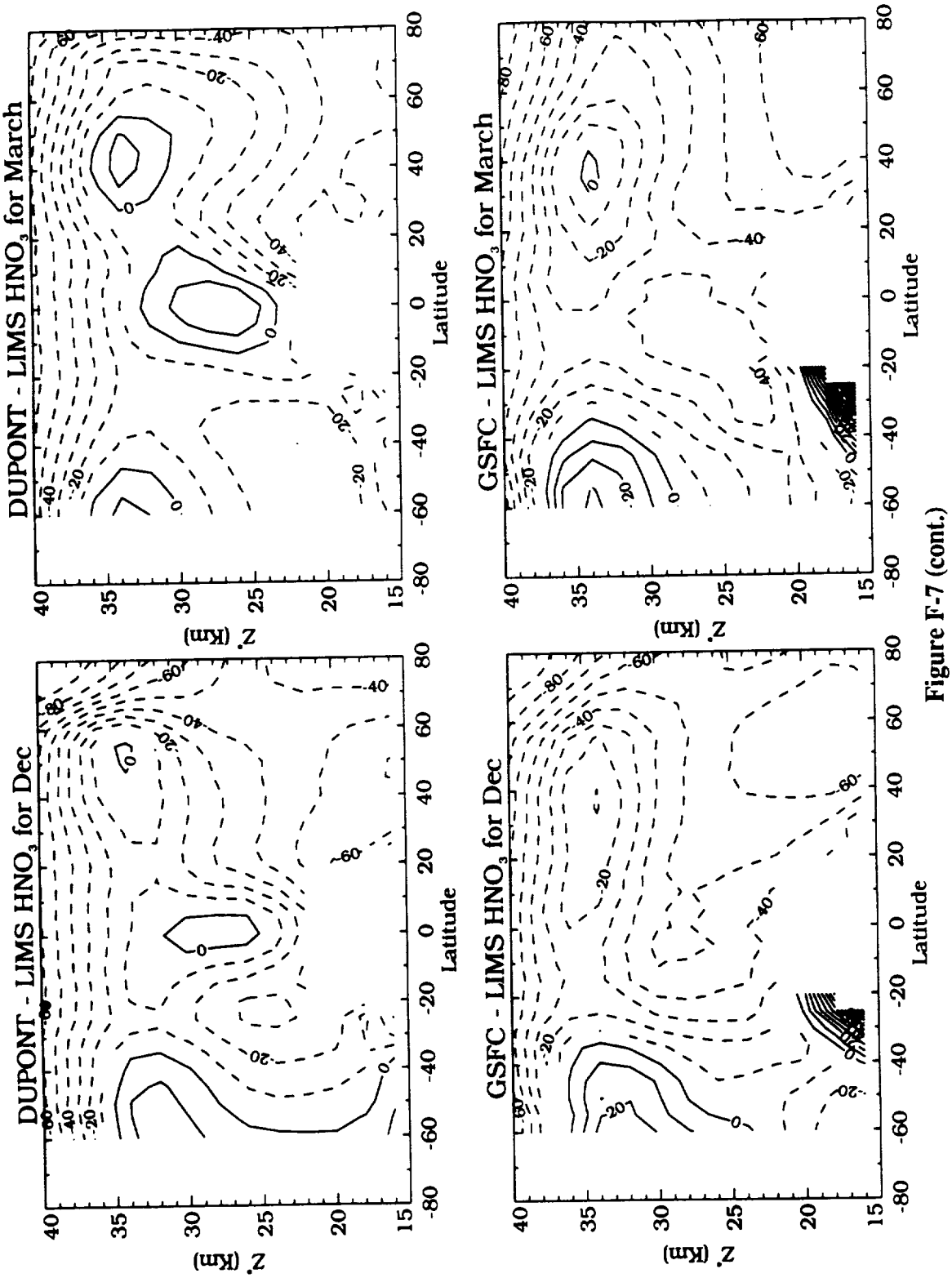

Figure F-7 (cont.)

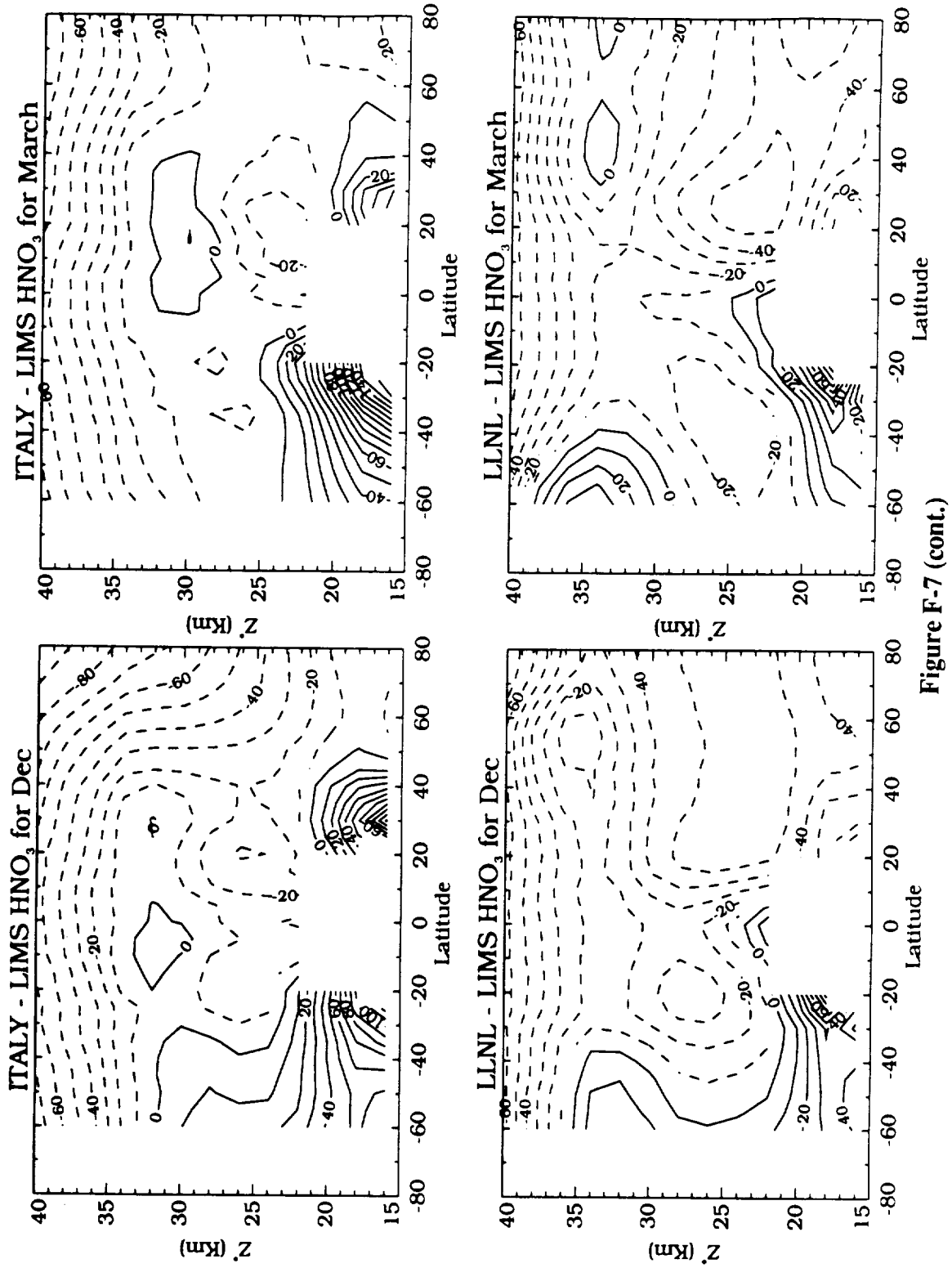

Figure F-7 (cont.)

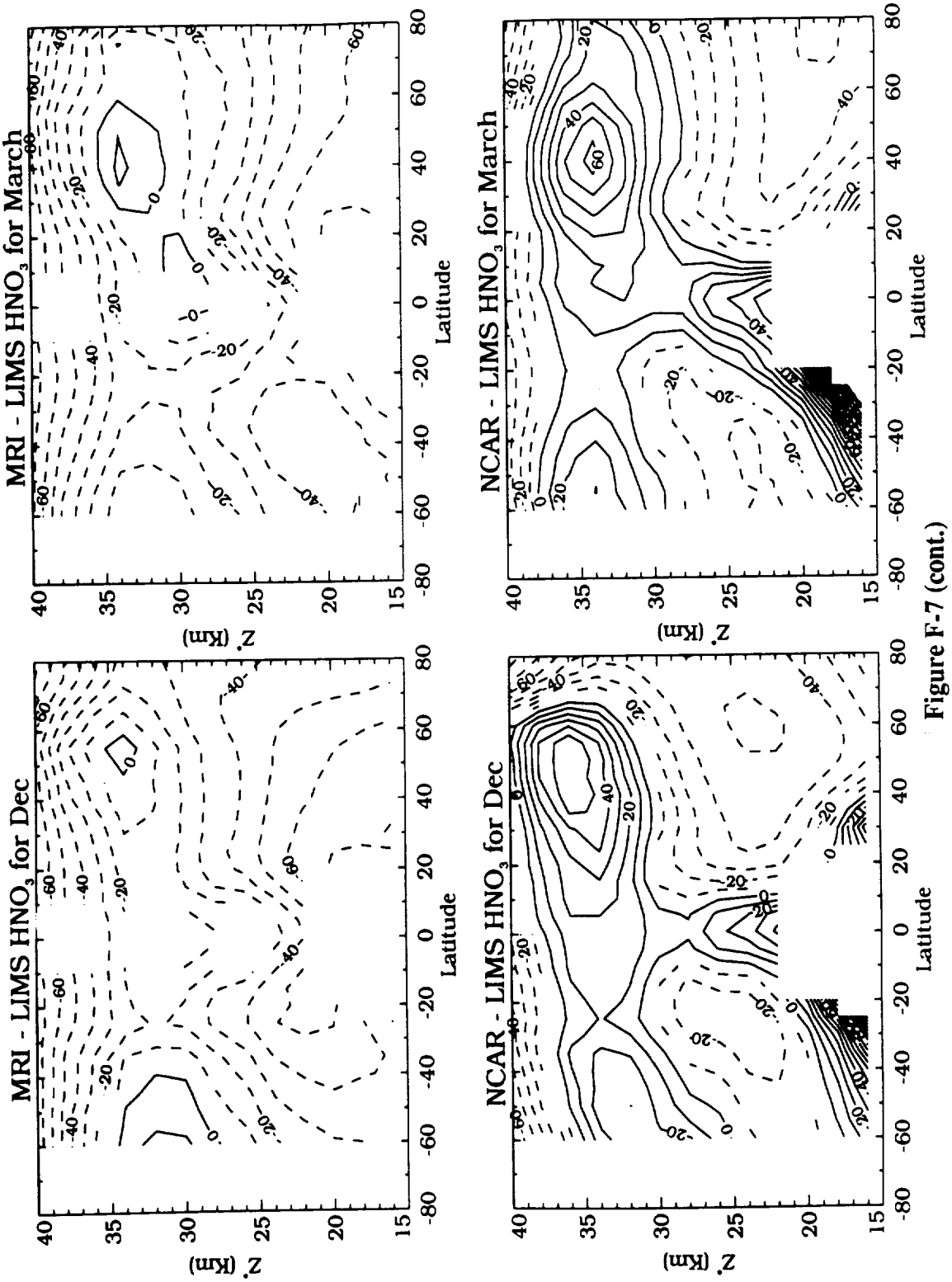

Figure F-7 (cont.)

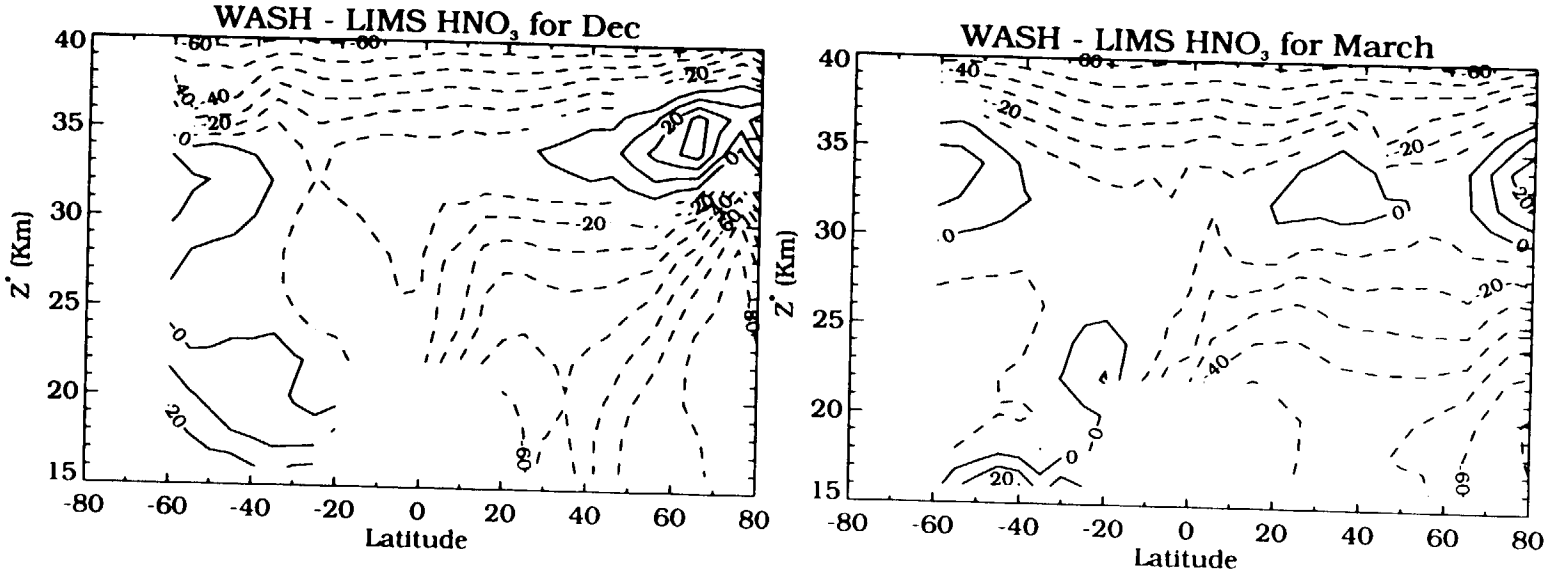

Figure F-7 (cont.)

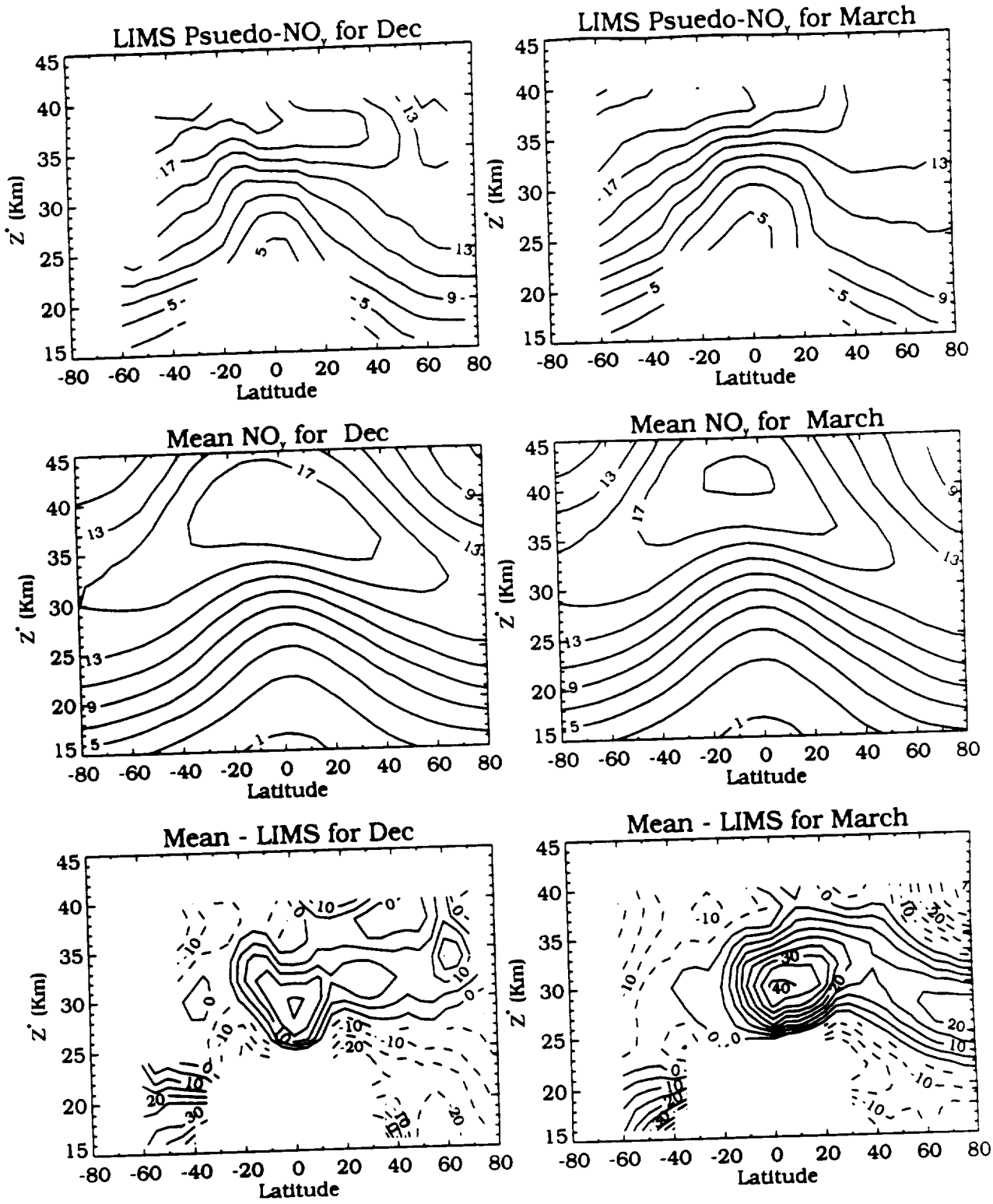
LIMS Psuedo-NOy for Dec
LIMS Psuedo-NOy for March
Mean NOy for Dec
Mean NOy for March
Mean - LIMS for Dec
Mean - LIMS for March
Z* (Km)
Latitude

Figure F-8

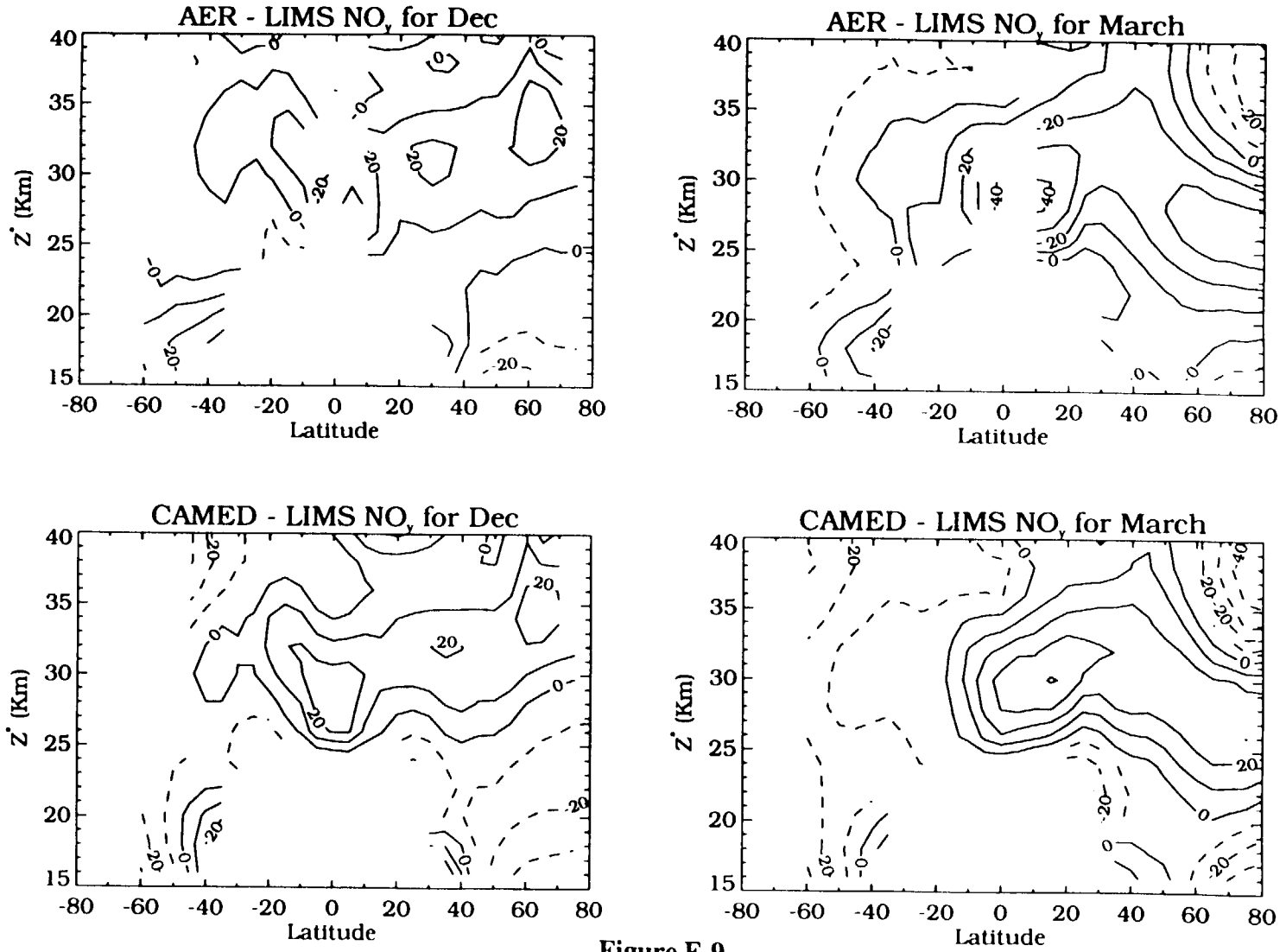
AER - LIMS NO$_y$ for Dec
AER - LIMS NO$_y$ for March
CAMED - LIMS NO$_y$ for Dec
CAMED - LIMS NO$_y$ for March
Z* (Km)
Latitude
40
35
30
25
20
15
-80 -60 -40 -20 0 20 40 60 80

Figure F-9

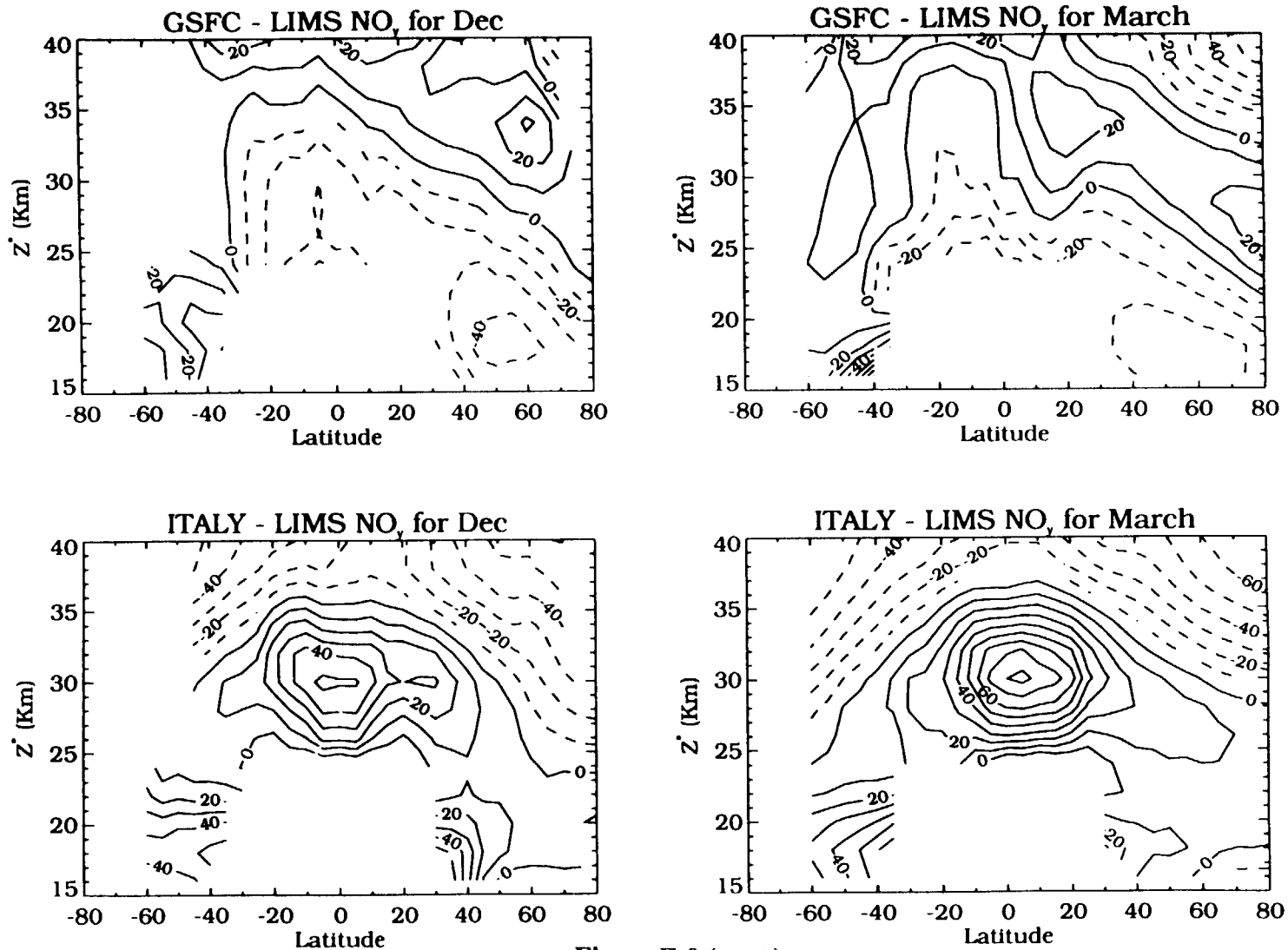

Figure F-9 (cont.)

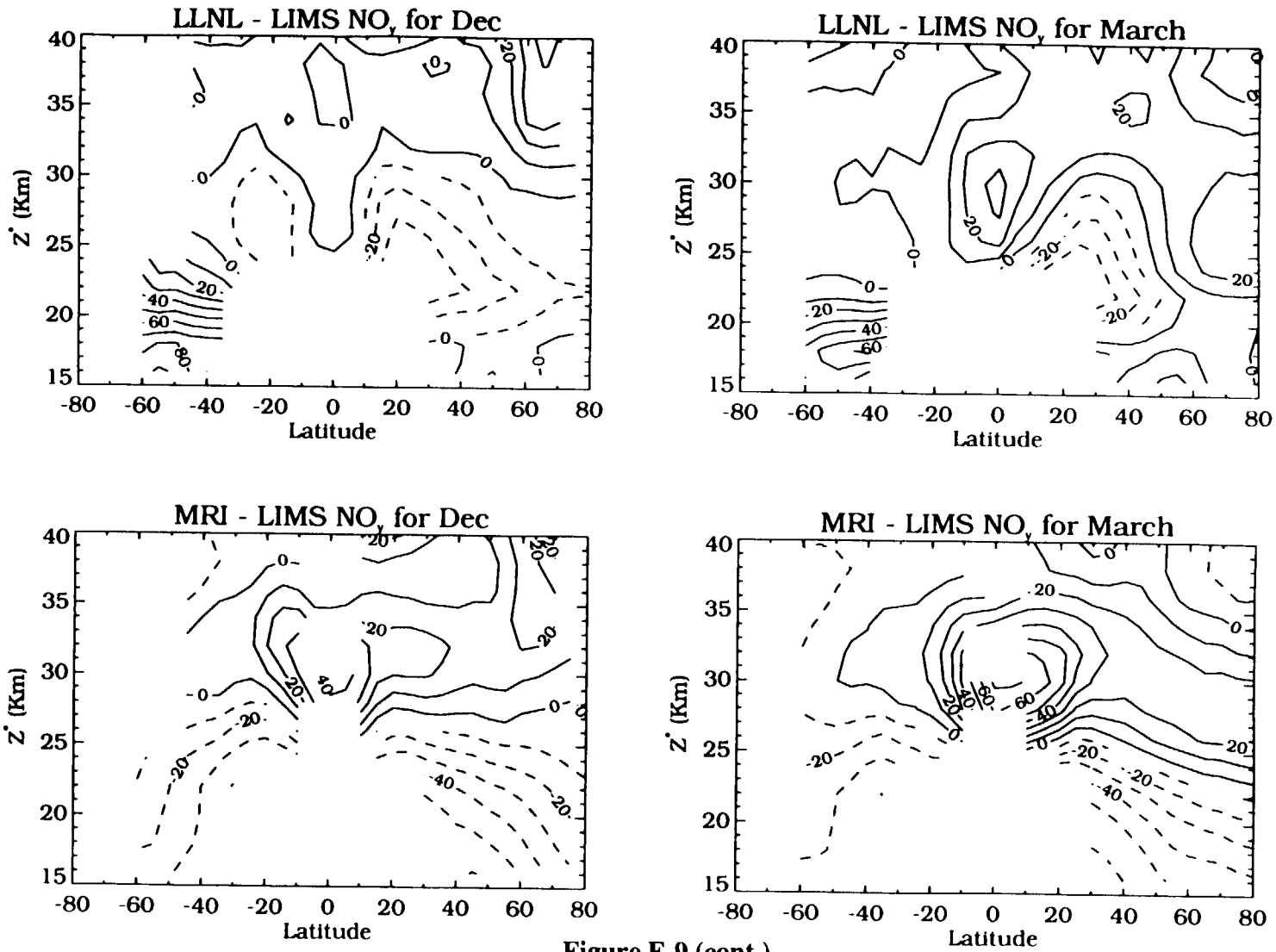

Figure F-9 (cont.)

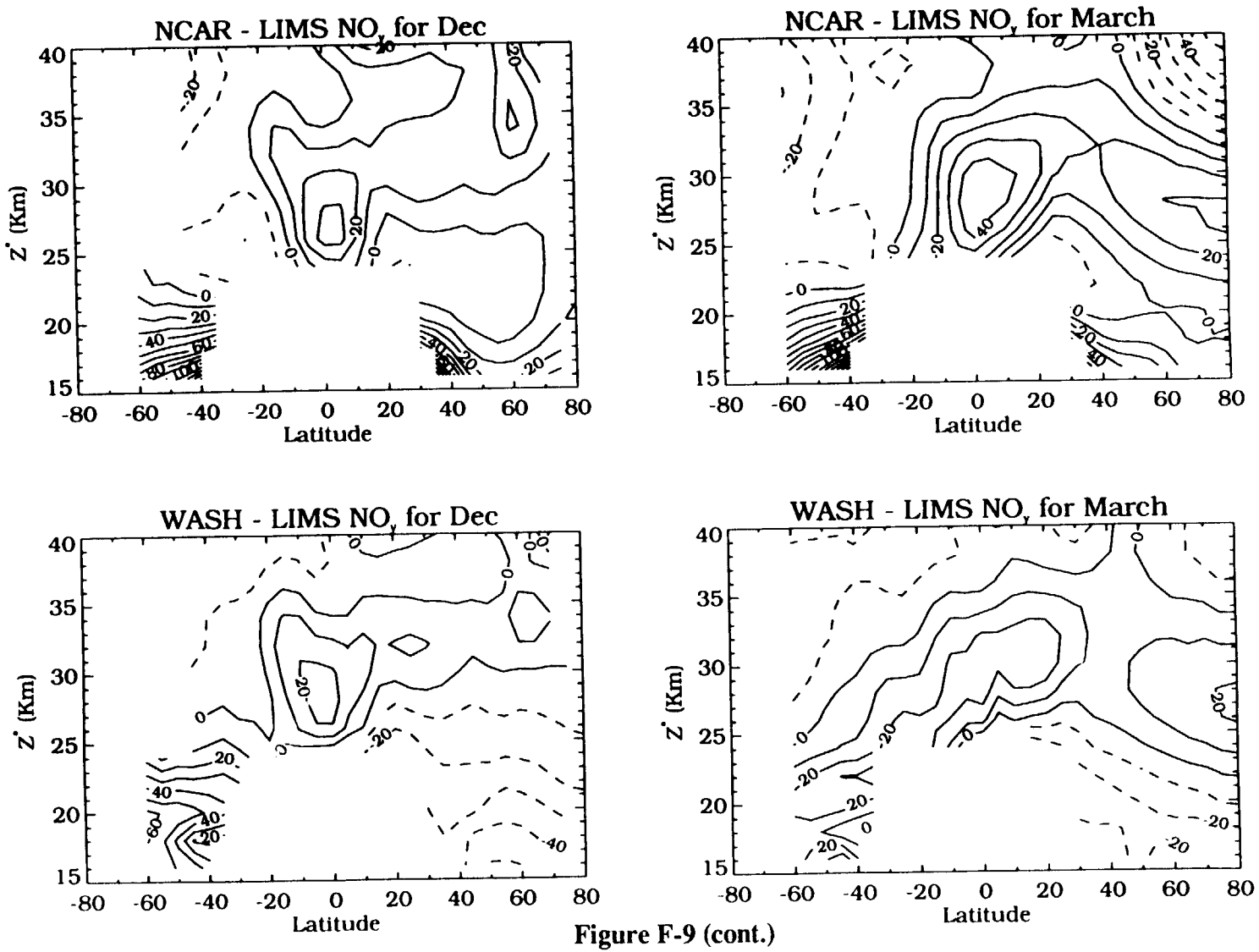

Figure F-9 (cont.)

G: Column Abundances of HF, HCl, HNO_3, $ClONO_2$ and NO_2

G: Column Abundances of HF, HCl, HNO_3, $ClONO_2$, and NO_2

Curtis P. Rinsland
NASA-Langley Research Center

In each section of this report the observational data and their uncertainties are first discussed; then the most important results of the model-measurement comparisons are reported.

Column amounts have been calculated from the model data provided to the High-Speed Research Program (HSRP) data base. Let C(x) be the column amount for species x where

$$C(x) = \int f_x(z)\, n(z)\, dz \tag{1}$$

and $f_x(z)$ and n(z) are the volume mixing ratio of species x and the atmospheric number density at altitude z, respectively. From the hydrostatic equation

$$dp = -\, g(z)\, n(z)\, M\, dz \tag{2}$$

where p is the pressure, g(z) is the gravitational acceleration, and M is the mean molecular weight of air. Substituting (2) into (1) yields the expression

$$C(x) = -\,(1/M) \int [f_x(p)/g(p)]\, dp \tag{3}$$

which has been computed from the HSRP gridded data with the expression

$$C(x) = (1/M) \sum_{i=2}^{N} [p(i-1)-p(i)]\; f_x\; \bar{g} \tag{4}$$

where

$$f_x = [f_x(i) + f_x(i-1)]/2 \tag{5}$$

$$\bar{g} = [g(i) + g(i-1)]/2 \tag{6}$$

and the summation is from layer 1 to layer N. The calculations include the variation of the acceleration of gravity with altitude and latitude.

HYDROGEN FLUORIDE (HF) AND HYDROGEN CHLORIDE (HCl)

Observational Data

Measurements of HF and HCl column amounts above a constant pressure level of 197 mb (11.9 km altitude) have been reported based on airborne solar absorption spectra recorded with the NCAR Fourier transform spectrometer between latitudes of 4.6N to 70.8N (Mankin and Coffey, 1983). The observations were recorded between January 1978 and July 1982. Mankin and Coffey (1983) fitted the measured column amounts C to the expression

$$C = \mathbf{a} + \mathbf{b} \cos \phi \tag{7}$$

where **a** and **b** are constants determined for each gas and ϕ is the latitude. The spectra were recorded during both summer and winter. Mankin and Coffey (1983) found no apparent seasonal difference in the columns for either gas. Seasonal variations of about ±10% have been deduced from ground-based total column measurements of HF and HCl (Zander et al., 1987a,b; Rinsland et al., 1991a).

Mankin and Coffey (1983) estimated that their measured column amounts have an absolute accuracy of 20%-25% and a precision of ~10%. However, simultaneous infrared aircraft measurements of stratospheric HF and HCl recorded during the Airborne Antarctic Ozone Expedition (AAOE) and Airborne Arctic Stratospheric Expedition (AASE) missions by the NCAR and JPL groups show large systematic differences. Compared with the NCAR column measurements, the retrieved JPL columns are about a factor of 1.7 higher for HF and a factor of 1.4 higher for HCl (G. C. Toon, private communication, 1992; *see also* Figure 2 of the article by Kaye et al. [1991]). The aircraft latitudinal surveys of HCl by Girard et al. (1983) and Karcher et al. (1988) also suggest that the Mankin and Coffey (1983) HCl values may be low by 40%. The cause of these differences is under investigation (M. T. Coffey, private communication, 1992). However, on a relative basis, the NCAR and JPL measurements are highly consistent (M. T. Coffey, private communication, 1992). The methods used to derive the 1978-1982 NCAR aircraft total columns (Mankin and Coffey, 1983) are consistent with those adopted in analyzing the NCAR measurements from the AAOE and AASE missions (M. T. Coffey, private communication, 1992).

To investigate the ability of the models to predict seasonal variations, HF columns above Kitt Peak (latitude 31.9N, altitude 2.09 km) have been computed for 1980 using the equations for case C defined in section 3 and the corresponding best-fit coefficients in Table 4 of Rinsland et al. (1991a). Estimates of the random and systematic errors in the Kitt Peak column measurements are reported in section 3.7 of the Rinsland et al. (1991a) article.

Model-Measurement Comparisons for HF

Model hydrogen fluoride columns for comparison with the aircraft measurements have been obtained by integrating the model profiles above $z^* = 12$ km. As expected, the columns computed by each group with gas phase chemistry alone did not differ significantly from those computed with lower-limit heterogeneous chemistry. Only the 1980 HF model runs have been compared with the 1978-1982 aircraft measurements because of the rapid rate of increase of the HF column (Zander et al., 1987; Rinsland et al., 1991a).

Four modeling groups (AER, GSFC, NCAR, and WASH) provided HF calculations. Of these, only GSFC and NCAR included the two relatively long-lived intermediate species COF_2 and COClF in their model runs. AER included COF_2, but an error was found in the production term (the model had COF_2 producing one HF molecule instead of two). This problem will be corrected (D. Weisenstein, private communication, 1992). To compare the abundances of COF_2 and COClF relative to HF, see the article by Kaye et al. (1991).

Figure G-1 shows the comparison of the model results with aircraft columns computed with equation (7) and the coefficients from Table 3 of Mankin and Coffey (1983). The comparison is restricted to the latitude range 5N to 70N to be consistent with the limits of the observational data (Mankin and Coffey, 1983). For each group, the model results are an average of values for the 5 months during which the aircraft measurements took place (December, January, February, June, and July). As illustrated in the figure, all of the models predict a poleward increase in the HF total column similar to the increase shown by aircraft measurements, but there are large differences in the absolute values of the model columns. The ratio of the model-calculated column to the aircraft

column has been computed at every 5 degree latitude between 5N and 70N. These values are given along with the average and standard deviation of the ratios in Table G-1. The following conclusions can be reached from the data in Figure G-1 and Table G-1:

- The absolute amounts computed by the GSFC and NCAR models are in better agreement with the aircraft data than the AER and WASH model values. However, if the aircraft columns are low by a factor of 1.7, as suggested by the JPL vs. NCAR aircraft column measurement comparisons, the AER model results would be in the best agreement with a corrected aircraft data set. The WASH model columns are too high.

- The NCAR model results are most successful in reproducing the measured latitudinal variation of the aircraft measurements. The GSFC model columns also agree very well with the observations, but the decrease below 30N is slightly more rapid than shown by the measurements. The WASH model columns do not increase as rapidly above 50N as the measurements.

Figure G-2 compares the calculated 1980 Kitt Peak HF columns with columns derived by integrating the 1980 30N gas phase model profiles above $z^* = 2$ km. To examine the seasonal variation, the value for each month has been divided by the 1980 annual mean. These "normalized" seasonal cycles are shown in Figure G-3 along with the Kitt Peak values normalized in the same fashion. The following conclusions can be reached from this figure:

- The GSFC model simulates very well the relative amplitude and phase of the Kitt Peak seasonal variations. An earlier study (Kaye et al., 1991) found that the GSFC model also did a good job in reproducing the phase of the HF seasonal cycle observed at the ISSJ (Jungfraujoch) station (46.5N), but the relative amplitude of the HF seasonal cycle was underestimated by the GSFC model.

- The WASH model reproduces very well the phase of the Kitt Peak seasonal cycle, but the model-calculated relative seasonal cycle amplitude is too high by about 50%.

- The NCAR model predicts a HF maximum in winter, whereas the Kitt Peak observations show a springtime maximum. The relative amplitude predicted by the NCAR model is less than the measured relative amplitude.

- In contrast to earlier AER model calculations (Rinsland et al., 1991a), the AER results in Figures G-2 and G-3 significantly underestimate the amplitude of the HF seasonal cycle. The difference is likely the result of changes in the treatment of the chemistry in the AER model (D. Weisenstein, private communication, 1992). Both the AER results presented in the present work and the earlier study (Rinsland et al., 1991a) predict a HF seasonal cycle maximum that occurs later in the year than indicated by the Kitt Peak measurements.

MODEL-MEASUREMENT COMPARISON FOR HCl

Nine groups provided hydrogen chloride model calculations. All except WASH provided both gas phase and lower-limit heterogeneous chemistry calculations.

There are significant differences among the model predictions of heterogeneous chemistry effects for HCl. To illustrate these differences, the ratio R has been computed where

$$R = H/G \tag{8}$$

and H is the 1980 HCl column above $z^* = 12$ km computed with lower-limit heterogeneous chemistry and G is the 1980 HCl column above $z^* = 12$ km computed with only gas phase chemistry. Figure G-4 shows contour maps of G and the ratio R as a function of latitude and season for the eight models. The following comments are based on an examination of the results in Figure G-4:

- The lower-limit heterogeneous chemistry calculations by GSFC and NCAR predict wintertime HCl columns at high latitudes that are ~30% lower than those computed with only gas phase chemistry. The differences are negligible between 45N and 45S.

- The lower-limit heterogeneous chemistry calculations by the ITALY group predict a wintertime enhancement in the HCl column at high latitudes in the northern hemisphere. These model results run counter to expectations that HCl should undergo heterogeneous loss. The ITALY model predicts ~10% changes in the HCl columns at high latitudes in the southern hemisphere; the heterogeneous chemistry calculations produce both enhancements and depletions of HCl relative to the standard gas phase calculations.

- The other models do not predict significant HCl column changes due to lower-limit heterogeneous chemistry ($0.9 \leq R \leq 1.1$).

It should be noted that the HCl observations during AAOE and AASE are extremely non-zonal (e.g., Kaye et al., 1990) so that while the above model-model differences are interesting, model-measurement comparisons of high-latitude wintertime HCl are not appropriate without detailed modeling of the observing conditions. This should be kept in mind during the following discussion.

As for HF, the model-generated HCl columns were obtained by integrating the 1980 model profiles above $z^* = 12$ km and then averaging over the 5 months of the NCAR aircraft measurements (Mankin and Coffey, 1983). The aircraft columns were computed with Eq. 7 and the appropriate coefficients from Table 3 of Mankin and Coffey (1983).

Figure G-5 shows the 1980 steady-state, gas phase model columns and aircraft data plotted as a function of latitude. Table G-2 provides a quantitative comparison of these data in the same format as Table G-1. Corresponding data for the 1980 steady-state lower-limit heterogeneous chemistry runs are given in Figure G-6 and Table G-3. The following comments are derived from inspection of these figures and tables:

- Most of the model-computed HCl columns are higher than the Mankin and Coffey (1983) columns. This may reflect problems with the aircraft absolute amounts and/or the limitations of the models. In most cases the model-measurement agreement would be improved if the aircraft data were increased by the factor of 1.4 discussed previously.

- At low latitudes, the model-measurement ratios are about two for CAMED and NCAR; these ratios are too large to attribute to aircraft data calibration uncertainties alone.

- In all cases, the latitudinal increase in HCl is less rapid in the models than in the Mankin and Coffey (1983) data. On a relative basis, the DUPONT gas phase model results best reproduce the measurements by Mankin and Coffey (1983).

- The heterogeneous model results from GSFC, and to a lesser extent those from MRI and NCAR, do not agree with the shape of the Mankin and Coffey latitudinal curve, especially above about 40N.

NITRIC ACID (HNO_3)

Column data for the nitric acid model-measurement comparison were derived from the LIMS satellite measurements (Gille et al., 1984), which span the November 1978 to May 1979 time period. The retrieved nighttime volume mixing ratios have been integrated above 100 mb except between 16S and 16N latitude where, because of interference due to emission from cirrus clouds, the integration was performed above the 70 mb level. The LAMAT data product (Remsberg et al., 1990) was used in computing the columns. Figure G-7 shows the LIMS HNO_3 columns as a function of latitude and season. To match these observations as closely as possible, columns were computed from the model-derived HNO_3 volume mixing ratios by integrating above $z^* = 16$ km except between 16S and 16N where the integration extended above $z^* = 18$ km.

The precision and accuracy of the LIMS HNO_3 column measurements have been reported by Gille et al. (1984). Based on the values shown in their Table 1, the LIMS HNO_3 columns are estimated to have absolute accuracies of about 35%. The precision of the HNO_3 columns is about 5%, as deduced from Figure 4 of Gille et al. (1984).

Before comparing the models with measurements, it is interesting to note the large increases in HNO_3 predicted when lower-limit heterogeneous chemistry is included in the model calculations. Figure G-8 shows contour maps of G and the ratio R as a function of latitude and season for the 1980 calculations of eight models where G and R are defined by Eq. 8. The column integrations have been performed as noted above. The following conclusions can be noted from these plots:

- All of the models predict increases in the HNO_3 column when lower-limit heterogeneous chemistry is included in the computations. The increases are largest in winter at high latitudes in both hemispheres.

- For most of the models, the increases in HNO_3 are significant at all latitudes and seasons except near the poles in summer when $R \sim 1.0$.

- There are significant model-to-model differences in R. The largest values of R are predicted by the GSFC model; the smallest are predicted by the ITALY and MRI models.

Ratios of the model-computed HNO_3 column to the LIMS column are listed as a function of latitude in Tables G-4 and G-5. The ratios are given for each month of the LIMS observations (November 1978 to May 1979) along with the corresponding LIMS nighttime column (in 10^{16} molecules cm^{-2}). Table G-4 presents the ratios for the standard gas phase model calculations; the ratios for the lower-limit heterogeneous model calculations are given in Table G-5. Mean and standard deviations of the ratios for each model are also given for each month. Figure G-9 shows model-by-model plots of column amount vs. latitude for the months of December 1978 and May 1979. Both gas phase and lower-limit heterogeneous chemistry model calculations are presented.

A few aspects of the results in Tables G-4 and G-5 and Figure G-9 are noted below:

- The range in the model columns is often a factor or two or more, with the largest differences occurring at high latitudes.

- The gas phase columns calculated by AER, CAMED, DUPONT, GSFC, and MRI consistently underestimate the measured LIMS columns, whereas the gas phase model calculations from the other groups are both higher and lower than the LIMS columns.

- All of the columns computed with standard gas phase chemistry underestimate the winter high northern latitude LIMS columns. The columns computed with lower-limit heterogeneous chemistry are much closer to the LIMS winter high-latitude data.

- The AER lower-limit heterogeneous model calculations provide the best overall agreement with the LIMS measurements. These calculations are mostly within 10% of the LIMS data, with maximum discrepancies never exceeding 20%. Several of the other lower-limit heterogeneous model calculations also do a good job in reproducing the LIMS measurements, for example, the LLNL model results.

- The general, improved model-to-LIMS HNO_3 agreement obtained with heterogeneous processing as compared to standard gas phase chemistry is consistent with the conclusions of Hofmann and Solomon (1989) and Considine et al. (1992).

- The NCAR model overpredicts the amount of tropical HNO_3. At the equator, the NCAR model-to-LIMS ratio is about 1.5 for the gas phase runs and 1.7 for the lower-limit heterogeneous chemistry runs.

The midlatitude and high-latitude seasonal variation of HNO_3 is a key challenge for modelers to reproduce. In Figure G-10, we present graphical comparisons of the seasonal variation of the HNO_3 columns measured near 45N with columns derived from the gas phase and lower-limit heterogeneous model calculations by the various groups. The ISSJ measurements were obtained between June 1986 and June 1990 at the International Scientific Station of the Jungfraujoch, Switzerland, which is at an altitude of 3.58 km and a latitude of 46.5N. The ISSJ curve in the figure shows a least-squares fit to the measurements, which assumes a sinusoidal seasonal cycle (Rinsland et al., 1991b). The LIMS curve shows the 45N nighttime data integrated above 100 mb. The model data have been integrated above $z^* = 4$ km. The following results can be noted from the figures:

- The ISSJ and LIMS HNO_3 show consistent seasonal cycles with the ISSJ columns higher than the LIMS HNO_3 columns by about 20%. The differences are likely the result of the contributions by layers below 100 mb to the ISSJ columns and errors in retrieving absolute HNO_3 amounts from the two data sets.

- The gas phase model calculations fail to predict the observed wintertime maximum in the HNO_3 column. The gas phase models predict maxima in the spring or summer.

- Although the absolute column amounts vary significantly, all of the lower-limit heterogeneous chemistry runs predict a HNO_3 column maximum in winter, in agreement with the ISSJ and LIMS measurements. The relative amplitude of the modeled seasonal cycle is roughly correct in all of the models.

CHLORINE NITRATE ($ClONO_2$)

Very few measurements of $ClONO_2$ column amounts have been reported. With the exception of high latitude values derived from IR aircraft spectra recorded during the AAOE and AASE missions (e.g., Coffey et al., 1989; Toon et al., 1989), the only published measurement is the single column amount derived from an average of early morning and late afternoon FTS solar absorption measurements at ISSJ in June 1986. The measured total column (Zander and Demoulin, 1988) is $(1.15 \pm 0.3) \times 10^{15}$ molecules cm^{-2} above the station. Column amounts above 18 and 20 km have also been derived by integrating the ATMOS/Spacelab 3 profiles measured near

30N (sunsets) and 48S (a single sunrise) (Zander et al., 1990). However, since the ATMOS/SL3 $ClONO_2$ measurements are considered as part of experiment M, we have restricted this study to a comparison of the model results with the single published ISSJ column (Zander and Demoulin, 1988).

Model $ClONO_2$ column amounts have been derived by integrating the model 45N profiles above $z^* = 4$ km. Figure G-11 shows the model data along with the measured ISSJ data point. Note the predicted seasonal variation and the predicted increase from 1980 to 1990. Because the ISSJ measurement was obtained in June 1986, nearly midway between the 1980 and 1990 model runs requested for this workshop, model values have been derived for the date of the ISSJ observation by linearly interpolating between the June 1980 and June 1990 model results. The diurnal variation of $ClONO_2$ is small below about 30 km (Ko and Sze, 1984, their Figure 6) so no attempt was made to restrict the selection of model runs on the basis of diurnal effects.

Table G-6 presents a comparison of the steady-state gas phase (SG) and steady-state lower-limit heterogeneous (SHL) model runs with the ISSJ column measurement. Several points of interest can be noted:

- Except for the MRI results, the $ClONO_2$ columns computed with LL-heterogeneous chemistry are 15% to 47% higher than the values computed with only gas phase reactions.
- Except for the AER results, all of the gas phase model results are below the measurement value (the WASH result, however, is within the quoted error bar).
- Except for the AER results, the lower-limit heterogeneous chemistry calculations are in better agreement with the measurement than the gas phase model data. The LLNL model column is in the best agreement with the ISSJ measurement.

Clearly, there is need for additional $ClONO_2$ column amount measurements especially in view of the significant model-predicted long-term trend and seasonal cycle. Such measurements are planned as part of the Network for the Detection of Stratospheric Change.

NITROGEN DIOXIDE (NO_2)

LIMS daytime and nighttime NO_2 values (Russell et al., 1984a) have been integrated to derive column amounts. As for HNO_3, the LAMAT data product (Remsberg et al., 1990) was used in computing these column amounts. The daytime columns have been derived by integrating from 30 to 3 mb, except in the tropics from February to May when the columns could only be integrated from 16 to 3 mb. Note that this change in integration limits produces a discontinuity in the variation of LIMS NO_2 column with latitude for these months. The model values for these daytime comparisons have been integrated from $z^* = 24$ to 40 km. The nighttime columns have been derived by integrating from 30 to 1.5 mb; limits for the corresponding model integrations have been set to $z^* = 24$ and 46 km. Some high-latitude LIMS data have been deleted to avoid terminator crossing effects. Note that the data set adopted here does not fully show the "Noxon cliff" phenomenon. Special processing by radiance-averaging methods (Russell et al., 1984b) is required to obtain sufficient signal-to-noise to do retrievals in the region of the cold vortex.

From Remsberg and Russell (1987, their Table 2) a column uncertainty of 20% in NO_2 above 30 mb is inferred. The precision in the NO_2 columns above 30 mb is about 5% (Russell et al., 1984, Table 1).

The strong diurnal variation of NO_2 must be considered in selecting the model runs for comparison with the LIMS observations. For the daytime LIMS data, which correspond nominally to 1:30 p.m. local time observations, the following sets of model calculations have been used for the comparisons:

- 1980 AER noon gas phase and lower-limit heterogeneous chemistry runs
- 1980 CAMED-theta daytime average gas phase and lower-limit heterogeneous chemistry runs
- 1980 GSFC daytime average gas phase and lower-limit heterogeneous chemistry runs
- 1980 LLNL noon gas phase and lower-limit heterogeneous chemistry runs
- 1980 WASH daytime gas phase run

Figure G-12 shows contour maps of G and the ratio R as a function of latitude and season. Graphs are shown for the runs by the four modeling groups reporting both gas phase and lower-limit heterogeneous chemistry calculations. Based on an examination of the plots, it can be noted that all of the models predict pronounced depletions in column NO_2 at winter polar latitudes in both hemispheres when lower-limit heterogeneous chemistry is included. Note that the predicted NO_2 column depletions extend to all latitudes and seasons, even the tropics. The relative magnitude of the NO_2 column changes, however, are less dramatic than those for column HNO_3 (Figure G-4). This can be attributed to the fact that the base pressure for the NO_2 column integrations is 30 mb. As illustrated in Figure G-13, the relative magnitude of the NO_2 depletion is much greater at low altitude. This reflects the low altitude location specified for the lower-limit heterogeneous chemistry aerosol layer.

Figure G-14 presents plots comparing the daytime LIMS columns and the model column as a function of latitude for December and May. Tables G-7 and G-8 give a complete month-by-month listing of the computed LIMS daytime columns and the ratios of the model-to-measurement data. The ratios for the gas phase model runs are in Table G-7 and the lower-limit heterogeneous chemistry runs are in Table G-8. When comparing the measured and model columns, recall that for February to May the tropical LIMS columns were integrated above 16 mb, so that the LIMS columns should be systematically lower that the model columns for these cases. The following comments refer to Figure G-14 and Tables G-7 and G-8:

- Except for a few data points, the model columns are lower than the LIMS columns. The differences are often near the estimated uncertainty limit of the LIMS NO_2 columns ($\pm$20%).

- The lower-limit heterogeneous chemistry model columns are mostly in poorer agreement with the LIMS measurements than are the gas phase model results. This conclusion is consistent with the study by Considine et al. (1992).

- On a relative basis, the WASH model is generally the most successful in reproducing the strong interhemispheric differences in column NO_2 observed from December to March.

Unfortunately, no model results appropriate for comparison with columns derived from the LIMS nighttime measurements were received. Note, however, that in experiment F a comparison is presented between model NO_y and lower-limit NO_y computed by summing LIMS HNO_3 and nighttime NO_2 data sets.

Comparisons of the model NO_2 calculations with sunset measurements (e.g., the aircraft measurements by Mankin and Coffey [1983]) were anticipated as part of this experiment, but only two modeling groups submitted sunset data (AER and LLNL). Model comparisons with sunset column measurements and with the LIMS nighttime columns as well as new column data as they become available are recommended in the future.

REFERENCES

Coffey, M. T., W. G. Mankin, and A. Goldman, Airborne measurements of stratospheric constituents over Antarctica in the austral spring, 1987: 2. Halogen and nitrogen trace gases, *J. Geophys. Res.*, *94*, 16,597-16,613, 1989.

Considine, D. B., A. R. Douglass, and R. S. Stolarski, Heterogeneous conversion of N_2O_5 to HNO_3 on background stratospheric aerosols: Comparisons of model results with data, *Geophys. Res. Lett.*, *19*, 397-400, 1992.

Gille, J. C., J. M. Russell III, P. L. Bailey, E. E. Remsberg, L. L. Gordley, W. F. J. Evans, H. Fischer, B. W. Gandrud, A. Girard, J. E. Harries, and S. A. Beck, Accuracy and precision of the nitric acid concentrations determined by the limb infrared monitor of the stratosphere experiment on NIMBUS 7, *J. Geophys. Res.*, *89*, 5179-5190, 1984.

Girard, A., G. Fergant, L. Gramont, O. Lado-Bordowsky, J. Laurent, S. Le Boiteux, M. P. Lemaitre, and N. Louisnard, Latitudinal distribution of ten stratospheric species deduced from simultaneous spectroscopic measurements, *J. Geophys. Res.*, *88*, 5377-5392, 1983.

Hofmann, D. J., and S. Solomon, Ozone destruction through heterogeneous chemistry following the eruption of El Chichon, *J. Geophys. Res.*, *94*, 5029-5041, 1989.

Karcher, F., M. Amodei, G. Armand, C. Besson, B. DuFour, G. Froment, and J. P. Meyer, Simultaneous measurements of HNO_3, NO_2, HCl, O_3, N_2O, CH_4, H_2O and CO and their latitudinal variations as deduced from air-borne infrared spectrometry, *Ann. Geophys.*, *6*, 425-444, 1988.

Kaye, J. A., A. R. Douglass, R. B. Rood, R. S. Stolarski, P. A. Newman, D. J. Allen, E. M. Larson, M. T. Coffey, W. G. Mankin, and G. C. Toon, Three-dimensional simulation of hydrogen chloride and hydrogen fluoride during the airborne Arctic stratospheric expedition, *Geophys. Res. Lett.*, *17*, 529-532, 1990.

Kaye, J. A., A. R. Douglass, C. H. Jackman, R. S. Stolarski, R. Zander, and G. Roland, Two-dimensional model calculation of fluorine-containing reservoir species in the stratosphere, *J. Geophys. Res.*, *96*, 12,865-12,881, 1991.

Ko, M. K. W., and N. D. Sze, Diurnal variation of ClO: Implications for the stratospheric chemistry of $ClONO_2$, HOCl, and HCl, *J. Geophys. Res.*, *83*, 11,619-11,632, 1984.

Mankin, W. G., and M. T. Coffey, Latitudinal distributions and temporal changes of stratospheric HCl and HF, *J. Geophys. Res.*, *88*, 10,776-10,784, 1983.

Remsberg, E. E., and J. M. Russell III, The near global distributions of middle atmospheric H_2O and NO_2 measured by the NIMBUS 7 LIMS experiment, in *Transport Processes in the Middle Atmosphere*, G. Visconti and R. Garcia, eds., pp. 87-102, Reidel (1987).

Remsberg, E. E., K. V. Haggard, and J. M. Russell III, Estimation of synoptic fields of middle atmosphere parameters from NIMBUS-7 LIMS profile data, *J. Atmos. and Oceanic Technol.*, *7*, 689-705, 1990.

Rinsland, C. P., J. S. Levine, A. Goldman, N. D. Sze, M. K. W. Ko, and D. W. Johnson, Infrared measurements of HF and HCl total column abundances above Kitt Peak, 1977-1990: Seasonal cycles, long-term increases, and comparisons with model calculations, *J. Geophys. Res.*, *96*, 15,523-15,540, 1991a.

Rinsland, C. P., R. Zander, and P. Demoulin, Ground-based infrared measurements of HNO_3 total column abundances: Long-term trend and variability, *J. Geophys. Res.*, *96*, 9379-9389, 1991b.

Russell, J. M. III, J. C. Gille, E. E. Remsberg, L. L. Gordley, P. L. Bailey, S. R. Drayson, H. Fischer, A. Girard, J. E. Harries, and W. F. J. Evans, Validation of nitrogen dioxide results measured by the Limb Infrared Monitor of the Stratosphere (LIMS) experiment on NIMBUS 7, *J. Geophys. Res.*, *89*, 5099-5107, 1984a.

Russell, J. M. III, S. Solomon, L. L. Gordley, E. E. Remsberg, and L. B. Callis, The variability of stratospheric and mesospheric NO_2 in the polar winter night observed by LIMS, *J. Geophys. Res.*, *89*, 7267-7275, 1984b.

Toon, G. C., C. B. Farmer, L. L. Lowes, P. W. Schaper, J.-F. Blavier, and R. H. Norton, Infrared aircraft measurements of stratospheric composition over Antarctica during September 1987, *J. Geophys. Res.*, *94*, 16,571-16,596, 1989.

Zander, R., G. Roland, L. Delbouille, A. Sauval, C. B. Farmer, and R. H. Norton, Monitoring of the integrated column of hydrogen fluoride above the Jungfraujoch station since 1977 - the HF/HCl column ratio, *J. Atmos. Chem.*, *5*, 385-394, 1987a.

Zander, R., G. Roland, L. Delbouille, A. Sauval, C. B. Farmer, and R. H. Norton, Column abundance and long-term trend of hydrogen chloride (HCl) above the Jungfraujoch station, *J. Atmos. Chem.*, *5*, 395-404, 1987b.

Zander, R., and Ph. Demoulin, Spectroscopic evidence for the presence of the ν_4-Q branch of chlorine nitrate ($ClONO_2$) in ground-based infrared solar spectra, *J. Atmos. Chem.*, *6*, 191-200, 1988.

Zander, R. (1991), M. R. Gunson, J. C. Foster, C. P. Rinsland, and J. Namkung, Stratospheric $ClONO_2$, HCl, and HF concentration profiles derived from atmospheric trace molecule spectroscopy experiment Spacelab 3 observations: An update, *J. Geophys. Res.*, *95*, 20519-20525, 1990.

Table G-1. Comparison of HF Columns above z*=11.9 km Computed for 1980 with Steady-State Gas Phase Chemistry and the Aircraft Column Measurements of Mankin and Coffey (1983)

Latitude	Aircraft	(Model/Aircraft) Columns Ratio			
(°)	Column†	AER	GSFC	NCAR	WASH
5N	1.369	1.414	0.780	1.123	2.299
10N	1.426	1.451	0.904	1.124	2.387
15N	1.520	1.541	0.993	1.129	2.408
20N	1.652	1.597	1.053	1.139	2.474
25N	1.818	1.661	1.083	1.153	2.483
30N	2.020	1.682	1.087	1.168	2.510
35N	2.254	1.671	1.074	1.180	2.495
40N	2.520	1.644	1.071	1.185	2.437
45N	2.814	1.609	1.058	1.183	2.366
50N	3.136	1.558	1.056	1.172	2.285
55N	3.482	1.498	1.048	1.154	2.205
60N	3.850	1.424	1.051	1.130	2.099
65N	4.237	1.349	1.048	1.105	2.003
70N	4.640	1.266	1.058	1.076	1.884
	MEAN	1.526	1.026	1.144	2.310
	STD DEV	0.130	0.085	0.032	0.196

† In 10^{14} molecules cm^{-2} above 197 mbar. Computed with Eq. 7 and the fitted parameters reported by Mankin and Coffey (1983).

Table G-2. Comparison of HCℓ Columns above z*=11.9 km Computed for 1980 with Steady-State Gas Phase Chemistry and the Aircraft Column Measurements of Mankin and Coffey (1983)

Latitude (°)	Aircraft Column†	(Model/Aircraft Columns Ratio)								
		AER	CAMED	DUPONT	GSFC	ITALY	LLNL	MRI	NCAR	WASH
5N	0.651	1.733	2.124	1.855	1.213	1.431	1.574	1.550	1.990	1.646
10N	0.682	1.723	2.093	1.826	1.267	1.429	1.548	1.537	1.945	1.670
15N	0.734	1.744	2.104	1.791	1.279	1.515	1.491	1.482	1.888	1.643
20N	0.807	1.732	2.076	1.769	1.263	1.549	1.451	1.445	1.832	1.648
25N	0.900	1.733	2.059	1.739	1.222	1.588	1.424	1.383	1.785	1.616
30N	1.011	1.708	2.033	1.710	1.167	1.589	1.370	1.340	1.748	1.586
35N	1.141	1.673	2.029	1.705	1.105	1.536	1.382	1.284	1.714	1.537
40N	1.288	1.630	1.984	1.694	1.071	1.475	1.363	1.229	1.679	1.468
45N	1.451	1.588	1.909	1.669	1.032	1.382	1.340	1.173	1.641	1.398
50N	1.629	1.541	1.810	1.639	1.004	1.296	1.312	1.130	1.598	1.348
55N	1.821	1.492	1.698	1.604	0.973	1.205	1.267	1.088	1.549	1.298
60N	2.025	1.443	1.578	1.561	0.920	1.124	1.212	1.033	1.483	1.218
65N	2.239	1.395	1.464	1.510	0.873	1.052	1.148	0.985	1.409	1.147
70N	2.463	1.317	1.138	1.454	0.867	0.988	1.081	0.932	1.361	1.047
	MEAN	1.604	1.864	1.680	1.090	1.368	1.355	1.256	1.687	1.448
	STD DEV	0.144	0.295	0.117	0.149	0.203	0.143	0.207	0.194	0.208

† In 10^{15} molecules cm^{-2} above 197 mbar. Computed with Eq. 7 and the fitted parameters reported by Mankin and Coffey (1983).

Table G-3. Comparison of HCℓ Columns above z*=11.9 km Computed for 1980 with Steady-State Lower Limit Heterogeneous Chemistry and the Aircraft Column Measurements of Mankin and Coffey (1983)

Latitude (°)	Aircraft Column†	(Model/Aircraft Columns Ratio)							
		AER	CAMED	DUPONT	GSFC	ITALY	LLNL	MRI	NCAR
5N	0.651	1.695	2.114	1.825	1.202	1.410	1.569	1.569	1.974
10N	0.682	1.680	2.081	1.793	1.247	1.407	1.541	1.548	1.926
15N	0.734	1.687	2.081	1.755	1.253	1.484	1.482	1.493	1.865
20N	0.807	1.662	2.043	1.726	1.223	1.513	1.435	1.456	1.801
25N	0.900	1.644	2.015	1.687	1.173	1.536	1.397	1.393	1.742
30N	1.011	1.605	1.978	1.648	1.107	1.526	1.337	1.348	1.687
35N	1.141	1.557	1.957	1.635	1.037	1.465	1.327	1.290	1.628
40N	1.288	1.503	1.898	1.612	0.982	1.398	1.293	1.233	1.562
45N	1.451	1.447	1.811	1.574	0.928	1.326	1.261	1.175	1.487
50N	1.629	1.392	1.710	1.533	0.859	1.257	1.228	1.130	1.401
55N	1.821	1.341	1.605	1.493	0.798	1.209	1.185	1.085	1.303
60N	2.025	1.307	1.491	1.452	0.716	1.163	1.137	1.031	1.191
65N	2.239	1.282	1.381	1.410	0.646	1.128	1.082	0.982	1.087
70N	2.463	1.223	1.079	1.368	0.658	1.095	1.021	0.929	1.043
	MEAN	1.502	1.803	1.608	0.988	1.351	1.307	1.261	1.550
	STD DEV	0.168	0.312	0.143	0.223	0.155	0.168	0.213	0.308

† In 10^{15} molecules cm^{-2} above 197 mbar. Computed with Eq. 7 and the fitted parameters reported by Mankin and Coffey (1983).

Table G-4. Comparison of Model-Calculated Gas-Phase HNO_3 Columns with LIMS HNO_3 Zonal Mean Columns for 1978-1979 († in 10^{16} molecules cm^{-2})

MODEL-LIMS HNO_3 COMPARISON: NOVEMBER 1978

Latitude	LIMS	(Gas Phase Model Column/LIMS Column)								
(°)	Column†	AER	CAMED	DUPONT	GSFC	ITALY	LLNL	MRI	NCAR	WASH
60S	1.014	0.832	0.679	0.998	0.810	1.244	1.061	0.748	0.929	1.093
55S	0.990	0.807	0.704	0.946	0.759	1.204	1.023	0.717	0.918	1.077
50S	0.942	0.798	0.742	0.906	0.759	1.191	1.003	0.694	0.910	1.054
45S	0.881	0.796	0.783	0.870	0.771	1.191	0.988	0.679	0.906	1.044
40S	0.815	0.796	0.817	0.831	0.803	1.198	0.968	0.648	0.902	1.015
35S	0.751	0.793	0.827	0.781	0.837	1.179	0.933	0.610	0.894	0.977
30S	0.689	0.789	0.817	0.729	0.833	1.154	0.883	0.579	0.887	0.918
25S	0.615	0.765	0.806	0.690	0.844	1.106	0.873	0.553	0.903	0.863
20S	0.517	0.751	0.822	0.682	0.854	1.093	0.895	0.573	0.982	0.881
15S	0.381	0.866	0.981	0.776	0.956	1.194	1.060	0.661	1.235	0.997
10S	0.322	0.779	0.893	0.785	0.765	0.968	0.988	0.682	1.171	0.937
5S	0.274	0.865	0.983	0.854	0.699	0.978	1.051	0.735	1.333	0.945
0	0.257	0.880	0.981	0.882	0.717	0.869	1.065	0.774	1.403	0.920
5N	0.269	0.943	0.950	0.857	0.658	0.923	0.963	0.728	1.348	0.793
10N	0.309	0.921	0.847	0.799	0.675	0.885	0.858	0.685	1.208	0.725
15N	0.366	0.936	0.790	0.750	0.658	0.996	0.751	0.622	1.074	0.641
20N	0.491	0.905	0.754	0.669	0.654	1.085	0.683	0.563	1.019	0.598
25N	0.595	0.845	0.723	0.651	0.611	1.132	0.640	0.528	0.914	0.573
30N	0.706	0.795	0.699	0.638	0.568	1.153	0.601	0.531	0.842	0.584
35N	0.824	0.754	0.686	0.629	0.532	1.118	0.606	0.529	0.790	0.588
40N	0.955	0.710	0.661	0.616	0.500	1.075	0.597	0.526	0.739	0.567
45N	1.060	0.691	0.650	0.621	0.487	1.025	0.606	0.538	0.717	0.565
50N	1.147	0.680	0.644	0.631	0.482	0.998	0.623	0.561	0.705	0.532
55N	1.239	0.665	0.631	0.633	0.477	0.941	0.628	0.578	0.690	0.501
60N	1.346	0.637	0.597	0.620	0.462	0.880	0.617	0.578	0.664	0.419
65N	1.468	0.604	0.555	0.599	0.446	0.807	0.591	0.572	0.632	0.345
70N	1.575	0.573	0.517	0.581	0.433	0.751	0.566	0.565	0.606	0.271
75N	1.658	0.551	0.490	0.569	0.428	0.710	0.542	0.567	0.589	0.210
80N	1.724	0.533	0.474	0.559	0.430	0.680	0.524	0.577	0.575	0.262
	MEAN	0.768	0.741	0.729	0.652	1.025	0.800	0.617	0.913	0.721
	STD DEV	0.114	0.143	0.124	0.158	0.160	0.195	0.076	0.235	0.271

Table G-4 (continued)

MODEL-LIMS HNO_3 COMPARISON: DECEMBER 1978

Latitude	LIMS	(Gas Phase Model Column/LIMS Column)								
(°)	Column†	AER	CAMED	DUPONT	GSFC	ITALY	LLNL	MRI	NCAR	WASH
60S	0.948	0.886	0.726	1.058	0.930	1.323	1.173	0.805	0.986	1.141
55S	0.909	0.873	0.757	1.013	0.911	1.292	1.144	0.772	0.983	1.084
50S	0.857	0.869	0.794	0.974	0.919	1.275	1.118	0.742	0.983	1.065
45S	0.800	0.869	0.830	0.935	0.935	1.267	1.087	0.712	0.979	1.051
40S	0.742	0.869	0.860	0.892	0.928	1.259	1.049	0.681	0.973	1.036
35S	0.684	0.869	0.866	0.841	0.919	1.233	1.002	0.643	0.966	1.018
30S	0.624	0.873	0.853	0.792	0.897	1.209	0.942	0.612	0.966	0.971
25S	0.555	0.848	0.852	0.757	0.883	1.162	0.942	0.584	0.990	0.928
20S	0.483	0.795	0.856	0.726	0.851	1.108	0.942	0.583	1.043	0.908
15S	0.370	0.881	0.992	0.800	0.899	1.172	1.082	0.646	1.264	0.979
10S	0.296	0.847	0.962	0.861	0.784	1.028	1.086	0.717	1.268	0.987
5S	0.268	0.883	1.003	0.883	0.685	0.995	1.085	0.739	1.360	0.936
0	0.258	0.875	0.986	0.890	0.705	0.885	1.066	0.770	1.395	0.891
5N	0.272	0.935	0.961	0.864	0.664	0.948	0.956	0.734	1.339	0.770
10N	0.327	0.875	0.832	0.771	0.664	0.879	0.809	0.667	1.154	0.707
15N	0.409	0.841	0.763	0.684	0.620	0.926	0.666	0.578	0.981	0.618
20N	0.579	0.772	0.695	0.580	0.567	0.959	0.579	0.496	0.883	0.555
25N	0.683	0.744	0.658	0.580	0.536	1.018	0.560	0.479	0.820	0.554
30N	0.775	0.735	0.657	0.595	0.510	1.080	0.553	0.497	0.792	0.587
35N	0.885	0.712	0.673	0.599	0.479	1.058	0.565	0.499	0.752	0.601
40N	1.013	0.678	0.658	0.592	0.449	1.023	0.561	0.503	0.705	0.556
45N	1.153	0.642	0.620	0.579	0.421	0.938	0.551	0.500	0.657	0.516
50N	1.274	0.617	0.587	0.573	0.409	0.885	0.550	0.501	0.626	0.450
55N	1.378	0.599	0.556	0.568	0.403	0.825	0.549	0.507	0.604	0.401
60N	1.456	0.585	0.532	0.565	0.406	0.786	0.550	0.514	0.592	0.338
65N	1.492	0.581	0.521	0.571	0.419	0.761	0.557	0.534	0.594	0.289
70N	1.519	0.577	0.512	0.580	0.433	0.746	0.561	0.556	0.599	0.246
75N	1.523	0.579	0.509	0.594	0.453	0.740	0.564	0.586	0.612	0.208
80N	1.532	0.577	0.504	0.600	0.468	0.732	0.563	0.611	0.620	0.262
	MEAN	0.768	0.744	0.735	0.660	1.018	0.807	0.613	0.913	0.712
	STD DEV	0.124	0.162	0.159	0.207	0.186	0.248	0.102	0.253	0.296

Table G-4 (continued)

MODEL-LIMS HNO_3 COMPARISON: JANUARY 1979

Latitude	LIMS	(Gas Phase Model Column/LIMS Column)								
(°)	Column†	AER	CAMED	DUPONT	GSFC	ITALY	LLNL	MRI	NCAR	WASH
60S	0.939	0.877	0.732	1.029	1.025	1.311	1.174	0.800	0.983	1.108
55S	0.891	0.869	0.760	0.993	1.014	1.288	1.153	0.768	0.988	1.062
50S	0.829	0.874	0.796	0.967	0.987	1.283	1.136	0.741	0.996	1.056
45S	0.763	0.885	0.834	0.942	0.960	1.289	1.110	0.713	1.006	1.054
40S	0.697	0.898	0.871	0.913	0.930	1.298	1.081	0.688	1.016	1.057
35S	0.631	0.915	0.889	0.880	0.893	1.292	1.046	0.657	1.029	1.059
30S	0.567	0.933	0.889	0.845	0.884	1.279	0.990	0.637	1.046	1.024
25S	0.505	0.901	0.880	0.808	0.866	1.221	0.990	0.609	1.071	0.974
20S	0.443	0.836	0.868	0.773	0.815	1.150	0.985	0.603	1.121	0.942
15S	0.345	0.913	0.997	0.844	0.824	1.196	1.118	0.658	1.337	0.995
10S	0.303	0.807	0.901	0.835	0.684	0.960	1.039	0.672	1.222	0.914
5S	0.270	0.854	0.964	0.872	0.639	0.954	1.058	0.710	1.333	0.867
0	0.249	0.881	1.001	0.921	0.707	0.900	1.091	0.784	1.437	0.886
5N	0.262	0.944	0.994	0.899	0.686	0.983	0.985	0.760	1.395	0.792
10N	0.323	0.859	0.851	0.782	0.683	0.897	0.814	0.679	1.182	0.737
15N	0.414	0.811	0.799	0.680	0.632	0.921	0.655	0.579	0.990	0.650
20N	0.594	0.744	0.731	0.574	0.560	0.942	0.572	0.493	0.884	0.595
25N	0.723	0.704	0.659	0.560	0.511	0.966	0.541	0.464	0.797	0.583
30N	0.853	0.674	0.615	0.554	0.462	0.982	0.515	0.461	0.739	0.571
35N	0.978	0.654	0.597	0.558	0.429	0.959	0.521	0.461	0.697	0.564
40N	1.087	0.642	0.598	0.569	0.409	0.955	0.530	0.474	0.669	0.534
45N	1.176	0.639	0.619	0.585	0.400	0.923	0.542	0.494	0.653	0.518
50N	1.269	0.626	0.607	0.590	0.396	0.891	0.547	0.500	0.633	0.472
55N	1.370	0.605	0.569	0.582	0.389	0.830	0.539	0.501	0.607	0.429
60N	1.455	0.581	0.534	0.571	0.391	0.786	0.529	0.499	0.588	0.351
65N	1.419	0.602	0.541	0.599	0.426	0.799	0.556	0.539	0.615	0.305
70N	1.343	0.636	0.564	0.643	0.476	0.835	0.596	0.599	0.658	0.278
75N	1.579	0.540	0.475	0.553	0.428	0.704	0.509	0.534	0.567	0.199
80N	1.591	0.535	0.466	0.554	0.440	0.693	0.506	0.553	0.570	0.250
	MEAN	0.767	0.745	0.741	0.653	1.017	0.808	0.608	0.925	0.718
	STD DEV	0.135	0.167	0.165	0.223	0.196	0.266	0.109	0.271	0.293

Table G-4 (continued)

MODEL-LIMS HNO_3 COMPARISON: FEBRUARY 1979

Latitude	LIMS	(Gas Phase Model Column/LIMS Column)								
(°)	Column†	AER	CAMED	DUPONT	GSFC	ITALY	LLNL	MRI	NCAR	WASH
55S	0.928	0.817	0.722	0.913	0.986	1.234	1.078	0.728	0.941	1.004
50S	0.856	0.829	0.752	0.899	0.937	1.246	1.068	0.708	0.960	1.009
45S	0.780	0.846	0.783	0.886	0.883	1.263	1.050	0.687	0.979	1.020
40S	0.701	0.868	0.815	0.873	0.860	1.288	1.033	0.666	1.000	1.022
35S	0.614	0.911	0.851	0.871	0.844	1.319	1.030	0.650	1.047	1.041
30S	0.529	0.964	0.877	0.873	0.845	1.352	1.009	0.657	1.109	1.040
25S	0.454	0.964	0.895	0.869	0.829	1.331	1.044	0.653	1.180	1.018
20S	0.394	0.901	0.885	0.843	0.803	1.252	1.045	0.655	1.248	0.988
15S	0.311	0.969	1.002	0.913	0.827	1.273	1.170	0.707	1.469	1.017
10S	0.278	0.840	0.892	0.889	0.674	0.984	1.078	0.707	1.311	0.915
5S	0.250	0.882	0.957	0.923	0.644	0.971	1.096	0.742	1.420	0.850
0	0.232	0.907	1.000	0.972	0.730	0.913	1.138	0.821	1.524	0.864
5N	0.247	0.955	0.993	0.936	0.717	0.997	1.025	0.789	1.462	0.759
10N	0.310	0.856	0.846	0.805	0.715	0.907	0.845	0.700	1.223	0.728
15N	0.387	0.838	0.791	0.721	0.686	0.959	0.705	0.616	1.050	0.680
20N	0.544	0.796	0.734	0.629	0.618	1.006	0.639	0.538	0.956	0.660
25N	0.701	0.719	0.655	0.585	0.533	0.977	0.574	0.480	0.820	0.627
30N	0.843	0.682	0.619	0.573	0.477	0.976	0.539	0.475	0.752	0.602
35N	0.985	0.653	0.599	0.570	0.437	0.944	0.535	0.472	0.701	0.584
40N	1.111	0.635	0.596	0.577	0.412	0.931	0.534	0.470	0.666	0.552
45N	1.215	0.628	0.612	0.591	0.400	0.906	0.541	0.479	0.647	0.539
50N	1.300	0.622	0.610	0.604	0.395	0.896	0.548	0.490	0.633	0.523
55N	1.378	0.613	0.591	0.607	0.392	0.863	0.547	0.502	0.619	0.512
60N	1.436	0.601	0.571	0.604	0.395	0.844	0.543	0.504	0.610	0.453
65N	1.481	0.588	0.549	0.594	0.401	0.814	0.535	0.511	0.602	0.402
70N	1.515	0.570	0.518	0.577	0.408	0.791	0.527	0.515	0.594	0.304
75N	1.545	0.551	0.483	0.555	0.416	0.765	0.517	0.520	0.583	0.212
80N	1.583	0.533	0.462	0.534	0.421	0.736	0.504	0.526	0.568	0.265
	MEAN	0.769	0.738	0.742	0.632	1.026	0.803	0.606	0.953	0.721
	STD DEV	0.145	0.166	0.156	0.202	0.194	0.260	0.110	0.312	0.264

Table G-4 (continued)

MODEL-LIMS HNO_3 COMPARISON: MARCH 1979

Latitude	LIMS	(Gas Phase Model Column/LIMS Column)								
(°)	Column†	AER	CAMED	DUPONT	GSFC	ITALY	LLNL	MRI	NCAR	WASH
55S	1.014	0.742	0.673	0.806	0.817	1.150	0.958	0.674	0.860	0.905
50S	0.935	0.754	0.692	0.797	0.819	1.170	0.951	0.654	0.879	0.919
45S	0.853	0.767	0.711	0.786	0.822	1.182	0.933	0.631	0.894	0.937
40S	0.769	0.782	0.729	0.773	0.795	1.200	0.914	0.612	0.914	0.930
35S	0.674	0.815	0.750	0.771	0.773	1.219	0.906	0.598	0.955	0.936
30S	0.562	0.887	0.791	0.800	0.783	1.284	0.914	0.620	1.043	0.960
25S	0.457	0.933	0.846	0.843	0.787	1.326	0.993	0.644	1.172	0.981
20S	0.380	0.905	0.866	0.854	0.798	1.286	1.027	0.674	1.292	0.986
15S	0.295	0.986	0.996	0.943	0.838	1.319	1.163	0.740	1.543	1.022
10S	0.262	0.859	0.893	0.926	0.682	1.012	1.086	0.740	1.383	0.916
5S	0.238	0.892	0.952	0.952	0.659	0.989	1.099	0.762	1.479	0.825
0	0.227	0.890	0.974	0.974	0.740	0.902	1.125	0.817	1.537	0.811
5N	0.245	0.924	0.961	0.931	0.736	0.992	1.022	0.777	1.455	0.705
10N	0.305	0.832	0.825	0.809	0.740	0.920	0.862	0.695	1.221	0.697
15N	0.381	0.824	0.752	0.727	0.712	0.972	0.731	0.612	1.045	0.661
20N	0.543	0.781	0.693	0.631	0.636	1.001	0.663	0.529	0.939	0.640
25N	0.678	0.732	0.660	0.611	0.567	0.994	0.615	0.488	0.831	0.630
30N	0.786	0.724	0.672	0.625	0.533	1.023	0.601	0.502	0.793	0.643
35N	0.905	0.710	0.696	0.637	0.501	1.005	0.606	0.508	0.757	0.646
40N	1.018	0.699	0.692	0.653	0.476	0.998	0.609	0.517	0.733	0.630
45N	1.112	0.697	0.668	0.675	0.464	0.985	0.617	0.534	0.720	0.627
50N	1.191	0.695	0.657	0.694	0.455	0.985	0.626	0.547	0.711	0.620
55N	1.267	0.689	0.650	0.701	0.448	0.970	0.627	0.561	0.700	0.616
60N	1.344	0.672	0.629	0.690	0.439	0.954	0.616	0.556	0.681	0.590
65N	1.432	0.646	0.597	0.661	0.427	0.916	0.594	0.547	0.653	0.563
70N	1.492	0.620	0.559	0.632	0.418	0.900	0.580	0.536	0.632	0.503
75N	1.528	0.600	0.523	0.604	0.415	0.884	0.569	0.533	0.617	0.455
80N	1.555	0.576	0.500	0.579	0.413	0.874	0.560	0.529	0.602	0.436
	MEAN	0.773	0.736	0.753	0.632	1.050	0.806	0.612	0.966	0.743
	STD DEV	0.109	0.135	0.119	0.159	0.141	0.207	0.093	0.303	0.177

Table G-4 (continued)

MODEL-LIMS HNO_3 COMPARISON: APRIL 1979

Latitude	LIMS	(Gas Phase Model Column/LIMS Column)								
(°)	Column†	AER	CAMED	DUPONT	GSFC	ITALY	LLNL	MRI	NCAR	WASH
55S	1.148	0.653	0.607	0.695	0.672	1.021	0.823	0.615	0.758	0.751
50S	1.055	0.668	0.629	0.692	0.681	1.060	0.827	0.596	0.779	0.776
45S	0.969	0.676	0.642	0.681	0.687	1.070	0.813	0.570	0.791	0.800
40S	0.882	0.682	0.648	0.666	0.688	1.084	0.792	0.546	0.803	0.812
35S	0.769	0.713	0.666	0.670	0.712	1.105	0.791	0.535	0.844	0.854
30S	0.642	0.771	0.696	0.695	0.729	1.156	0.797	0.549	0.923	0.881
25S	0.525	0.804	0.736	0.729	0.741	1.179	0.855	0.561	1.031	0.907
20S	0.421	0.806	0.779	0.769	0.764	1.177	0.911	0.610	1.175	0.909
15S	0.308	0.930	0.947	0.901	0.825	1.274	1.089	0.712	1.487	0.939
10S	0.266	0.833	0.869	0.911	0.672	0.997	1.043	0.729	1.373	0.851
5S	0.241	0.867	0.932	0.940	0.653	0.980	1.063	0.746	1.467	0.756
0	0.237	0.842	0.929	0.935	0.726	0.875	1.073	0.786	1.476	0.736
5N	0.260	0.847	0.898	0.875	0.717	0.946	0.967	0.738	1.360	0.638
10N	0.324	0.759	0.773	0.761	0.716	0.882	0.828	0.659	1.134	0.655
15N	0.405	0.756	0.706	0.686	0.685	0.925	0.711	0.580	0.965	0.638
20N	0.561	0.742	0.675	0.616	0.633	0.970	0.666	0.515	0.892	0.631
25N	0.643	0.760	0.704	0.651	0.616	1.038	0.671	0.516	0.858	0.669
30N	0.734	0.766	0.726	0.678	0.593	1.077	0.664	0.538	0.832	0.683
35N	0.828	0.772	0.755	0.709	0.573	1.075	0.687	0.554	0.814	0.693
40N	0.917	0.778	0.769	0.741	0.554	1.078	0.703	0.573	0.804	0.692
45N	1.006	0.780	0.766	0.767	0.540	1.063	0.713	0.590	0.794	0.693
50N	1.072	0.792	0.759	0.799	0.532	1.072	0.733	0.611	0.799	0.698
55N	1.132	0.803	0.738	0.823	0.528	1.077	0.747	0.633	0.799	0.708
60N	1.184	0.811	0.730	0.836	0.527	1.089	0.756	0.641	0.797	0.709
65N	1.226	0.820	0.730	0.841	0.529	1.103	0.763	0.654	0.793	0.716
70N	1.254	0.831	0.714	0.841	0.535	1.129	0.773	0.668	0.789	0.726
75N	1.275	0.844	0.692	0.837	0.544	1.152	0.770	0.685	0.783	0.739
80N	1.303	0.838	0.656	0.823	0.544	1.167	0.758	0.703	0.769	0.792
	MEAN	0.784	0.745	0.770	0.640	1.065	0.814	0.622	0.960	0.752
	STD DEV	0.064	0.093	0.093	0.087	0.093	0.126	0.076	0.248	0.088

Table G-4 (continued)

MODEL-LIMS HNO_3 COMPARISON: MAY 1979

Latitude	LIMS	(Gas Phase Model Column/LIMS Column)								
(°)	Column†	AER	CAMED	DUPONT	GSFC	ITALY	LLNL	MRI	NCAR	WASH
55S	1.303	0.580	0.536	0.605	0.556	0.876	0.706	0.551	0.663	0.589
50S	1.178	0.604	0.574	0.618	0.575	0.944	0.729	0.546	0.698	0.650
45S	1.059	0.622	0.606	0.624	0.596	0.989	0.741	0.537	0.727	0.722
40S	0.944	0.634	0.630	0.625	0.621	1.040	0.745	0.530	0.755	0.759
35S	0.845	0.634	0.635	0.615	0.643	1.040	0.730	0.512	0.777	0.792
30S	0.748	0.631	0.626	0.604	0.651	1.036	0.700	0.496	0.802	0.783
25S	0.639	0.645	0.634	0.606	0.674	1.012	0.716	0.485	0.858	0.785
20S	0.496	0.717	0.691	0.662	0.706	1.046	0.785	0.545	1.015	0.809
15S	0.342	0.882	0.889	0.825	0.789	1.203	0.996	0.676	1.362	0.879
10S	0.285	0.800	0.845	0.867	0.660	0.976	0.985	0.717	1.308	0.817
5S	0.256	0.833	0.906	0.900	0.634	0.965	1.017	0.732	1.403	0.710
0	0.252	0.802	0.894	0.891	0.704	0.856	1.035	0.755	1.402	0.715
5N	0.285	0.778	0.836	0.809	0.676	0.894	0.918	0.678	1.248	0.628
10N	0.350	0.700	0.725	0.713	0.668	0.839	0.802	0.600	1.049	0.624
15N	0.425	0.697	0.676	0.659	0.647	0.895	0.711	0.534	0.910	0.607
20N	0.574	0.703	0.665	0.608	0.625	0.952	0.676	0.488	0.864	0.598
25N	0.646	0.777	0.700	0.653	0.625	1.028	0.687	0.497	0.841	0.634
30N	0.716	0.823	0.735	0.698	0.619	1.091	0.695	0.531	0.837	0.672
35N	0.790	0.829	0.770	0.743	0.611	1.104	0.736	0.557	0.835	0.699
40N	0.870	0.830	0.787	0.781	0.596	1.109	0.760	0.590	0.832	0.703
45N	0.940	0.841	0.801	0.822	0.589	1.106	0.787	0.624	0.837	0.714
50N	0.992	0.865	0.814	0.868	0.592	1.123	0.823	0.659	0.854	0.729
55N	1.034	0.896	0.823	0.914	0.601	1.147	0.857	0.698	0.877	0.750
60N	1.069	0.929	0.839	0.955	0.616	1.176	0.886	0.734	0.893	0.775
65N	1.096	0.967	0.863	0.992	0.635	1.211	0.913	0.774	0.907	0.804
70N	1.115	1.003	0.873	1.027	0.677	1.254	0.938	0.827	0.920	0.855
75N	1.131	1.037	0.878	1.050	0.719	1.284	0.939	0.880	0.927	0.907
80N	1.141	1.058	0.860	1.061	0.726	1.319	0.938	0.904	0.930	0.923
	MEAN	0.790	0.754	0.778	0.644	1.054	0.820	0.631	0.940	0.737
	STD DEV	0.135	0.111	0.153	0.052	0.131	0.115	0.123	0.211	0.093

Table G-5. Comparison of Model-Calculated Lower Limit Heterogeneous Chemistry HNO_3 Columns with LIMS HNO_3 Zonal Mean Columns for 1978-1979 († in 10^{16} molecules cm^{-2})

MODEL-LIMS HNO_3 COMPARISON: NOVEMBER 1978

Latitude	LIMS	(Lower Limit Heterogeneous Chemistry Model Column/LIMS Column)							
(°)	Column†	AER	CAMED	DUPONT	GSFC	ITALY	LLNL	MRI	NCAR
60S	1.014	0.876	0.746	1.161	1.079	1.269	1.381	0.827	1.257
55S	0.990	0.869	0.786	1.111	1.011	1.233	1.351	0.802	1.236
50S	0.942	0.871	0.841	1.059	1.007	1.226	1.320	0.773	1.214
45S	0.881	0.878	0.899	1.008	1.016	1.229	1.278	0.752	1.196
40S	0.815	0.883	0.950	0.951	1.053	1.240	1.228	0.719	1.178
35S	0.751	0.884	0.967	0.881	1.092	1.223	1.159	0.678	1.156
30S	0.689	0.882	0.955	0.810	1.088	1.201	1.063	0.649	1.138
25S	0.615	0.856	0.936	0.756	1.105	1.156	1.042	0.624	1.158
20S	0.517	0.840	0.942	0.737	1.101	1.150	1.054	0.648	1.248
15S	0.381	0.971	1.115	0.835	1.204	1.264	1.235	0.750	1.552
10S	0.322	0.880	1.014	0.844	0.939	1.040	1.147	0.780	1.449
5S	0.274	0.991	1.118	0.921	0.833	1.057	1.214	0.845	1.657
0	0.257	1.023	1.121	0.957	0.864	0.948	1.235	0.900	1.758
5N	0.269	1.120	1.095	0.941	0.802	1.010	1.121	0.857	1.714
10N	0.309	1.116	0.987	0.890	0.860	0.971	1.015	0.808	1.564
15N	0.366	1.172	0.936	0.852	0.864	1.090	0.903	0.735	1.425
20N	0.491	1.158	0.912	0.777	0.899	1.180	0.839	0.661	1.423
25N	0.595	1.107	0.905	0.781	0.866	1.235	0.806	0.621	1.321
30N	0.706	1.060	0.894	0.788	0.825	1.261	0.772	0.627	1.254
35N	0.824	1.019	0.887	0.791	0.789	1.240	0.815	0.626	1.206
40N	0.955	0.978	0.867	0.803	0.766	1.207	0.827	0.636	1.153
45N	1.060	0.975	0.873	0.846	0.767	1.178	0.871	0.660	1.140
50N	1.147	0.984	0.888	0.896	0.786	1.172	0.928	0.705	1.139
55N	1.239	0.986	0.895	0.936	0.800	1.137	0.962	0.741	1.126
60N	1.346	0.966	0.868	0.951	0.795	1.093	0.969	0.763	1.088
65N	1.468	0.934	0.825	0.944	0.783	1.030	0.946	0.774	1.036
70N	1.575	0.900	0.783	0.936	0.790	0.985	0.920	0.807	0.988
75N	1.658	0.877	0.753	0.935	0.808	0.948	0.887	0.849	0.947
80N	1.724	0.855	0.773	0.930	0.824	0.925	0.861	0.862	0.913
	MEAN	0.962	0.915	0.897	0.911	1.134	1.040	0.741	1.263
	STD DEV	0.100	0.105	0.103	0.132	0.110	0.183	0.085	0.221

Table G-5 (continued)

MODEL-LIMS HNO_3 COMPARISON: DECEMBER 1978

Latitude	LIMS	(Lower Limit Heterogeneous Chemistry Model Column/LIMS Column)							
(°)	Column†	AER	CAMED	DUPONT	GSFC	ITALY	LLNL	MRI	NCAR
60S	0.949	0.877	0.764	1.155	1.103	1.346	1.381	0.853	1.240
55S	0.909	0.890	0.815	1.127	1.110	1.319	1.382	0.836	1.249
50S	0.857	0.904	0.873	1.090	1.135	1.306	1.363	0.807	1.251
45S	0.800	0.920	0.929	1.045	1.172	1.301	1.319	0.780	1.246
40S	0.742	0.929	0.977	0.989	1.166	1.296	1.265	0.744	1.234
35S	0.684	0.936	0.990	0.925	1.158	1.272	1.195	0.701	1.221
30S	0.624	0.947	0.978	0.866	1.130	1.250	1.107	0.676	1.218
25S	0.555	0.923	0.970	0.821	1.113	1.206	1.102	0.656	1.254
20S	0.483	0.870	0.965	0.780	1.061	1.157	1.095	0.657	1.314
15S	0.370	0.971	1.112	0.857	1.102	1.230	1.251	0.732	1.580
10S	0.296	0.945	1.080	0.924	0.945	1.092	1.253	0.820	1.567
5S	0.268	1.006	1.131	0.952	0.809	1.063	1.250	0.849	1.691
0	0.258	1.018	1.118	0.968	0.847	0.951	1.236	0.897	1.754
5N	0.272	1.120	1.106	0.952	0.811	1.024	1.114	0.865	1.711
10N	0.327	1.075	0.972	0.865	0.858	0.953	0.963	0.790	1.506
15N	0.409	1.076	0.920	0.786	0.833	1.007	0.809	0.687	1.314
20N	0.579	1.019	0.863	0.686	0.807	1.040	0.727	0.589	1.254
25N	0.683	1.014	0.848	0.714	0.794	1.119	0.730	0.571	1.210
30N	0.775	1.028	0.873	0.760	0.782	1.196	0.741	0.603	1.209
35N	0.885	1.019	0.917	0.786	0.756	1.204	0.810	0.616	1.180
40N	1.013	0.998	0.920	0.812	0.739	1.189	0.840	0.636	1.129
45N	1.153	0.976	0.896	0.837	0.718	1.129	0.866	0.646	1.072
50N	1.274	0.969	0.879	0.872	0.733	1.099	0.905	0.680	1.035
55N	1.378	0.971	0.866	0.911	0.754	1.060	0.938	0.717	1.009
60N	1.456	0.970	0.863	0.949	0.787	1.044	0.970	0.766	0.992
65N	1.495	0.985	0.879	0.995	0.839	1.038	1.004	0.832	0.998
70N	1.519	0.990	0.910	1.032	0.895	1.043	1.029	0.889	1.007
75N	1.523	1.001	0.955	1.065	0.962	1.050	1.040	0.957	1.021
80N	1.532	1.001	0.966	1.077	1.006	1.054	1.040	0.994	1.025
	MEAN	0.978	0.943	0.917	0.928	1.139	1.059	0.753	1.258
	STD DEV	0.059	0.094	0.125	0.160	0.116	0.204	0.113	0.223

Table G-5 (continued)

MODEL-LIMS HNO_3 COMPARISON: JANUARY 1979

Latitude	LIMS	(Lower Limit Heterogeneous Chemistry Model Column/LIMS Column)							
(°)	Column†	AER	CAMED	DUPONT	GSFC	ITALY	LLNL	MRI	NCAR
60S	0.939	0.871	0.763	1.119	1.213	1.336	1.330	0.848	1.184
55S	0.891	0.886	0.809	1.098	1.256	1.318	1.340	0.831	1.213
50S	0.829	0.906	0.863	1.074	1.227	1.318	1.336	0.806	1.235
45S	0.763	0.929	0.919	1.044	1.200	1.326	1.307	0.781	1.254
40S	0.697	0.950	0.969	1.004	1.150	1.338	1.271	0.752	1.270
35S	0.631	0.976	0.996	0.961	1.090	1.333	1.225	0.717	1.287
30S	0.567	1.003	1.000	0.922	1.086	1.322	1.151	0.704	1.310
25S	0.505	0.974	0.986	0.878	1.076	1.267	1.146	0.684	1.348
20S	0.443	0.907	0.964	0.833	0.998	1.199	1.136	0.681	1.404
15S	0.345	0.999	1.102	0.908	0.989	1.254	1.284	0.746	1.661
10S	0.303	0.895	0.998	0.899	0.810	1.018	1.192	0.770	1.499
5S	0.270	0.966	1.075	0.942	0.748	1.017	1.212	0.818	1.641
0	0.249	1.021	1.124	1.003	0.844	0.967	1.258	0.915	1.784
5N	0.262	1.124	1.129	0.991	0.836	1.059	1.145	0.897	1.756
10N	0.323	1.049	0.983	0.878	0.885	0.969	0.966	0.805	1.518
15N	0.414	1.031	0.959	0.781	0.853	0.996	0.796	0.689	1.302
20N	0.594	0.975	0.906	0.678	0.807	1.015	0.723	0.587	1.234
25N	0.723	0.956	0.851	0.689	0.768	1.051	0.713	0.554	1.156
30N	0.853	0.942	0.827	0.709	0.727	1.076	0.701	0.561	1.105
35N	0.978	0.939	0.840	0.734	0.700	1.077	0.768	0.569	1.068
40N	1.087	0.953	0.873	0.784	0.701	1.094	0.824	0.606	1.044
45N	1.176	0.984	0.930	0.853	0.715	1.097	0.895	0.648	1.034
50N	1.269	1.001	0.945	0.912	0.752	1.096	0.958	0.699	1.012
55N	1.370	1.003	0.926	0.955	0.779	1.064	0.993	0.738	0.980
60N	1.455	0.996	0.914	0.992	0.839	1.049	1.020	0.791	0.955
65N	1.419	1.062	0.976	1.096	0.968	1.106	1.109	0.909	1.010
70N	1.343	1.143	1.075	1.223	1.129	1.200	1.217	1.032	1.097
75N	1.579	0.985	0.950	1.084	1.052	1.035	1.049	0.940	0.956
80N	1.591	0.983	0.950	1.103	1.090	1.042	1.047	0.970	0.965
	MEAN	0.980	0.952	0.936	0.941	1.139	1.073	0.760	1.251
	STD DEV	0.063	0.092	0.141	0.181	0.130	0.204	0.127	0.244

Table G-5 (continued)

MODEL-LIMS HNO_3 COMPARISON: FEBRUARY 1979

Latitude	LIMS	(Lower Limit Heterogeneous Chemistry Model Column/LIMS Column)							
(°)	Column†	AER	CAMED	DUPONT	GSFC	ITALY	LLNL	MRI	NCAR
55S	0.928	0.884	0.794	1.048	1.269	1.280	1.275	0.802	1.184
50S	0.856	0.904	0.835	1.028	1.198	1.296	1.274	0.780	1.216
45S	0.780	0.927	0.877	1.005	1.118	1.314	1.252	0.756	1.245
40S	0.701	0.953	0.917	0.978	1.077	1.340	1.228	0.736	1.273
35S	0.614	1.002	0.960	0.965	1.041	1.373	1.217	0.720	1.333
30S	0.529	1.064	0.990	0.965	1.047	1.409	1.182	0.734	1.410
25S	0.454	1.064	1.005	0.954	1.033	1.391	1.217	0.736	1.505
20S	0.394	0.991	0.982	0.916	0.986	1.314	1.210	0.741	1.579
15S	0.311	1.069	1.104	0.987	0.993	1.344	1.346	0.804	1.835
10S	0.278	0.935	0.984	0.960	0.799	1.052	1.240	0.813	1.610
5S	0.250	0.996	1.057	0.997	0.756	1.042	1.257	0.858	1.742
0	0.232	1.042	1.110	1.055	0.875	0.985	1.309	0.960	1.876
5N	0.247	1.118	1.114	1.026	0.877	1.077	1.184	0.933	1.815
10N	0.310	1.020	0.958	0.894	0.922	0.981	0.993	0.829	1.542
15N	0.387	1.029	0.912	0.816	0.915	1.034	0.844	0.731	1.352
20N	0.544	1.001	0.868	0.727	0.869	1.077	0.792	0.636	1.300
25N	0.701	0.931	0.802	0.701	0.776	1.048	0.739	0.569	1.155
30N	0.843	0.903	0.786	0.708	0.725	1.047	0.713	0.567	1.091
35N	0.985	0.886	0.798	0.721	0.689	1.025	0.768	0.565	1.041
40N	1.113	0.886	0.838	0.759	0.684	1.022	0.811	0.585	1.009
45N	1.215	0.908	0.917	0.819	0.695	1.018	0.874	0.614	0.995
50N	1.300	0.934	0.949	0.884	0.732	1.028	0.945	0.664	0.985
55N	1.378	0.957	0.943	0.943	0.768	1.025	0.998	0.712	0.971
60N	1.436	0.982	0.952	1.001	0.840	1.036	1.046	0.772	0.961
65N	1.481	1.009	0.971	1.051	0.915	1.042	1.077	0.836	0.955
70N	1.515	1.017	0.973	1.096	1.008	1.055	1.095	0.900	0.951
75N	1.545	1.020	0.970	1.135	1.099	1.058	1.089	0.963	0.949
80N	1.583	1.006	0.959	1.153	1.153	1.056	1.071	0.980	0.944
	MEAN	0.980	0.940	0.939	0.923	1.135	1.073	0.761	1.279
	STD DEV	0.064	0.093	0.129	0.166	0.147	0.194	0.122	0.304

Table G-5 (continued)

MODEL-LIMS HNO_3 COMPARISON: MARCH 1979

Latitude	LIMS	(Lower Limit Heterogeneous Chemistry Model Column/LIMS Column)							
(°)	Column†	AER	CAMED	DUPONT	GSFC	ITALY	LLNL	MRI	NCAR
55S	1.014	0.876	0.781	0.995	1.129	1.226	1.211	0.761	1.158
50S	0.935	0.888	0.807	0.968	1.120	1.243	1.203	0.737	1.179
45S	0.853	0.900	0.830	0.938	1.112	1.252	1.170	0.709	1.195
40S	0.769	0.912	0.849	0.904	1.058	1.268	1.135	0.685	1.215
35S	0.674	0.947	0.870	0.886	1.008	1.288	1.112	0.667	1.263
30S	0.562	1.029	0.914	0.911	1.018	1.355	1.102	0.697	1.371
25S	0.457	1.075	0.966	0.947	1.018	1.404	1.186	0.733	1.539
20S	0.380	1.027	0.973	0.945	1.012	1.368	1.212	0.769	1.671
15S	0.295	1.115	1.106	1.031	1.032	1.410	1.358	0.849	1.959
10S	0.262	0.972	0.989	1.007	0.822	1.095	1.264	0.858	1.716
5S	0.238	1.016	1.053	1.033	0.780	1.073	1.270	0.888	1.821
0	0.227	1.023	1.075	1.057	0.892	0.982	1.299	0.961	1.887
5N	0.245	1.070	1.067	1.016	0.899	1.077	1.178	0.921	1.792
10N	0.305	0.971	0.920	0.889	0.943	0.997	1.007	0.823	1.517
15N	0.381	0.977	0.851	0.809	0.931	1.045	0.864	0.725	1.317
20N	0.543	0.938	0.798	0.712	0.861	1.066	0.803	0.622	1.241
25N	0.678	0.895	0.781	0.707	0.787	1.053	0.766	0.572	1.133
30N	0.786	0.897	0.822	0.739	0.760	1.080	0.762	0.588	1.108
35N	0.905	0.891	0.891	0.762	0.731	1.062	0.824	0.593	1.082
40N	1.018	0.893	0.908	0.805	0.724	1.055	0.868	0.614	1.067
45N	1.112	0.913	0.884	0.865	0.731	1.047	0.928	0.643	1.065
50N	1.191	0.935	0.897	0.928	0.756	1.052	0.996	0.683	1.068
55N	1.267	0.953	0.933	0.983	0.781	1.048	1.046	0.721	1.064
60N	1.344	0.964	0.961	1.021	0.817	1.042	1.077	0.755	1.042
65N	1.432	0.963	0.978	1.036	0.843	1.022	1.075	0.779	1.008
70N	1.492	0.976	0.990	1.063	0.895	1.023	1.078	0.827	0.985
75N	1.528	1.002	1.008	1.095	0.958	1.031	1.071	0.884	0.969
80N	1.555	1.010	1.011	1.107	1.042	1.044	1.062	0.948	0.954
	MEAN	0.965	0.925	0.934	0.909	1.132	1.069	0.750	1.299
	STD DEV	0.064	0.093	0.115	0.129	0.134	0.166	0.111	0.309

Table G-5 (continued)

MODEL-LIMS HNO_3 COMPARISON: APRIL 1979

Latitude	LIMS	(Lower Limit Heterogeneous Chemistry Model Column/LIMS Column)							
(°)	Column†	AER	CAMED	DUPONT	GSFC	ITALY	LLNL	MRI	NCAR
55S	1.148	0.863	0.765	0.944	1.035	1.148	1.154	0.720	1.118
50S	1.055	0.871	0.787	0.914	1.027	1.173	1.146	0.695	1.133
45S	0.969	0.871	0.797	0.873	1.011	1.174	1.106	0.660	1.133
40S	0.882	0.864	0.794	0.827	0.995	1.176	1.057	0.629	1.134
35S	0.769	0.894	0.809	0.811	1.009	1.194	1.033	0.612	1.176
30S	0.642	0.959	0.834	0.828	1.021	1.242	1.007	0.635	1.270
25S	0.525	0.985	0.867	0.850	1.021	1.270	1.066	0.657	1.409
20S	0.421	0.961	0.893	0.875	1.022	1.270	1.112	0.717	1.572
15S	0.308	1.092	1.070	1.007	1.052	1.380	1.304	0.840	1.938
10S	0.266	0.969	0.976	1.006	0.829	1.091	1.236	0.867	1.735
5S	0.241	1.006	1.042	1.029	0.782	1.073	1.242	0.890	1.830
0	0.237	0.974	1.033	1.020	0.879	0.956	1.249	0.929	1.825
5N	0.260	0.977	1.002	0.954	0.874	1.028	1.121	0.864	1.675
10N	0.324	0.874	0.863	0.832	0.899	0.954	0.967	0.767	1.401
15N	0.405	0.874	0.795	0.754	0.876	0.990	0.837	0.672	1.200
20N	0.561	0.861	0.769	0.681	0.823	1.027	0.795	0.591	1.154
25N	0.643	0.886	0.817	0.732	0.812	1.091	0.814	0.590	1.136
30N	0.734	0.896	0.853	0.772	0.791	1.126	0.815	0.612	1.123
35N	0.828	0.903	0.897	0.807	0.773	1.120	0.881	0.628	1.119
40N	0.917	0.914	0.932	0.858	0.765	1.119	0.928	0.655	1.122
45N	1.006	0.926	0.957	0.911	0.760	1.102	0.976	0.678	1.125
50N	1.072	0.948	0.962	0.973	0.775	1.110	1.041	0.715	1.148
55N	1.132	0.968	0.943	1.029	0.793	1.114	1.090	0.752	1.162
60N	1.184	0.984	0.962	1.074	0.820	1.125	1.125	0.784	1.170
65N	1.226	1.003	1.003	1.108	0.851	1.138	1.147	0.820	1.179
70N	1.254	1.025	1.024	1.140	0.899	1.164	1.165	0.861	1.189
75N	1.275	1.049	1.038	1.164	0.950	1.187	1.165	0.905	1.195
80N	1.303	1.053	1.007	1.154	0.954	1.202	1.150	0.948	1.156
	MEAN	0.945	0.910	0.926	0.896	1.134	1.062	0.739	1.305
	STD DEV	0.066	0.097	0.133	0.101	0.095	0.141	0.112	0.260

Table G-5 (continued)

MODEL-LIMS HNO_3 COMPARISON: MAY 1979

Latitude	LIMS	(Lower Limit Heterogeneous Chemistry Model Column/LIMS Column)							
(°)	Column†	AER	CAMED	DUPONT	GSFC	ITALY	LLNL	MRI	NCAR
55S	1.303	0.855	0.754	0.906	0.964	1.058	1.105	0.686	1.052
50S	1.178	0.870	0.788	0.892	0.964	1.107	1.118	0.670	1.086
45S	1.059	0.875	0.814	0.866	0.959	1.136	1.106	0.647	1.109
40S	0.944	0.868	0.828	0.832	0.976	1.166	1.080	0.630	1.129
35S	0.844	0.850	0.819	0.789	0.980	1.154	1.024	0.597	1.139
30S	0.748	0.829	0.794	0.756	0.979	1.134	0.937	0.583	1.154
25S	0.639	0.832	0.782	0.737	0.995	1.106	0.938	0.574	1.218
20S	0.496	0.901	0.824	0.778	1.004	1.140	0.996	0.646	1.402
15S	0.342	1.085	1.038	0.945	1.051	1.314	1.225	0.802	1.823
10S	0.285	0.961	0.970	0.974	0.841	1.074	1.190	0.855	1.684
5S	0.256	0.987	1.033	0.997	0.772	1.059	1.202	0.874	1.774
0	0.252	0.940	1.012	0.978	0.859	0.936	1.215	0.890	1.749
5N	0.285	0.901	0.945	0.885	0.826	0.969	1.069	0.790	1.544
10N	0.350	0.803	0.818	0.778	0.830	0.904	0.937	0.695	1.295
15N	0.425	0.796	0.766	0.720	0.813	0.955	0.835	0.615	1.125
20N	0.574	0.798	0.752	0.664	0.791	1.004	0.799	0.557	1.103
25N	0.646	0.882	0.801	0.721	0.797	1.075	0.817	0.565	1.091
30N	0.716	0.931	0.845	0.774	0.792	1.134	0.830	0.599	1.099
35N	0.790	0.927	0.886	0.817	0.784	1.143	0.898	0.624	1.111
40N	0.870	0.921	0.911	0.866	0.771	1.144	0.941	0.658	1.118
45N	0.940	0.929	0.937	0.923	0.768	1.138	0.989	0.692	1.135
50N	0.992	0.947	0.957	0.985	0.782	1.153	1.049	0.734	1.168
55N	1.034	0.969	0.968	1.046	0.802	1.173	1.097	0.779	1.205
60N	1.069	0.986	0.976	1.093	0.823	1.199	1.125	0.816	1.229
65N	1.096	1.004	0.987	1.121	0.849	1.230	1.139	0.857	1.248
70N	1.115	1.020	0.982	1.128	0.847	1.268	1.145	0.891	1.250
75N	1.131	1.036	0.971	1.134	0.848	1.295	1.140	0.926	1.230
80N	1.141	1.048	0.957	1.140	0.839	1.328	1.135	0.954	1.220
	MEAN	0.920	0.890	0.902	0.868	1.125	1.039	0.722	1.267
	STD DEV	0.079	0.093	0.142	0.087	0.108	0.128	0.123	0.229

Table G-6. Comparison of Model-Calculated $C\ell ONO_2$ Columns at 45N with the June 1986 ISSJ Total Column Measurement of Zander and Demoulin (1988)

Modeling Group	$C\ell ONO_2$ Column Amount†					
	1980SG	1990SG	1986SG‡	1980SLH	1990SHL	1986SHL‡
AER	9.98	14.65	12.78(1.11)	11.98	17.22	15.12(1.32)
CAMED	5.82	7.21	6.65(0.58)	6.72	8.19	7.60(0.66)
DUPONT	5.78	8.51	7.42(0.66)	7.65	11.05	9.69(0.84)
GSFC	5.07	7.14	6.31(0.55)	6.06	8.45	7.49(0.65)
LLNL	7.89	10.95	9.73(0.85)	9.57	12.98	11.62(1.01)
MRI	5.77	8.27	7.27(0.63)	5.70	8.19	7.19(0.63)
NCAR	5.81	8.16	7.22(0.63)	7.16	9.78	8.73(0.76)
WASH	7.68	10.41	9.32(0.81)			

† Column in 10^{14} $C\ell ONO_2$ molecules cm^{-2} above 4 km.

‡ Model $C\ell ONO_2$ column in June 1986 derived by linearly interpolating between the June 1980 and June 1990 model columns. Values in parenthesis are the interpolated model column divided by the measured ISSJ column of Zander and Demoulin (1988).

Table G-7. Comparison of NO_2 Columns Computed for 1980 with Steady-State Gas Phase Chemistry and LIMS Daytime NO_2 Zonal Mean Columns from 1978-1979 († in 10^{15} molecules cm^{-2})

MODEL-LIMS DAYTIME NO_2 COMPARISON: NOVEMBER 1978

Latitude	LIMS	(Gas Phase Model/LIMS Columns Ratio)				
(°)	Column†	AER	CAMED	GSFC	LLNL	WASH
60S	3.128	0.744	0.700	0.886	0.799	0.781
55S	3.003	0.783	0.761	0.881	0.839	0.805
50S	2.893	0.814	0.831	0.894	0.860	0.824
45S	2.833	0.824	0.880	0.892	0.853	0.830
40S	2.822	0.809	0.906	0.868	0.826	0.821
35S	2.869	0.774	0.890	0.828	0.776	0.795
30S	2.905	0.739	0.861	0.754	0.729	0.763
25S	2.841	0.715	0.841	0.706	0.707	0.757
20S	2.609	0.726	0.862	0.680	0.727	0.792
15S	2.350	0.755	0.897	0.657	0.768	0.842
10S	2.152	0.771	0.915	0.663	0.807	0.875
5S	2.097	0.780	0.897	0.625	0.799	0.853
0	2.080	0.781	0.864	0.640	0.798	0.825
5N	2.078	0.816	0.863	0.651	0.791	0.792
10N	2.109	0.839	0.850	0.677	0.777	0.780
15N	2.172	0.857	0.858	0.692	0.754	0.757
20N	2.260	0.859	0.857	0.690	0.725	0.733
25N	2.319	0.851	0.868	0.697	0.708	0.720
30N	2.322	0.855	0.894	0.701	0.708	0.712
35N	2.262	0.867	0.933	0.726	0.728	0.723
40N	2.216	0.867	0.947	0.727	0.744	0.712
45N	2.093	0.888	0.966	0.756	0.783	0.727
50N	1.974	0.896	0.965	0.761	0.820	0.722
55N	1.902	0.869	0.923	0.748	0.833	0.699
60N	1.853	0.805	0.875	0.683	0.824	0.657
	MEAN	0.811	0.876	0.739	0.779	0.772
	STD DEV	0.053	0.058	0.086	0.048	0.055

Table G-7 (continued).

MODEL-LIMS DAYTIME NO_2 COMPARISON: DECEMBER 1978

Latitude	LIMS	(Gas Phase Model/LIMS Columns Ratio)				
(°)	Column†	AER	CAMED	GSFC	LLNL	WASH
60S	3.364	0.753	0.718	0.899	0.842	0.798
55S	3.266	0.774	0.772	0.887	0.856	0.805
50S	3.176	0.789	0.819	0.893	0.856	0.811
45S	3.087	0.797	0.853	0.898	0.846	0.818
40S	3.064	0.781	0.854	0.852	0.811	0.796
35S	3.010	0.766	0.841	0.814	0.776	0.781
30S	2.996	0.737	0.800	0.734	0.728	0.754
25S	2.911	0.710	0.784	0.670	0.701	0.745
20S	2.670	0.713	0.814	0.640	0.709	0.773
15S	2.406	0.735	0.849	0.610	0.739	0.814
10S	2.226	0.736	0.855	0.608	0.762	0.832
5S	2.140	0.750	0.855	0.579	0.758	0.817
0	2.108	0.751	0.837	0.605	0.760	0.796
5N	2.081	0.791	0.854	0.630	0.761	0.773
10N	2.063	0.829	0.872	0.675	0.766	0.795
15N	2.153	0.832	0.886	0.684	0.734	0.777
20N	2.222	0.838	0.898	0.687	0.711	0.758
25N	2.198	0.858	0.909	0.718	0.719	0.772
30N	2.090	0.904	0.963	0.752	0.757	0.790
35N	2.009	0.921	1.016	0.780	0.772	0.799
40N	1.908	0.939	1.052	0.791	0.797	0.785
45N	1.805	0.943	1.047	0.804	0.814	0.770
50N	1.674	0.942	1.041	0.796	0.837	0.761
55N	1.661	0.852	0.944	0.730	0.778	0.698
60N	1.618	0.730	0.903	0.564	0.693	0.656
	MEAN	0.807	0.881	0.732	0.771	0.779
	STD DEV	0.075	0.088	0.106	0.050	0.038

Table G-7 (continued).

MODEL-LIMS DAYTIME NO_2 COMPARISON: JANUARY 1979

Latitude (°)	LIMS Column†	(Gas Phase Model/LIMS Columns Ratio)				
		AER	CAMED	GSFC	LLNL	WASH
60S	3.412	0.740	0.735	0.910	0.896	0.785
55S	3.299	0.760	0.779	0.917	0.911	0.801
50S	3.202	0.776	0.816	0.925	0.908	0.810
45S	3.118	0.784	0.835	0.929	0.889	0.817
40S	3.039	0.784	0.836	0.882	0.858	0.816
35S	2.981	0.772	0.812	0.827	0.809	0.809
30S	2.900	0.761	0.782	0.754	0.759	0.789
25S	2.807	0.736	0.757	0.679	0.722	0.771
20S	2.648	0.720	0.751	0.628	0.697	0.766
15S	2.383	0.741	0.788	0.596	0.714	0.795
10S	2.159	0.756	0.823	0.601	0.740	0.824
5S	2.033	0.782	0.849	0.579	0.740	0.817
0	2.005	0.777	0.839	0.613	0.736	0.812
5N	1.904	0.847	0.901	0.674	0.759	0.837
10N	1.997	0.837	0.885	0.693	0.727	0.825
15N	2.076	0.844	0.942	0.716	0.706	0.820
20N	2.148	0.849	0.979	0.723	0.694	0.802
25N	2.194	0.851	0.953	0.739	0.696	0.795
30N	2.074	0.910	0.996	0.778	0.754	0.816
35N	1.962	0.950	1.023	0.820	0.791	0.837
40N	1.878	0.966	1.044	0.826	0.820	0.818
45N	1.737	1.000	1.113	0.860	0.848	0.825
50N	1.695	0.955	1.085	0.816	0.801	0.778
55N	1.664	0.879	1.013	0.765	0.706	0.723
60N	1.674	0.733	0.901	0.538	0.533	0.653
	MEAN	0.820	0.889	0.751	0.769	0.798
	STD DEV	0.082	0.110	0.119	0.087	0.039

Table G-7 (continued).

MODEL-LIMS DAYTIME NO_2 COMPARISON: FEBRUARY 1979

Latitude	LIMS	(Gas Phase Model/LIMS Columns Ratio)				
(°)	Column†	AER	CAMED	GSFC	LLNL	WASH
55S	3.153	0.743	0.769	0.895	0.869	0.792
50S	3.109	0.754	0.794	0.896	0.864	0.800
45S	3.051	0.762	0.807	0.900	0.852	0.812
40S	2.995	0.763	0.800	0.856	0.828	0.809
35S	2.928	0.761	0.780	0.812	0.794	0.809
30S	2.834	0.762	0.754	0.750	0.762	0.793
25S	2.713	0.752	0.734	0.689	0.740	0.784
20S	2.550	0.743	0.724	0.645	0.725	0.778
15S	2.191	0.806	0.794	0.649	0.784	0.840
10S	1.932	0.849	0.850	0.675	0.837	0.887
5S	1.790	0.892	0.900	0.664	0.851	0.888
0	1.771	0.882	0.895	0.703	0.840	0.881
5N	1.383	1.169	1.187	0.942	1.049	1.108
10N	1.856	0.902	0.922	0.773	0.790	0.873
15N	1.943	0.910	0.967	0.806	0.766	0.879
20N	2.022	0.919	1.005	0.813	0.759	0.873
25N	2.201	0.876	0.963	0.783	0.728	0.829
30N	2.150	0.919	1.017	0.805	0.775	0.838
35N	2.035	0.975	1.075	0.854	0.834	0.874
40N	1.958	1.007	1.114	0.869	0.881	0.875
45N	1.861	1.041	1.163	0.895	0.922	0.885
50N	1.816	1.026	1.146	0.880	0.922	0.852
55N	1.746	1.004	1.115	0.876	0.908	0.830
60N	1.757	0.916	1.033	0.762	0.811	0.749
65N	1.693	0.854	0.996	0.678	0.781	0.698
	MEAN	0.879	0.932	0.795	0.827	0.841
	STD DEV	0.114	0.148	0.092	0.074	0.074

Table G-7 (continued).

MODEL-LIMS DAYTIME NO_2 COMPARISON: MARCH 1979

Latitude (°)	LIMS Column†	(Gas Phase Model/LIMS Columns Ratio)				
		AER	CAMED	GSFC	LLNL	WASH
55S	2.842	0.749	0.781	0.878	0.847	0.760
50S	2.845	0.760	0.807	0.883	0.844	0.772
45S	2.864	0.759	0.808	0.883	0.827	0.779
40S	2.884	0.749	0.792	0.827	0.799	0.773
35S	2.865	0.743	0.769	0.782	0.769	0.777
30S	2.795	0.746	0.746	0.718	0.750	0.763
25S	2.674	0.742	0.732	0.664	0.742	0.763
20S	2.516	0.737	0.725	0.635	0.742	0.765
15S	1.490	1.168	1.157	0.952	1.183	1.212
10S	1.399	1.166	1.170	0.953	1.198	1.204
5S	1.332	1.197	1.213	0.936	1.198	1.173
0	1.310	1.196	1.223	1.001	1.189	1.171
5N	1.290	1.259	1.299	1.066	1.178	1.166
10N	1.671	1.009	1.051	0.904	0.918	0.955
15N	2.041	0.882	0.935	0.807	0.764	0.827
20N	2.136	0.894	0.963	0.812	0.753	0.836
25N	2.364	0.846	0.925	0.771	0.712	0.796
30N	2.419	0.858	0.949	0.763	0.725	0.780
35N	2.358	0.897	0.997	0.792	0.765	0.803
40N	2.231	0.961	1.052	0.829	0.829	0.833
45N	2.115	1.020	1.066	0.865	0.888	0.863
50N	1.974	1.079	1.094	0.907	0.957	0.902
55N	1.835	1.130	1.129	0.956	1.025	0.948
60N	1.774	1.117	1.101	0.958	1.035	0.942
65N	1.729	1.082	1.051	0.951	1.062	0.927
70N	1.715	1.025	1.003	0.879	1.088	0.867
75N	1.762	0.934	0.928	0.778	1.030	0.778
	MEAN	0.952	0.980	0.857	0.919	0.894
	STD DEV	0.173	0.167	0.102	0.172	0.154

Table G-7 (continued).

MODEL-LIMS DAYTIME NO_2 COMPARISON: APRIL 1979

Latitude (°)	LIMS Column†	(Gas Phase Model/LIMS Columns Ratio)				
		AER	CAMED	GSFC	LLNL	WASH
55S	2.412	0.769	0.804	0.864	0.844	0.738
50S	2.470	0.782	0.831	0.859	0.843	0.753
45S	2.564	0.772	0.827	0.843	0.820	0.757
40S	2.647	0.755	0.808	0.796	0.790	0.752
35S	2.651	0.753	0.793	0.775	0.771	0.770
30S	2.583	0.764	0.786	0.731	0.772	0.780
25S	2.502	0.757	0.772	0.688	0.770	0.794
20S	2.355	0.757	0.773	0.668	0.788	0.797
15S	1.996	0.846	0.869	0.714	0.898	0.886
10S	1.398	1.141	1.183	0.979	1.239	1.193
5S	1.382	1.134	1.186	0.950	1.213	1.135
0	1.371	1.129	1.191	1.010	1.197	1.135
5N	1.476	1.089	1.157	0.987	1.089	1.047
10N	2.030	0.825	0.883	0.780	0.802	0.818
15N	2.207	0.820	0.883	0.775	0.752	0.805
20N	2.331	0.832	0.903	0.774	0.737	0.810
25N	2.441	0.841	0.929	0.777	0.737	0.820
30N	2.487	0.866	0.967	0.777	0.755	0.816
35N	2.488	0.895	0.997	0.790	0.779	0.828
40N	2.408	0.951	1.041	0.816	0.830	0.846
45N	2.278	1.029	1.080	0.861	0.895	0.885
50N	2.177	1.085	1.093	0.895	0.948	0.915
55N	2.110	1.112	1.071	0.918	0.975	0.932
60N	2.118	1.084	1.007	0.912	0.948	0.907
65N	2.002	1.110	0.998	0.962	0.979	0.937
70N	2.031	1.055	0.954	0.962	0.943	0.901
75N	2.059	1.000	0.923	0.963	0.929	0.867
	MEAN	0.924	0.952	0.845	0.890	0.875
	STD DEV	0.148	0.136	0.098	0.148	0.123

Table G-7 (continued).

MODEL-LIMS DAYTIME NO_2 COMPARISON: MAY 1979

Latitude (°)	LIMS Column†	(Gas Phase Model/LIMS Columns Ratio)				
		AER	CAMED	GSFC	LLNL	WASH
55S	2.129	0.727	0.780	0.787	0.804	0.683
50S	2.120	0.788	0.854	0.828	0.840	0.735
45S	2.156	0.817	0.894	0.851	0.851	0.771
40S	2.179	0.833	0.920	0.854	0.857	0.807
35S	2.248	0.815	0.901	0.839	0.833	0.825
30S	2.343	0.779	0.856	0.774	0.801	0.802
25S	2.288	0.777	0.848	0.759	0.808	0.833
20S	2.093	0.818	0.885	0.762	0.869	0.873
15S	1.958	0.835	0.907	0.741	0.913	0.893
10S	1.924	0.808	0.884	0.726	0.911	0.861
5S	1.526	1.005	1.104	0.881	1.127	1.025
0	1.435	1.059	1.167	0.979	1.179	1.095
5N	1.528	1.038	1.144	0.961	1.089	1.032
10N	2.070	0.802	0.883	0.767	0.817	0.821
15N	2.250	0.801	0.876	0.760	0.768	0.809
20N	2.417	0.807	0.878	0.751	0.743	0.798
25N	2.525	0.836	0.906	0.760	0.749	0.807
30N	2.523	0.890	0.963	0.784	0.786	0.831
35N	2.529	0.921	0.998	0.805	0.818	0.852
40N	2.550	0.945	1.012	0.814	0.843	0.848
45N	2.515	0.987	1.028	0.840	0.880	0.863
50N	2.488	1.014	1.027	0.856	0.910	0.877
55N	2.448	1.035	1.019	0.876	0.935	0.896
60N	2.411	1.050	1.016	0.904	0.946	0.907
65N	2.398	1.049	1.006	0.924	0.983	0.909
70N	2.385	1.021	0.955	0.956	1.042	0.913
75N	2.339	0.996	0.901	1.002	1.066	0.931
	MEAN	0.898	0.948	0.835	0.895	0.863
	STD DEV	0.109	0.095	0.079	0.117	0.088

Table G-8. Comparison of NO_2 Columns Computed for 1980 with Lower Limit Heterogeneous Chemistry and LIMS Daytime NO_2 Zonal Mean Columns from 1978-1979 († in 10^{15} molecules cm^{-2})

MODEL-LIMS DAYTIME NO_2 COMPARISON: NOVEMBER 1978

Latitude (°)	LIMS Column†	(Lower Limit Heterogeneous Model/LIMS Columns Ratio) AER	CAMED	GSFC	LLNL
60S	3.128	0.586	0.689	0.801	0.749
55S	3.003	0.614	0.744	0.804	0.777
50S	2.893	0.642	0.808	0.821	0.794
45S	2.833	0.654	0.852	0.823	0.791
40S	2.822	0.647	0.875	0.803	0.769
35S	2.869	0.623	0.858	0.767	0.728
30S	2.905	0.597	0.829	0.694	0.689
25S	2.841	0.583	0.810	0.645	0.672
20S	2.609	0.603	0.831	0.626	0.694
15S	2.350	0.635	0.867	0.610	0.736
10S	2.512	0.657	0.886	0.621	0.776
5S	2.097	0.668	0.868	0.590	0.771
0	2.080	0.670	0.836	0.603	0.769
5N	2.078	0.697	0.833	0.611	0.762
10N	2.109	0.712	0.820	0.628	0.746
15N	2.172	0.717	0.822	0.635	0.720
20N	2.260	0.710	0.816	0.624	0.689
25N	2.319	0.696	0.820	0.622	0.668
30N	2.322	0.696	0.841	0.622	0.665
35N	2.262	0.706	0.882	0.641	0.677
40N	2.216	0.702	0.893	0.630	0.687
45N	2.093	0.706	0.900	0.642	0.713
50N	1.974	0.694	0.886	0.626	0.732
55N	1.902	0.651	0.829	0.593	0.730
60N	1.853	0.580	0.764	0.530	0.710
	MEAN	0.658	0.834	0.665	0.729
	STD DEV	0.045	0.049	0.084	0.041

Table G-8. (continued)

MODEL-LIMS DAYTIME NO_2 COMPARISON: DECEMBER 1978

Latitude	LIMS	(Lower Limit Heterogeneous Model/LIMS Columns Ratio)			
(°)	Column†	AER	CAMED	GSFC	LLNL
60S	3.364	0.607	0.712	0.855	0.813
55S	3.266	0.615	0.760	0.838	0.817
50S	3.176	0.628	0.801	0.840	0.814
45S	3.087	0.636	0.831	0.842	0.804
40S	3.064	0.626	0.830	0.798	0.771
35S	3.010	0.616	0.815	0.760	0.739
30S	2.996	0.594	0.773	0.682	0.695
25S	2.911	0.579	0.758	0.618	0.670
20S	2.670	0.593	0.788	0.593	0.680
15S	2.406	0.619	0.822	0.568	0.710
10S	2.226	0.627	0.829	0.570	0.733
5S	2.140	0.643	0.829	0.547	0.730
0	2.108	0.646	0.810	0.569	0.732
5N	2.081	0.677	0.823	0.591	0.732
10N	2.063	0.705	0.837	0.623	0.733
15N	2.153	0.697	0.843	0.623	0.699
20N	2.222	0.691	0.846	0.613	0.672
25N	2.198	0.697	0.853	0.629	0.673
30N	2.090	0.725	0.898	0.653	0.701
35N	2.009	0.734	0.945	0.670	0.703
40N	1.908	0.735	0.970	0.662	0.713
45N	1.805	0.711	0.946	0.655	0.711
50N	1.674	0.677	0.913	0.619	0.708
55N	1.661	0.576	0.794	0.537	0.641
60N	1.618	0.468	0.725	0.405	0.562
	MEAN	0.645	0.830	0.654	0.718
	STD DEV	0.062	0.065	0.112	0.057

Table G-8. (continued)

MODEL-LIMS DAYTIME NO_2 COMPARISON: JANUARY 1979

Latitude	LIMS	(Lower Limit Heterogeneous Model/LIMS Columns Ratio)			
(°)	Column†	AER	CAMED	GSFC	LLNL
60S	3.412	0.606	0.731	0.876	0.871
55S	3.299	0.615	0.770	0.871	0.877
50S	3.202	0.626	0.802	0.876	0.870
45S	3.118	0.632	0.818	0.877	0.851
40S	3.039	0.634	0.817	0.834	0.821
35S	2.981	0.625	0.792	0.782	0.774
30S	2.900	0.616	0.759	0.707	0.726
25S	2.807	0.603	0.734	0.630	0.693
20S	2.648	0.600	0.729	0.584	0.670
15S	2.383	0.625	0.765	0.557	0.687
10S	2.159	0.645	0.799	0.564	0.713
5S	2.033	0.670	0.824	0.546	0.714
0	2.005	0.670	0.813	0.577	0.708
5N	1.904	0.727	0.870	0.632	0.730
10N	1.997	0.714	0.851	0.639	0.695
15N	2.076	0.708	0.895	0.649	0.670
20N	2.148	0.701	0.922	0.642	0.653
25N	2.194	0.689	0.895	0.643	0.647
30N	2.074	0.725	0.931	0.666	0.691
35N	1.962	0.748	0.954	0.690	0.710
40N	1.878	0.742	0.965	0.674	0.721
45N	1.737	0.733	1.009	0.679	0.726
50N	1.695	0.660	0.954	0.608	0.663
55N	1.664	0.560	0.851	0.529	0.571
60N	1.674	0.439	0.717	0.359	0.430
	MEAN	0.653	0.839	0.668	0.715
	STD DEV	0.069	0.084	0.128	0.097

Table G-8. (continued)

MODEL-LIMS DAYTIME NO_2 COMPARISON: FEBRUARY 1979

Latitude (°)	LIMS Column†	(Lower Limit Heterogeneous Model/LIMS Columns Ratio) AER	CAMED	GSFC	LLNL
55S	3.153	0.605	0.753	0.834	0.840
50S	3.109	0.613	0.776	0.837	0.833
45S	3.051	0.620	0.787	0.845	0.821
40S	2.995	0.623	0.781	0.805	0.797
35S	2.928	0.621	0.759	0.767	0.763
30S	2.834	0.620	0.731	0.702	0.731
25S	2.713	0.616	0.711	0.639	0.711
20S	2.550	0.619	0.704	0.601	0.698
15S	2.191	0.679	0.772	0.607	0.756
10S	1.932	0.723	0.828	0.634	0.807
5S	1.790	0.764	0.876	0.625	0.822
0	1.771	0.758	0.871	0.660	0.810
5N	1.383	1.001	1.154	0.882	1.010
10N	1.856	0.770	0.894	0.714	0.756
15N	1.943	0.764	0.933	0.736	0.730
20N	2.022	0.759	0.965	0.731	0.717
25N	2.201	0.711	0.922	0.692	0.680
30N	2.150	0.736	0.967	0.701	0.717
35N	2.035	0.775	1.019	0.733	0.754
40N	1.958	0.786	1.045	0.723	0.781
45N	1.861	0.784	1.072	0.720	0.794
50N	1.816	0.735	1.032	0.665	0.765
55N	1.746	0.674	0.969	0.617	0.732
60N	1.757	0.571	0.852	0.503	0.641
65N	1.693	0.485	0.765	0.409	0.624
	MEAN	0.696	0.877	0.695	0.764
	STD DEV	0.103	0.126	0.107	0.077

Table G-8. (continued)

MODEL-LIMS DAYTIME NO_2 COMPARISON: MARCH 1979

Latitude (°)	LIMS Column†	(Lower Limit Heterogeneous Model/LIMS Columns Ratio) AER	CAMED	GSFC	LLNL
55S	2.842	0.608	0.751	0.788	0.805
50S	2.845	0.619	0.775	0.800	0.801
45S	2.864	0.621	0.778	0.806	0.787
40S	2.884	0.615	0.763	0.762	0.761
35S	2.865	0.610	0.740	0.727	0.733
30S	2.795	0.609	0.715	0.663	0.715
25S	2.674	0.611	0.702	0.608	0.709
20S	2.516	0.616	0.697	0.586	0.711
15S	1.490	0.988	1.115	0.887	1.136
10S	1.399	0.997	1.126	0.892	1.153
5S	1.332	1.027	1.166	0.882	1.155
0	1.310	1.028	1.175	0.941	1.148
5N	1.290	1.079	1.245	1.001	1.138
10N	1.671	0.861	1.004	0.840	0.885
15N	2.041	0.741	0.893	0.743	0.734
20N	2.136	0.740	0.919	0.741	0.720
25N	2.364	0.691	0.886	0.697	0.676
30N	2.419	0.694	0.912	0.685	0.684
35N	2.358	0.724	0.963	0.707	0.710
40N	2.231	0.768	1.015	0.726	0.759
45N	2.115	0.798	1.021	0.743	0.796
50N	1.974	0.822	1.034	0.752	0.835
55N	1.835	0.832	1.042	0.762	0.870
60N	1.774	0.787	0.983	0.722	0.859
65N	1.729	0.721	0.899	0.673	0.868
70N	1.715	0.629	0.812	0.584	0.883
75N	1.762	0.514	0.704	0.476	0.843
	MEAN	0.754	0.920	0.748	0.847
	STD DEV	0.156	0.164	0.115	0.158

Table G-8. (continued)

MODEL-LIMS DAYTIME NO_2 COMPARISON: APRIL 1979

Latitude	LIMS	(Lower Limit Heterogeneous Model/LIMS Columns Ratio)			
(°)	Column†	AER	CAMED	GSFC	LLNL
55S	2.412	0.607	0.750	0.725	0.778
50S	2.470	0.626	0.781	0.736	0.779
45S	2.564	0.626	0.782	0.737	0.763
40S	2.647	0.619	0.768	0.705	0.739
35S	2.651	0.618	0.756	0.695	0.724
30S	2.583	0.626	0.748	0.656	0.728
25S	2.502	0.625	0.735	0.619	0.729
20S	2.355	0.636	0.739	0.610	0.750
15S	1.996	0.718	0.832	0.664	0.858
10S	1.398	0.979	1.134	0.916	1.188
5S	1.382	0.977	1.137	0.895	1.168
0	1.371	0.976	1.141	0.950	1.155
5N	1.476	0.937	1.110	0.927	1.053
10N	2.030	0.705	0.848	0.727	0.774
15N	2.207	0.690	0.850	0.718	0.723
20N	2.331	0.690	0.871	0.713	0.706
25N	2.441	0.689	0.900	0.713	0.704
30N	2.487	0.704	0.940	0.713	0.718
35N	2.488	0.729	0.973	0.727	0.736
40N	2.408	0.771	1.015	0.744	0.779
45N	2.278	0.823	1.046	0.779	0.831
50N	2.177	0.855	1.053	0.801	0.867
55N	2.110	0.862	1.029	0.811	0.881
60N	2.118	0.828	0.962	0.790	0.846
65N	2.002	0.836	0.946	0.817	0.863
70N	2.031	0.779	0.882	0.774	0.820
75N	2.059	0.722	0.828	0.733	0.802
	MEAN	0.750	0.909	0.755	0.832
	STD DEV	0.121	0.136	0.087	0.143

Table G-8. (continued)

MODEL-LIMS DAYTIME NO_2 COMPARISON: MAY 1979

Latitude (°)	LIMS Column†	(Lower Limit Heterogeneous Model/LIMS Columns Ratio) AER	CAMED	GSFC	LLNL
55S	2.129	0.532	0.683	0.594	0.683
50S	2.120	0.600	0.766	0.654	0.727
45S	2.155	0.640	0.817	0.700	0.753
40S	2.179	0.669	0.854	0.720	0.771
35S	2.248	0.664	0.843	0.725	0.759
30S	2.343	0.638	0.803	0.672	0.741
25S	2.288	0.643	0.799	0.664	0.753
20S	2.093	0.687	0.841	0.683	0.817
15S	1.958	0.711	0.866	0.685	0.866
10S	1.924	0.697	0.848	0.678	0.870
5S	1.526	0.870	1.062	0.830	1.083
0	1.435	0.919	1.125	0.921	1.135
5N	1.528	0.896	1.107	0.901	1.051
10N	2.070	0.688	0.857	0.717	0.787
15N	2.250	0.678	0.853	0.707	0.739
20N	2.417	0.672	0.855	0.696	0.714
25N	2.525	0.684	0.882	0.703	0.718
30N	2.523	0.722	0.939	0.729	0.753
35N	2.529	0.752	0.977	0.752	0.782
40N	2.550	0.771	0.993	0.759	0.804
45N	2.515	0.799	1.007	0.782	0.837
50N	2.488	0.815	1.007	0.793	0.860
55N	2.448	0.825	1.002	0.809	0.882
60N	2.411	0.833	1.001	0.832	0.893
65N	2.398	0.832	0.993	0.847	0.932
70N	2.385	0.820	0.937	0.903	0.993
75N	2.339	0.815	0.875	0.974	1.014
	MEAN	0.736	0.911	0.757	0.841
	STD DEV	0.097	0.107	0.093	0.122

FIGURE CAPTIONS

Figure G-1. Comparison of HF columns above 11.9 km (Mankin and Coffey, 1983) with 1980 gas phase model HF columns derived from integrations of the profiles above $z^* = 12$ km.

Figure G-2. Comparison of calculated 1980 Kitt Peak HF total columns with columns derived by integrating the 1980 30N gas phase model profiles above $z^* = 2$ km.

Figure G-3. Same as Figure G-2 except the columns have been normalized by dividing each curve from Figure G-2 by its mean value.

Figure G-4. Contour maps of *G* (left panel) and the ratio *R* (right panel) as a function of latitude and season where R = H/G, *H* is the 1980 HCl column above $z^* = 12$ km computed with lower limit heterogeneous chemistry, and *G* is the 1980 HCl column above $z^* = 12$ km computed with gas phase chemistry only. Contours are in units of 10^{15} molecules cm^{-2}.

Figure G-5. Steady-state, gas phase 1980 HCl model columns and the Mankin and Coffey (1983) aircraft data plotted as a function of latitude.

Figure G-6. Same as Figure G-5 with the 1980 steady-state lower-limit heterogeneous chemistry runs instead of the 1980 steady-state, gas phase HCl model columns.

Figure G-7. LIMS HNO_3 columns as a function of latitude and season.

Figure G-8. Contour maps of *G* (left panel) and the ratio *R* (right panel) as a function of latitude and season where R = H/G, *H* is the 1980 HNO_3 column computed with lower limit heterogeneous chemistry, and *G* is the 1980 HNO_3 column computed with gas phase chemistry only. See text for the column integration limits, which vary with latitude. Contours are in units of 10^{15} molecules cm^{-2}.

Figure G-9. Comparison of LIMS HNO_3 columns for the months of December 1978 and May 1979 with 1980 model columns derived from calculations performed with standard gas phase chemistry and columns derived from calculations including lower-limit heterogeneous chemistry. See text for the column integration limits, which vary with latitude.

Figure G-10. Comparisons of the seasonal variation of the HNO_3 columns measured near 45N with columns derived from the gas phase and lower limit heterogeneous model calculations. The LIMS curve shows the 45N nighttime data integrated above 100 mb. The ISSJ data are total columns measured above 3.58 km from a latitude of 46.5N. The NCAR lower limit heterogeneous chemistry model values are all above 2×10^{16} molecules cm^{-2} and therefore do not appear in the figure.

Figure G-11. Comparison of CAMED and DUPONT gas phase and lower limit heterogeneous chemistry model $ClONO_2$ columns above $z^* = 4$ km with a measured ISSJ $ClONO_2$ column of $(1.15 \pm 0.3) \times 10^{15}$ molecules cm^{-2} above the Jungfraujoch (ISSJ) station (46.5N lat., 3.58 km altitude) in June 1986 (Zander and Demoulin, 1988).

Figure G-12. Contour maps of *G* (left panel) and the ratio *R* (right panel) as a function of latitude and season where R = H/G, *H* is the 1980 NO_2 column computed with lower-limit heterogeneous chemistry, and *G* is the 1980 NO_2 column computed with gas phase chemistry only. See text for the column integration limits of the LIMS and model data. Contours are in units of 10^{15} molecules cm^{-2}.

Figure G-13. AER noon gas phase and lower-limit heterogeneous chemistry NO_2 vertical profiles for March 1980 at 3 latitudes (left panels) and vertical profiles of the ratio of the volume mixing ratios from the profiles (right panels).

Figure G-14. Comparison of LIMS daytime NO_2 columns for the months of December 1978 and May 1979 with 1980 model columns derived from calculations performed with standard gas phase chemistry and columns derived from calculations including lower-limit heterogeneous chemistry. See text for a description of the model runs and the column integration limits.

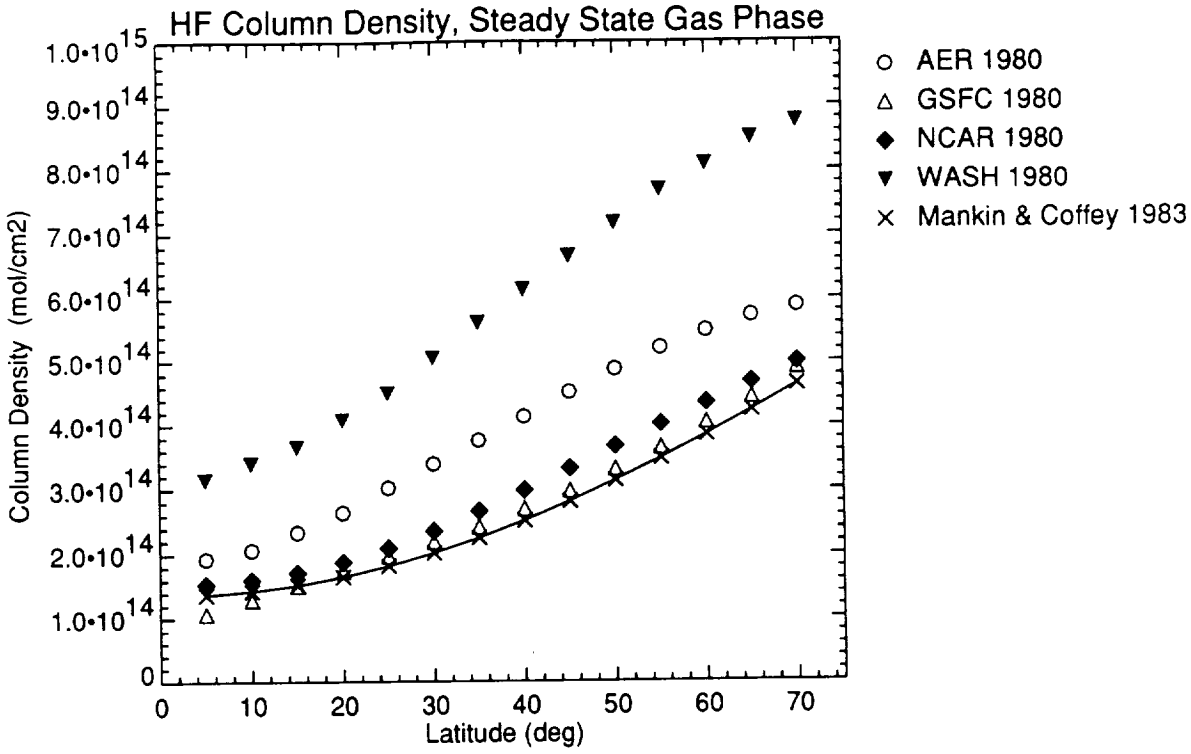
HF Column Density, Steady State Gas Phase
Column Density (mol/cm2)
1.0•10^15
9.0•10^14
8.0•10^14
7.0•10^14
6.0•10^14
5.0•10^14
4.0•10^14
3.0•10^14
2.0•10^14
1.0•10^14
0
0
10
20
30
40
50
60
70
Latitude (deg)
AER 1980
GSFC 1980
NCAR 1980
WASH 1980
Mankin & Coffey 1983

Figure G-1

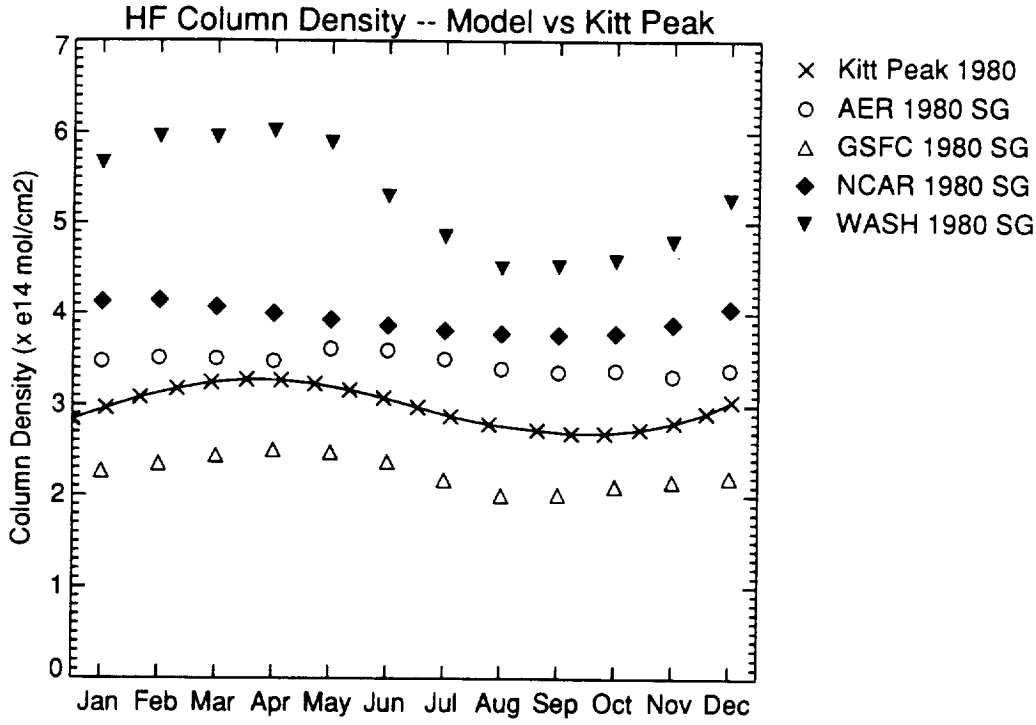

Figure G-2

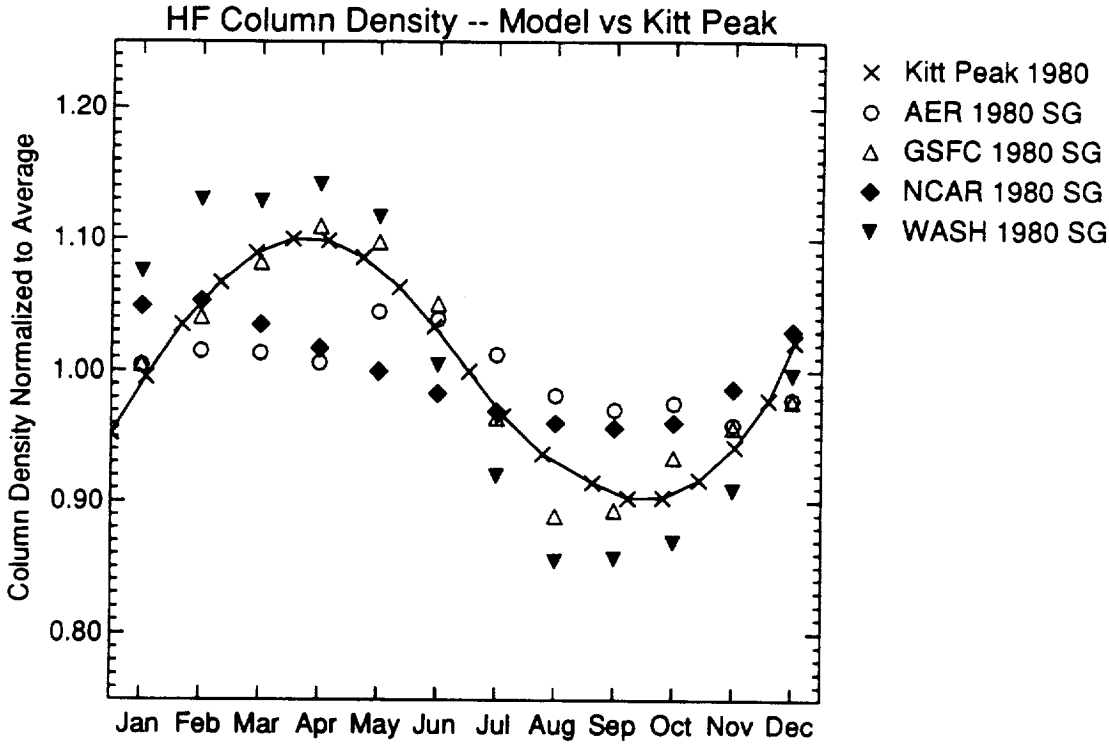

Figure G-3

HCl Column Density

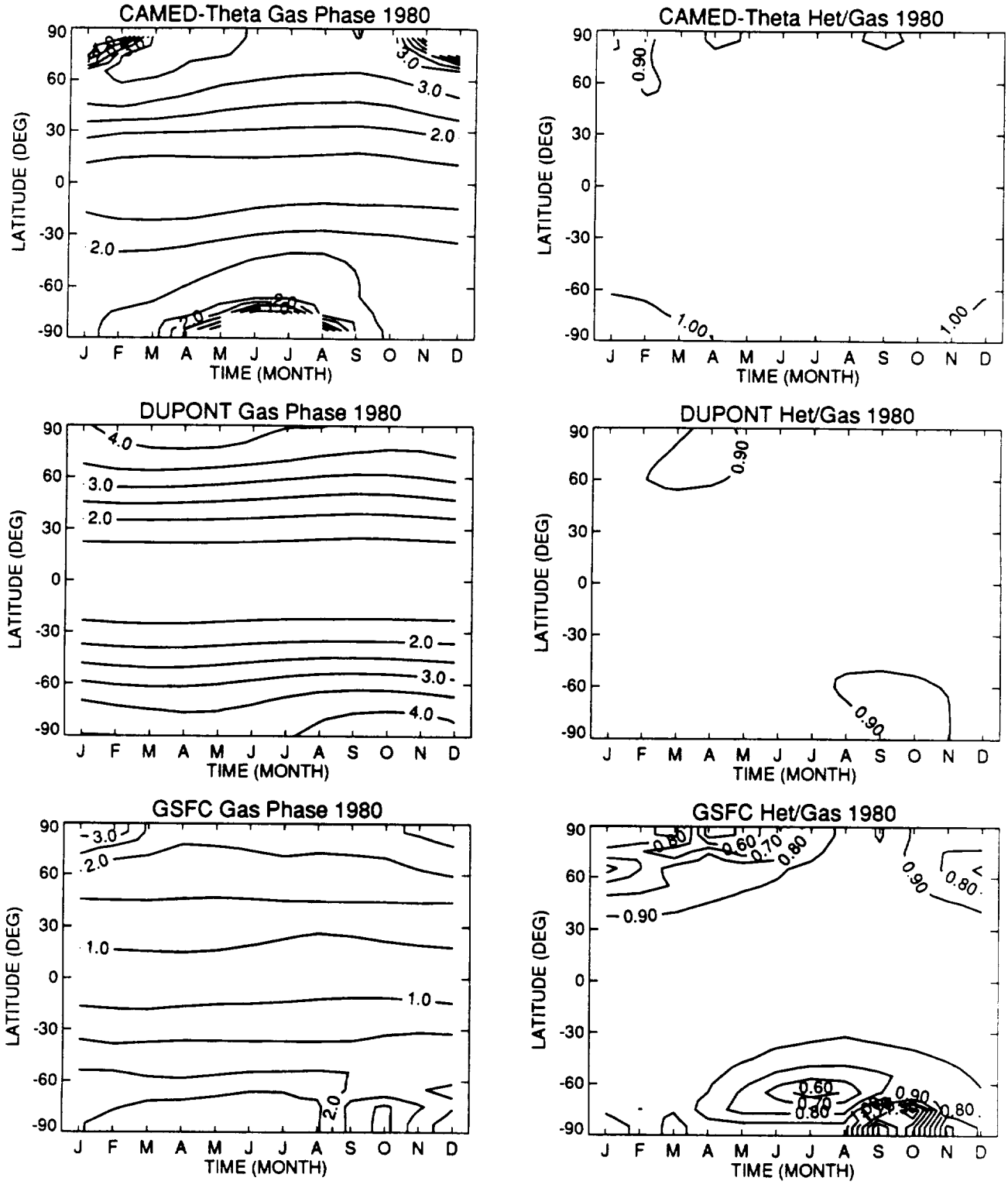

Figure G-4

HCl Column Density

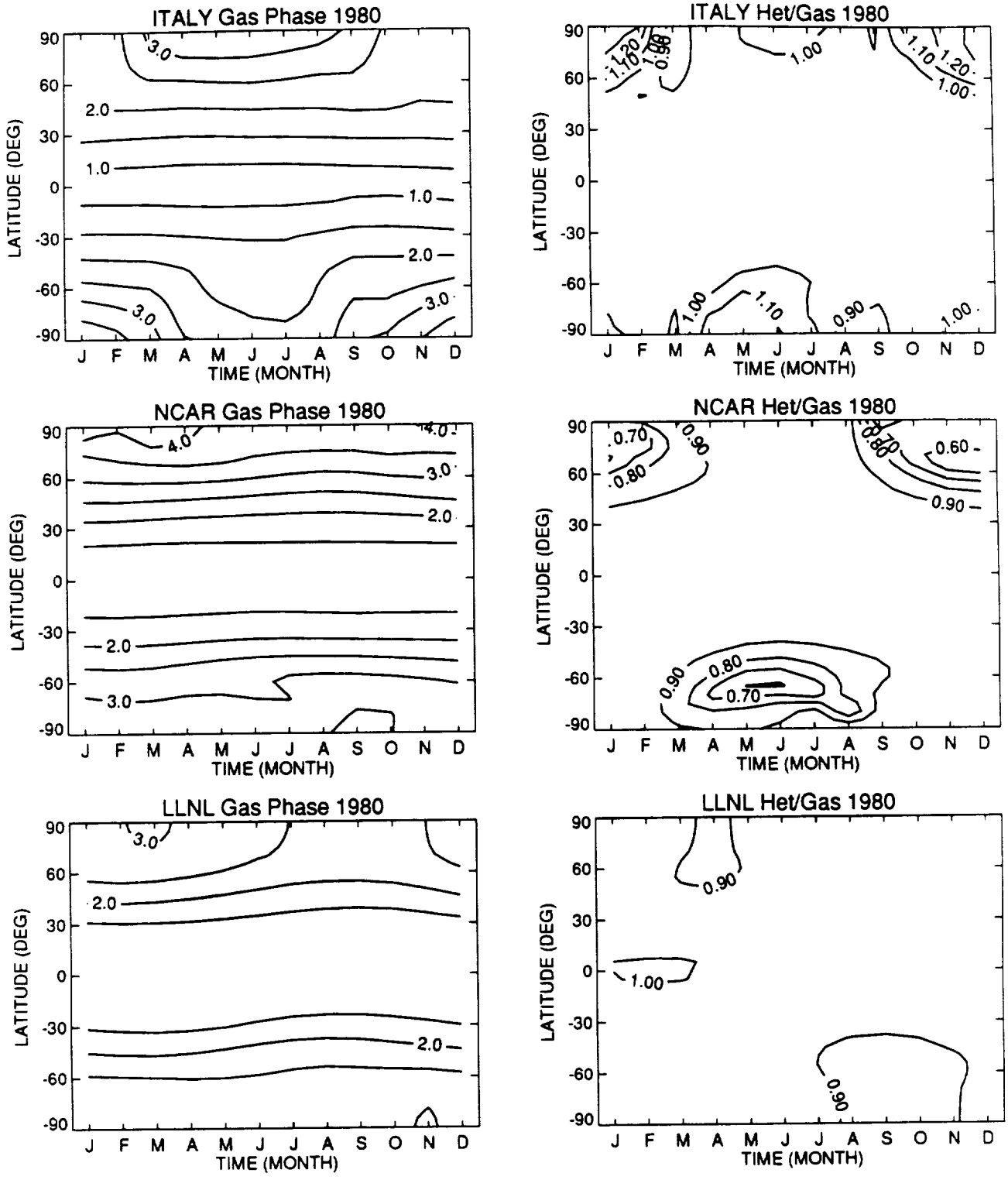

Figure G-4 (cont.)

HCl Column Density

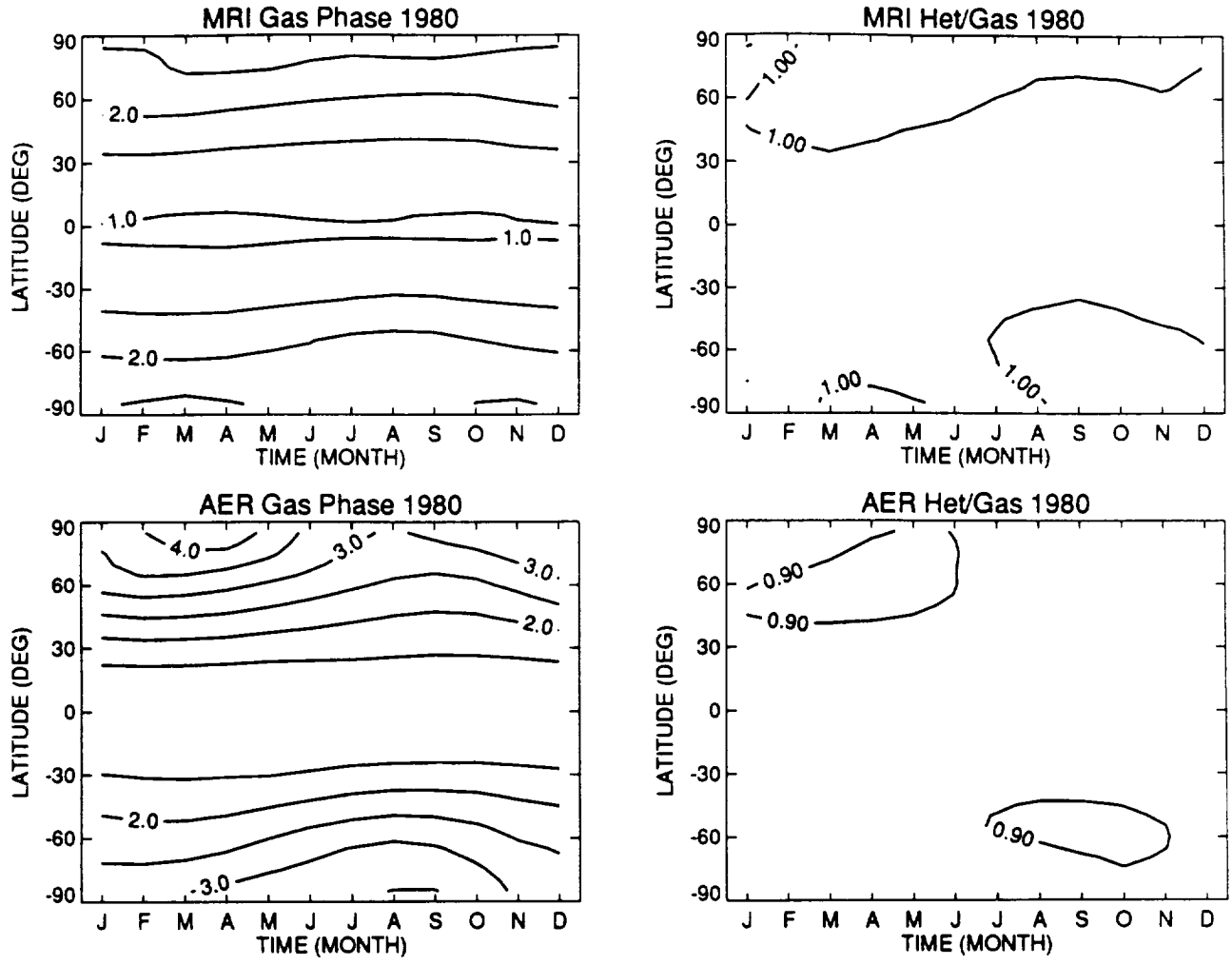

Figure G-4 (cont.)

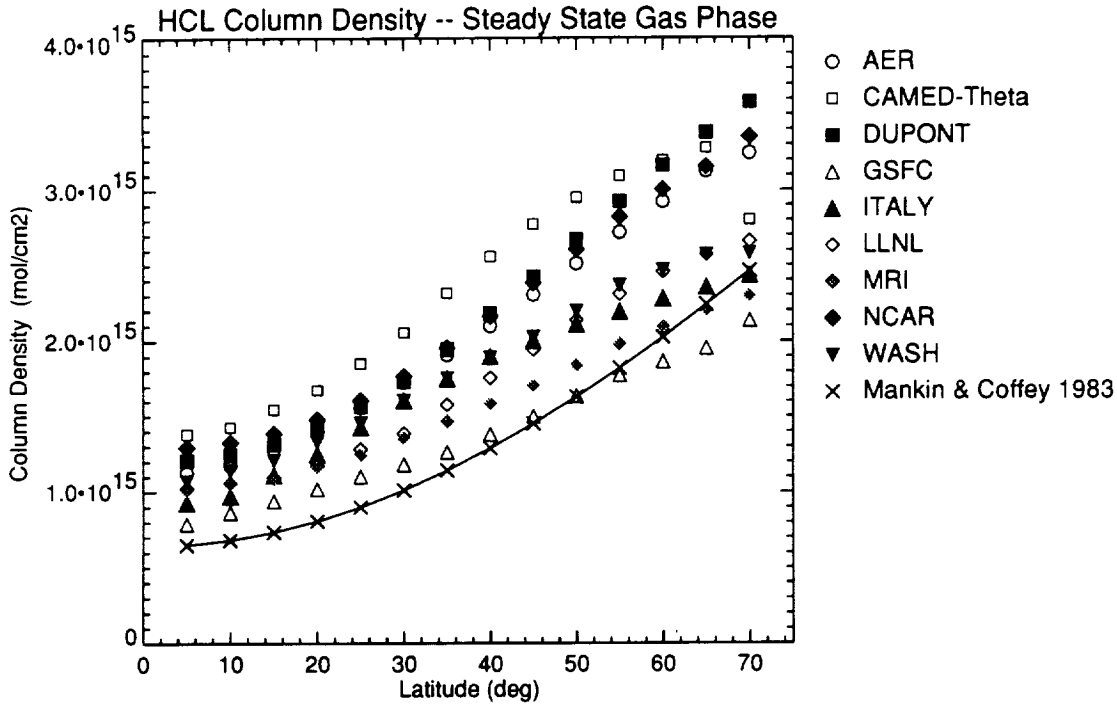

Figure G-5

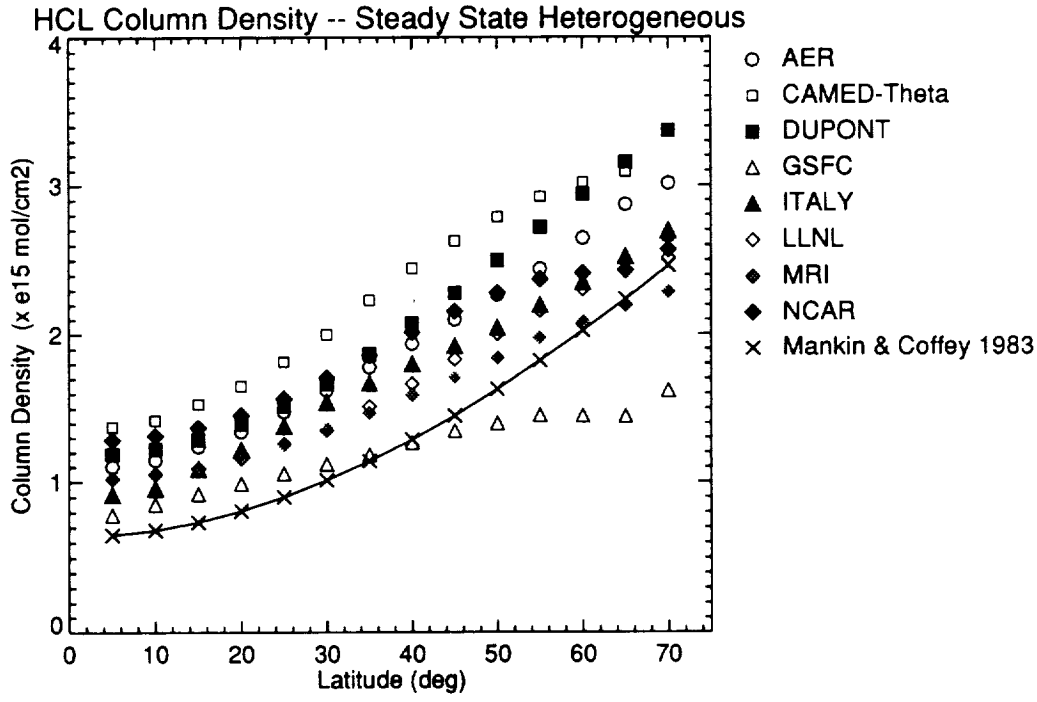

Figure G-6

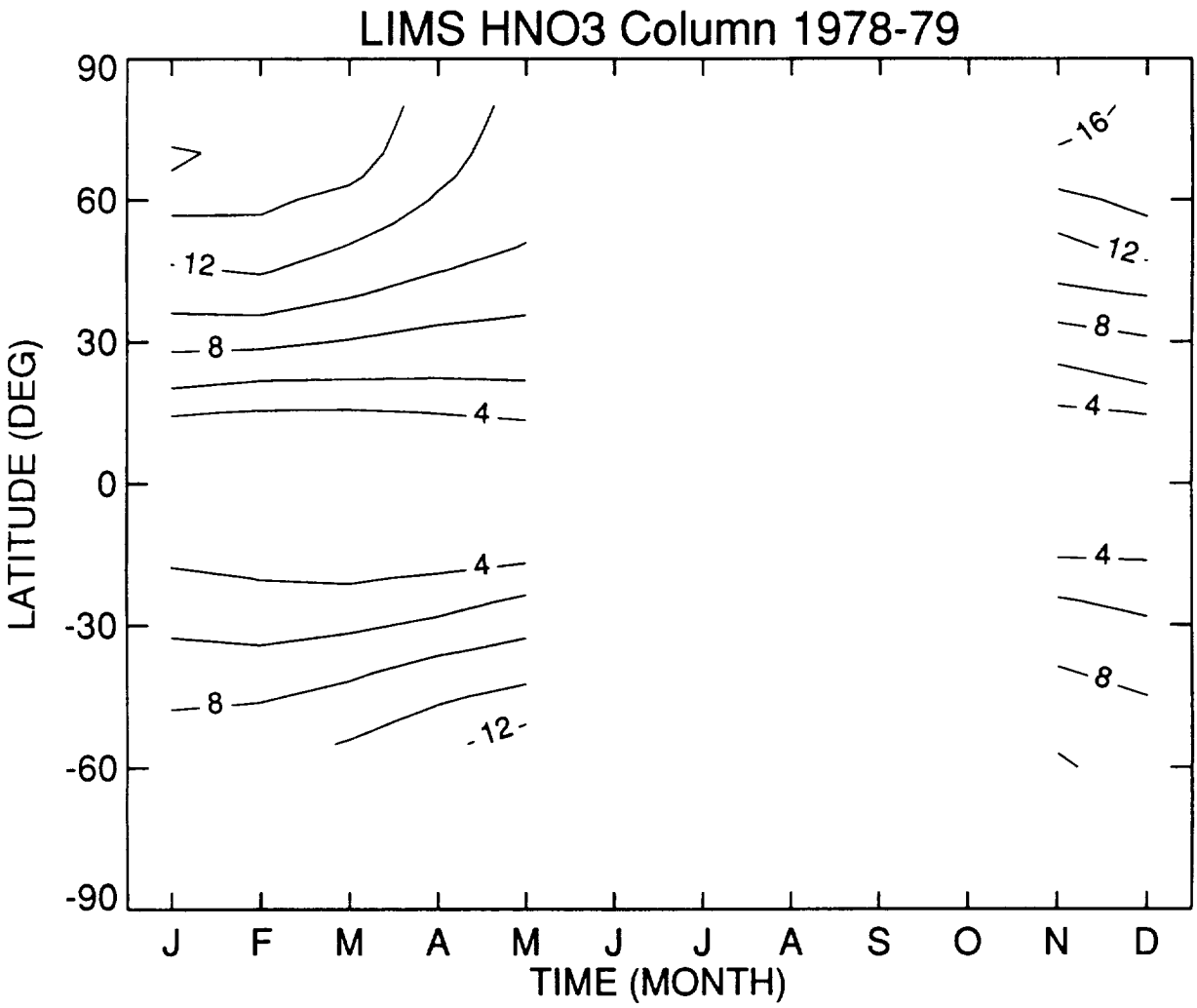
LIMS HNO3 Column 1978-79
90
60
30
0
-30
-60
-90
LATITUDE (DEG)
J
F
M
A
M
J
J
A
S
O
N
D
TIME (MONTH)
16
12
8
4
4
8
12
16
12
8
4
4
8

Figure G-7

HNO3 Column Density

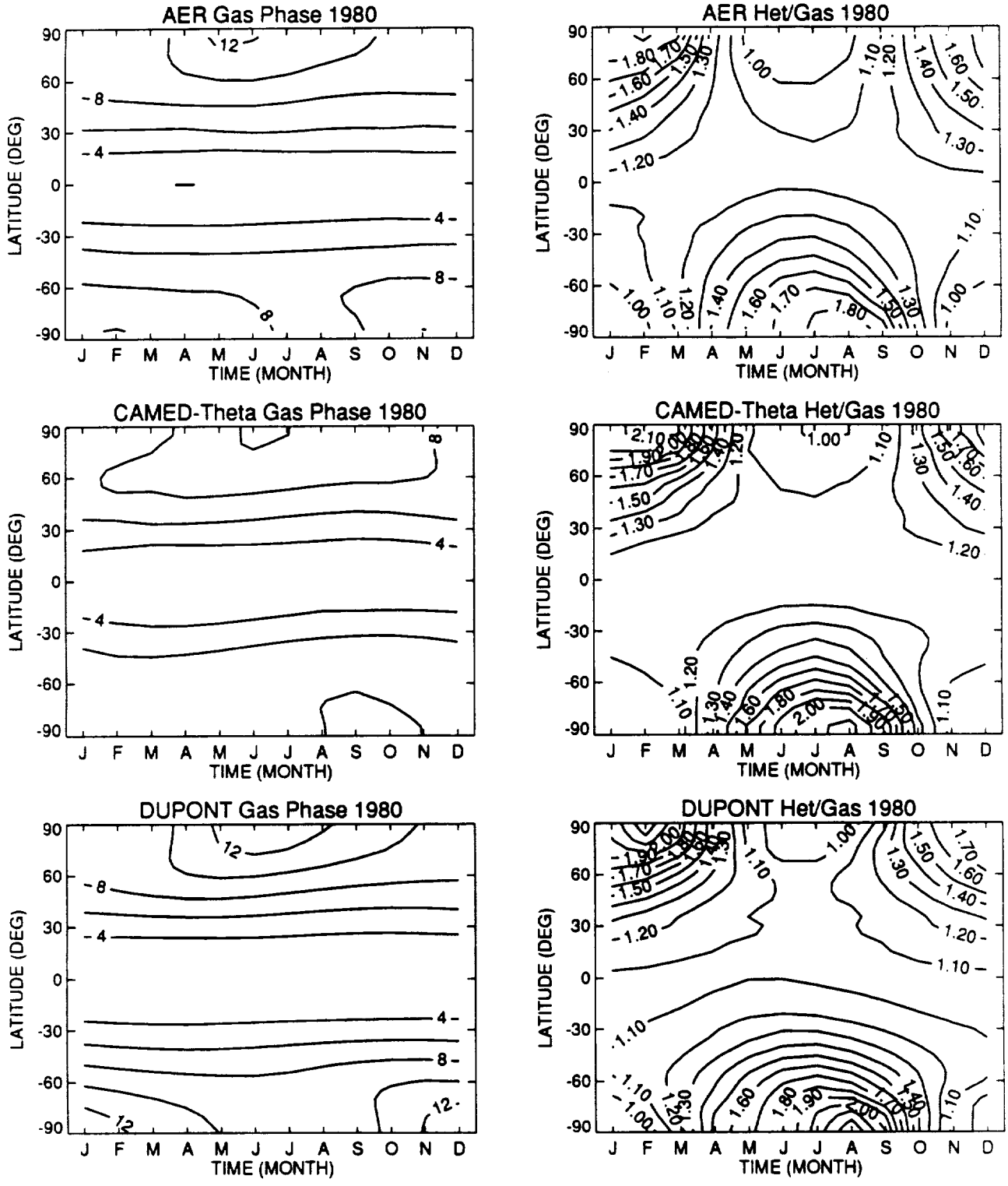

Figure G-8

HNO3 Column Density

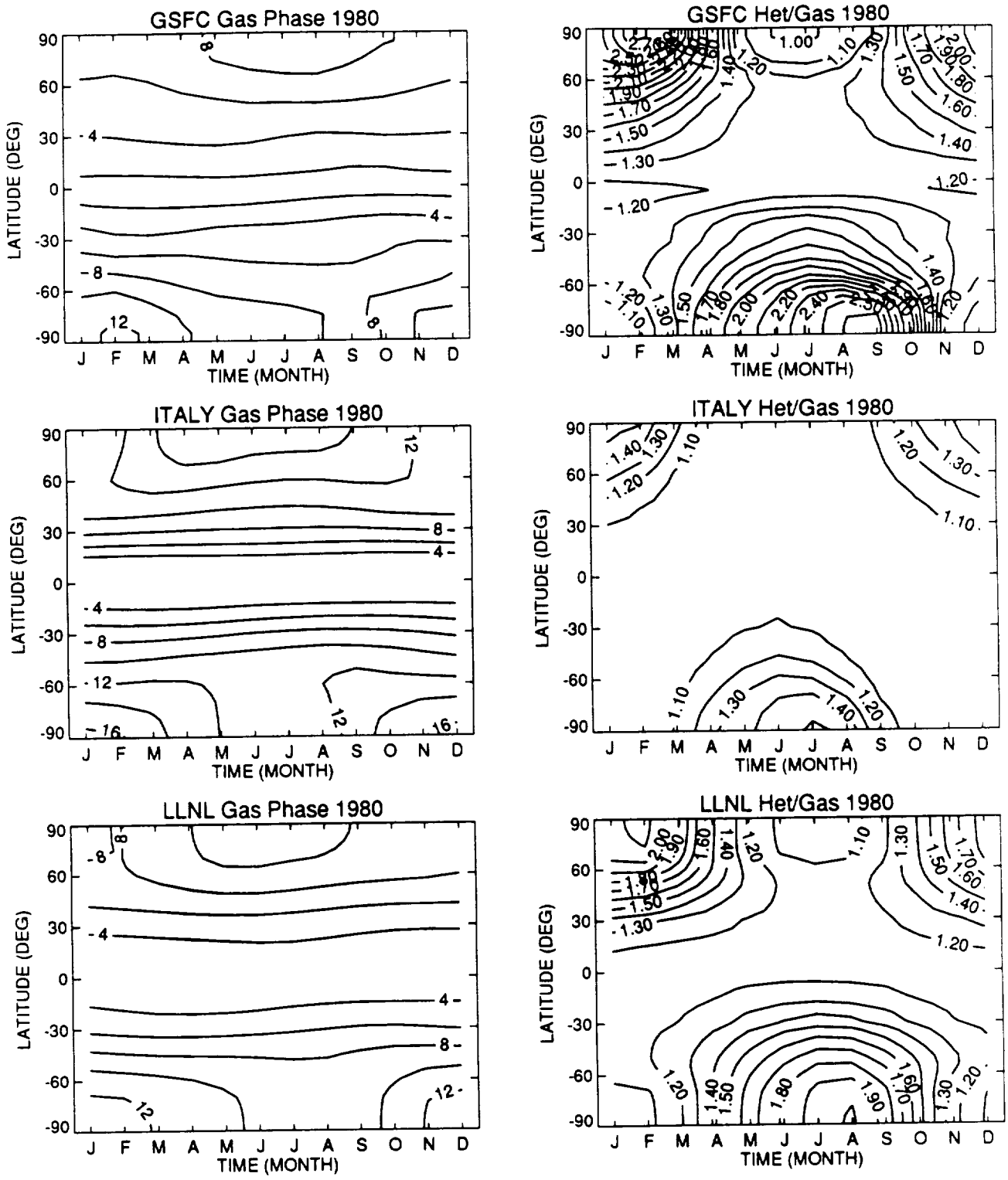

Figure G-8 (cont.)

HNO3 Column Density

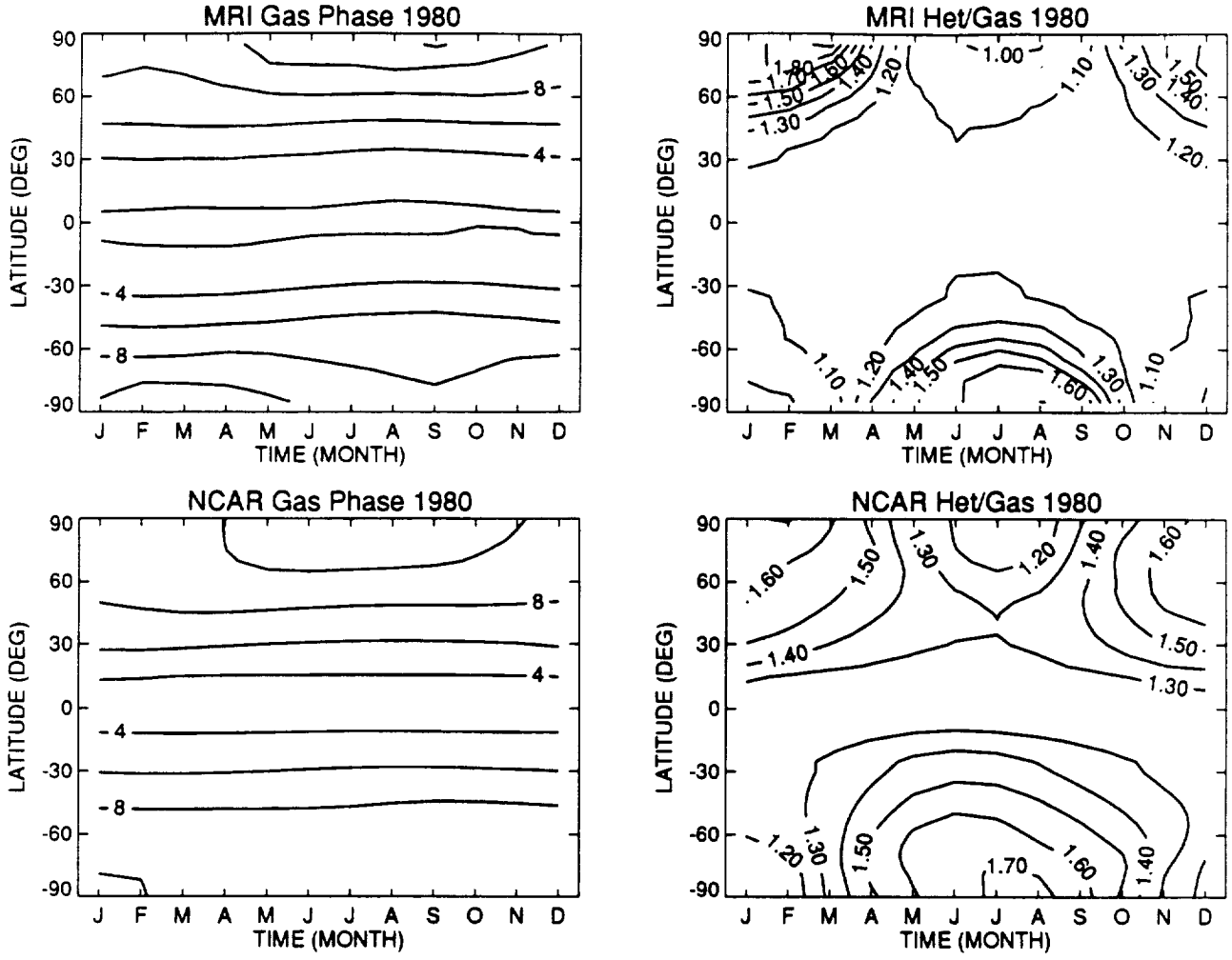

Figure G-8 (cont.)

HNO3 Column -- Model vs. LIMS Night

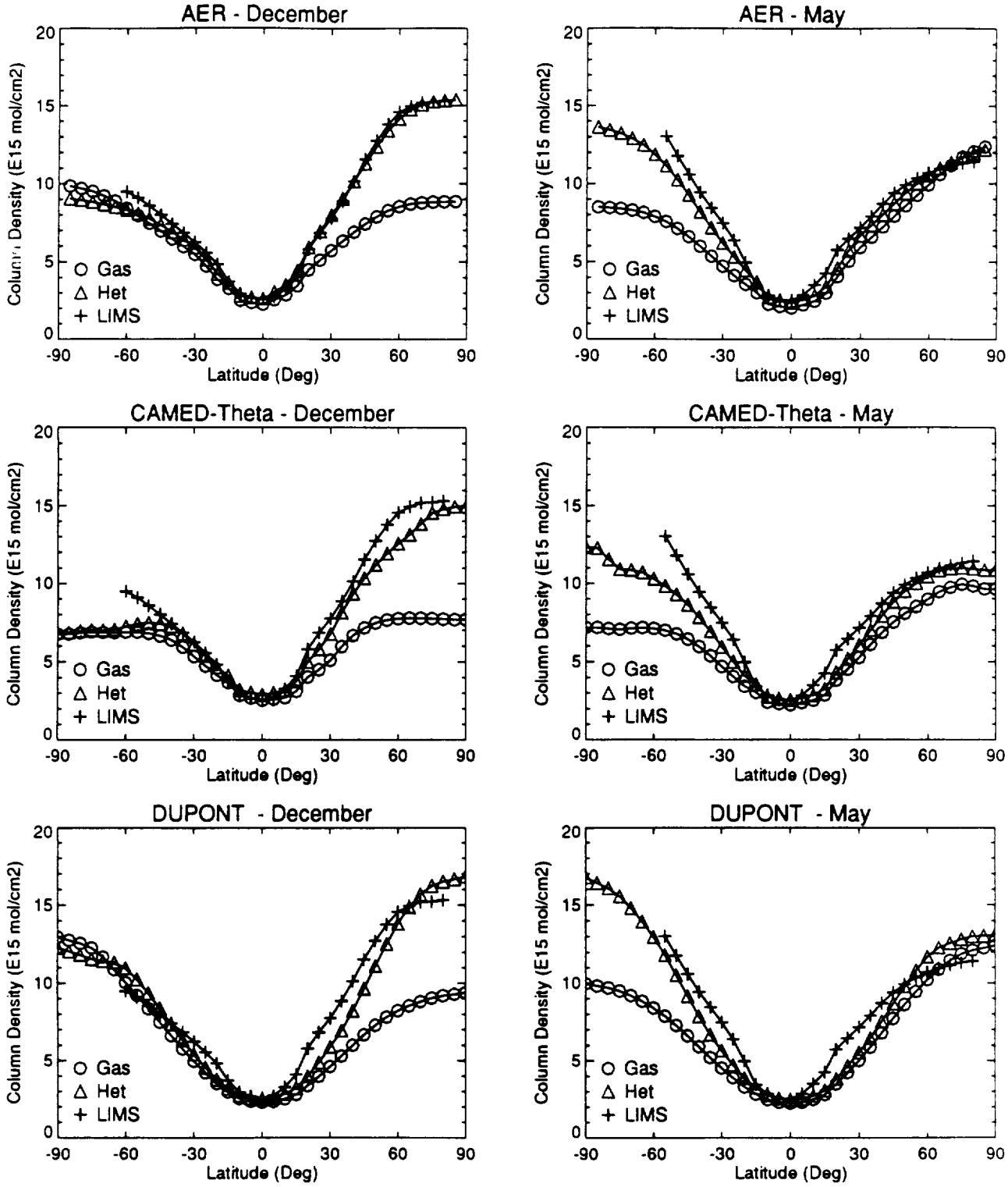

Figure G-9

HNO3 Column -- Model vs. LIMS Night

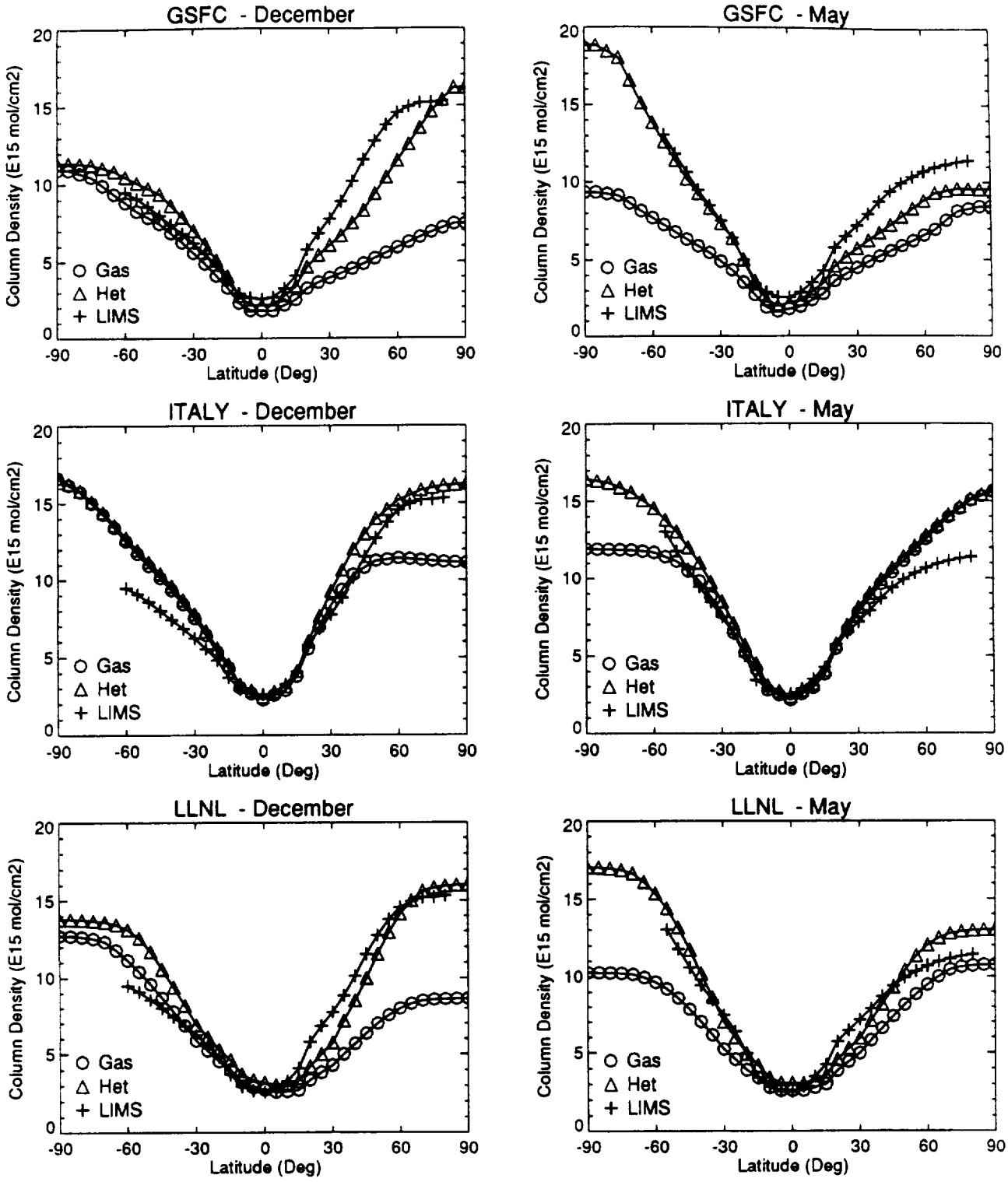

Figure G-9 (cont.)

HNO3 Column -- Model vs. LIMS Night

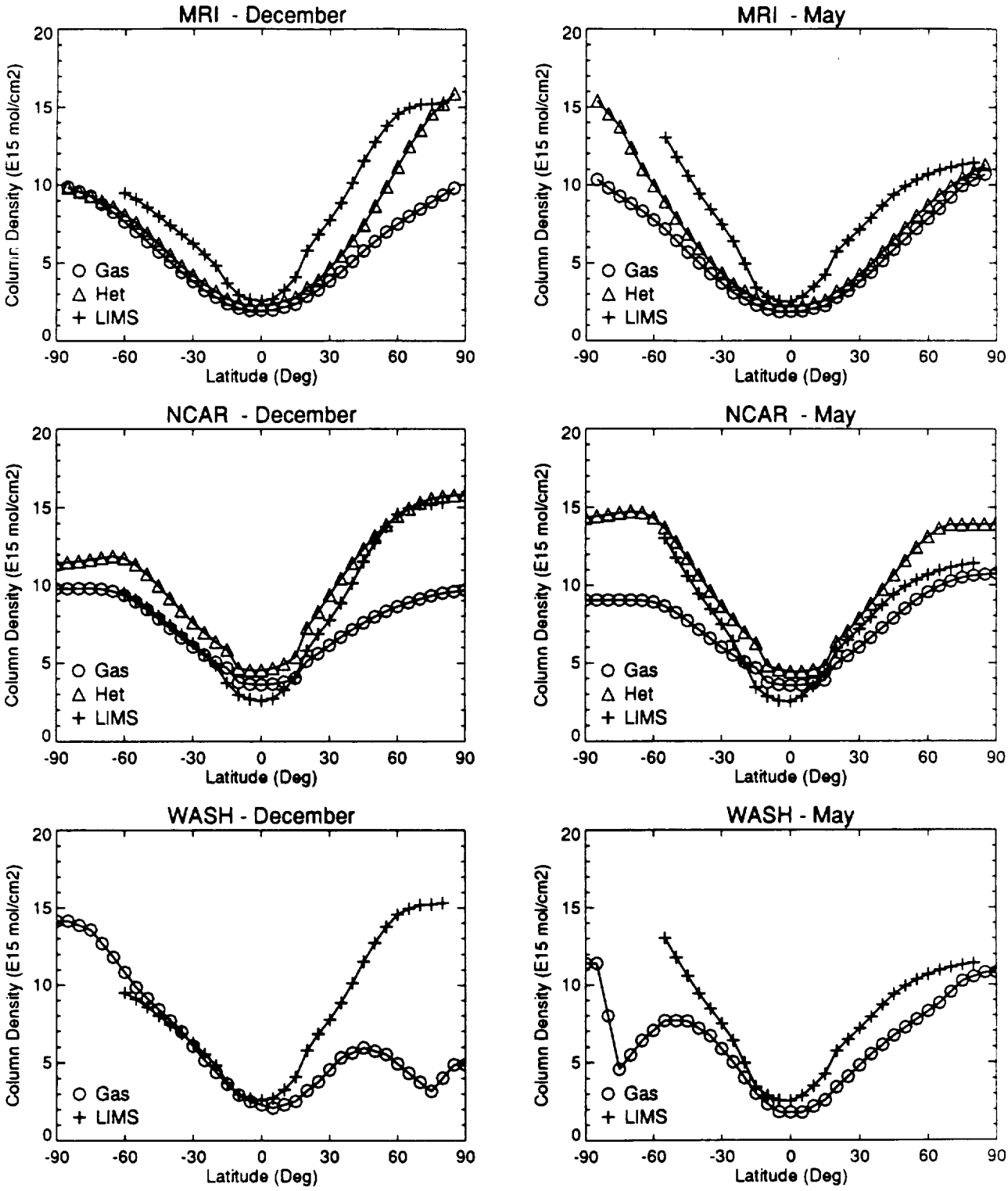

Figure G-9 (cont.)

HNO3 Near Latitude 45N

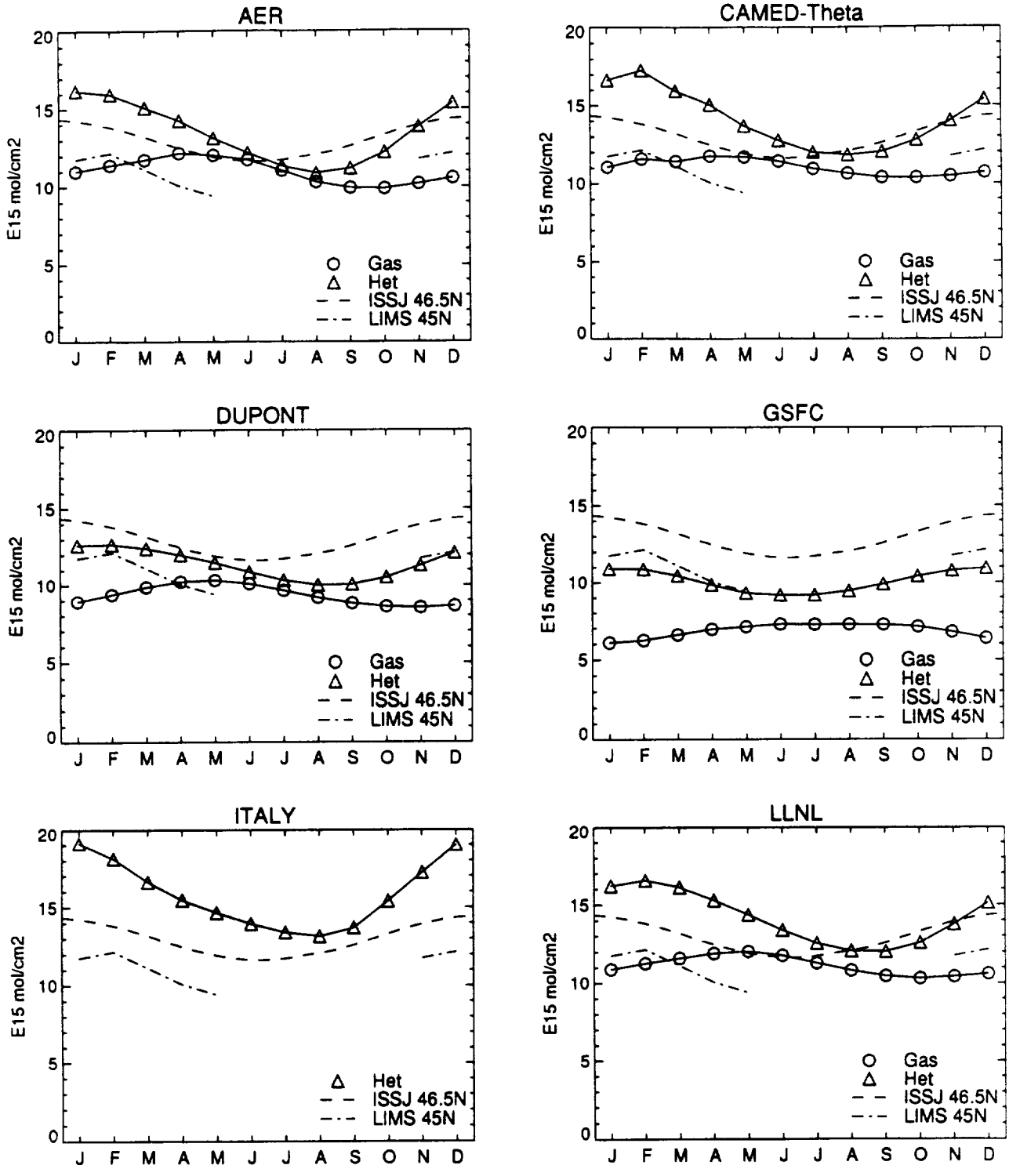

Figure G-10

HNO3 Near Latitude 45N

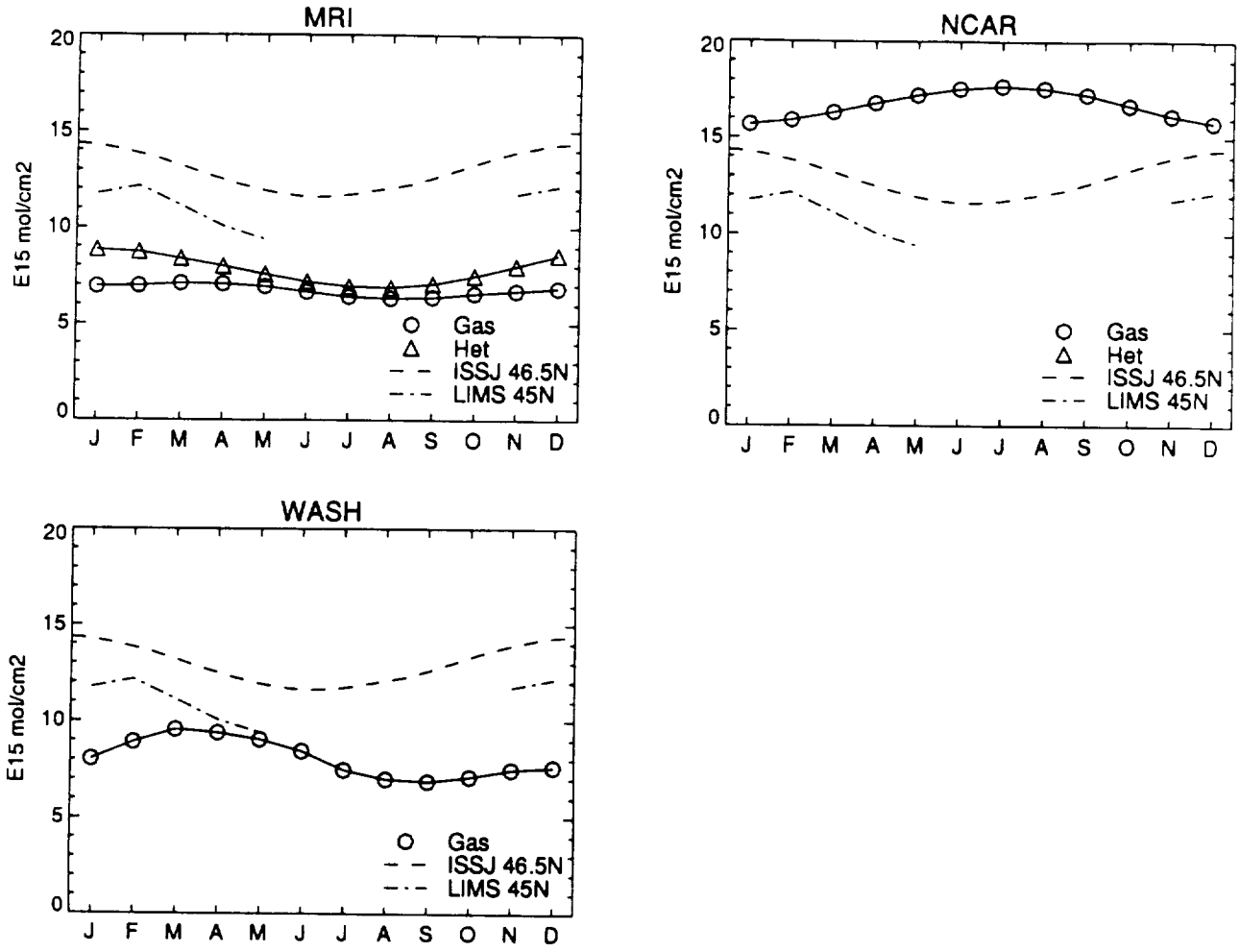

Figure G-10 (cont.)

ClONO2 at Latitude = 45N

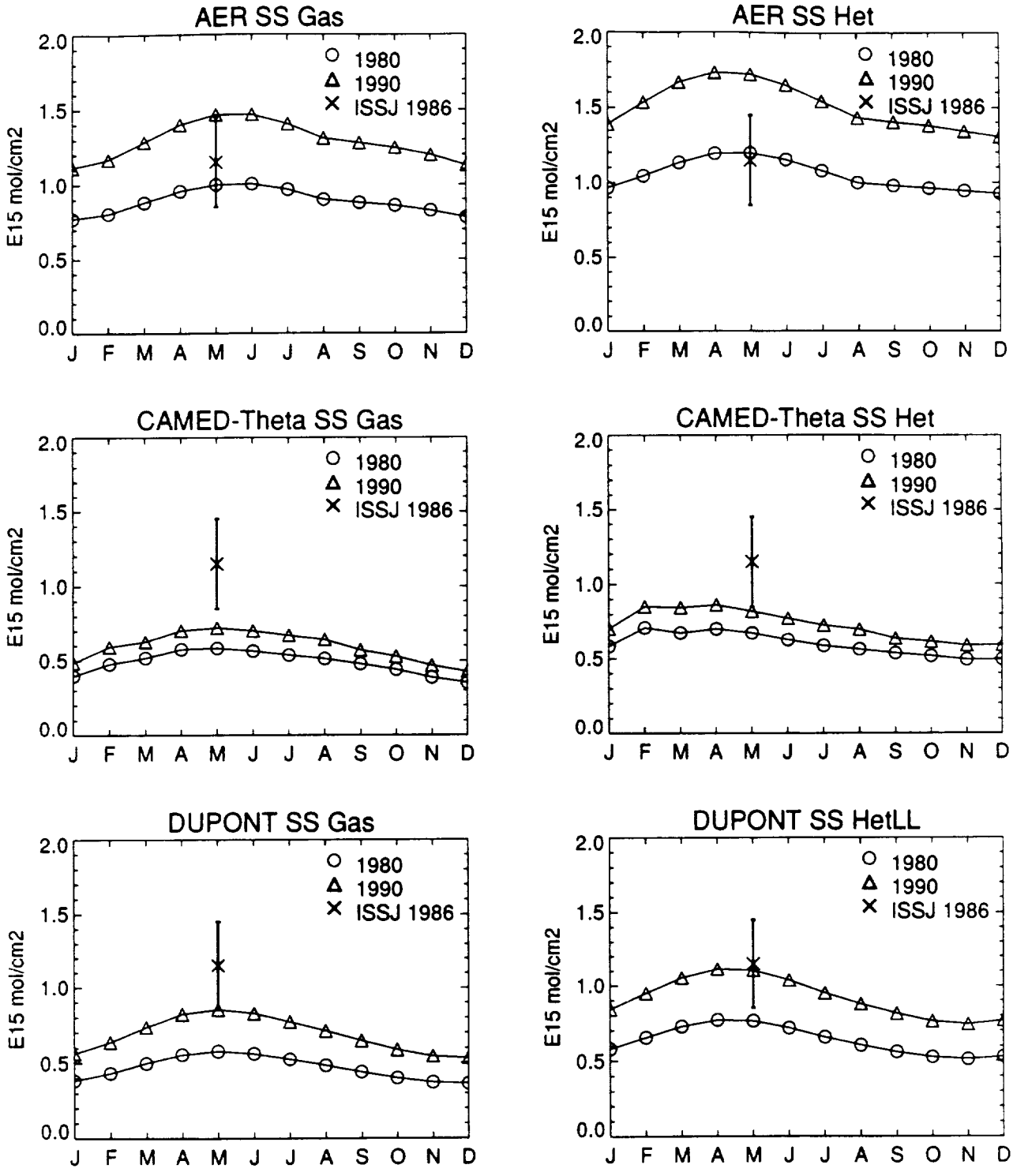

Figure G-11

ClONO2 at Latitude = 45N

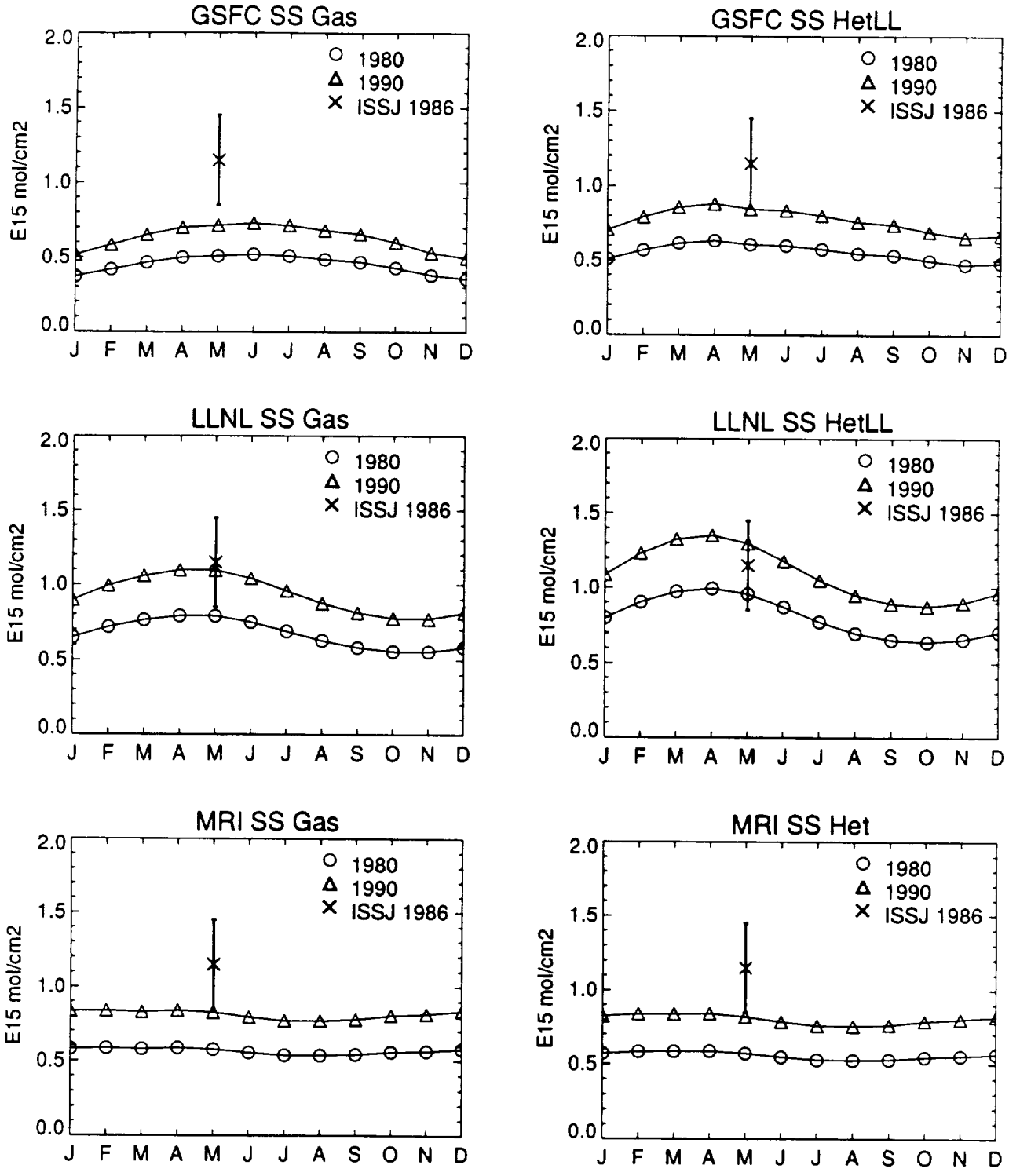

Figure G-11 (cont.)

ClONO2 at Latitude = 45N

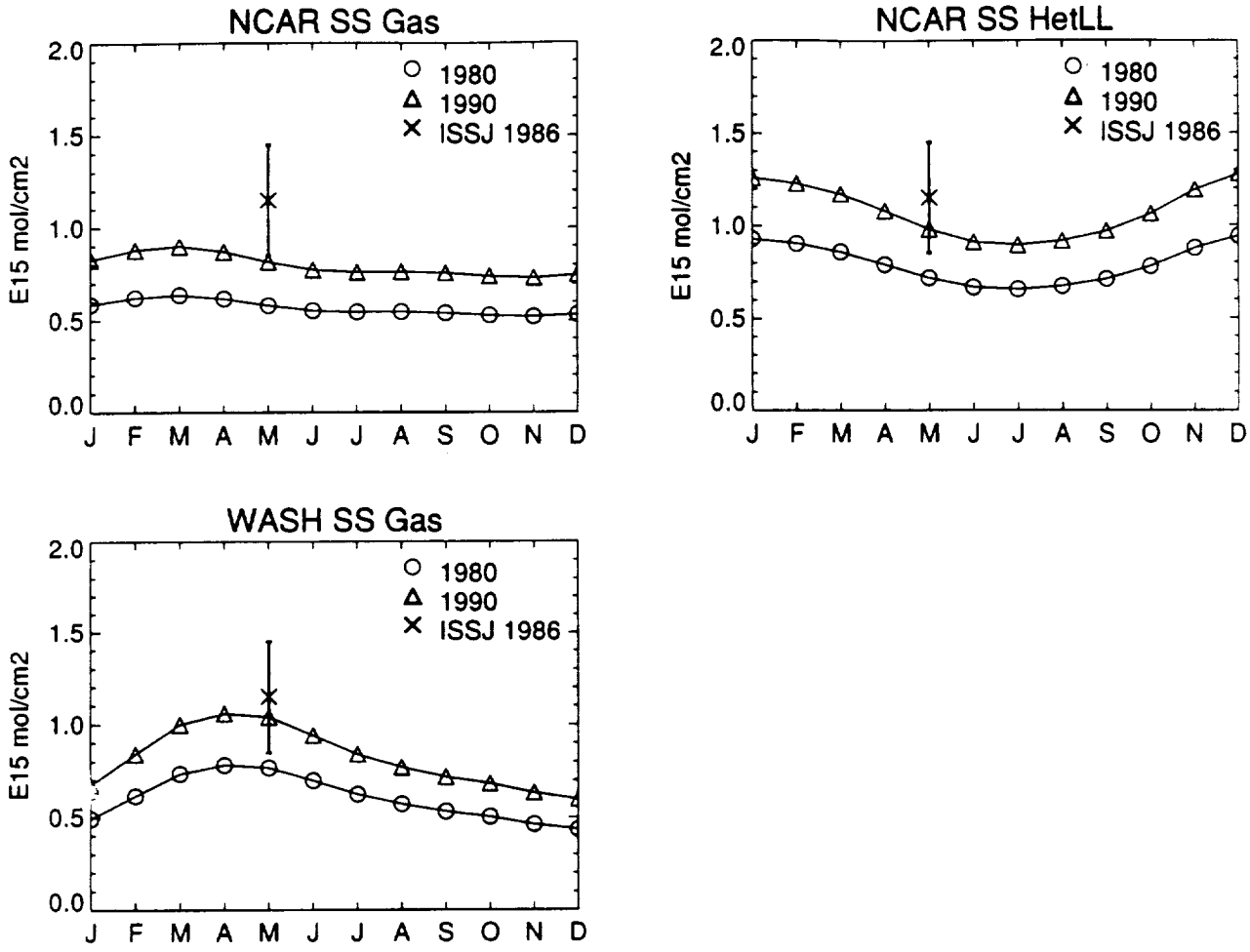

Figure G-11 (cont.)

NO2 Column Density

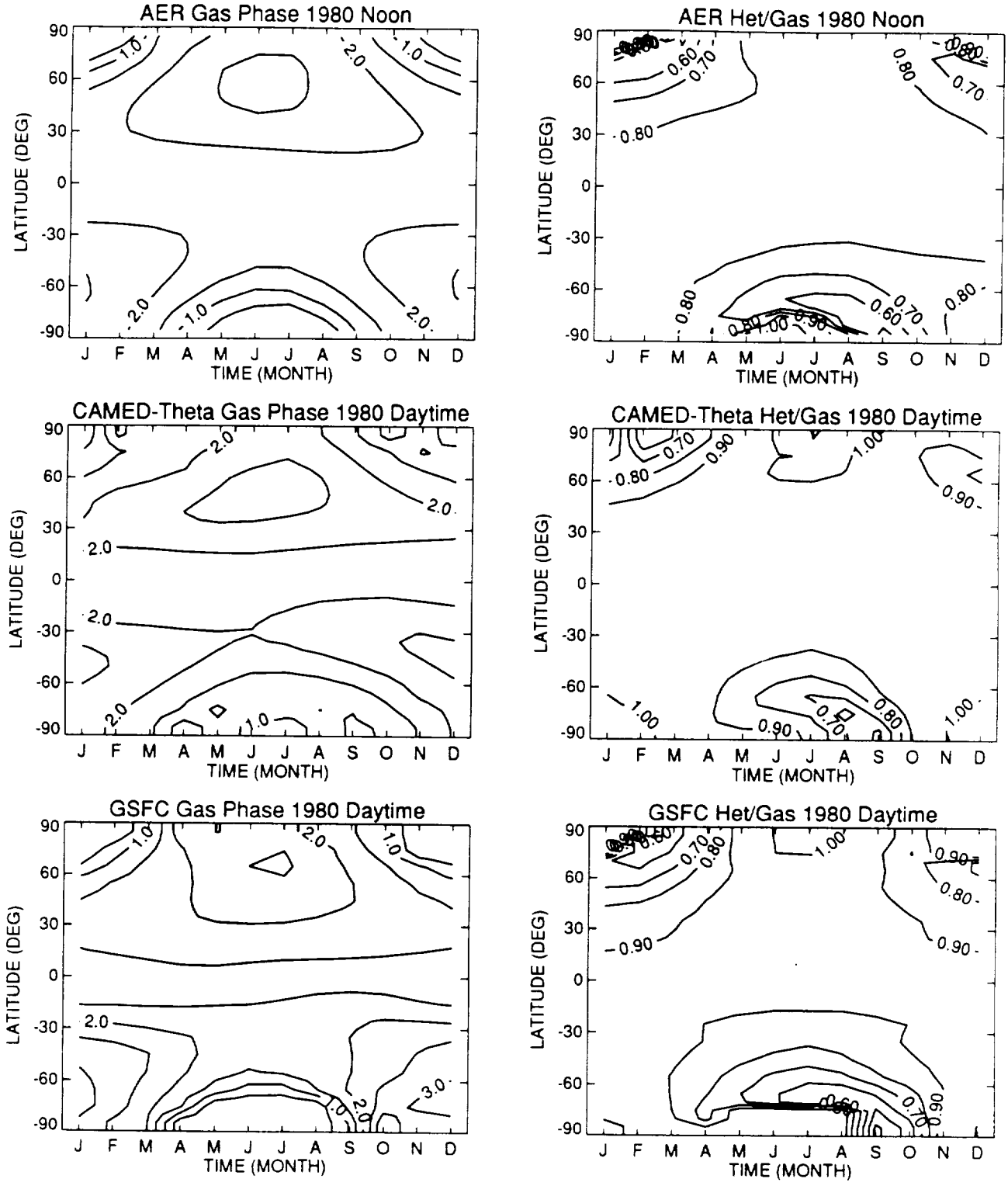

Figure G-12

NO2 Column Density

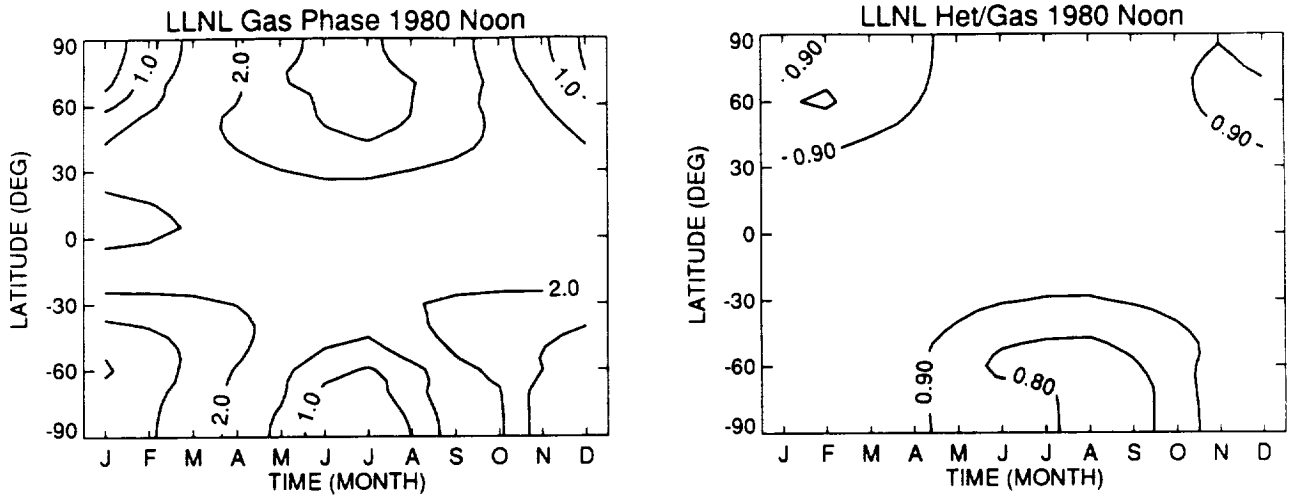

Figure G-12 (cont.)

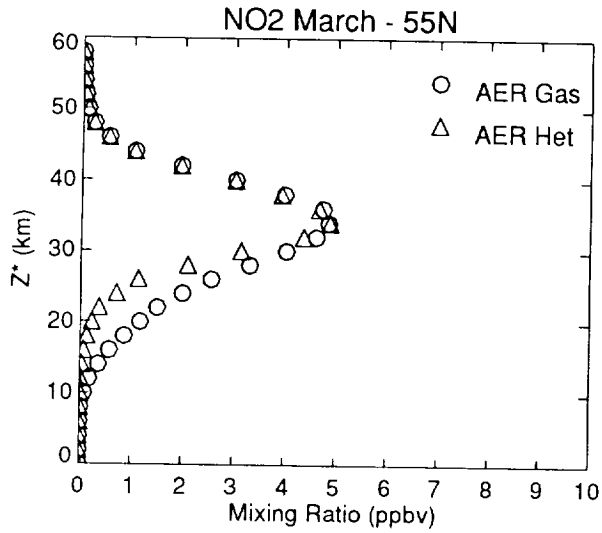
NO2 March - 55N
AER Gas
AER Het
Z* (km)
Mixing Ratio (ppbv)

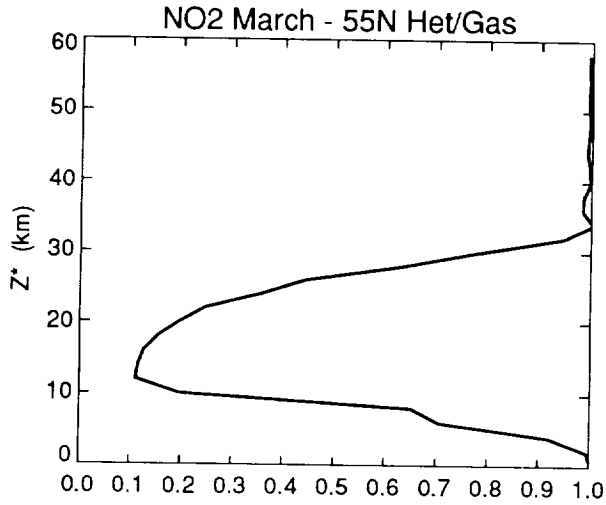
NO2 March - 55N Het/Gas
Z* (km)

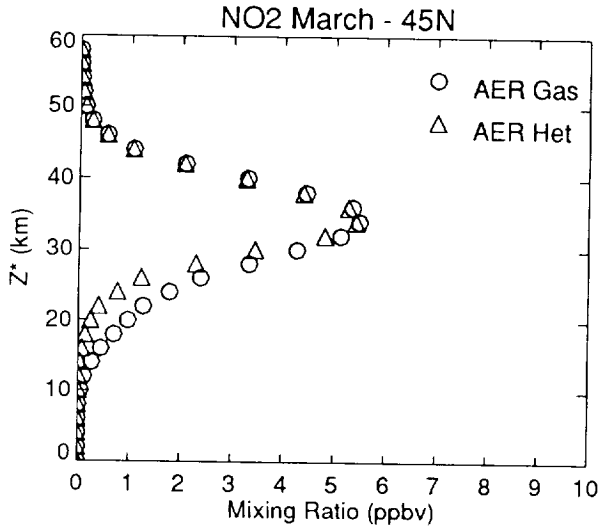
NO2 March - 45N
AER Gas
AER Het
Z* (km)
Mixing Ratio (ppbv)

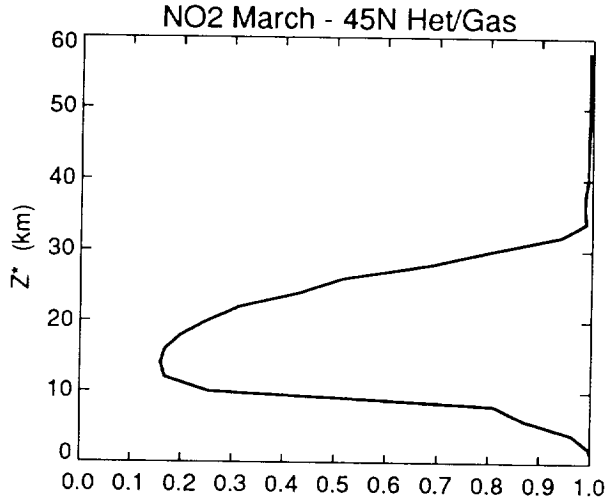
NO2 March - 45N Het/Gas
Z* (km)

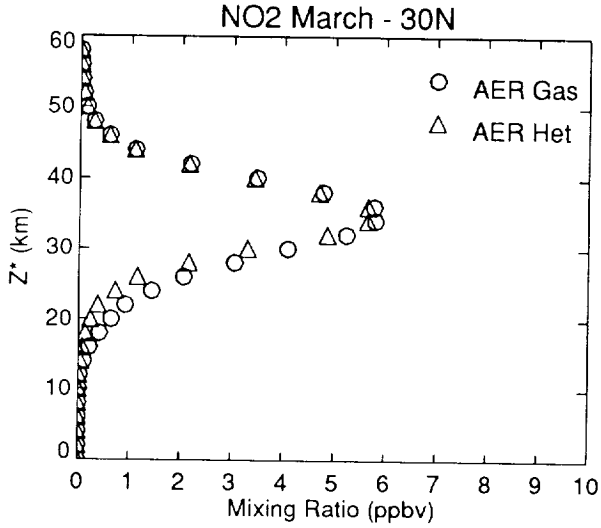
NO2 March - 30N
AER Gas
AER Het
Z* (km)
Mixing Ratio (ppbv)

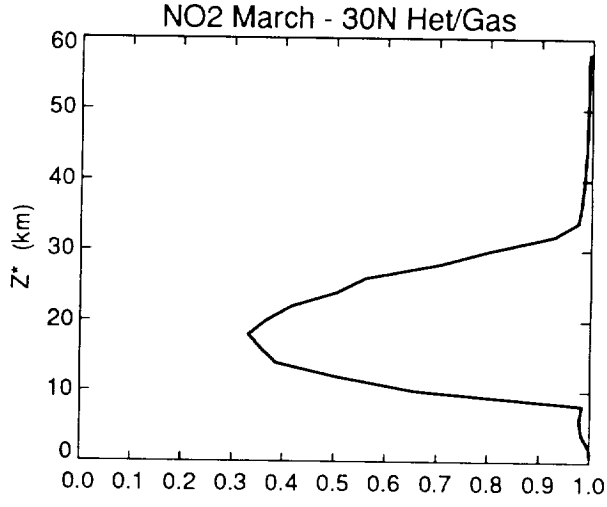
NO2 March - 30N Het/Gas
Z* (km)

Figure G-13

NO2 Column -- Model vs. LIMS Day

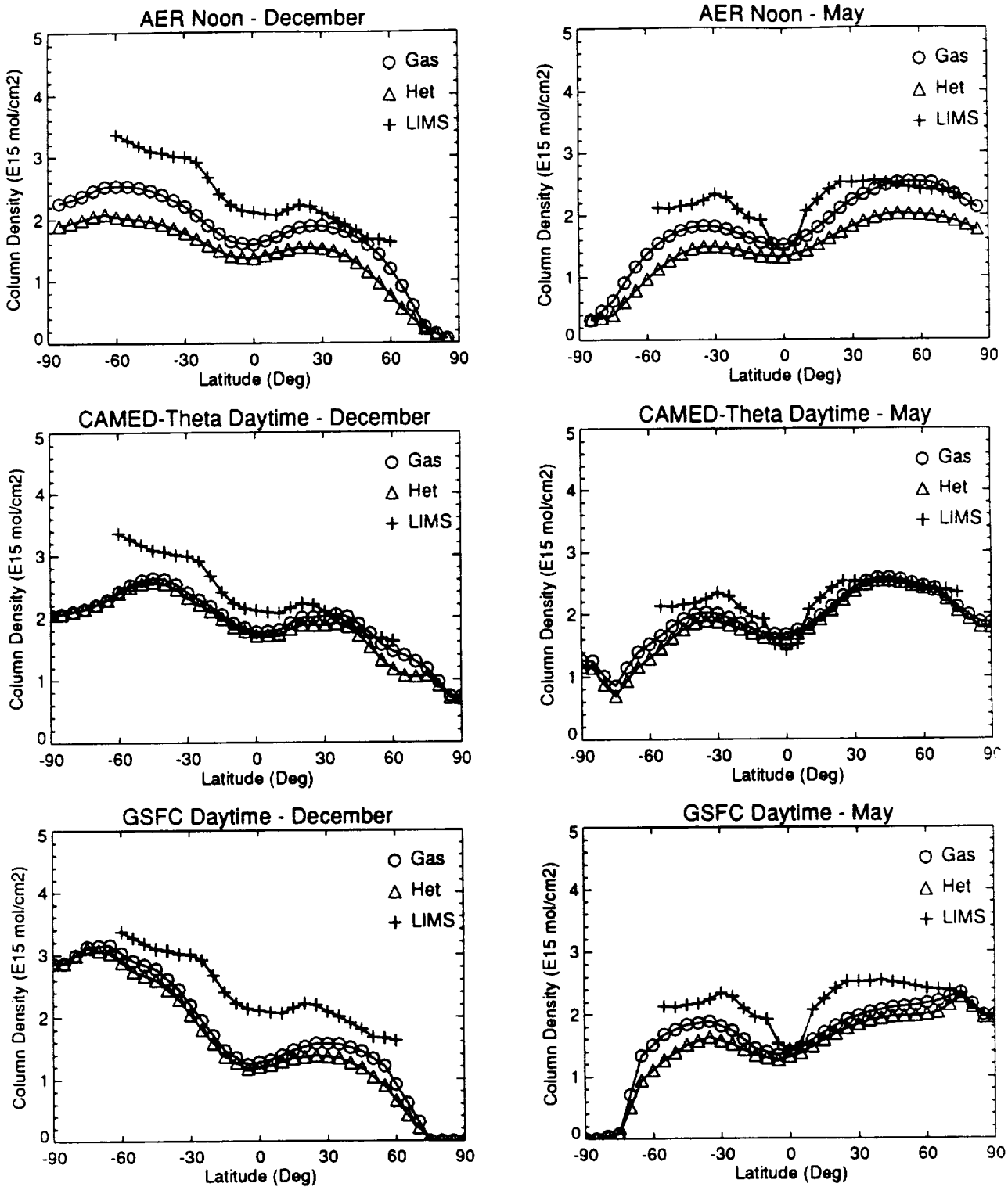

Figure G-14

NO2 Column -- Model vs. LIMS Day

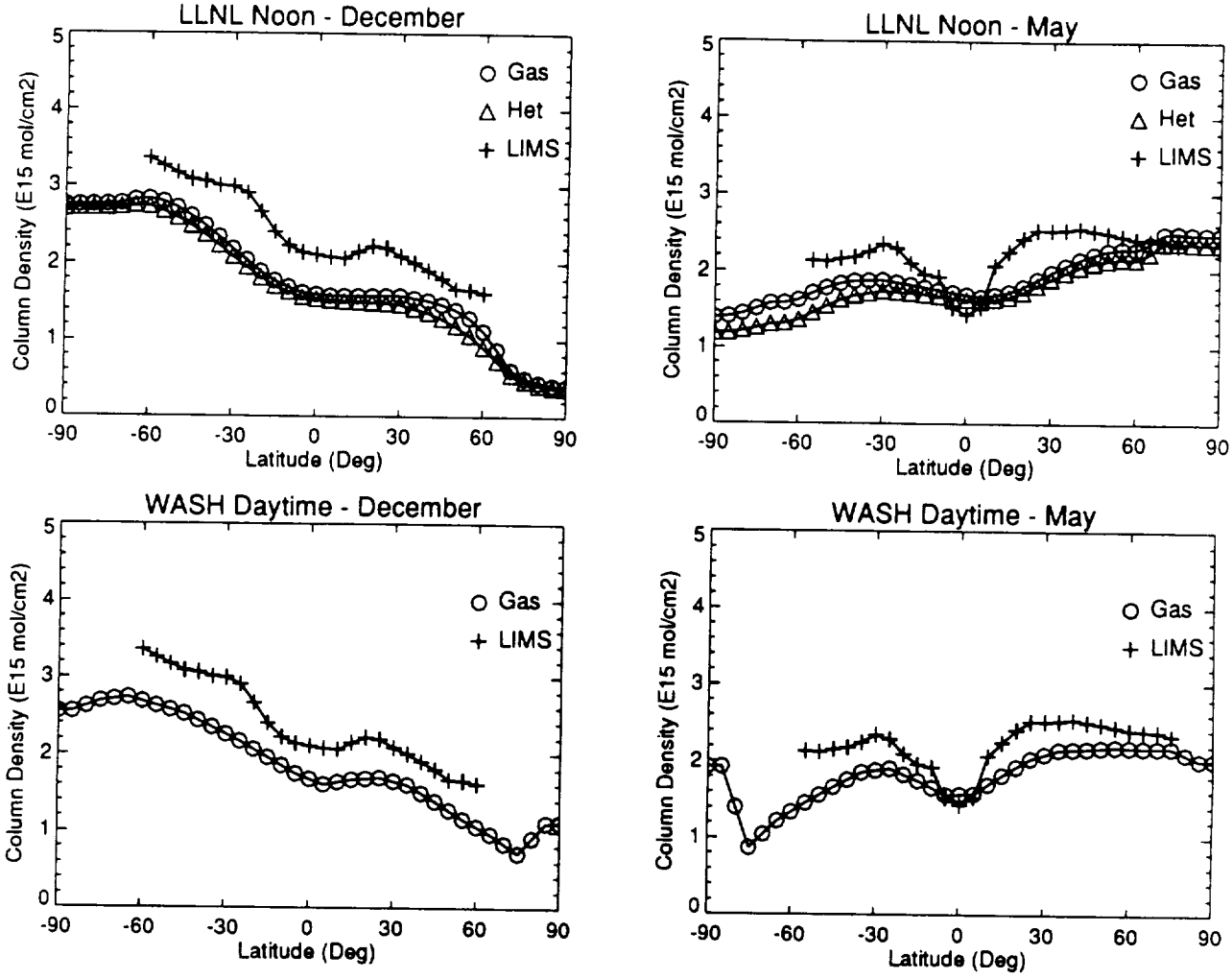

Figure G-14 (cont.)

NASA

Report Documentation Page

1. Report No.	2. Government Accession No.	3. Recipient's Catalog No.
NASA RP-1292, Vol. II		

4. Title and Subtitle

The Atmospheric Effects of Stratospheric Aircraft:
Report of the 1992 Models and Measurements Workshop
Volume II—Comparisons With Global Atmospheric Measurements

5. Report Date
March 1993

6. Performing Organization Code

7. Author(s)
Michael J. Prather and Ellis E. Remsberg, Editors

8. Performing Organization Report No.

10. Work Unit No.

9. Performing Organization Name and Address
NASA Office of Space Science and Applications
Earth Science and Applications Division

11. Contract or Grant No.

12. Sponsoring Agency Name and Address
National Aeronautics and Space Administration
Washington, DC 20546

13. Type of Report and Period Covered
Reference Publication

14. Sponsoring Agency Code

15. Supplementary Notes

Prather: NASA Office of Space Science and Applications, Washington, D.C.;
Remsberg: Langley Research Center, Hampton, VA.

16. Abstract

This Workshop on Stratospheric Models and Measurements (M&M) marks a significant expansion in the history of model intercomparisons. It provides a foundation for establishing the credibility of stratospheric models used in environmental assessments of chlorofluorocarbons, aircraft emissions, and climate-chemistry interactions. The core of the M&M comparisons involves the selection of observations of the current stratosphere (i.e., within the last 15 years): these data are believed to be accurate and representative of certain aspects of stratospheric chemistry and dynamics that the models should be able to simulate.

17. Key Words (Suggested by Author(s))	18. Distribution Statement
The stratosphere; Observations; Chemical models; Dynamical models; Ozone	Unclassified - Unlimited Subject Category 45

19. Security Classif. (of this report)	20. Security Classif. (of this page)	21. No. of pages	22. Price
Unclassified	Unclassified	268	A12

NASA FORM 1626 OCT 86